



University of Kentucky
UKnowledge

Theses and Dissertations--Chemical and
Materials Engineering

Chemical and Materials Engineering

2016

SYNTHESIS OF TITANIA THIN FILMS WITH CONTROLLED MESOPORE ORIENTATION: NANOSTRUCTURE FOR ENERGY CONVERSION AND STORAGE

Suraj R. Nagpure

University of Kentucky, suraj.nagpure@uky.edu

Digital Object Identifier: <http://dx.doi.org/10.13023/ETD.2016.381>

[Right click to open a feedback form in a new tab to let us know how this document benefits you.](#)

Recommended Citation

Nagpure, Suraj R., "SYNTHESIS OF TITANIA THIN FILMS WITH CONTROLLED MESOPORE ORIENTATION: NANOSTRUCTURE FOR ENERGY CONVERSION AND STORAGE" (2016). *Theses and Dissertations--Chemical and Materials Engineering*. 67.

https://uknowledge.uky.edu/cme_etds/67

This Doctoral Dissertation is brought to you for free and open access by the Chemical and Materials Engineering at UKnowledge. It has been accepted for inclusion in Theses and Dissertations--Chemical and Materials Engineering by an authorized administrator of UKnowledge. For more information, please contact UKnowledge@lsv.uky.edu.

STUDENT AGREEMENT:

I represent that my thesis or dissertation and abstract are my original work. Proper attribution has been given to all outside sources. I understand that I am solely responsible for obtaining any needed copyright permissions. I have obtained needed written permission statement(s) from the owner(s) of each third-party copyrighted matter to be included in my work, allowing electronic distribution (if such use is not permitted by the fair use doctrine) which will be submitted to UKnowledge as Additional File.

I hereby grant to The University of Kentucky and its agents the irrevocable, non-exclusive, and royalty-free license to archive and make accessible my work in whole or in part in all forms of media, now or hereafter known. I agree that the document mentioned above may be made available immediately for worldwide access unless an embargo applies.

I retain all other ownership rights to the copyright of my work. I also retain the right to use in future works (such as articles or books) all or part of my work. I understand that I am free to register the copyright to my work.

REVIEW, APPROVAL AND ACCEPTANCE

The document mentioned above has been reviewed and accepted by the student's advisor, on behalf of the advisory committee, and by the Director of Graduate Studies (DGS), on behalf of the program; we verify that this is the final, approved version of the student's thesis including all changes required by the advisory committee. The undersigned agree to abide by the statements above.

Suraj R. Nagpure, Student

Dr. Stephen E. Rankin, Major Professor

Dr. Thomas D. Dziubla, Director of Graduate Studies

SYNTHESIS OF TITANIA THIN FILMS WITH CONTROLLED
MESOPORE ORIENTATION: NANOSTRUCTURE FOR ENERGY
CONVERSION AND STORAGE

DISSERTATION

A dissertation submitted in partial fulfillment of the
requirements for the degree of Doctor of Philosophy in the
College of Engineering at the University of Kentucky

By

Suraj R. Nagpure

Lexington, KY

Director: Dr. Stephen E. Rankin, Professor of Chemical Engineering

Lexington, Kentucky

2016

Copyright © Suraj R. Nagpure 2016

ABSTRACT OF DISSERTATION

SYNTHESIS OF TITANIA THIN FILMS WITH CONTROLLED MESOPORE ORIENTATION: NANOSTRUCTURE FOR ENERGY CONVERSION AND STORAGE

This dissertation addresses the synthesis mechanism of mesoporous titania thin films with 2D Hexagonal Close Packed (HCP) cylindrical nanopores by an evaporation-induced self-assembly (EISA) method with Pluronic surfactants P123 and F127 as structure directing agents, and their applications in photovoltaics and lithium ion batteries. To provide orthogonal alignment of the pores, surface modification of substrates with crosslinked surfactant has been used to provide a chemically neutral surface. GISAXS studies show not only that aging at 4 °C facilitates ordered mesostructure development, but also that aging at this temperature helps to provide orthogonal orientation of the cylindrical micelles which assemble into an ordered mesophase directly by a disorder-order transition. These films provide pores with 8-9 nm diameter, which is precisely the structure expected to provide short carrier diffusion length and high hole conductivity required for efficient bulk heterojunction solar cells. In addition, anatase titania is a n-type semiconductor with a band gap of +3.2 eV. Therefore, titania readily absorbs UV light with a wavelength below 387 nm. Because of this, these titania films can be used as window layers with a p-type semiconductor incorporated into the pores and at the top surface of the device to synthesize a photovoltaic cell. The pores provide opportunities to increase the surface area for contact between the two semiconductors, to align a p-type semiconductor at the junction, and to induce quantum confinement effects.

These titania films with hexagonal phase are infiltrated with a hole conducting polymer, poly(3-hexylthiophene) (P3HT), in order to create a p-n junctions for organic-inorganic hybrid solar cells, by spin coating followed by thermal annealing. This assembly is hypothesized to give better photovoltaic performance compared to disordered or bicontinuous cubic nanopore arrangements; confinement in cylindrical nanopores is expected to provide isolated, regioregular “wires” of conjugated polymers with tunable optoelectronic properties, such as improved hole conductivity over that in bicontinuous cubic structure. The kinetics of infiltration into the pores show that maximum infiltration occurs within less than one hour in these films, and give materials with improved photovoltaic performance relative to planar TiO₂/P3HT assemblies. These oriented mesoporous titania films are also used to develop an inorganic solar cell by depositing CdTe at the top using the Close Spaced Sublimation (CSS) technique. A power conversion efficiency of 5.53% is measured for heterostructures built using mesoporous titania films, which is significantly enhanced relative to planar TiO₂/CdTe devices and prior reports in the literature. These mesoporous titania films have a great potential in inorganic solar cell development and can potentially replace CdS window layers which are conventionally used in inorganic CdS-CdTe solar cells. The last part of the dissertation addresses layer-by-layer

synthesis to increase the thickness of mesoporous titania films with vertically oriented 2D-HCP nanopores, and their use in lithium ion batteries as negative electrodes because of advantages such as good cycling stability, small volume expansion (~3%) during intercalation/extraction and high discharge voltage plateau. The high surface area and small wall thickness of these titania films provide excellent lithium ion insertion and reduced ion diffusion length, resulting in stable capacities as high as 200-250 mAh/g over 200 cycles.

KEYWORDS: Mesoporous, self-assembly, orthogonal alignment, solar cells, lithium ion battery

Suraj R. Nagpure

08/11/2016

SYNTHESIS OF TITANIA THIN FILMS WITH CONTROLLED
MESOPORE ORIENTATION: NANOSTRUCTURE FOR ENERGY
CONVERSION AND STORAGE

By

Suraj R. Nagpure

Dr. Stephen E. Rankin

Director of Dissertation

Dr. Thomas D. Dziubla

Director of Graduate Study

Date: 08/11/2016

ACKNOWLEDGEMENTS

First and foremost, I would like to express my deepest gratitude to my advisor, Dr. Stephen E. Rankin for his continuous encouragement and support during my doctoral research. He is one of very few inspiring people with profound knowledge and a subject matter expert in his field. He always had the patience to listen to me and guide me whenever I approached him with new ideas. During my research I failed several occasions but he never lost his patience and always advised me to find the solution. Most important of all, he taught me how to be “Accountable” for my own actions and decisions in life and this teaching from him will help me throughout my life. He influenced me a lot in developing systematic research and development approach and problem solving skills. In a sentence, without his consistent scholarly guidance and support throughout these years, this research work and this dissertation would have never existed. I am really thankful to him for being my advisor. Above all he is very nice person by heart and I have a lot of respect for him as a person.

I am also extremely grateful to my committee members, Dr. Barbara Knutson, Dr. Vijay Singh, and Dr. Yang-Tse Cheng for their precious time and valuable suggestions.

I would like to thank Nicholas Briot and Dali Qian of the Electron Microscopy Facility for their valuable time in training me to operate electron microscopes independently, which were crucial tools for characterizing my samples. I would also like to thank Mr. Jason Backus of Kentucky Geological Survey for training and help with using their XRD instrument. I would also like give my thanks to Dr. Joseph W Strzalka at Argonne National Laboratory for his help to analyze my samples through GISAXS. I would also like to thank Dr. James Browning at Oak Ridge National Laboratory for his help to analyze neutron reflectometry data. I would also like to thank my friend Sai Guduru Dr. Vijay Singh for teaching me fundamentals of semiconductor fabrication techniques. I would like to thank Qinglin Zhang and Jiagang Xu for electrochemical characterization. I would also like to thank all my previous and current lab members, especially Dr. Suvid Joshi, Dr. Ravinder Garlapalli, Dr. Saikat Das and Syed Zahadul Islam, for their continuous support.

I am extremely grateful for the support and encouragement from my parents Ramkrushna Nagpure and Kiran Nagpure, my grandparents Shriram Nagpure and Sarubai Nagpure, my sister Poonam Nagpure and Brother Sagar Nagpure for their perennial love and support throughout my entire life. My friends are a special part of my life. My special thanks go to all my childhood friends from Nagpure, friends from UDCT and Gazette Gang especially Raghav, Purujit, Suvid, Pratik, Anwasha, Prachi, Sonam, Srishti, Amit, Sumesh, Ravinder, Saket, Rutooj, Vinod for making my stay in Lexington special.

Finally, this work was supported by the U.S. Department of Energy under grant number DE-FG02-07ER46375 and National Science Foundation ESPCoR grant number 1355438. The work at the Argonne National Laboratory was supported by the U.S. Department of Energy, Office of Science, Office of Basic Energy Science, under contract No. DE-AC02-06CH11357. I am thankful for the financial support from DOE, NSF and the Chemical and Materials Engineering Department at the University of Kentucky.

TABLE OF CONTENTS

ACKNOWLEDGEMENTS.....	iii
TABLE OF CONTENTS.....	iv
LIST OF TABLES.....	vii
LIST OF FIGURES.....	viii
Chapter 1. Overview of Mesoporous Titania Thin Films and their Applications for Energy Conversion and Storage.....	1
1.1. Soft-templating method.....	3
1.2. Titania Thin Films with Orthogonally Oriented 2D-Hexagonal Close Packed (HCP) Cylindrical Nanopores.....	10
1.3. Characterization of Titania Thin Films.....	13
1.3.1. Grazing-incidence Small Angle X-ray Scattering (GISAXS).....	13
1.3.2. X-ray Diffraction.....	16
1.3.3. Electron Microscopy.....	18
1.3.4. Solar Cells.....	21
1.3.4.1. p-n junctions.....	22
1.3.4.2. Photovoltaic Effect.....	23
1.3.4.3. Thin Film Solar Cells.....	24
1.3.4.4. Solar Cell Characterization.....	25
1.3.5. Electrochemical Characterization.....	27
1.4. Dissertation Outline.....	30
Chapter 2. <i>In Situ</i> GISAXS Investigation of Low-Temperature Aging in Oriented Surfactant-Mesostructured Titania Thin Films.....	36
Reproduced with permission from Nagpure, S., Das, S., Garlapalli, R., Strzalka, J., Rankin, S. E., Journal of Physical Chemistry C, 2015, 119, 22970-22984.....	36
2.1. Summary.....	36
2.2. Introduction.....	37
2.3 Experimental Section.....	41

2.4. Results and Discussion.....	43
2.5. Conclusions.....	60
Chapter 3. Incorporating Poly(3-hexyl thiophene) into Orthogonally Aligned Cylindrical Nanopores of Titania for Inorganic-Organic Hybrid Solar Cells.....	73
3.1. Summary.....	73
3.2. Introduction.....	74
3.3. Experimental Section.....	77
3.4. Results and Discussion.....	80
3.5. Conclusions.....	87
Chapter 4. Nanoporous n-TiO ₂ /p-CdTe Heterojunction Solar Cells with Enhanced Response in the Near-UV Region of the Solar Spectrum.....	97
4.1. Summary.....	97
4.2. Introduction.....	98
4.3. Experimental Section.....	101
4.4. Results and Discussion.....	104
4.5. Conclusion.....	111
Chapter 5. Layer-by-layer Synthesis of Thick Mesoporous Titania Films with Vertically Oriented 2D-HCP Nanopores and Their Application as Negative Electrodes in Lithium Ion Batteries.....	119
5.1. Summary.....	119
5.2. Introduction.....	120
5.3. Experimental Section.....	124
5.4. Results and Discussion.....	126
5.5. Conclusion.....	133
Chapter 6. Conclusions and Future Work.....	143
6.1. Conclusions.....	143
6.2. Future Work.....	148
APPENDIX A. Nafion-Titania Polymer Hybrids for Solid State Batteries.....	159
A.1. Introduction.....	159

A.2. Experimental Section.....	161
A.3. Results and Discussion.....	162
A.4. Conclusion.....	165
APPENDIX B. Electrochemical Impedance Spectroscopy (EIS) Characterization of Titania Films with Controlled Pore Orientation and Incorporation of Lipid Bilayers into the Nanopores of Titania.....	170
B.1. Introduction.....	170
B.2. Experimental Section.....	172
B.3. Results and Discussion.....	173
B.4. Conclusion.....	176
APPENDIX C. Supporting Information of Chapter 2.....	182
References.....	186
Vita.....	211

LIST OF TABLES

Table 2.1. Parameters found by fitting the Avrami equation to each of the films aged at 4 °C and high relative humidity.....	72
Table 3.1. Characteristics of layers obtained by fitting a multilayer model to the neutron reflectivity profile of P3HT infiltrated into the nanopores of titania after annealing at 200° C for 30 minutes.....	96
Table 3.2. Characteristics of layers obtained by fitting a multilayer model to the neutron reflectivity profile of P3HT infiltrated into the nanopores of titania after annealing at 200° C for 60 minutes.....	96
Table 4.1. Photovoltaic parameters and results from Mott-Schottky analysis of nanoporous TiO ₂ /CdTe and planar TiO ₂ /CdTe Solar Cell.....	118

LIST OF FIGURES

Figure 1.1. Orientations of a p6mm hexagonal mesophase (above) and the corresponding predicted diffraction patterns (below). (a) mesophase with channels perpendicular to the substrate, (b) channels parallel to substrate and 100 face parallel to the surface. Adapted from Hillhouse et al. ¹ (c) 2D-GISAXS pattern for mesophase with channels perpendicular to the substrate. Adapted from Das et al. ²	32
Figure 1.2. Cross-section of a solar cell.....	33
Figure 1.3. A typical current–voltage characteristic of a solar cell in the dark and under illumination.....	34
Figure 1.4. (a) Controlling profile of a CV test. (b) An example of CV of TiO ₂ vs. Li...35	35
Figure 2.1. Scattering geometry for <i>in situ</i> dip coating GISAXS measurements. For each experiment, a vertically oriented sample slide is raised from a resevoir at a controlled rate. X-rays are incident on the sample at an angle α_i and specularly reflected at angle α_f in the horizontal plane, normal to the plane of the sample. The projection of the scattering angle onto the vertical plane is 2θ , and the wave-vector transfer components q_z and q_y are perpendicular and parallel to the sample plane, respectively.....	63
Figure 2.2. 2D GISAXS patterns showing the evolution of mesostructure for thin (~60 nm thick) titania film on modified substrate after aging at 4 °C and ~80% RH for a) 10 min b) 15 min c) 20 min and d) 75 min after coating.....	64
Figure 2.3. Waterfall plot showing the evolution of the mesostructure for thin titania film on modified substrate during aging 4 °C for the first 30 minutes. The plots were generated by integrating slices from the 2D GISAXS patterns for q_z values from 0.025 to 0.03 Å ⁻¹ ..	65
Figure 2.4. Evolution of the integrated intensities of the (100) peak of the o-HCP structure vs. time for (a) thin titania film on modified substrate, (b) thin titania film on unmodified substrate, (c) thick titania film on modified substrate, and (d) thick titania film on unmodified substrate during aging at 4 °C at 13.5 mm above the bottom of the coating or at a set of four other points (averaged). The error bars represent the standard deviation of the intensity of the four points excluding the measurement at 13.5 mm.....	66
Figure 2.5. FWHM (full width at half maximum) for (a) thin titania film on modified substrate, (b) thin titania film on unmodified substrate, (c) thick titania film on modified substrate, (d) thick titania film on unmodified substrate at 13.5 mm above the bottom of the coating or at a set of four other points (averaged). The error bars represent the standard deviation of the FWHM of the four points excluding the measurement at 13.5 mm.....	67
Figure 2.6. The linearized Avrami equation fit to data for (a) thin titania film on modified substrate, (b) thin titania film on unmodified substrate, (c) thick titania film on modified substrate, and (d) thick titania film on unmodified substrate during aging at 4 °C. The filled symbols were fit and the open symbols were not, either because they were measured during the induction period (for early data) or because they were measured after significant radiation damage was observed (for late data).....	68

Figure 2.7. Selected representative 2D GISAXS patterns collected during the aging of a thin P123-templated titania film on a modified substrate during aging at 23 °C for aging times of (a) 5 min, (b) 8 min, (c) 10 min and (d) 15 min.....	69
Figure 2.8. Top view SEM images of thin titania films on modified substrate aged at (a) 4 °C and (c) 23 °C after calcination at 400 °C for 10 minutes using a ramp rate of 25 °C/min; and GISAXS patterns after 30 minutes of aging at (b) 4 °C or (d) 23° C.....	70
Figure 2.9. (a) Evolution of the integrated intensity of the diffraction peak vs. time for thin titania film on modified substrate during aging at 23 °C at a point 13.5 mm above the bottom of the coating or at a set of four other points (averaged). The error bars represent the standard deviation of the intensity of the four points excluding the measurement at 13.5 mm. (b) The linearized Avrami equation fit to data for thin film on modified substrate during aging at 23 °C. The filled symbols were fit and the open symbols were not, because they were measured during the induction period (Induction period = 2 min, Avrami parameters, $n = 2.0$, $k = 0.00388 \text{ min}^{-2}$).....	71
Figure 3.1. Representative plan view SEM images of mesoporous titania films prepared on (a) plain glass and (b) F127-modified glass prepared from sols containing 1.26 g F127 and 30 g of ethanol, aged at 4 °C and calcined at 400 °C at the rate of 25 °C/min.....	89
Figure 3.2. (a) GISAXS pattern of nanoporous titania film prepared on modified glass after calcination at 400° C at a rate of 25 °C/min and (b) the corresponding 1D linecut derived by integrating along the q_z direction from 0.08-0.1 Å ⁻¹	90
Figure 3.3. UV-vis absorption spectra of (a) regioregular P3HT and (b) regioregular P3HT infiltrated into titania films with thickness of 120 nm after annealing under vacuum for the indicated times at 200° C (The data has been shifted in part (b) for absorbance values)..	91
Figure 3.4. (a) Blue shift of P3HT UV-vis absorbance maximum as a function of annealing time and (b) optical density of embedded P3HT after infiltration for varying periods of time at 200 °C under vacuum.....	92
Figure 3.5. Neutron reflectivity profile of P3HT infiltrated into the nanopores of titania after annealing at 200° C for 30 minutes. The inset shows that scattering length density (SLD) profile of the fitted model.....	93
Figure 3.6. Neutron reflectivity profile of P3HT infiltrated into the nanopores of titania after annealing at 200° C for 60 minutes. The inset shows that scattering length density (SLD) profile of the fitted model.....	94
Figure 3.7. (a).PL spectra for P3HT infiltrated into nanoporous TiO ₂ by spin coating 1 wt% P3HT solution followed by annealing at 200 °C for the indicated time and comparison with as spun P3HT, and (b) integrated PL intensity for P3HT infiltrated into nanoporous TiO ₂ as a function of annealing time. The error bars represent the standard deviation of the PL intensity of three different samples.....	95

Figure 4.1. (a) Device structure for CdTe/nanoporous-TiO ₂ solar cells, and (b) Device structure for CdTe/planar-TiO ₂ solar cells c) Band alignment diagram for CdTe- TiO ₂ system. E _g is energy band gap, φ is electron affinity, E _F is fermi level, E _{vac} is vacuum EC and E _v are edges conduction and valence bands, δ is energy band offset.....	112
Figure 4.2. (a) SEM image (b) SAXS pattern (c) SAED pattern, and (d) HRTEM of titania film on modified glass from sols prepared using F127 with M= 0.01 and 30 g of ethanol, aged at 4° C and calcined at 400° C at the rate of 25°/min.....	113
Figure 4.3. Cross-sectional SEM image of (a) Titania film with vertically oriented cylindrical nanopores (b, c) CdTe infiltrated into the nanopores of titania at low magnification (b) and at high magnification (c).....	114
Figure 4.4. GISAXS Pattern of titania thin films with o-HCO microstructure after CdTe Sublimated from CdTe-titania samples.....	115
Figure 4.5. Solar cell performance of (a) CdTe-nanoporous TiO ₂ solar cell, and (b) Cdte-planar TiO ₂ solar cell.....	116
Figure 4.6. (a) Mott-schottky analysis of Planar TiO ₂ /CdTe and porous TiO ₂ /CdTe on a semi-log scale, and (b) External quantum efficiency of porous TiO ₂ /CdTe solar cell...	117
Figure 5.1. (a) Top view SEM image of a single-layer nanoporous titania film prepared on F127-modified titanium foil prepared from sols containing 1.26 g F127 and 18.43 g of ethanol, aged at 4 °C and calcined at 400 °C at the rate of 25 °C/min and (b) Cycling performance for titania thin films with different pore orientation and its comparison with a nonporous titania film up to 200 cycles at C/3 rate.....	135
Figure 5.2. Thickness of films as a function of number of layers measured using profilometry. The error bars represent standard deviation in thickness values for three samples.....	136
Figure 5.3. XRD patterns of calcined titania films on unmodified glass and modified glass for three different thicknesses from sols prepared using 1.26 g F127 and 18.43 g of ethanol, aged at 4° C and calcined at 400° C at the rate of 25°/min.....	137
Figure 5.4. Top-view SEM images of titania thin films after (a) one layer and (b) three layers from sols prepared using 1.26 g F127 and 18.43 g of ethanol, aged at 4° C and calcined at 400° C at the rate of 25°/min. The thicknesses of titania film measured using profilometry were around 186 nm and 434 nm respectively.....	138
Figure 5.5. Cross-sectional SEM images of titania thin films after (a) one, (b) three, (c) five, or (d) eight layers were deposited from sols prepared using 1.26 g F127 and 18.43 g of ethanol, aged at 4° C and calcined at 400° C at the rate of 25°/min.....	139
Figure 5.6. Cyclic voltammetry of (a) one layer for five cycles and (b) multilayer titania films for indicated layers for the first cycle, measured in 1 M LiPF ₆ salt in an equal volume mixture of ethylene carbonate and dimethyl carbonate.....	140

Figure 5.7. Cycling performance of titania films with vertical pore orientation for indicated thicknesses up to 200 cycles at C/3 rate.....	141
Figure 5.8. XPS spectra of TiO ₂ thin films before electrochemical characterization and after the completion of the 200 th discharging cycle.....	142
Figure 6.1. Energy level diagram for TiO ₂ +N719+P3HT system.....	156
Figure 6.2. Schematics for incorporation of Sn/Si into the nanopores of titania for lithium ion battery applications.....	157
Figure 6.3. Chemical structure of dopamine.....	158

Chapter 1. Overview of Mesoporous Titania Thin Films and their Applications for Energy Conversion and Storage

Titania is an important material for applications in various fields including medicine³, environmental remediation⁴⁻⁵ and energy storage and conversion⁶⁻⁷. It is non-toxic, photoactive and has unique optical, physical and chemical properties. Titania (TiO₂) is a highly biocompatible material⁸ and used as a drug host for controlled release over a long period of time⁹. Titania has excellent photocatalytic performance¹⁰⁻¹¹ and has been widely used in environmental and waste water applications for oxidation of a large variety of living cells and organics¹²⁻¹⁵. Grätzel and co-workers have highlighted that nanocrystalline titania thin films can be used as electrodes for photoelectrochemical cells and have potential applications in the areas of electrochromic devices, photocatalysts, sensors, etc¹⁶⁻¹⁷. Titania has excellent charge transport properties which can be utilized to synthesize liquid electrolyte dye-sensitized solar cells¹⁶. In general, titania based systems have great advantages such as high efficiency, low cost, chemical inertness, and photostability which makes them useful for these and other applications¹¹.

Anatase titania is a n-type semiconductor with the valence and conduction bands located at +3.1 and -0.1 eV relative to the Fermi level, thus giving a band gap of +3.2 eV. Therefore, titanium dioxide readily absorbs UV light with a wavelength below 387 nm¹⁸⁻¹⁹. Because of this property, titania films can be used as a window layer with a p-type semiconductor incorporated into the pores and at the top surface of the device to synthesize a photovoltaic cell. Mesoporous TiO₂ has been considered as a suitable photoanode material for dye sensitized solar cells since it could provide rapid electron transport, large surface area for superior contact with other semiconductors, and close electrical contact with the redox electrolyte²⁰⁻²¹. This puts TiO₂ in a position to potentially address the

utilization of solar energy as a substitute for nonrenewable fossil fuel resources²²⁻²³. Another important potential application of titania is in the field of energy storage, such as in lithium ion batteries. Nanoporous titania can be used as anode materials in lithium ion batteries because of advantages including small volume expansion (~3%) during intercalation/extraction of Li⁺ ions²⁴, good cycling stability²⁵ and high discharge voltage plateau (~1.7 V)²⁶. A significant amount of work has recently been done in this area using titania²⁷⁻²⁹. In this and other applications, introduction of well-defined pores into titania can significantly enhance the effectiveness of charge transport, adsorption and catalysis at the interface between titania and other media. An established approach to achieving this is by surfactant templating.

Structured mesoporous titania was first reported by Antonelli and Ying in 1995³⁰. Since then, different mesoporous structures of titania have been synthesized including 2D hexagonal, 3D cubic, lamellar, hollow-sphere, wormhole-like, rice-like, sphere-like, tube-like, sponge-like, spindle-like, and bipyramidal Wulff-shape TiO₂ using various methods such as sol-gel, hydrothermal, solvothermal, microwave, and sonochemical approaches³¹⁻⁴⁵. Liu et al. synthesized spindle shaped mesoporous TiO₂ by using an aqueous peroxotitanium solution with polyacrylamide³³. Da Silva et al. prepared truncated bipyramidal Wulff-shaped mesoporous TiO₂ that exhibited superior photocatalytic activity by using a non-aqueous sol-gel approach³⁵. Guo et al. prepared three-dimensional mesoporous TiO₂ microsphere catalysts via a one-step solvothermal process without templates⁴⁰. Yu et al. prepared trimodally sponge-like macro-/mesoporous titania by hydrothermal treatment of precipitates of tetrabutyl titanate (Ti(OC₄H₉)₄) in pure water³¹. Wang et al. developed mesoporous spherical aggregates of anatase nanocrystals with

wormhole-like framework using cetyltrimethylammonium bromide (CTAB) as structure directing agent³². Han et al. synthesized a lamellar titania microstructure using cetyltrimethylammonium bromide (CTAB) as ionic template and ammonium titanyl oxalate as titania precursor⁴⁵. We have previously synthesized mesoporous titania thin films with cubic miscostructure⁴⁴ and orthogonally oriented 2D-hexagonal close packed (HCP) cylindrical nanopores⁴¹⁻⁴³ using an evaporation induced self-assembly (EISA) technique with Pluronic surfactants (P123 and F127) as structure directing agents and titanium tetrachloride and titanium ethoxide as titania precursors. Thus, various mesostructures of titania can be obtained using different synthesis routes and precursors. This chapter will provide an overview of soft templating method along with relevant characterization techniques and an outline of the dissertation.

1.1. Soft-templating method

The soft-templating method usually occurs by a co-assembly process of the precursors (silica, metal oxides, polymers, *etc.*) and surfactant templates or other self-assembling species⁴⁶. Since the success in the synthesis of periodic mesoporous silicates⁴⁷⁻⁴⁸, there has been a tendency to extend this methodology to more chemically and electronically active transition metal oxides. Since the soft-templating method is based on the co-assembly of reacting metal oxide precursors with surfactants, the chemistry of the precursors needs to be understood and controlled to give the best chance of producing a desired material. Titania precursors (e.g. titanium (IV) ethoxide and titanium tetrachloride) are more reactive than silica precursors such as tetraethoxysilane. In these precursors, the oxidation state of the metal is smaller than its preferred coordination number. To increase its coordination number the metal uses its vacant *d* orbitals to accept lone pairs from nucleophiles, such as oxygen atoms of water. In addition, transition metals can form M-

OH-M bridges through olation reactions, leading to rapid precipitation of hydroxyl species under uncontrolled conditions. Thus, titania precursors can be very difficult to work with if care is not taken in the design of the synthesis procedure.

In 1995, Antonelli and Ying first reported the synthesis of mesoporous TiO₂ (named as Ti-TMS1), which has been accomplished through a modified sol-gel process involving titanium isopropoxide as a precursor and an alkylphosphate surfactant as the template³⁰. Acetylacetone was used to decrease the hydrolysis and condensation rate of titanates and reduce the size of their oligomers to obtain a strong interaction with the phosphate head groups of a tetradecylphosphate surfactant in an aqueous solution. However, a significant amount of phosphorus remained after the surfactant template was removed leading to relatively low photocatalytic activity because of poisoning of active catalytic sites due to residual phosphorus. In 1999, Antonelli et al. reported the synthesis of nonphosphated mesoporous TiO₂ by using dodecylamine as the template combined with a dry aging technique⁴⁹. However, the obtained materials were found to have poor thermal stability. It was not possible to synthesize thermally stable mesoporous titania with active catalytic sites by the approach developed by Antonelli. Also, controlling the hydrolysis and polymerization of titania precursors was shown to be essential to obtain high mesostructural regularity over large domains. A significant breakthrough in controlled formation of mesoporous films and particles was realized when Brinker and co-workers developed the evaporation-induced self-assembly (EISA) method to prepare mesoporous silica thin films⁵⁰. Because of its versatility, this approach was almost immediately adopted as an efficient strategy to synthesize mesoporous TiO₂⁵¹⁻⁵³.

In EISA, dip coating of substrates from a solution containing inorganic precursors, surfactant and solvent accompanied by rapid evaporation of volatile solvents (ethanol and water) drives the formation of an ordered mesoporous structure. One important advantage of EISA for the preparation of mesoporous transition metal based thin films is that the pH of the initial sol can be adjusted to stabilize the coating sol, and to favor a final material with desired properties. In order to inhibit rapid oligation and condensation of the titania precursors to allow self-assembly to occur, protons (H^+ ions) have been used as inhibitors⁵⁴. Although different ligands (such as acetylacetonate) can also be used as inhibitors of the hydrolysis and condensation of metal alkoxides, they can interfere in the interactions between titanium species and surfactants, so it is common to use H^+ as inhibitors in the synthesis of surfactant templated mesoporous titania films⁵⁵⁻⁵⁸. We generally start with a highly acidic sol to prevent uncontrolled condensation of transition metal precursors to promote slow formation of the inorganic network within the liquid crystal mesophases formed after coating. Gradual elimination of the acid by evaporation provides a way to control the polymerization of the inorganic components while allowing a fully cured inorganic network to form⁵⁹.

Many researchers have investigated the titanium hydrolysis process and interactions of transition metal ion with organic templates. Livage et al.⁶⁰ reviewed the sol-gel chemistry of most of the transition metal oxides and found that the hydrolysis reaction mechanism of the metal ions depends on several factors including the electron affinities, sizes and the charges of metal ions and alkoxy groups, and the size and number of the alkoxy groups. Kim et al.⁶¹ proposed two kinds of mechanisms for the hydrolysis of titanium alkoxides. One is an associative mechanism, in which the entering group enters

into a complex with the metal first, then a detectable intermediate of expanded coordination number is formed. The other mechanism is an interchange associative (Ia) mechanism in which the transition state is reached mostly through formation of the bond of the entering group. In this mechanism, the bond weakening of the leaving group also takes place in the course of reaching the transition state. An associative (A) mechanism is most appropriate to describe the hydrolysis of $\text{Ti}(\text{OEt})_4$, whereas the transition states for the hydrolysis for $\text{Ti}(\text{O}^i\text{Pr})_4$ and $\text{Ti}(\text{O}^i\text{Bu})_4$ are reached through the interchange associative (Ia) mechanism. Sanchez and coworkers⁵³ studied the role of water in the hydrolysis reaction in the presence of Pluronic surfactants and found that during anhydrous or low water conditions, there are strong Ti-polymer interactions which hinder the assembly of the template, leading to a final wormlike structure. In contrast, a high water / high acid environment hinders Ti-polymer interactions, which allows the micelles to assemble into well-ordered mesoporous structures. Henry et al.⁶² studies the mechanistic aspects of the hydrolysis and condensation of titanium alkoxides complexed by tripodal ligands and found that bridging positions for OR groups are sites of preferential attack for substitution by OH and/or OX groups and the basic structure of the Ti_4O_{16} core can be conserved upon hydrolysis and can be used as a building block for building complexes of higher nuclearity.

In addition to precursor chemistry, the choice of the surfactant template as structure directing agent is an important parameter to control the final mesostructure in mesoporous titania films^{55, 63}. For example, by using titanium isopropoxide as inorganic precursor, films with an anisotropic 2D-hexagonal mesostructure are obtained using the Pluronic surfactant P123 (a triblock copolymer with average formula $\text{EO}_{20}\text{PO}_{70}\text{EO}_{20}$, where EO is ethylene oxide and PO is propylene oxide), while cubic mesostructure arrangement of spherical

micelles is favored with Pluronic F127 (EO₁₀₆PO₇₀EO₁₀)⁶⁴. In addition to the template itself, the molar ratio (M) of surfactant template to the titania precursor also influences the type of mesostructure formed^{51, 55, 63}. Changing M changes the amount of inorganic precursors incorporated with the hydrated PEO head groups and the number density of micelles after coating. In other words, increasing M increases the packing parameter (P) of the micelles, which is defined as $P=V_0/(A_e*L_0)$, where V_0 is the surfactant tail volume, A_e is the equilibrium area per molecule at the aggregate interface and L_0 is the surfactant tail length. Films with cubic, hexagonal and lamellar phase can be obtained by varying M . Crepaldi et al.⁵¹ synthesized mesoporous titania films using TiCl₄ as titania precursor using various surfactants and found that for P123, titania films with 2D hexagonal phase are obtained for M values in between 0.05-0.09 and lamellar phase is obtained for higher values of M . With F127 as template, a cubic phase is obtained for M values in between 0.003-0.006 and 2D hexagonal phase is obtained for M in between 0.008-0.01. Consistent with this idea, Alberius et al.⁵⁵ showed that the final mesophases in surfactant-templated materials can often be predicted based on the volume fraction of surfactant (Φ), which is defined as the ratio of the volume of surfactant in the dried film to the volume of the nonvolatile (polar) components in the final film. They predicted based on the observed phase behavior of P123 in water that for titania films synthesized using P123 as the surfactant and titanium ethoxide as the titania precursor, the mesophase should be cubic, 2D hexagonal or lamellar for Φ in the ranges from 29%-36%, 38%-55% or 61%-75% respectively. Wu et al.⁶⁵ reported the synthesis of titania films using P123 and Ti(OEt)₄ for M ratios between 0.006 and 0.012, which is expected to correspond to Φ in the range from 26% to 41%⁶⁵. The mesostructure should vary from 2D hexagonal, to a cubic mesophase

of undefined symmetry, to a disordered micellar solution sequentially, as the molar ratio (M) decreases from 0.0122 to 0.01, 0.008 and 0.006 according to Alberius et al.⁵⁵. However, Wu et al.⁶⁵ found for a P123 to Ti ratio as low as 0.006, a stable well-ordered mesostructure is still obtained, which is similar to the results obtained by Crepaldi et al.⁵¹ and unlike Alberius et al.⁵⁵. This might be because the formation mechanism of the mesoporous titania-based thin films is influenced by many factors besides the templates and precursor volume fractions, including aging temperature, aging time, relative humidity of atmosphere^{51, 66}, the acidity of the solution^{51, 66}, etc. Most of these factors have been ignored by Alberius et al.⁵⁵.

Low temperature aging during high relative humidity (RH) plays a vital role for mesostructure self-assembly. The objectives of using a low temperature are to slow titanium precursor condensation and to provide a driving force for mesophase formation, similar to the subambient temperatures used by Alberius et al.⁵⁵. A highly humid environment is important during the aging of these films to slow down the evaporation of the water from the films (to provide sufficient time for reorientation and ordering of the mesostructure) and also to control the mesoscopic ordering of the surfactant^{56, 58, 67-69}. Crepaldi et al.⁵¹ provided a thorough discussion of the complete synthesis and characterization procedures to obtain ordered mesoporous titania films and discussed all important chemical and processing parameters important for reproducible construction of mesoporous titania thin films and explained that humidity during aging determines the water content in the coatings. This water content determines the fluidity of deposited coating and the possibility of occurrence of the disorder-to-order transition. The continuous exchange of water between the film and the atmosphere during the first hour of aging after

deposition allows the condensation of the organic framework around micellar aggregates and controls the final mesophase. Jang et al.⁶⁶ studied the effects of pH of the coating sol as well as the humidity of the curing environment on the mesostructure of titania films obtained. They suggest an optimum pH (~ -0.6) and humidity (~ 80% RH) values to synthesize highly organized mesoporous titania films. In this work, we have used aging at 4 °C at slightly higher humidity (~ 94%) as higher humidity is better to prevent condensation of inorganic precursor (Chapter 2-5).

In the last stage of their processing, calcination of titania film after aging removes surfactant molecules, stabilizes the coating, causes structural contraction and induces anatase crystallization from the initially amorphous titania structure formed during the sol-gel process⁵¹. These mesoporous titania films are stable up to a certain level of thermal treatment, but as the time and temperature used for calcination increase, they begin to lose mesopore order. This is because high temperatures induce the nucleation and growth of anatase nanocrystallites, which can destroy mesopore ordering due to extensive atomic rearrangement and modification of the oxidation state of the titanium by redox reactions⁵⁷. Kirsch et al.⁵⁶ studied the crystallization kinetics of mesoporous titania thin films using in-situ x-ray diffraction and found that short calcination times at high temperatures are better to produce crystalline films with minimal loss of mesoporous order. However, the exact time and temperature required vary for different synthesis procedures. Das et al.⁴² investigated the effects of pore orientation on the mesostructural stability for 2D-hexagonal close packed (HCP) cylindrical nanopores of titania and found that films with pores oriented orthogonal to the substrate at the top surface retain their long-range pore order at higher calcination temperatures (500 °C) as compared to the films with pores oriented

parallel to the substrate. The reasons for this difference are ascribed to greater resistance to anisotropic stress during heating of the orthogonally oriented pores and titania crystallization nucleation at the top surface of the films with orthogonally oriented pores. Consequently, activation energy for mesostructure loss of orthogonally oriented mesostructure is greater than that for films with mixed orientation (mixture of parallel and orthogonal orientation)⁴³. Nearly perfect orthogonal orientation contributes to the larger activation energy by supporting the anisotropic stresses that develops orthogonal to the films during annealing. In the next section, we will shine some light over the mesopore alignment, advantages and applications of 2D-hexagonal close packed (HCP) cylindrical nanopores.

1.2. Titania Thin Films with Orthogonally Oriented 2D-Hexagonal Close Packed (HCP) Cylindrical Nanopores

Using highly acidic conditions, mesoporous titania films with several 1D, 2D and 3D pore geometries have been synthesized^{66, 69-71}. Of all these pore geometries, the 2D Hexagonal Close Packed (HCP) arrangement of cylindrical nanopores is an important geometry because it provides non-interconnecting pores beneficial for some applications and as model systems for well-defined convection, diffusion and reactions in these pores. This particular geometry is especially important for infiltration of electronically conductive organic polymers (such as P3HT) because several studies have shown that the transport, absorption, and emission properties of these polymers can be tuned to great advantage inside of HCP pores⁷²⁻⁷³. The problem with this structure is that HCP structures cast onto hydrophilic oxide surfaces (such as those of titania or fluorinated tin oxide that might be present in bulk heterojunction materials) usually align parallel to the surface because of the

preferential interactions between the polar substrate surface and polar surfactant headgroups. Orthogonal alignment of the HCP phase with accessible pores is essential to utilize the films for all applications. This problem can be solved by surface modification of the substrates in order to provide equal interactions with polar and nonpolar components (which we call “neutral” surfaces) prior to the coating of titania sols.

By analogy with surface chemistry strategies used to orient block copolymer films⁷⁴⁻⁷⁹, the Rankin group has reported the synthesis of mesoporous titania thin films with o-HCP cylindrical nanopores using EISA with P123 as structure directing agent and titanium(IV) ethoxide as titania precursor⁸⁰⁻⁸¹. The hypothesis underlying this approach is that orthogonal alignment of the HCP mesophase can be achieved in EISA-derived ceramic film by modifying the substrate surface so that it interacts equally with both blocks of the P123 template, making it chemically “neutral” towards the template surfactant. By cross linking a layer of Pluronic surfactant on the substrate surface and using this modified surface to coat titania films, we can eliminate all preferential interactions between the substrate surface and surfactant molecules, resulting in orthogonal alignment of HCP mesophases templated using the same Pluronic surfactant^{80, 82-83}. Monte Carlo simulations⁸⁴⁻⁸⁵ have shown that this is the expected outcome for mixtures of surfactants and small molecules, and not just for neat block copolymers⁷⁸. A related epitaxial orientation procedure was demonstrated recently by Tolbert and coworkers, where HCP film was cast onto a cubic template film to induce orthogonal alignment⁸⁶.

In addition to surface modification, the synthesis procedure for o-HCP TiO₂ films includes aging after coating in a refrigerator at 4 °C under high relative humidity (approx. 94%). Even though this aging procedure has been found to be an essential part of o-HCP

TiO₂ film formation, little is known about the o-HCP mesostructure formation mechanism other than what has been inferred by characterization of the films before and after calcination². Grosso et al. analyzed the mechanisms involved in the formation of 2D-hexagonal templated SiO₂ and TiO₂ mesostructured films during dip coating using Brij-58 as surfactant and found that the self-assembly leads to the formation of organized phase at the final stage of the drying process and involves the formation of an intermediate disorganized phase⁵². The disorder to order transition took place on the order of 2-3 minutes after the start of coating for TiO₂ under the conditions studied. Other reports have shown that for dip-coated thin films, the mesostructure generally forms through a disorder-to-order transition which may involve intermediate hybrid mesophases that are related to the concentration gradient⁸⁷⁻⁸⁹. Previous studies show that the formation of vertically oriented cylindrical channels by transformation of a cubic phase and merging of the pores normal to the film also showed diffraction spots consistent with the cubic phase prior to thermal treatment^{71, 90-91}. However, according to Koganti et al.⁸⁰, vertical channels simply form due to reorientation of the HCP phase in response to the modification of the surface of the substrate with a chemically neutral crosslinked P123 layer. Thus, it is essential to study growth mechanism of vertically oriented cylindrical channels during low-temperature aging which will be a significant investigation and accomplishment of this dissertation (Chapter 2).

One important application area for the mesoporous titania films with 2D HCP cylindrical nanopores, and one which motivates the present study is in photovoltaic materials. Because TiO₂ is an n-type semiconductor, infiltrating the pores with a p-type organic semiconductor can be done to synthesize an organic-inorganic hybrid bulk

heterojunction solar cell⁹². These are ideal components for improved photovoltaics based on the principle of Grätzel cells¹⁶, and can serve as high-surface area components of photoelectrochemical (PEC) cells⁹³. They feature a continuous pathway for electron transport through the TiO₂ and tremendous surface areas (> 250 cm² of pore surface / cm² of substrate for a 240 nm thick film) for photo- generation of electron/hole pairs or reactions. These surfaces can be readily functionalized by post-synthesis attachment of sensitizer dyes⁹⁴⁻⁹⁵ or deposition of semiconductor particles/wires⁹⁶⁻⁹⁷. They provide short carrier diffusion length and high hole conductivity for charge carriers⁹⁸. A hole conducting polymer such as poly-3-hexylthiophene (P3HT) when loaded into perpendicular 2D hexagonal close-packed (HCP) channels conduct holes 5 orders of magnitude faster than in interconnected cubic channels^{92, 99}. Confinement in cylindrical nanopores provides isolated, regioregular “wires” of conjugated polymers with tunable optoelectronic properties. These titania films with vertically aligned cylindrical nanopores are ideal material for improved photovoltaics. This property of 2D-HCP films will be explored in chapter 3 which is dedicated incorporation of polymer P3HT into the nanopores of titania.

1.3. Characterization of Titania Thin Films

1.3.1. Grazing-incidence Small Angle X-ray Scattering (GISAXS)

One important aspect of the work being conducted for this dissertation is the investigation of growth mechanism for orthogonally oriented hexagonal close packed (o-HCP) mesostructures during aging of surfactant-templated titania thin films using *in-situ* grazing incidence small-angle X-ray scattering (GISAXS) in a controlled-environment chamber. Chapter 2 will be dedicated to this study. GISAXS is a suitable technique to characterize the structure of thin mesoporous films since the angle of incidence of the x-

ray beam can be adjusted to provide scattering information near the top surface of the film or across the entire film. Using GISAXS, information about the orientation, the anisotropy of the mesostructure and the coexistence of several mesophases can be determined. These techniques also typically employ a 2D CCD detector, thus providing more information about the full symmetry and geometry of a film. GISAXS experiments with high intensity x-ray sources are also widely used for in-situ studies of the mesostructured formation mechanism and mesophase transformation in thin films (e.g. uniaxial contraction and/or crystallization of inorganic walls)^{71, 100-103}. This technique is well suited to directly determining the orientation of mesopores in thin ceramic films.

Grosso et al. analyzed the mechanisms involved in the formation of 2D-hexagonal templated SiO₂ and TiO₂ mesostructured films during dip coating using Brij-58 as surfactant and found that the self-assembly leads to the formation of organized phase at the final stage of the drying process and involves the formation of an intermediate disorganized phase⁵². The disorder to order transition takes place on the order of 2-3 minutes after the start of coating for TiO₂ and SiO₂ under the conditions studied. Other reports have shown that for dip-coated thin films, the mesostructure generally forms through a disorder-to-order transition which may involve intermediate hybrid mesophases that are related to the concentration gradient⁸⁷⁻⁸⁹. Doshi et al. studied the self-assembly of surfactant templated thin-film silica mesophases synthesized using surfactants cetyltrimethylammonium bromide (CTAB) and Brij-56 and found that 2D HCP mesostructure (*p6mm*) forms from a lamellar mesophase through a correlated micellar intermediate¹⁰⁴. Gibaud et al. studied EISA of silica mesophases synthesized using surfactant CTAB and found that the final structure of the film is strongly influenced by the rate of evaporation, which presumably

governs the concentration gradient inside the film¹⁰⁵. While *in situ* SAXS studies of EISA have provided magnificent insights, most have been restricted to the dip-coating process itself and the time span on the order of seconds after the coating process. Also, most of the studies have been done for mesoporous silica films synthesized with small surfactant molecules (CTAB and Brij surfactants) and very few studies have been done for TiO₂ films. Thus, it is not known to what extent their findings can be extrapolated to the conditions used to synthesize o-HCP titania films. Grosso and coworkers discuss in reviews of the fundamentals of mesostructuring through EISA, a tunable steady state (TSS) occurs in some cases, during which the inorganic framework is still flexible and susceptible to modification by changing aging conditions¹⁰⁶⁻¹⁰⁷. The TSS helps to explain why the structure of EISA-derived films can be tuned by adjusting variables such as the humidity of the vapor¹⁰⁸⁻¹¹⁰, the sol aging time (which affects the time scale for condensation after coating)¹¹⁰⁻¹¹¹, the pH of the film¹¹²⁻¹¹⁴, the presence of solvent vapors¹¹⁵, and confining the coating using materials of different surface energy¹¹⁶⁻¹²⁰. Generally for silica, this TSS lasts from a few seconds at low humidity to 10 minutes at high humidity¹²¹. However, for TiO₂ system, the condensation of titania oligomers has been proposed to be triggered by evaporation of HCl. Because HCl departs very slowly, TSS for some TiO₂ sol compositions of more than 1 hour duration have been observed¹⁰⁶. Because the TSS plays an important role in the formation of o-HCP TiO₂ films, studying the process *in situ* will provide novel insights into how to engineer and tune EISA films for new applications requiring an active oxide component.

In this dissertation, the GISAXS technique was performed to investigate the mechanism of forming orthogonally oriented hexagonal close packed (o-HCP)

mesostructures during aging of surfactant-templated titania thin films. GISAXS data were obtained at the Advanced Photon Source at Argonne National Labs on beamline 8-ID-E. Unlike the usual scattering geometry for GISAXS at Beamline 8-ID-E, the vertical sample meant the scattering plane was horizontal. A small piece of tungsten, $1 \times 2 \times 15 \text{ mm}^3$ attached horizontally to the end of the GISAXS beamstop served as the beamstop for the *in situ* dip coating GISAXS measurements. Samples for *in situ* dip coating were prepared within a sealed chamber with inner dimensions $5 \times 5 \times 6.5 \text{ in}^3$ with aluminum side walls and copper lid and base plate. The sol prepared as explained above was contained in a plastic container, (the lid of a 50 mL Falcon tube) approximately 10 mm deep, resting on a copper block in thermal contact with a thermoelectric element so that its temperature could be changed independently. The specific apparatus and scattering geometry is explained in more detail in chapter 2. The analysis of the GISAXS data in this dissertation was done using the GIXSGUI package for Matlab developed by our collaborators at Argonne National Lab¹²². Generally the presence of the o-HCP cylindrical mesophase is indicated by two intense rods parallel to the scattered beam, located on both sides of the beam stop indexed to the (100) plane of the HCP structure as shown in Figure 1.1c². GISAXS patterns were collected for increasing aging times and the intensity of (100) diffraction peak has been used to show the effect of surface modification, film thickness and aging temperature over the o-HCP mesostructure development. Detailed data analysis for these experiments have been described in chapter 2.

1.3.2. X-ray Diffraction

1D X-ray diffraction (XRD) is the most widely accepted technique to assess the structure of the mesoporous thin films due to its widespread availability. X-rays are

produced by bombarding a metal target (Cu in our case) with a beam of electrons emitted from a hot filament (often tungsten). The incident beam will ionize electrons from the K-shell (1s) of the target atom and X-rays are emitted as the resultant vacancies are filled by electrons dropping down from the L (2P) or M (3p) levels. This gives rise to K_{α} and K_{β} lines which provide the most definitive structural information about the material. We generally select a monochromatic beam of single wavelength by using a nickel filter for a copper metal target. In this dissertation, most samples were characterized by the 1D XRD technique by employing a Bruker D8 diffractometer using K_{α} radiation and a copper source with a wavelength of 1.54 \AA ($\text{Cu } K_{\alpha} = 1.54 \text{ \AA}$).

Because the pore spacings are on the order of a few nanometers, the diffracted reflections appear at low angles. The geometry used to obtain 1-D XRD patterns is known as the Bragg-Brentano geometry, where both the incident beam and the detector move simultaneously to develop the XRD pattern of the film. According to Bragg's law, constructive wave interference, and hence the appearance of diffraction peaks occurs when the following equation is satisfied:

$$n\lambda = 2d\sin\theta \quad (1.1)$$

Where λ is the wavelength of the x-rays, n is an integer, d is the spacing between planes of objects (in this case pores), and θ is the angle between the incident beam and the detector. Depending on the pore symmetry, we will observe peaks from different planes in the ordered structure. Based on the relationship between the d-spacings of these peaks, the pore symmetry and unit cell parameter can be determined. For instance, the 2D hexagonal phase ($p6mm$ symmetry group) of nanoporous material is identified by well resolved Bragg reflections with the ratio of 1/d-spacing values $1:\sqrt{3}:2:\sqrt{7}:3:\dots$ that can be indexed to the

(100), (110), (210), (300) ,... reflections, respectively. However, 1D XRD in the Bragg-Brentano geometry is not sufficient to determine the symmetry of all phases, especially when mesophases are oriented with respect to the substrate. Because of the weak diffraction occurring from mesophases, only a few reflections can be observed even for well-ordered samples. Therefore, even for phases that are not intentionally aligned, preferential orientation with respect to the substrate can lead to an even smaller number of reflections that are difficult to assign. Fortunately, Hillhouse et al.¹ described an alternate way to verify the orientation of HCP channels by observing films in several x-ray diffraction (XRD) modes. For ordered HCP mesoporous films, reflections corresponding to (100) and (200) lattice planes can be observed in the powder XRD mode when the mesostructure is oriented with the (100) plane parallel to the substrate (Fig. 1.1b). However, in the Bragg-Bentano geometry used for XRD, diffraction in the plane of substrate is not detected¹. When the mesopores are aligned orthogonally to the substrate, most of the diffraction will take place in the plane of the substrate (Fig. 1.1a). Thus, completely orthogonally tilted mesophase should not yield any XRD diffraction intensity or the intensity should decrease for more orthogonal structure. This particular property makes XRD a very effective tool to study pore orientation. The combination of top view and cross-sectional SEM along with XRD will be shown to be a powerful approach to assess the orientation of mesochannels for multilayered titania films in chapter 5.

1.3.3. Electron Microscopy

Scanning Electron Microscopy (SEM) is a powerful characterization technique to provide direct information about the surface of films. Unlike TEM, this technique does not require extensive sample preparation (such as scraping samples from substrates) to create

an electron-transparent sample. This makes SEM an ideal technique to obtain orientation information because the mesoporous film structure is undisturbed by sample preparation. Electrons are produced at the top of the column, accelerated down and passed through a combination of lenses and apertures to produce a focused beam of electrons which hits the surface of the sample. The sample is placed on the SEM sample stage in the chamber area and both the column and chamber are evacuated by a combination of pumps. The sample is then scanned with electron beam. The position of the electron beam on the sample is controlled by scan coils situated above the objective lens. These coils allow the beam to be scanned over the surface of the sample. As a result of electron-sample interaction, a number of signals are produced. The signals from the scattering of electrons from the surface are detected by appropriate detectors (such as CCD) and are measured to obtain the image. We used secondary electron detection by CCD detector to produce an SEM image.

However, because of the poor electrical conductivity of a semiconductor such as titania, the accumulation of charge on the surface of samples always results in the deterioration of image quality. Therefore, to improve the electrical conductivity, the edges of the sample were coated with colloidal graphite (isopropanol base, Ted Pella, Inc.) to increase conductivity by keeping the top surface in electrical contact with the lower surface. The samples were aged at 120 °C overnight (approx. 12 hours) to evaporate all the solvent from the colloidal graphite solution. Using SEM we could characterize the uniformity of the films down to a size scale of approximately 10-20 nm. Scanning Electron Microscope (SEM) images were subsequently collected with a Hitachi S-4300 microscope at 3kV for plan-view imaging of the pore accessibility (Chapter 2-5). We also performed cross-sectional SEM imaging to check the thickness and orientation of mesopores and to

study the incorporation of CdTe into the nanopores of titania (Chapter 4). Cross-sectional SEM was also performed to evaluate the texture and thickness of thicker titania films synthesized using a layer-by-layer approach (Chapter 5). To observe the cross-section of the films, samples were prepared on silicon wafer and mechanically fractured by bending before mounting onto the stage. For CdTe-titania samples on FTO coated glass slides, samples were fractured on the back uncoated side of FTO coated slides using diamond cutter. Using a special SEM stub, the samples were mounted vertically facing towards the inner side of the stub attached with carbon tape to the stub. The outer side and the edges of the sample were coated with colloidal silver (isopropanol base, Ted Pella, Inc.) to increase conductivity by keeping the top surface in electrical contact with the lower surface.

Transmission electron microscopy (TEM) is also a powerful imaging technique to image features down to the nanometer range. In this work we use JEOL 2010F (field emission) microscope. Unlike in SEM, TEM the imaging is done using the electrons transmitted through the sample. Therefore, this requires the sample to be electron transparent and also for the sample to hang in space in the path of the electrons. To achieve this, Cu grids are typically used to suspend an electron transparent sample. The sample is then transported onto the grids and this grid is placed in the path of the electrons. Since glass slides or even thinner cover slips are electron opaque, typical sample preparation requires scraping off the film from the glass slides and suspending the scraped powder onto the Cu grid, which is then observed in the microscope. This sample preparation technique obscures the orientation information of the mesochannels because the pieces of film removed by scraping are randomly oriented on the grid. With this sample preparation procedure, we only learn about the long-range order of the sample by observing projections

of the 2D HCP structure. To preserve the orientation information, conventional TEM sample preparation would require thinning the substrate from the back side by polishing, dimpling, and ion milling. Instrumental difficulties made this not possible. However, TEM combined with XRD can give insights into the long range order of the mesopores. Also, it is an essential technique to study crystallinity of the materials and to identify various phases of the crystalline materials using scanning area electron diffraction (SAED) technique and obtaining high resolution transmission electron microscopy (HRTEM) images¹²³. Use of electrons in this case allows one to obtain crystallinity information for smaller regions and smaller crystallites than can be measured by x-ray diffraction, and their indexing is similar to 2-D XRD. Obtaining data from a smaller region allowed us to prove the presence of crystalline titania walls even though the crystallite size and small film thickness gives rise to broad, weak features that cannot be readily observed using XRD (Chapter 4).

1.3.4. Solar Cells

A solar cell or photovoltaic cell is a device which converts sunlight into electricity. Light shining on the solar cell produces both a current and a voltage. When light strikes the cell, a certain part of it is absorbed in the semiconductor materials which ionizes crystal atoms, thereby creating free, negatively charged electrons and positively charged ions. If these ions are created from the basic crystal atoms, then their ionized state can be exchanged readily to a neighbor from which it can be exchanged to another neighbor and so forth. In other words, this ionized state is mobile and it is called a hole. It has properties similar to a free electron except that it has the opposite charge. These holes are reduced by electron donation from a counter electrode and the circuit gets completed by electron migration through the external load and work is done or electricity is generated. This

process requires a material to absorb light and raise electrons to a higher energy state, and the transport of this higher energy electron from the solar cell into an external circuit. Then, electrons dissipate their energy in the external circuit and returns to the solar cell. Figure 1.2 shows the cross section of a solar cell¹²⁴. Photovoltaic energy conversion often uses semiconductor materials and inorganic-organic materials in the form of p-n junctions.

1.3.4.1. p-n junctions

In a typical photovoltaic cell, p-n junctions are formed by joining *n*-type with *p*-type semiconductor materials. Since the *n*-type region has a high concentration of electrons and the *p*-type region has a high concentration of holes, electrons diffuse from the *n*-type side to the *p*-type side. Similarly, holes diffuse from the *p*-type side to the *n*-type side. If the electrons and holes were not charged, this diffusion process would continue until the concentration of electrons and holes on the two sides were the same, as happens if two gases come into contact with each other. However, in a *p-n* junction, when the electrons and holes diffuse to the other side of the junction, they leave behind exposed charges on dopant atom sites, which are fixed in the crystal lattice and are unable to move. On the *n*-type side, positive ion cores are exposed. On the *p*-type side, negative ion cores are exposed. An electric field forms between the positive ions in the *n*-type material and negative ions in the *p*-type material. This region is called the depletion region since the electric field quickly sweeps free carriers out, hence the region is depleted of free carriers. A built-in potential V_{bi} due to electrical field of depletion region is formed at the junction, which is a difference between the electric potential at the edges of the depletion layer¹²⁵. The electric field at depletion region creates an energy barrier that prevents electrons from diffusing into *p*-type side, and similarly, prevents holes from diffusing into *n*-type side. Most of electrons in the *n*-type region are unable to move into the *p*-type side because they cannot have enough energy to overcome

the energy barrier at the p-n junction. On the other hand, any electron from the p-type region as minority carriers can move into the n-type region, because there is no any barrier to stop it. Because they are minority carriers, the concentration of these electrons is very small, however, and it is sufficient to produce transitions of electrons from the p-type to the n-type side that exactly compensate for the diffusion current in the opposite direction.

1.3.4.2. Photovoltaic Effect

The collection of light-generated carriers does not by itself give rise to power generation. In order to generate power, a voltage must be generated as well as a current. Voltage is generated in a solar cell by a process known as the photovoltaic effect ¹²⁶. The collection of light-generated carriers by the *p-n* junction causes movement of electrons to the *n*-type side and holes to the *p*-type side of the junction. Under short circuit conditions, there is no build-up of charge, as the carriers exit the device as light-generated current. However, if the light-generated carriers are prevented from leaving the solar cell, then the collection of light-generated carriers causes an increase in the number of electrons on the *n*-type side of the *p-n* junction and a similar increase in holes in the *p*-type material. This separation of charge creates an electric field at the junction which is in opposition to that already existing at the junction, thereby reducing the net electric field. Since the electric field represents a barrier to the flow of the forward bias diffusion current, the reduction of the electric field increases the diffusion current. A new equilibrium is reached in which a voltage exists across the *p-n* junction. The current from the solar cell is the difference between light-generated current and the forward bias current. Under open circuit conditions, the forward bias of the junction increases to a point where the light-generated current is exactly balanced by the forward bias diffusion current, and the net current is zero.

The voltage required to cause these two currents to balance is called the open-circuit voltage V_{oc} .

1.3.4.3. Thin Film Solar Cells

For thin film solar cells, due to the close proximity to the surface with its high surface recombination rate, electron-hole pairs recombine rapidly near the surface, resulting in low quantum efficiencies. Since electron-hole pairs should not be generated in this layer, it must have a large energy gap. It is referred to as a window layer, through which photons should pass unimpeded, but which is able to protect electrons and holes from recombining at the front contact. The interface between the window layer and the absorber should have a low density of interface states in order to prevent recombination at the interface and enhance photocurrent. A disadvantage of many materials with direct transitions and favorable energy gaps, is that they can't be doped equally well as n-type and p-type semiconductors. Thus, the structure required for solar cells demands heterojunctions. Cadmium sulfide (CdS) has been used as a window layer because it has a wide bandgap (2.41 eV) and is able to protect electrons and holes from recombining at the front surface. CdS can be natively *n*-doped and the interface between the CdS window layer and the absorber has a low density of interface states. Heterojunction solar cells with window layers and absorbers include n-type CdS/p-type CdTe, n-type CdS/p-type CIGS, and n-type CdS/p-type CZTS (CIGS stands for cadmium indium gallium selenide and CZTS for cadmium zinc tin sulfide).

However, when trying to maximize device performance, improvements have been hindered by the loss of photocurrent caused by light absorption in the n-type cadmium sulfide (CdS) window layer. A significant amount of radiation in the solar spectrum, with

wavelength less than 512 nm, gets absorbed by CdS and does not contribute to the collected photocurrent. The resulting loss in photocurrent is estimated to be 7 mA/ cm^2 ¹²⁷. Also, forming a thinner layer of CdS to reduce its absorption has significant challenges of its own, such as formation of pinholes in the CdS which can cause the p-type semiconductor to come into direct contact with the transparent electrode forming micro-junctions and micro-shunts which degrade cell performance¹²⁸. This problem of CdS absorption can be effectively solved by replacing CdS with titanium dioxide (TiO₂) as a window layer. Since TiO₂ has higher energy band gap than CdS (3.2 eV), it is expected to improve the spectral response at low wavelengths, especially in the 400-500 nm range, thereby improving quantum efficiency¹²⁹⁻¹³¹. This hypothesis will be explored in chapter 4 where we will use nanoporous titania thin films as window layer to improve the performance of CdTe-TiO₂ solar cell and will show an expansion in photoactive window as compared to CdS-CdTe solar cells.

1.3.4.4. Solar Cell Characterization

Typical current–voltage (J–V) curves of a solar cell in the dark and under illumination are shown in Figure 1.3. Power is generated when the cell operates in the fourth quadrant of the graph where voltage is positive and current is negative. The solar cell operates in the fourth quadrant. Under illumination, the dark curve will be shifted by the photogenerated current density (J_L). The light has the effect of shifting the J-V curve down into the fourth quadrant where power can be extracted from the diode. Illuminating a cell adds to the normal "dark" current density in the diode as described mathematically by Equation 2

$$J = J_0 \left[\exp\left(\frac{qV}{nkT}\right) - 1 \right] - J_L \quad (2)$$

Where J_o = Reverse saturation current density; J_L = Light generated current density; n = Diode ideality factor; V = applied voltage across the terminals of the diode; q = absolute value of electron charge; k = Boltzmann's constant; and T = absolute temperature (K).

The primary parameters that describe the performance of a photovoltaic device are the short-circuit current density (J_{sc}), open-circuit voltage (V_{oc}), fill-factor (FF) and power conversion efficiency (η).

The short circuit current J_{sc} is the current density that flows through the junction under illumination at zero applied bias. In the ideal case, J_{sc} equals the photogenerated current density (J_L). Therefore, the short-circuit current is the largest current which may be drawn from the solar cell. The short-circuit current mainly depends on the quantum efficiency and spectrum of the incident light (the number of photons).

The open-circuit voltage V_{oc} is the maximum voltage available from a solar cell when the current through the junction is zero, and can be expressed in Equation 3.

$$V_{OC} = \frac{nkT}{q} \ln\left(\frac{J_L}{J_o} + 1\right) \quad (3)$$

Eq. 3 shows that V_{oc} depends on the saturation current of the solar cell and the light-generated current. The reverse saturation current density J_o , plays in a key role in V_{oc} . J_o depends on the recombination rate and energy band structure of the solar cell. Open-circuit voltage can identify the amount of recombination and junction quality in the device.

The short-circuit current density and the open-circuit voltage are the maximum current density and voltage respectively from a solar cell. However, at both of these operating points, the power from the solar cell is zero. The point on the J–V curve that yields the maximum power is referred to as the maximum power point; the corresponding

current density and voltage are maximum current J_{mp} and maximum voltage V_{mp} . The fill factor (FF) is a parameter which determines the maximum power from a solar cell. The FF is defined as the ratio of the maximum power from the solar cell to the product of V_{oc} and J_{sc} . The FF is a measure of the squareness of the J–V curve and is also the area of the largest rectangle which will fit in the J–V curve. The FF is given by

$$FF = \frac{V_{mp}J_{mp}}{V_{oc}J_{sc}} \quad (4)$$

The power conversion efficiency (η) is the most commonly used parameter to compare the performance of a solar cell. The efficiency of a solar cell is defined as the ratio of the maximum output power P_{max} to the input power (incident power) P_{inc} , and can be expressed as

$$\eta = \frac{V_{oc}J_{sc}FF}{P_{inc}} \quad (5)$$

The efficiency depends on the spectrum and intensity of the incident sunlight and the temperature of the solar cell. Therefore, conditions under measurement of efficiency need to be carefully controlled. Terrestrial solar cells are measured under AM1.5 conditions and at a temperature of 25 °C.

1.3.5. Electrochemical Characterization

Electrochemical characterization techniques can provide useful fundamental information about electrochemical systems, including equilibrium potential of reactions and types of reactions occurring in electrodes, reaction kinetics, thermodynamics, and lithium diffusion in electrodes and electrolytes. Typically, electrochemical techniques require static or dynamic control of voltage or current while monitoring the change of both voltage and current.

Cyclic voltammetry (CV) is one of the most commonly used electrochemical techniques to investigate chemical reactions, Nernstian (reversible) or non-Nernstian (irreversible) behavior of redox couples, formation potentials, and reaction mechanisms. CV is convenient and efficient in obtaining qualitative information, though it is usually not a good technique for quantitative studies. In a CV test, the potential of the system is swept linearly towards a peak position, and then returned to the initial value linearly. The procedure can be repeated multiple times. During the potential sweep, current is monitored by a potentiostat. An illustration of a CV controlling profile is shown in Figure 1.4 (a)¹³². The result of CV experiments is usually plotted as current vs. applied potential. An example of the CV curve of TiO₂ vs. Li is shown in Figure 1.4 (b). In chapter 5, the electrochemical performance of titania films was tested in CR2025 coin cells using titania foils as the working electrodes (WE) and pure Li metal foils as the counter electrodes (CE). Cells were fabricated in an Ar-filled glovebox (MBraun), where the oxygen and moisture levels were below 0.1 ppm. The electrolyte was 1 M LiPF₆ salt dissolved in an equal-volume mixture of ethylene carbonate and dimethyl carbonate (Novolyte). CV has been used to study insertion and extraction process of lithium ions into and from mesoporous anatase titania anode according to the following equation:



We can clearly see one pair of redox peaks when scanning between 1 and 3 V vs. Li⁺/Li at various cycles, around 1.7 and 1.95 V. These correspond to the insertion and extraction process of lithium ions into and from mesoporous an anatase titania anode according to equation (6). One more interesting observation is the broadening of peaks at the lower potentials. According to previous studies, this broadening indicates the presence

of amorphous titania¹³³. These results further indicate that these sol-gel titania films contain a combination of anatase and amorphous titania. More CV tests were performed for increasing number of cycles and different thickness of titania films which can be found in chapter 5 of the dissertation.

Galvanostatic cycling is a very important electrochemical technique for LIB research, which provides charging and discharging profiles for LIBs under practical applications. In a galvanostatic cycling test, a cell is charged and discharged galvanostatically (at constant current) between upper and lower voltage limits. The upper and lower voltage limits are determined by the Gibbs free energy of the electrode materials and their products during lithiation. For alloy-type negative electrodes, the lower limits are typically 10 to 50 mV, and the upper limits are typically 1 to 2 V, depends on the type of alloys. The lower limits are chosen to be higher than 0 V vs. Li/Li⁺ because at low potentials lithium tends to deposit on electrode surface, which eventually causes the growth of lithium dendrites, causing safety issues. The applied current is directly related to the power output of the electrode. Usually “C rate” is used to define the cycling rate of LIBs, where $x\text{C}$ is defined as $1/x$ hours per charge or discharge of the full capacity of the battery. Practically C/10 or C/5 is considered slow cycling, though it is non-equilibrium. There are three ways of plotting the results of galvanostatic cycling, namely potential capacity profiles, differential potential-capacity profiles, and cycling performance. From galvanostatic cycling, we can obtain information about phase transformations in electrodes under different kinetics, rate performance, structure of the intermetallics during lithiation (crystalline or amorphous), potential range for practical use, and cycle life of LIBs. We mainly performed these electrochemical characterization techniques to study the

applications of multilayer titania films as negative electrodes in lithium ion batteries in chapter 5. Experimental details will be given in chapter 5. A battery capacity as high as 254 mAh/g has been obtained after 200 cycles for titania film with vertical pore orientation. The effect of porosity, pore orientation and thickness of titania films have been investigated in chapter 5 using galvanostatic cycling.

1.4 Dissertation Outline

The dissertation is organized as follows. Chapter 2 will describe a study of the mechanism of forming orthogonally oriented hexagonal close packed (o-HCP) mesostructures during aging of surfactant-templated titania thin films using *in situ* grazing incidence small-angle x-ray scattering (GISAXS) in a controlled-environment chamber. The effect of surface modification, film thickness and aging temperature on the growth of orthogonally oriented micelles will be studied. Chapter 3 will focus on incorporating hole conducting polymer poly(3-hexyl thiophene) into orthogonally aligned cylindrical nanopores of titania for inorganic-organic hybrid solar cells. Chapter 4 will be dedicated to fabricate nanoporous n-TiO₂/p-CdTe heterojunction solar cell with enhanced response in the near-UV region of the solar spectrum as compared to conventional CdS-CdTe solar cells. In chapter 5, the layer-by-layer synthesis of thick mesoporous titania films with vertically oriented 2D-HCP nanopores and their application in lithium ion batteries as negative electrodes will be described and the effect of pore orientation and film thickness over cycling performance will be discussed. Chapter 6 will include a summary of the dissertation and recommendations for future work.

This dissertation primarily focuses on understanding a few limited aspects of the formation and use of nanoporous titania thin films, especially the growth mechanism of

surfactant templated sol-gel thin films formed using the EISA process and the applications of these ceramic films in the energy conversion field as window layers and energy storage field as electrodes for lithium ion batteries. The most significant impacts of this dissertation are expected to be: i) guidance in methods to investigate the crystal growth mechanisms for different metal oxides and use this information for materials design; ii) new design ideas for the fabrication of inorganic solar cells and inorganic-organic hybrid solar cells using nanoporous titania thin films as window layers; iii) development and application of methods to characterize materials with nanoporous features; and iv) demonstration for application of these titania thin films in energy storage. In addition to the significance of the findings reported here for titania thin film formation, the methods developed can also be used to develop future studies of surfactant templated titania thin films and their applications.

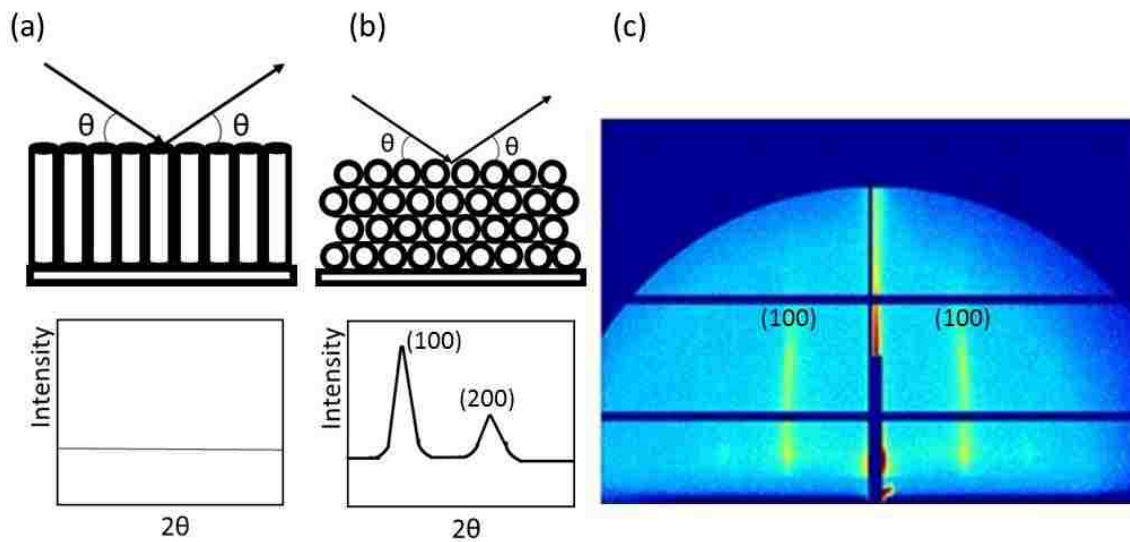


Figure 1.1. Orientations of a $p6mm$ hexagonal mesophase (above) and the corresponding predicted diffraction patterns (below). (a) mesophase with channels perpendicular to the substrate, (b) channels parallel to substrate and 100 face parallel to the surface. Adapted from Hillhouse et al.¹ (c) 2D-GISAXS pattern for mesophase with channels perpendicular to the substrate. Adapted from Das et al.²

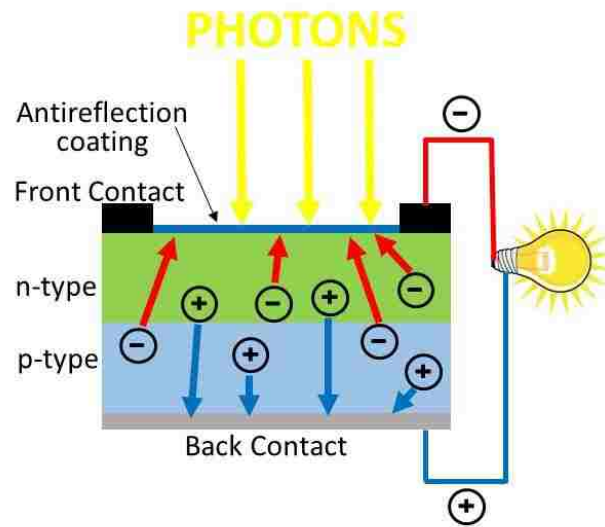


Figure 1.2. Cross-section of a solar cell. Adapted from ¹²⁴

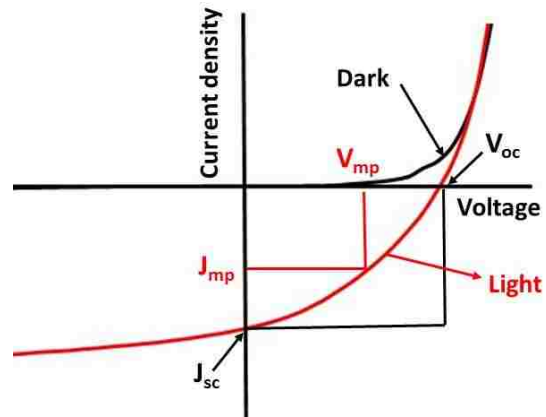


Figure 1.3. A typical current–voltage characteristic of a solar cell in the dark and under illumination.

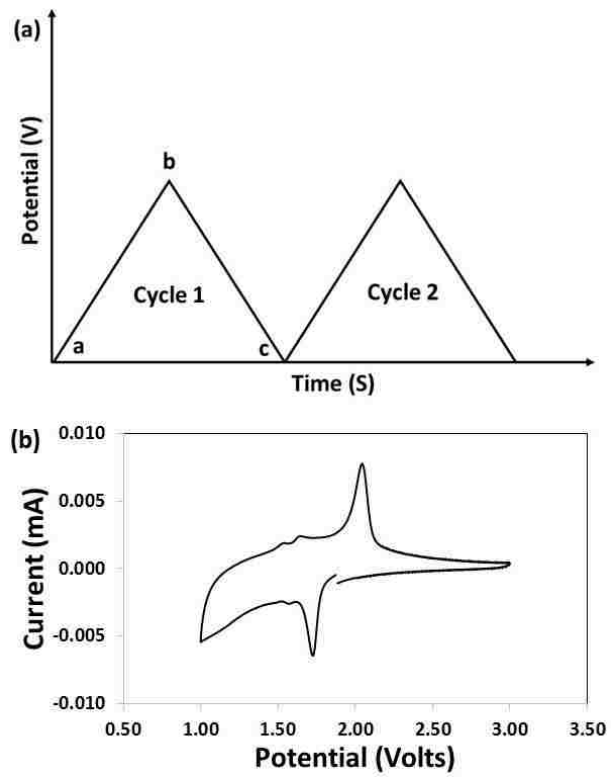


Figure 1.4. (a) Controlling profile of a CV test and (b) An example of CV of TiO_2 vs. Li

Copyright © Suraj R. Nagpure 2016

Chapter 2. *In Situ* GISAXS Investigation of Low-Temperature Aging in Oriented Surfactant-Mesostructured Titania Thin Films

Reproduced with permission from Nagpure, S., Das, S., Garlapalli, R., Strzalka, J., Rankin, S. E., Journal of Physical Chemistry C, 2015, 119, 22970-22984⁴¹

2.1. Summary

The mechanism of forming orthogonally oriented hexagonal close packed (o-HCP) mesostructures during aging of surfactant-templated titania thin films is elucidated using *in situ* grazing incidence small-angle x-ray scattering (GISAXS) in a controlled-environment chamber. To promote orthogonal orientation, glass slides are modified with crosslinked Pluronic P123, to provide surfaces chemically neutral towards both blocks of mesophase template P123. At 4 °C and 80% RH, the o-HCP mesophase emerges in thin (~60 nm) films by a direct disorder-to-order transition, with no intermediate ordered mesophase. The Pluronic/titania o-HCP GISAXS intensity emerges only after ~10-12 minutes, much slower than previously reported for small-molecule surfactants. The Avrami model applied to the data suggests 2D growth with nucleation at the start of the process with a half-life of 39.7 minutes for the aging time just after the induction period of 7 minutes followed by a period consistent with 1D growth kinetics. Surprisingly, films that are thicker (~250 nm) or cast on unmodified slides form o-HCP mesophase domains, but by a different mechanism (2D growth with continuous nucleation) with faster and less complete orthogonal alignment. Thus, the o-HCP mesophase is favored not only by modifying the substrate, but also by aging at 4 °C, which is below the lower consolute temperature (LCST) of the poly(propylene oxide) block of P123. Consistent with this, *in situ* GISAXS shows that films aged at room temperature (above the LCST of the PPO block) have randomly oriented HCP mesostructure.

2.2. Introduction

The Evaporation Induced Self Assembly (EISA) process¹³⁴ is a rapid, scalable approach to preparing surfactant-templated ordered mesostructured silica films by evaporation of solvents during spin¹³⁵⁻¹³⁷ and dip coating¹³⁸. Because of the well-defined structure of these engineered nanostructured thin films, EISA has been adopted for a wide variety of applications^{107, 139-142} including protective films¹⁴³⁻¹⁴⁴, low-k dielectrics¹⁴⁵⁻¹⁴⁷, sensors¹⁴⁸⁻¹⁵³, nanomaterial templates^{96, 154-160} and membranes¹⁶¹⁻¹⁶⁹. Titania is of particular interest for its optical, electronic and chemical properties¹⁷⁰⁻¹⁷⁹ and by using highly acidic conditions, mesoporous titania films with several pore geometries have been synthesized^{66, 69-71}. However, of all possible structures, films with hexagonally close packed pores oriented orthogonal to the film (o-HCP architecture) are desirable because they provide an accessible array of nonintersecting channels for rapid transport of reactants or charge carriers¹⁸⁰⁻¹⁸⁵, for creating devices with confinement-induced properties¹⁸⁶⁻¹⁹⁰, and for templating of nanowire arrays¹⁹¹⁻¹⁹⁵. Related orthogonally oriented TiO₂ nanotube arrays prepared by anodizing titanium¹⁹⁶ have been used to demonstrate some of these advantages¹⁹⁷⁻²⁰², but contain relatively large pores (>25 nm diameter) and do not have the processing flexibility provided by the EISA method. TiO₂ films with bicontinuous cubic pores also provide accessible, nm-scale pores without requiring special alignment procedures²⁰³⁻²⁰⁴, but interconnected pores are not desired for some applications. Also, with some templates, cubic films form over narrow composition ranges²⁰⁵ and are fragile because of their high porosity.

By analogy with surface chemistry strategies used to orient block copolymer films⁷⁴⁻⁷⁹, the Rankin group has reported the synthesis of mesoporous titania thin films with

o-HCP cylindrical nanopores using EISA with P123 (a triblock copolymer with composition $\text{HO}(\text{CH}_2\text{CH}_2\text{O})_x(\text{CH}_2\text{CH}(\text{CH}_3)\text{O})_y(\text{CH}_2\text{CH}_2\text{O})_x\text{H}$, where on average $x = 20$ and $y = 70$) as structure directing agent and titanium(IV) ethoxide as titania precursor⁸⁰⁻⁸¹. The hypothesis underlying this approach is that orthogonal alignment of the HCP mesophase can be achieved in a EISA-derived ceramic film by modifying the substrate surface so that it interacts equally with both blocks of the P123 template, making it chemically “neutral” towards the template surfactant. Monte Carlo simulations⁸⁴⁻⁸⁵ have shown that this is the expected outcome for mixtures of surfactants and small molecules, and not just for neat block copolymers⁷⁸. A related epitaxial orientation procedure was demonstrated by Tolbert and coworkers, where HCP film was cast onto a cubic template film to induce orthogonal alignment⁸⁶. In addition to surface modification, the synthesis procedure for o-HCP TiO_2 films includes aging after coating in a refrigerator at 4 °C under high relative humidity (approx. 94%). The objectives of using a low temperature are to slow titanium precursor condensation and to provide a driving force for mesophase formation, similar to the subambient temperatures used by Alberius et al.⁵⁵ Even though this aging procedure has been found to be an essential part of o-HCP TiO_2 film formation, little is known about the o-HCP mesostructure formation mechanism other than what has been inferred by characterization of the films before and after calcination².

To understand the mesostructure evolution of thin films during EISA, several groups have used a wide range of techniques including grazing incidence small angle x-ray scattering (GISAXS), transmission electron microscopy and time resolved Fourier transform infrared spectroscopy (FTIR)^{87-88, 104-106, 206-212}. Among these techniques, GISAXS is most relevant here because it can be conducted *in situ*, and it provides insight

into mesostructure development and organization during the formation of self-assembled particles²¹³ and EISA thin films²¹⁰. Grosso et al. analyzed the mechanisms involved in the formation of 2D-hexagonal templated SiO₂ and TiO₂ mesostructured films during dip coating using Brij-58 as surfactant and found that the self-assembly leads to the formation of organized phase at the final stage of the drying process and involves the formation of an intermediate disorganized phase⁵². The disorder to order transition takes place within 2-3 minutes after the start of coating for TiO₂ and SiO₂ under the conditions studied. Other reports have shown that for dip-coated thin films, the mesostructure generally forms through a disorder-to-order transition which may involve intermediate hybrid mesophases that are related to the concentration gradient⁸⁷⁻⁸⁹. Doshi et al. studied the self-assembly of surfactant template thin-film silica mesophases synthesized using surfactants cetyltrimethylammonium bromide (CTAB) and Brij-56 and found that 2D HCP mesostructure (*p6mm*) forms from a lamellar mesophase through a correlated micellar intermediate¹⁰⁴. Gibaud et al. studied EISA of silica mesophases synthesized using surfactant CTAB and found that the final structure of the film is strongly influenced by the rate of evaporation which itself governs the concentration gradient inside the film¹⁰⁵. While *in situ* SAXS studies of EISA have provided magnificent insights, most have been restricted to the dip-coating process itself and the time span on the order of seconds after the coating process. Also, most of the studies have been done for mesoporous silica films synthesized with small surfactant molecules (CTAB and Brij surfactants) and very few studies have been done for TiO₂ films. Thus, it is not known to what extent their findings can be extrapolated to the conditions used to synthesize o-HCP films.

One surprising finding for o-HCP TiO₂ films is that, while most prior *in situ* GISAXS studies of EISA suggest that the final mesostructure forms during (or within seconds after) dip coating, mesophase orientation can be controlled by sandwiching ~250 nm thick films with a second chemically neutral slide well after the coating process is complete (on the order of up to 20 minutes)^{80, 119}. However, this type of post-coating modification is not unprecedented; as Grosso and coworkers discuss in reviews of the fundamentals of mesostructuring through EISA, a tunable steady state (TSS) occurs in some cases, during which the inorganic framework is still flexible and susceptible to modification by changing aging conditions¹⁰⁶⁻¹⁰⁷. The TSS helps to explain why the structure of EISA-derived films can be tuned by adjusting variables such as the humidity of the vapor¹⁰⁸⁻¹¹⁰, the sol aging time (which affects the time scale for condensation after coating)¹¹⁰⁻¹¹¹, the pH of the film¹¹²⁻¹¹⁴, the presence of solvent vapors¹¹⁵, and confining the coating using materials of different surface energy^{116-117, 119-120, 214}. Generally for silica, this TSS lasts from a few seconds at low humidity to 10 minutes at high humidity¹²¹. However, for TiO₂ system, the condensation of titania oligomers has been proposed to be triggered by evaporation of HCl. Because HCl departs very slowly, TSS for some TiO₂ sol compositions of more than 1 hour duration have been observed¹⁰⁶. Because the TSS plays an important role in the formation of o-HCP TiO₂ films, studying the process *in situ* will provide novel insights into how to engineer and tune EISA films for new applications requiring an active oxide component.

Here, *in situ* GISAXS is used to monitor the formation of the o-HCP mesophase in P123 templated TiO₂ films during a relatively long time frame as the films age (which corresponds to the TSS). The objective is to directly test the hypothesis that o-HCP

structure develops during film formation due to modification of the surface with crosslinked P123⁸⁰⁻⁸¹. A possible alternative hypothesis is that the o-HCP structure emerges via anisotropic merging of pores in a precursor $Im\bar{3}m$ phase, which has been observed by other researchers in TiO₂ films with accessible vertical pores^{90-91, 106}. The measurements will be made using a linear actuator enclosed in a controlled-environment chamber to withdraw a coated film and to monitor its evolution by GISAXS during aging. Results will be compared for thin (~60 nm) films on modified and unmodified glass surfaces, thicker films, and as a function of aging temperature. The kinetics of the mesostructure evolution will be modeled using the Avrami equation and will be compared to relevant o-HCP structures in block copolymer films.

2.3 Experimental Section

NoChromix powder (Godax Laboratories, Inc.), concentrated sulfuric acid (95-98%, Sigma Aldrich), P123 (poly(ethylene glycol)-block-poly(propylene glycol)-block-poly(ethylene glycol) with $M_n \sim 5800$, Sigma-Aldrich), 1,6-diisocyanatohexane (98%, Sigma Aldrich), glycerol (99+%, Sigma Aldrich), titanium ethoxide (Technical grade, Sigma Aldrich), HCl (36 wt%, EMD Chemicals), ethanol (200 Proof, Decon Laboratories) and acetone (Fisher Scientific) were all used as received.

The sol required for titania film synthesis was prepared based on the procedures of Koganti et al.⁸⁰ Prior to depositing any material, borosilicate glass slides (1 in \times 2 in) were cleaned with a NoChromix glass cleaning solution in sulfuric acid prepared according to the manufacturer's instructions. To modify slides with crosslinked P123 (when this was done), cleaned glass slides were dip coated using an acetone-based solution containing equimolar amounts (0.415 mM) of Pluronic surfactant P123 and 1,6-diisocyanatohexane. To this solution, a single drop of glycerol was added to serve as a cross-linker so that the

films would be stable. The slides with modifying coating were aged at 120 °C overnight to drive the cross-linking reaction to completion. The thickness of cross-linked P123 as measured using profilometry was ~30 nm with surface roughness of 4-5 nm. This cross-linked P123 layer is expected to be removed completely after calcination at 400 °C as shown previously⁸¹. Titania sols were prepared by adding 2.1 g of titanium ethoxide to 1.53 g concentrated HCl, stirring for 10 min and adding 0.65 g of P123 dissolved in variable amount of ethanol. 32 g of ethanol was used for thin films and 6 g for thick films.

In situ aging GISAXS experiments were done at the Advanced Photon Source (APS) at Argonne National Labs on beamline 8-ID-E using an x-ray beam 100 μm (H) x 50 μm (V) with wavelength of 1.6868 Å²¹⁵. The APS operated in top-up mode, i.e. at constant storage ring current, during the measurements. Figure 2.1 shows the chamber and scattering geometry for *in situ* GISAXS experiment. Samples for *in situ* dip coating were prepared within a sealed chamber with inner dimensions 5 × 5 × 6.5 in³ with aluminum side walls and copper lid and base plate. Unless otherwise noted, the base plate was in thermal contact with a circulating chiller maintained at 4 °C. Helium gas bubbled through saturated potassium sulfate solution into the chamber to maintain constant relative humidity. A digital hygrometer (VWR model 35519-050) with probe inserted in the lid monitored the relative humidity inside the chamber, typically RH > 80%. The sol prepared as explained above was contained in a plastic container, (the lid of a 50 mL Falcon tube) approximately 10 mm deep, resting on a copper block in thermal contact with a thermoelectric element so that its temperature could be changed independently. A small translation stage raised a glass slide out of the solution at about 15 mm/min. X-rays entered the chamber through a mica window and were incident on the sample several mm above

the surface of the solution. Scattered x-rays exited the chamber through a Kapton window. Unlike the usual scattering geometry for GISAXS at Beamline 8-ID-E, the vertical sample meant the scattering plane was horizontal with the phi-circle of the diffractometer controlling the incident angle. A small piece of tungsten, $1 \times 2 \times 15 \text{ mm}^3$ attached horizontally to the end of the GISAXS beamstop served as the beamstop for the *in situ* dip coating GISAXS measurements. The distance from the sample to the detector (Pilatus 1M, Dectris) was 1474 mm. The analysis of the GISAXS data was done using the GIXSGUI package for Matlab²¹⁶. Consideration of the scattering geometry shows that corrections for the instrumental resolution are negligible compared to the experimentally observed peak widths described below²¹⁷.

To understand the effect of aging temperature on mesostructure development and orientation, scanning electron microscopy (SEM) was performed using a Hitachi S-4300 at 3 kV. The films after *in situ* GISAXS were calcined in a muffle furnace (Vulcan 3-550) at 400° C for 10 minutes after heating at a ramp rate of 25° C/min followed by rapid cooling. SEM samples were prepared by cutting the glass slide to the desired shape using a glass cutter and then mounting exactly at the center of an SEM stub coated with carbon tape. The edges of the sample were coated with colloidal graphite (isopropanol base) to increase conductivity by keeping the top surface in electrical contact with the lower surface. SEM samples were aged at 120° C overnight (~12 h).

2.4 Results and Discussion

The thickness of the thin titania films in this study (prepared using 32 g of ethanol) was determined by ellipsometry to be ~60 nm after aging, which has previously been found to be thin enough to give orthogonally oriented pores without sandwiching the films with

a second neutral surface^{80, 82}. *In situ* GISAXS patterns were recorded for this sample in intervals of 1 minute from the start of the aging process until 30 minutes of aging time at one spot on the film, located 13.5 mm above the bottom of the coated section. The sampling geometry of the sampling is shown schematically in Figure 2.1 and described in more detail in the Experimental Section. After this period, patterns were collected with the beam at this spot and four additional spots to determine spot-to-spot variability and to test for beam damage, at 45 min, 60 min and 75 min of aging. Figure 2.2 shows selected 2D GISAXS patterns at representative times during the evolution of the mesostructure for a thin titania film on modified substrate during aging at 4 °C. Generally the presence of the o-HCP cylindrical mesophase is indicated by two intense rods parallel to the scattered beam, located on both sides of the beam stop. These rods can be indexed to the (100) plane of the HCP structure and their rod shape can be attributed to the finite cylindrical shape of the micelles (Kiessig fringes are most likely not observed because of a distribution of rod lengths and orientations)⁸¹. The GISAXS patterns show that in the first 10 minutes of aging (Fig. 2.2a), there is no indication of mesostructure development as we do not see any spots or rods in the pattern. After 15 minutes (Fig. 2.2b), faint spots can be seen on both sides of the beam stop due to diffraction in the plane of the film, which indicates that mesostructure started developing even though it is still not well defined. After 20 minutes of aging (Fig. 2.2c), clear vertical rods are visible on both sides of the beam stop indicating that the orthogonally oriented cylindrical micelles started developing. The intensity of the vertical rods further increases for longer aging times (for example, the pattern at 75 min, Fig. 2.2d).

While only selected time points are shown in Fig. 2.2, no distinct out-of-plane diffraction spots (which indicate parallel alignment of micelles or a mesophase with 3D

symmetry) are visible at any other time points. Other studies that showed the formation of vertically oriented cylindrical channels by transformation of a cubic phase and merging of the pores normal to the film also showed diffraction spots consistent with the cubic phase prior to thermal treatment^{71,90-91}. The absence of out-of-plane diffraction spots is consistent with the hypothesis underlying the work of Koganti et al.⁸⁰ that vertical channels simply form due to reorientation of the HCP phase in response to the modification of the surface of the substrate with a chemically neutral crosslinked P123 layer. The o-HCP structure is the first ordered mesophase formed, and it emerges slowly by a disorder-order transition consistent with the TSS proposed for highly acidic TiO₂ sols¹⁰⁶⁻¹⁰⁷. The slow mesophase formation and long TSS may also be accentuated by the use of P123 as a template²¹⁸.

Many more GISAXS patterns were collected than those shown in Fig. 2.2, but it is not easy to discern the quantitative variation in the intensity of the (100) rods by direct inspection of the 2D patterns. Therefore, linecuts were generated by integrating the 2D patterns for q_z values covering the Yoneda band from 0.025 to 0.03 Å⁻¹. Figure C.1a (Appendix C) shows a representative 2D GISAXS pattern along with the region of integration for the linecut shown using vertical lines. The resulting linecut is shown in Figure C.1b on a semilog scale. The high intensity peaks at $q_y = \pm 0.0425$ Å⁻¹ are the orthogonally oriented (100) diffraction peaks. Note that the beamstop was asymmetrically positioned to optimize the view at low q_y values on the positive side of the beamstop (a gap in the CCD array was positioned to the left of the beamstop).

Figure 2.3 shows a waterfall plot illustrating the evolution of the 1D linecut patterns on a log-log scale for a thin titania film on modified substrate during aging at 4 °C and ~80% RH. The Yoneda band includes a shoulder at low q_y values whose intensity increases

for the first 10 minutes and then reaches a plateau with very little change afterwards, either in amplitude (see Appendix C Figure C.2a) or position (Figure C.2b). The growth of this shoulder shows that there is no indication of beam damage to the sample prior to mesostructure development. For the first few minutes of aging, the intensity of the (100) diffraction peak is very low, indicating that the development of an ordered mesostructure has not begun. After an induction period on the order of several minutes, (100) diffraction peaks appear symmetrically and grow in intensity until 25 minutes of aging. However, after 25 min, the intensity of the peak decreases until the end of the 30 min initial kinetic period (see below). Throughout the kinetic measurement, the shape of the diffraction pattern and the position of (100) diffraction peak does not change significantly, indicating growth of a mesophase with constant structure. A similar disorder-to-order transition was reported during the formation of vertically oriented cylindrical block copolymer mesophases during solvent annealing²¹⁹ and thermal treatment²²⁰, although detailed kinetics were not reported. To quantify the kinetics in the present case, the integrated intensity of the (100) peak in the linecuts (after baseline correction) was used as a measure of the extent of development of the o-HCP phase with respect to time during aging.

Figure 2.4a shows the evolution of o-HCP ordering in a thin film on modified substrate during aging at 4 °C. The measured integrated intensity at a fixed position (13.5 mm above the bottom of the slide) is shown with filled circles starting from 1 minute to 75 minutes of aging. The trend in these detailed data is consistent with the qualitative description of Figure 2.2. The intensity initially is close to zero, and increases little for the first 7 minutes of aging. The mesophase transformation then accelerates in accordance with a disorder-order transition, with a maximum rate of intensity increase at about 16

minutes, and continued slow mesostructure development up to 25 minutes. The intensity then decreases somewhat for the remainder of the period of frequent GISAXS scanning. This most likely is a result of accumulated radiation damage due to frequent exposure of the same spot on the sample to the high intensity x-ray beam. Note that this is the first and only indication of beam damage during sampling and suggests only mild deformation of the long-range order of an assembling mesostructure since P123 mesophases in water melt at temperatures ranging from 45 to 85 °C²²¹. We attribute this accumulated radiation damage to the kinetics/thermal effect described previously by Malfatti et. al²²² during mesophase transitions. Consistent with this explanation, the intensity increases again at later times, when the frequency of scanning decreases. This shows that the damage is reversible, although the extent of reversibility is limited by ongoing polycondensation of titania. The increase in intensity is accompanied by a decrease in the width of the peak consistent with continuous mesophase nucleation and growth (see below).

Varying the vertical position of the sample allowed us to measure fresh parts of the sample that were not exposed to the x-ray beam during the earlier time series (at $z = 13$, 13.3, 14 and 14.2 mm, as compared to $z = 13.5$ mm for the initial time series. Note that the vertical size of the beam was 0.05 mm). The patterns obtained were qualitatively the same, only differing in the intensity of the features, indicating that the material curing away from the beam evolves to the same structure as the part of the sample where the evolution was observed with the series of x-ray exposures at short times. Performing similar integrations and plotting the intensities shows that the intensity can be smoothly interpolated between the initial part of the time-resolved series at small t ($t < 25$ minutes) and the intensity from fresh regions of the sample at later times (open symbols in Figure 2.4a). From this study,

it appears that 45 minutes is the minimum aging time to develop the o-HCP mesostructure close to its full extent at 4 °C.

To understand the role of surface modification in the development of the o-HCP mesostructure, a GISAXS study was conducted during aging at 4 °C for a thin titania film on unmodified substrate. According to the hypothesized effect of the substrate surface chemistry, this would have been expected to give out of plane diffraction consistent with the HCP mesophase oriented parallel to the glass slide. Instead, the same type of pattern developed as in Fig. 2.2, corresponding to an o-HCP mesophase. This surprising result indicates that the orthogonal orientation is promoted not only by the surface modification, but also by the temperature and humidity of the system during aging. Unlike prior studies in which the films were coated at room temperature and then transferred to a refrigerator for aging^{80, 223}, here the films were coated and aged at the same low temperature. This is significant because of the temperature-dependent behavior of P123. A comprehensive study of Pluronic surfactants (triblock copolymers of poly(ethylene oxide)-b-poly(propylene oxide)-b-poly(ethylene oxide) ($\text{EO}_x\text{PO}_y\text{EO}_x$) in water by Wanka et al.²²¹ showed that significant thermotropic behavior occurs in Pluronics because of changes in the solubility of the poly(propylene oxide) (PPO) blocks. In a temperature range from 15-20 °C, P123/water mixtures were reported to transition from ordered mesophase (at high temperature) to isotropic mixtures and from micelles to dissolved monomers (depending on the concentration)²²¹. Thus, at 4 °C, the contrast in hydrophilicity between PPO and poly(ethylene oxide) (PEO) is reduced and the polymer may find hydrophilic surfaces to be "neutral". However, the titanate species mixed with the PEO blocks still provide sufficient driving force for mesophase formation by increasing the Flory-Huggins

interaction parameter of the system leading to microphase separation²²⁴, as a result of which orthogonal alignment of the cylindrical micelles occurred on an unmodified substrate also. The high relative humidity during aging may also contribute to the orthogonal alignment; a recent self-consistent field study by Fredrickson and coworkers showed that orthogonal cylinders are favored by slow evaporation and weak block segregation when a good solvent for both blocks is used²²⁵. This contradicts the trend in many solvent-annealed block copolymer hexagonal films, but the solvent used for annealing usually has a strong preference for one block²²⁶. Here, both volatile species (ethanol and water) are good solvents for PEO and PPO at 4 °C, so slow evaporation due to the low temperature and high RH are expected to favor the o-HCP phase.

Figure 2.4b shows the evolution of the intensity of the (100) peak on unmodified substrate during aging at 4 °C at 13.5 mm above the bottom of the slide, along with the average intensity curve with the error bars as standard deviation. The same procedure was followed as for the film on modified substrate for measurement and analysis. In the beginning, the mesostructure development takes place more rapidly as compared to the film on modified glass. However, the values for average maximum intensity at steady state are lower than those observed for the modified substrate. The maximum average intensity for unmodified substrate is 0.34 ± 0.066 which is half as compared to the average maximum intensity of 0.68 ± 0.073 for the film on a modified substrate. This large difference in intensity indicates that even though vertical alignment of cylindrical micelles occurs for unmodified substrate after aging at 4 °C, it is only partial; a larger amount of material with well-ordered o-HCP domains is found with glass modification.

Because a contrast in orientability has been found in the past between thin films (<100 nm) and thicker films, thick films (thickness ~ 250 nm) were also studied by GISAXS by preparing films with less ethanol (6 g). According to Koganti et al.⁸⁰, for thick films, complete orthogonal HCP orientation is best achieved by sandwiching the films between two modified surfaces. This sandwiching is thought to be necessary because the orthogonal orientation from one modified surface does not propagate across the entire film. Thin films are advantageous because they do not need to be sandwiched between two modified surfaces in order to fully orient the HCP phase orthogonal to the substrate. Figures 2.4c and d show the evolution of the (100) Bragg rod of thick films on modified and unmodified substrates, respectively, during aging at 4 °C at a fixed position (13.5 mm above the bottom of the coating) along with the average intensity at four other positions at later times where error bars represent standard deviations among those four points. For thick films, orthogonal domains were observed even without sandwiching them between two modified surfaces (sandwiched films were not studied here due to difficulty focusing the beam on a sandwiched film). However, the average maximum intensity observed was significantly lower than for the thin film on modified substrate, which indicates that the degree of o-HCP mesophase formation is less. While this is surprising (again) relative to prior observations of the effects of film thickness^{80, 223}, coating and aging the films at 4 °C from the outset may have favored the o-HCP structure due to weak segregation between PPO and PEO and slow evaporation of ethanol and water²²⁵.

Evolution of the sample structure is also evident in the changing width of the diffraction peak. Figure 2.5 shows the full width at half maximum (FWHM) of the (100) peak for different titania films at 13.5 mm above the bottom of the coating or at a set of

four other points (averaged). The error bars represent the standard deviation of the FWHM of the four points excluding the measurement at 13.5 mm. The FWHM for the thin titania film on modified substrate (Fig. 2.5a) changes continuously during the aging process, as does the size of ordered domains²¹⁷. Scherer grain-size analysis can estimate the average number of layers contributing to the diffraction peak, $N = q_{hkl} / \Delta q_{hkl}$.²¹⁷ When the peak first appears, $N < 2$, then increases to $N \sim 8$ as FWHM decreases over the first 25 minutes of aging. The narrowing of the peak corresponds to the increase in intensity in Fig. 2.4a, suggesting that both nucleation and growth of ordered domains occurs during the first 25 minutes of aging. After 25 minutes, the FWHM begins increasing as the (100) intensity decreases. Correspondingly, N decreases, probably due to radiation damage, and then returns to $N \sim 8$ when the scanning frequency decreases. All of the other titania films follow the same trends as in Fig. 2.4 (Figs. 2.5b-d). The average FWHM values for the films was estimated using four spots not subject to high-frequency sampling and are shown in Fig. 2.5 by unfilled diamonds. The mean FWHM is generally smaller for the thin titania film on modified substrate relative to unmodified and thicker substrates, although the only statistically significant difference is between the thin film on modified substrate and the thick film on unmodified substrate.

Further quantitative insight into the kinetics of mesostructure development was gained by fitting the (100) peak intensity vs. time data to the *Kolmogorov-Johnson-Mehl-Avrami (KJMA)* model, more simply known as the Avrami equation²²⁷⁻²³⁰. The Avrami equation is used to understand the kinetics of phase transformation when nucleation and growth give rise to a sigmoidal curve. The kinetic curves shown in Fig. 2.4 for all films

during aging at 4 °C have a sigmoidal form, so the KJMA equation was applied. The simplest form of the Avrami equation is

$$f(t) = 1 - \exp(-kt^n) \quad (2.1)$$

where $f(t)$ is fraction of transformation that has happened at time t , k is the rate coefficient and n is the Avrami index. This form of the Avrami equation was derived assuming that (a) nucleation occurs randomly and homogeneously over the entire untransformed portion of the material, (b) the growth rate does not depend on the extent of transformation, and (c) growth occurs at the same rate in all directions consistent with the dimensionality implied by the Avrami index²³¹. The Avrami equation in linearized form is rewritten as:

$$\ln \left[\ln \left(\frac{1}{1-f(t)} \right) \right] = \ln(k) + n \ln(t) \quad (2.2)$$

Eq. 2.2 allows us to determine constants n and k from by linear regression from a plot of $\ln[\ln(1/(1-f(t)))]$ vs. $\ln(t)$. If the transformation follows the Avrami equation, the data on this plot should follow a single straight line for a given set of conditions. In our case, the value of $f(t)$ has been calculated by dividing the actual intensity of the (100) diffraction by the maximum average intensity observed. For example, the average maximum intensity for a thin titania film on modified substrate (Fig. 2.4a) was approximately 0.68 using the value obtained at large time from freshly exposed regions of the sample in order to remove the effects of radiation damage late in the kinetics of transformation. The intensity of the diffraction peak depends on the electron density contrast between the titania walls and the mesophase, which may be influenced by the degree of polycondensation of the mesophase. However, the polycondensation rate of the inorganic matrix is not expected to be significantly affected by film thickness or surface modification. Therefore, any effects of

polycondensation on the Avrami parameters should be consistent between samples at a given temperature.

Figure 2.6 shows the Avrami equation fit for the evolution of each of the titania films during aging at 4 °C. For each sample, a straight line was observed for the filled symbols, indicating that the Avrami equation could be applied over this range of times. However, the unfilled data points did not follow the Avrami equation. The early data (before ~7 minutes for the thin film on modified substrate during aging at 4 °C) represent an induction period during which formation of the micelles is likely to be occurring²³² (indicated by the increase in scattered intensity at low angles²³³, Fig. C.2a) but not giving rise to noticeable diffraction. Once sufficient radiation damage accumulated in the samples (e.g. after 25 min for thin film on modified substrate), a net decrease in $f(t)$ was observed and the Avrami equation was no longer applied.

Table 2.1 summarizes the Avrami equation parameters found for each of the titania films. The induction time is highest for the thin film on modified substrate (7 min) as compared to all other films (3 min), which indicates relatively slow mesostructure growth in this sample. This can also be seen from Fig. 2.4 where the thin film on modified substrate has a longer low-intensity initial period. We can clearly see from Fig. 2.6a that for thin film on modified substrate, there are two distinct linear regions over which the Avrami equation can be applied. The first is for aging times between 8 to 14 minutes and the other one from 16 to 25 minutes. The value of n in the Avrami equation reflects the nature of transformation and is associated with the mechanism of crystal growth. An Avrami index of 3 is usually interpreted as three-dimensional growth of nuclei formed instantaneously or two-dimensional growth with a constant nucleation rate, whereas an Avrami index of 2 is

interpreted as two-dimensional growth with nucleation at the start of the process²³⁴⁻²³⁵. The value of n in Table 2.1 is approximately 2 (within the estimated uncertainty) for the titania thin film on modified substrate until 14 minutes of aging which is interpreted as two-dimensional growth with nucleation at the start of the process. An Avrami index of value 1 might indicate one dimensional growth for later (16-25 mins) aging times for titania thin film on modified substrate. The value of the Avrami index for the thin film on unmodified substrate is calculated to be 3, which indicates two-dimensional growth with a constant nucleation rate since the films are confined in one dimension and the o-HCP phase would be expected to grow laterally in the plane of the films. Thus there is a clear difference in mesostructure growth mechanism for thin films on modified and unmodified substrate. This may be because a better oriented mesophase on modified substrate requires nucleation during the transformation process, whereas less oriented mesophase for thin film on unmodified substrate grows throughout the film from randomly oriented nuclei present at the end of the micelle formation process. The values of the Avrami index for thicker films are estimated to be 3, indicating two-dimensional growth with constant nucleation rate. The rate constant k for different films can be calculated from the y-intercept of the Avrami fit. Direct comparison of rate constants might be misleading, as they have different units. However, the kinetics of different films can be compared by calculating the half-life ($t_{1/2}$) for different films. In this case $t_{1/2}$ will be defined as the time required for the mesostructured development to evolve to half of its final value ($f(t) = 0.5$ at $t_{1/2}$). Half-life can be calculated from Eq. 2.2 as:

$$t_{1/2} = \left(\frac{\ln 2}{k} \right)^{1/n} \quad (2.3)$$

Table 2.1 summarizes half-lives for different titania films. For thin titania film on modified substrate, the half-life (39.7 min for parameters found during aging between 8 to 14 min and 24.7 min for aging between 16 to 25 min) is higher than for the thin film on unmodified substrate, which further indicates that the transformation is slower for the thin film on modified substrate. The half-lives for thick films on both modified and unmodified substrates are also comparable to the value for thin films on unmodified substrates. However, the maximum average intensity is highest for the thin film on modified substrate ($\sim 0.68 \pm 0.073$), which indicates that even though the evolution of orthogonal orientation is slower for thin film on modified substrate, it is the most complete and well-defined for these films. In fact, hindered diffusion of micelles (or surfactants) in a well-oriented thin film is most likely responsible for the relatively slow kinetics of mesostructure development for the thin film on modified substrate. Films which are not as well oriented show faster evolution of the phase, whether the cause is the thickness of the film or the surface chemistry²³⁴⁻²³⁵.

To verify the hypothesis that orthogonal orientation is favored (even in thin films on unmodified substrates or thick films) by aging at 4 °C due to weak segregation between PEO and PPO and slow solvent evaporation, GISAXS studies were also performed at room temperature (23 °C). The relative humidity in the aging chamber was in the range of 90-95% during these measurements. Figure 2.7 shows selected 2D GISAXS patterns showing how the mesostructure of thin titania film on modified substrates evolves during aging at 23 °C. Here, no evidence of correlated scattering is observed during the first 5 min of aging (Fig. 2.7a). After 8 min of aging (Fig. 2.7b), a diffuse ring pattern appears surrounding the beam stop and scattered beam. The intensity of the diffuse ring further

increases and it becomes more distinct with increasing aging time (Fig. 2.7c/d). However, unlike all of the patterns collected at 4 °C, no rods suggesting in-plane diffraction were observed at any point in the aging process. Instead, the diffuse ring indicates that randomly oriented HCP domains form in the films, with no preferred orientation.

To confirm and to better understand the effects of aging temperature on mesostructure orientation, *ex situ* SEM characterization was done. The samples used for *in situ* GISAXS were calcined at 400 °C for 10 minutes after heating at a rate of 25 °C/min. Figures 2.8a and 2.8c show representative SEM images for P123-templated titania thin films aged on modified substrates aged at 4 °C and 23 °C, respectively. For the film aging at 4 °C (Fig. 2.8a), a very well-ordered, accessible porous structure was observed everywhere indicating vertical alignment of the cylindrical micelles, which is consistent with the corresponding 2D GISAXS pattern collected after 30 minutes of aging (Fig. 2.8b), which shows (100) diffraction peak on either sides of the beam stop. When a film of the same composition deposited onto the same type of modified slide was aged at 23 °C (Fig. 2.8c), randomly oriented parallel stripes were observed everywhere at the top surface of the film, indicating that the cylindrical micelles were arranged parallel to the substrate but with no preferred in-plane orientation. To verify that the difference is not caused by a change in adhesion of the titania film due to removal of the organic layer during calcination, a low magnification plan view SEM image (Appendix C Figure C.3) shows no cracks or defects in the film on modified substrate. Also, x-cut adhesion (ASTM standard D3359) ratings of 4A (out of 5) were measured for films with and without the crosslinked P123 layer, revealing no difference in adhesion. From the 2D GISAXS pattern collected after 30 min of aging (Fig. 2.8d), it is clear that the overall mesostructure during aging at 23 °C has

random orientation throughout the film, but with some degree of parallel orientation near the film surface (Fig. 2.8c). This suggests that there may be a gradient in the mean orientation of the micelle domains, with domains near the surface aligned parallel to the substrate, domains near the thin film/substrate interface oriented orthogonal to the substrate, and domains in the interior of the thin film randomly oriented, combining so that overall a powder diffraction ring is obtained due to the range of orientations of the HCP domains.

In order to test this hypothesis, SEM images were collected of the base of the films (at the film / substrate interface). To do this, one side of a glass slide was covered with masking tape after cleaning. Both sides were coated with the crosslinking P123 solution and cured, and then both sides were coated with titania sol and aged for 2 h in the refrigerator (4 °C) or at room temperature (23 °C). Before calcining as usual, the tape from one side was peeled off and remounted upside down on another glass slide. The tape was completely removed during calcination, thus allowing the underside of the coating to be visualized. The plan view SEM images (Appendix C Figure C.4) show that for the film aging at 23 °C (Fig. C.4a), the mesostructure at the underside of the film consists of poorly ordered accessible pores consistent with local orthogonal orientation. In contrast, the film aged at 4 °C (Fig. C.4b) exhibits ordered, accessible mesopores indicating orthogonal orientation throughout the film. This additional SEM characterization is consistent with random average orientation of the HCP mesophase throughout films aged at 23 °C, but domains predominantly parallel to the film/vapor interface and orthogonal to the film/substrate interface. This type of mixed orientation has been predicted in mesoscopic

simulations of surfactants confined between flat surfaces with significantly dissimilar interactions with the mesophase components²³⁶.

As suggested above, the reason for the difference in orthogonally oriented domains for films aged at 4 °C and 23 °C might have to do with the temperature dependence of hydrophobic behavior of the PPO block of the surfactant P123. Since Wanka et al.²²¹ showed that significant thermotropic behavior occurs in Pluronics because of changes in the hydrophilicity of the PPO blocks at around 15-20 °C, for films aged at 4 °C, the "contrast" between hydrophobic PPO and hydrophilic PEO is expected to be small and the polymer may find hydrophilic surfaces to be "neutral". This would be expected to promote orthogonal alignment of the mesophase during low temperature aging. On the other hand, at 23 °C, PPO becomes hydrophobic and the usual contrast mechanisms return. A study of Pluronic F127 [EO₁₀₆PO₇₀EO₁₀₆] in water by FTIR agrees with the conclusion that there is a hydrophilic/hydrophobic transition of PPO somewhere near 20 °C²³⁷.

To quantify the evolution of thin titania film on modified substrate during aging at 23 °C, the intensity was integrated along the polar coordinate in the detector plane, φ , for $30^\circ < \varphi < 40^\circ$ and over the range of total q from 0-0.1 \AA^{-1} . Figure 2.9a shows evolution of the integrated intensity of the diffraction peak vs. time for thin titania film on modified substrate during aging at 23 °C at 13.5 mm above the bottom of the coating or at a set of four other points (averaged). The error bars represent the standard deviation of the intensity of the four points. The intensity changes slowly for the first five minutes, and then increases almost linearly until 15 min of aging. The average intensity of the spots not exposed to repeated x-ray doses is just slightly higher than the intensity at 13.5 mm and the difference is not significant. Figure 2.9b shows the fit of the Avrami equation to the (100) peak

intensity data for the thin titania film on modified substrate during aging at 23 °C. A good fit was found for the filled data points, but the unfilled data points did not follow the Avrami equation. The early data (before ~2 minutes) represent an induction period during which formation of the micelles is likely to be occurring but not giving rise to noticeable diffracted intensity. The rate constant k for thin titania film on modified substrate at 23 °C is 0.00388 min⁻². The value of Avrami Index n is 2.0 at 23 °C, which is interpreted as two-dimensional growth with nucleation at the start of the process²³⁴⁻²³⁵. Thus there is no clear difference in mesostructure growth mechanism for thin films on modified substrates at different aging temperatures. Also, there is no significant difference in the d-spacing for different aging conditions, suggesting that the primary effects of temperature are to change the rate and degree of orientation of the structure. The half-life $t_{1/2}$ calculated from equation 3 for aging at 23 °C comes out to be 13.3 min, which is less than that calculated for thin titania film on modified substrate during aging at 4 °C. This result further indicates that randomly oriented structure allows faster evolution of the mesophase.

The observations made here both confirm the hypothesis that o-HCP films are formed directly by a disorder-order transition for P123-templated films cast onto P123-modified glass slides, and suggest unexpectedly important roles of the environment of the film on the formation of the orthogonally aligned phase. These observations are consistent with modification of the film inducing orthogonal alignment at the substrate/film interface. However, the results also are consistent with orthogonal alignment at the vapor/film interface when the films are aged at 4 °C, and parallel alignment when the films are aged at 23 °C. This leads to the strongest orthogonal alignment when both factors are combined and the films are thin (thin films on modified substrates aged at 4 °C) and random

orientation consistent with parallel HCP at the top / orthogonal HCP at the bottom when thin films on modified surfaces are aged at 23 °C. When we compare these results to prior results where the films started aging for a few minutes at 23 °C before being placed in a 4 °C environment, it seems that some degree of parallel micelle alignment may have begun before the films were placed in the refrigerator, which led to a mixed orientation for films on plain glass and fully orthogonal alignment for films on modified substrates. The long TSS observed in the present study helps to explain why orthogonal HCP mesostructures could be obtained by aging at 4 °C shortly after film formation, with sandwiching of thick films to help reorient random domains that may have started to form initially.

2.5 Conclusions

The development of mesostructure and orientation during low temperature aging at 4 °C under high humidity in surfactant-templated titania films was investigated using *in situ* GISAXS. Modification of glass slides with crosslinked template (Pluronic surfactant P123) was used to control surface chemistry to enhance orthogonal orientation of the hexagonal close packed (HCP) mesophase. For a thin (~60 nm) titania film on modified substrate, orthogonally oriented HCP cylindrical micelles start developing after a 7 minute induction period and the intensity evolution followed Avrami kinetics with an index of 2, most likely indicating a mechanism of two dimensional growth of the o-HCP mesophase with nucleation at the start of the process. At the end of the aging period, intense vertical rods due to scattering in the film were observed on both sides of the beam stop, indicating that only the o-HCP phase forms. Unlike prior GISAXS studies based on small molecule surfactant templates^{71, 90-91}, no intermediate phase was observed during the development of the o-HCP cylindrical micelles; it formed directly by a disorder-order transition. This observation is consistent with the expected effect of modifying the surface to give an

interface equally attractive towards the PEO and PPO blocks of the template, and therefore to reorient the HCP phase orthogonal to the solid substrate. The half-life for o-HCP development in this film after the induction period was about 39.7 min, and led to a well-ordered mesostructure within an hour. Although radiation damage interfered with the GISAXS intensity observed during repeated sampling of a single spot, the intensity recovered when the sampling frequency decreased and was found to be increased in regions of low sampling frequency.

Similar *in situ* GISAXS experiments at 4 °C were performed for three additional samples: thin films on unmodified slides and thicker films (~250 nm) on both modified and unmodified slides. Using plain glass and thicker films were both anticipated to reduce the degree of orthogonal orientation of the HCP phase. Surprisingly, only the o-HCP phase was observed in the GISAXS patterns of all of these samples. No evidence for HCP domains oriented parallel to the substrate or randomly could be found, although the ultimate intensity of these three samples was less than for the thin film on modified substrate (for example, the intensity was about half for the thin film on unmodified substrate than for the modified substrate). The finding of only an o-HCP GISAXS pattern contradicted prior studies which showed randomly oriented HCP patterns for thin films on unmodified substrates⁸⁰ or thick films without sandwiching with a second modified slide.²²³ This was attributed to the low temperature and high relative humidity used from the start of the coating process (in prior studies, films were cast at room temperature and moderate RH prior to being transferred to a refrigerated high RH box for aging). The low temperature (4 °C) is below the temperature where PPO blocks have been shown in previous studies to exhibit a thermotropic shift from hydrophobic (high temperature)

behavior to hydrophilic. Also, by analogy with solvent annealing mechanisms of orthogonally orienting HCP block copolymer phases^{225,135}, the high RH may contribute to an orthogonal orientation at the film/vapor interface. For all three samples at 4 °C, a similar Avrami coefficient was found ($n \sim 3$) indicating two-dimensional growth with constant nucleation rate. Thus there is a clear difference in crystal growth mechanism for thin film on modified substrate and other films. Also the induction period was reduced to ~3 min with increased rate of the mesostructure evolution. Also the half-life for thin film on modified substrate is higher than other three films indicating better orthogonal structure develops slowly. To confirm the temperature effect, aging a thin film sample on a modified substrate at 23 °C was found to lead to randomly oriented HCP channels.

The results obtained here suggest that the most well-defined orthogonally aligned HCP mesophase is obtained by a direct disorder-to-order transition during the transient steady state period after the coating has been deposited. However, the results indicate that aging at low temperature (4 °C) at high RH also contributes substantially to orthogonal orientation of the HCP phase, and that while the order and orientation may not be as complete, these conditions alone can induce partial o-HCP formation for thin films on unmodified slides or thick films. Thus, a temperature below the thermotropic transition temperature of the block copolymer template and a high relative humidity are suggested to be essential to forming orthogonally oriented block copolymer template films, while modifying the substrate for chemical neutrality towards the templating surfactant gives more complete orthogonal orientation across the entirety of the film.

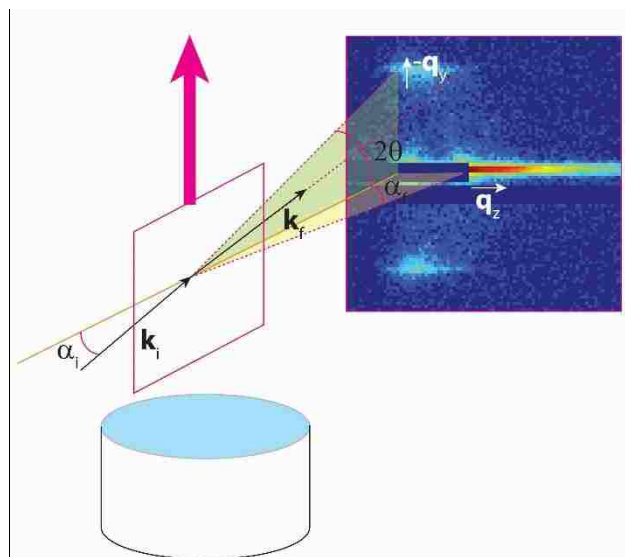


Figure 2.1. Scattering geometry for *in situ* dip coating GISAXS measurements. For each experiment, a vertically oriented sample slide is raised from a reservoir at a controlled rate. X-rays are incident on the sample at an angle α_i and specularly reflected at angle α_f in the horizontal plane, normal to the plane of the sample. The projection of the scattering angle onto the vertical plane is 2θ , and the wave-vector transfer components q_z and q_y are perpendicular and parallel to the sample plane, respectively.

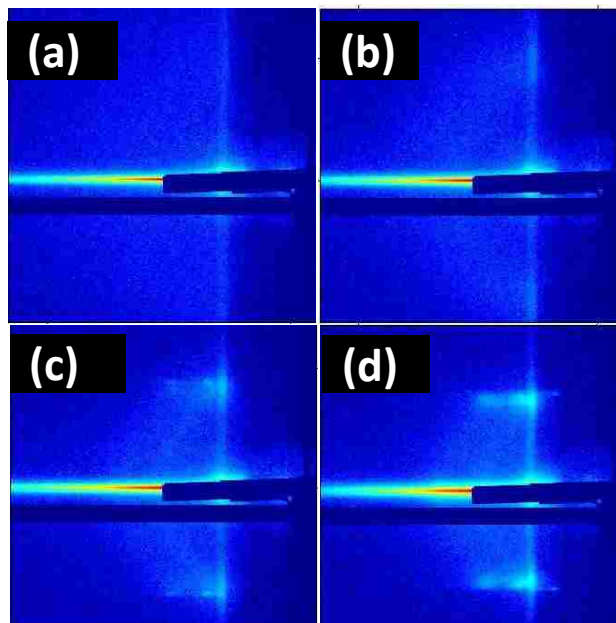


Figure 2.2. 2D GISAXS patterns showing the evolution of mesostructure for thin (~60 nm thick) titania film on modified substrate after aging at 4 °C and ~80% RH for a) 10 min b) 15 min c) 20 min and d) 75 min after coating.

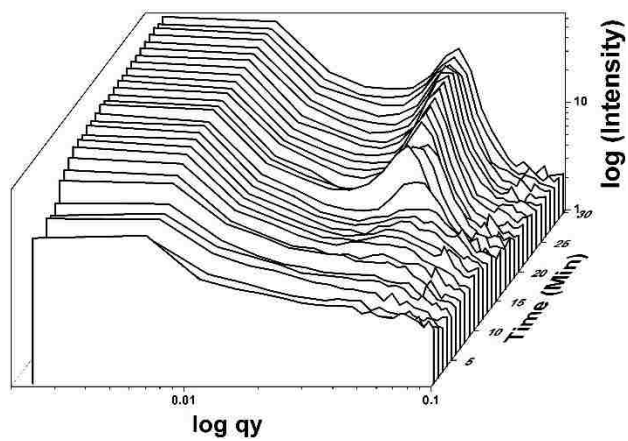


Figure 2.3. Waterfall plot showing the evolution of the mesostructure for thin titania film on modified substrate during aging 4 °C for the first 30 minutes. The plots were generated by integrating slices from the 2D GISAXS patterns for q_z values from 0.025 to 0.03 \AA^{-1} .

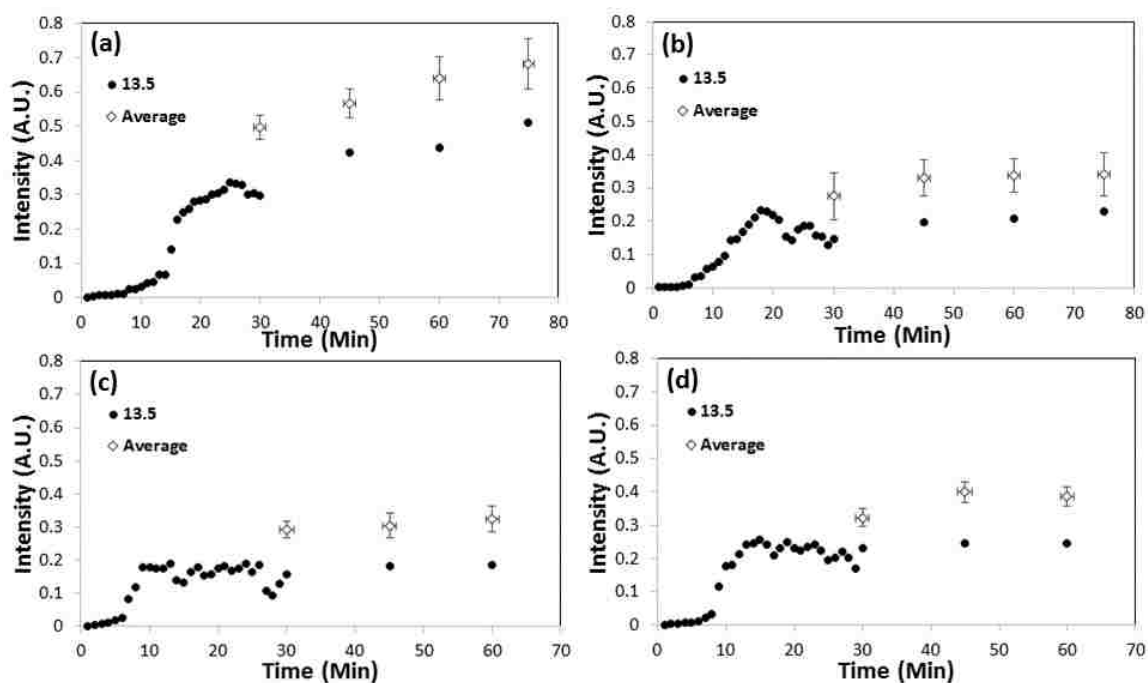


Figure 2.4. Evolution of the integrated intensities of the (100) peak of the o-HCP structure vs. time for (a) thin titania film on modified substrate, (b) thin titania film on unmodified substrate, (c) thick titania film on modified substrate, and (d) thick titania film on unmodified substrate during aging at 4 °C at 13.5 mm above the bottom of the coating or at a set of four other points (averaged). The error bars represent the standard deviation of the intensity of the four points excluding the measurement at 13.5 mm.

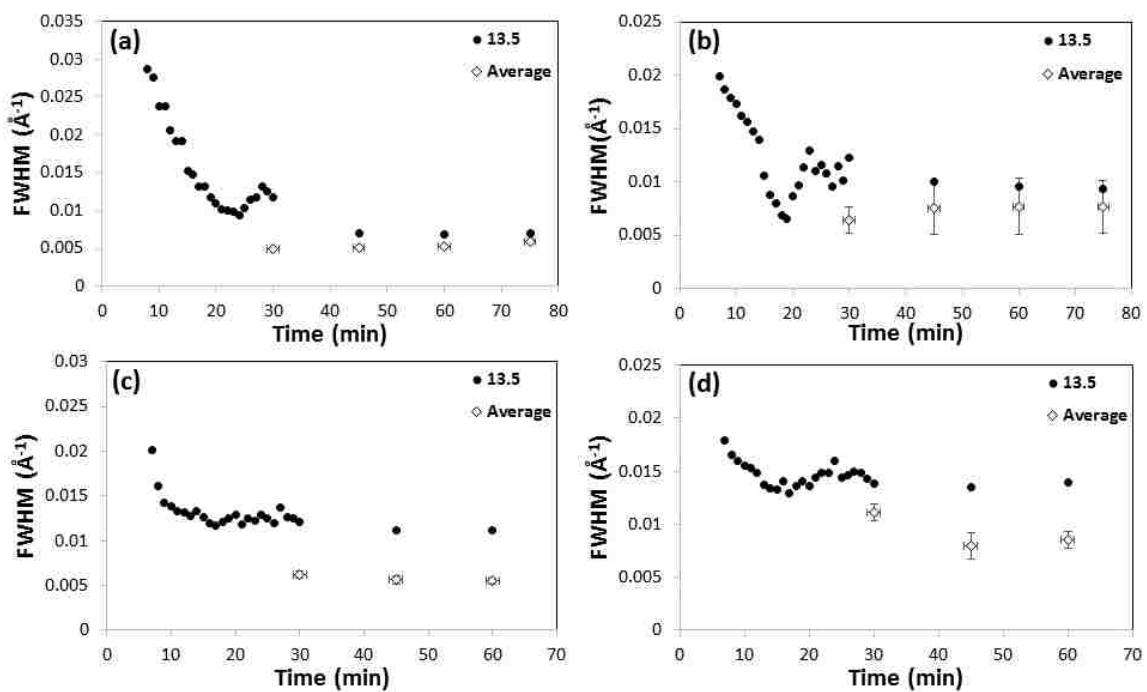


Figure 2.5. FWHM (full width at half maximum) for (a) thin titania film on modified substrate, (b) thin titania film on unmodified substrate, (c) thick titania film on modified substrate, and (d) thick titania film on unmodified substrate at 13.5 mm above the bottom of the coating or at a set of four other points (averaged). The error bars represent the standard deviation of the FWHM of the four points excluding the measurement at 13.5 mm.

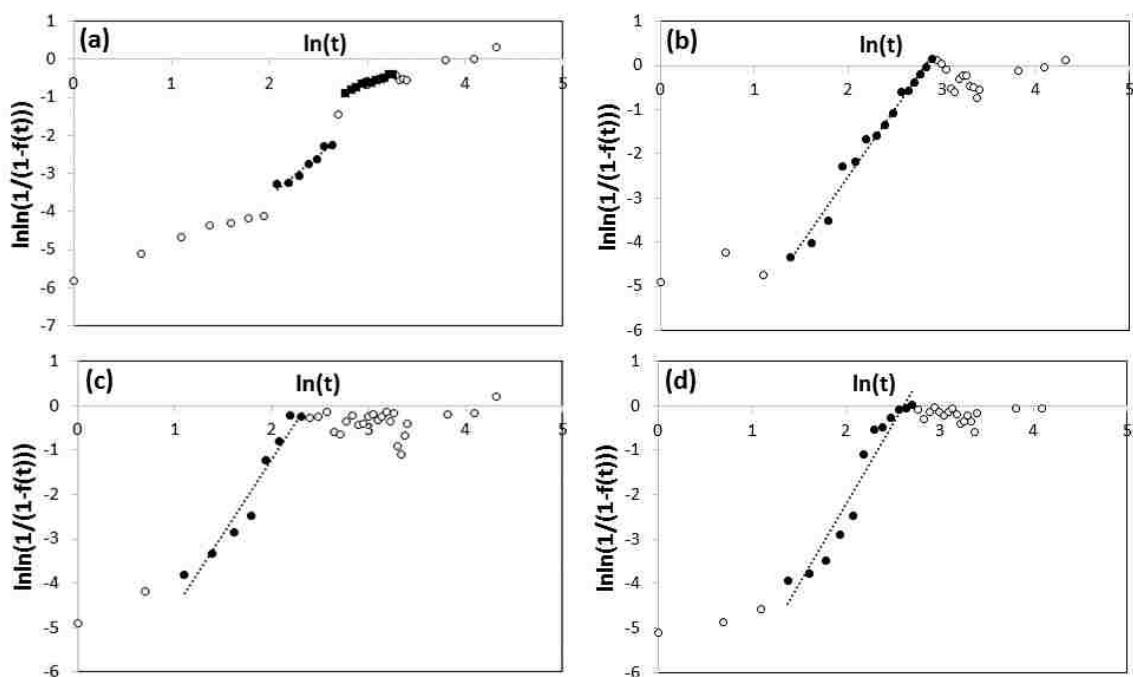


Figure 2.6. The linearized Avrami equation fit to data for (a) thin titania film on modified substrate, (b) thin titania film on unmodified substrate, (c) thick titania film on modified substrate, and (d) thick titania film on unmodified substrate during aging at 4 °C. The filled symbols were fit and the open symbols were not, either because they were measured during the induction period (for early data) or because they were measured after significant radiation damage was observed (for late data).

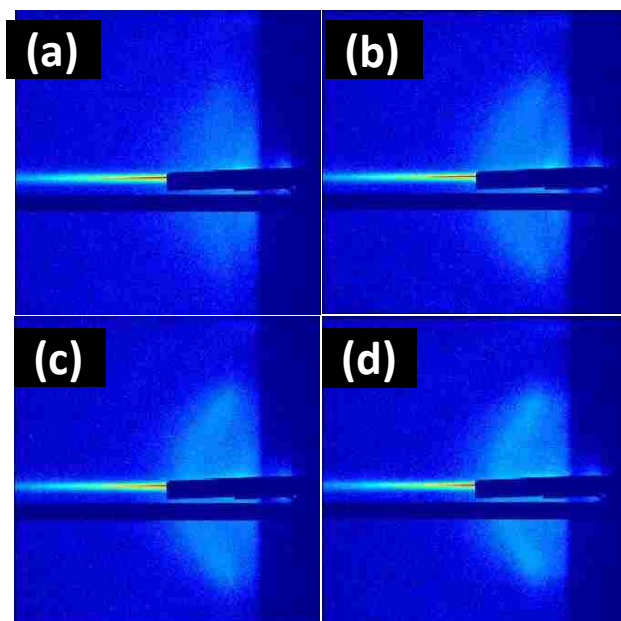


Figure 2.7. Selected representative 2D GISAXS patterns collected during the aging of a thin P123-templated titania film on a modified substrate during aging at 23 °C for aging times of (a) 5 min, (b) 8 min, (c) 10 min and (d) 15 min.

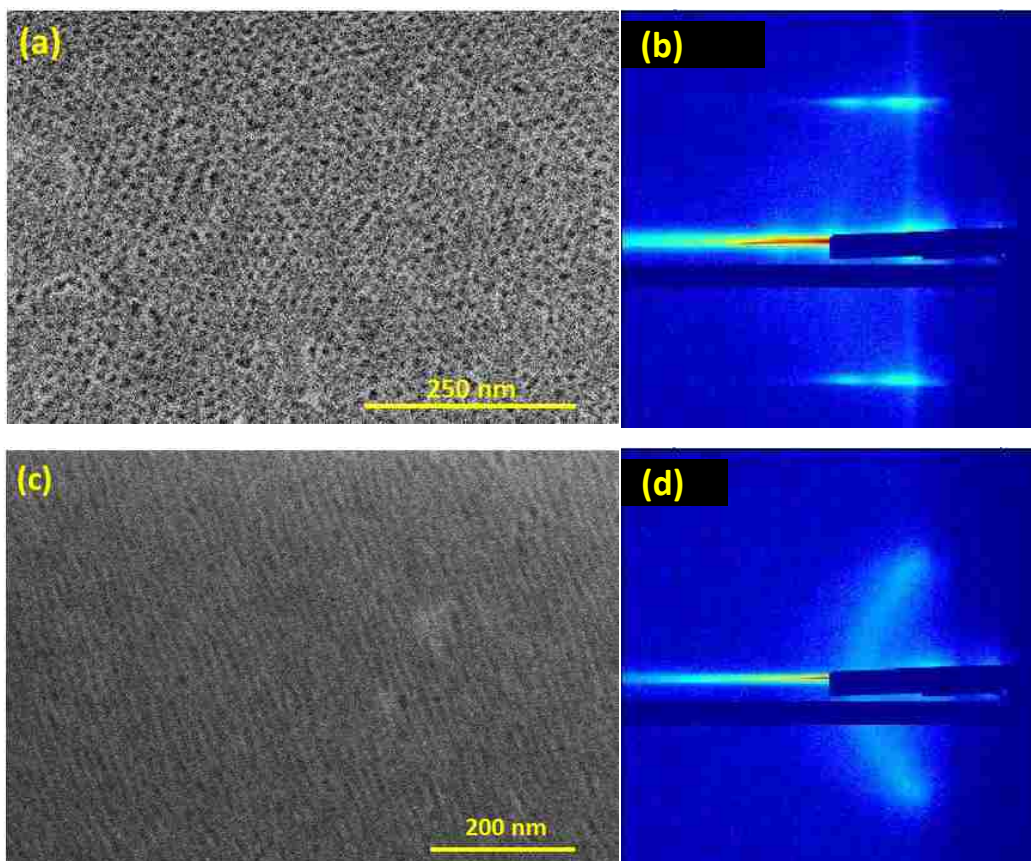


Figure 2.8. Top view SEM images of thin titania films on modified substrate aged at (a) 4 °C and (c) 23 °C after calcination at 400 °C for 10 minutes using a ramp rate of 25 °C/min; and GISAXS patterns after 30 minutes of aging at (b) 4 °C or (d) 23° C.

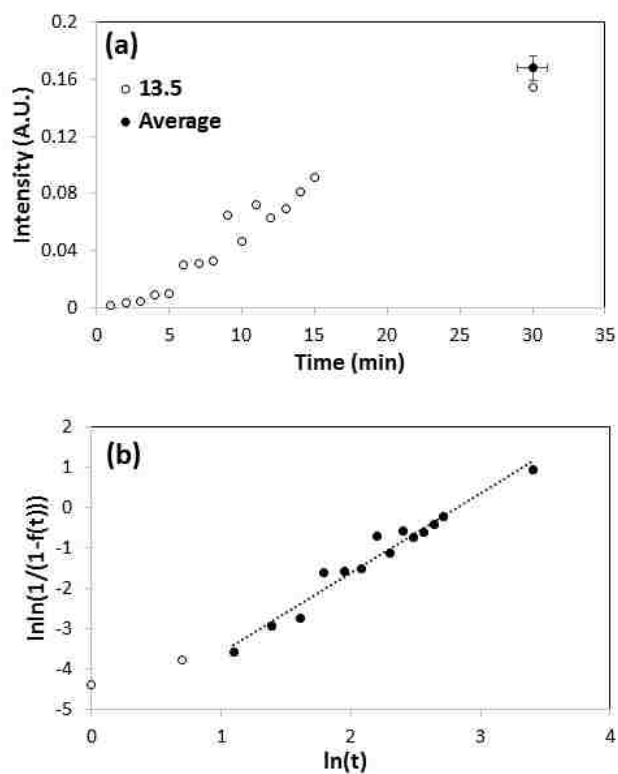


Figure 2.9. (a) Evolution of the integrated intensity of the diffraction peak vs. time for thin titania film on modified substrate during aging at 23 °C at a point 13.5 mm above the bottom of the coating or at a set of four other points (averaged). The error bars represent the standard deviation of the intensity of the four points excluding the measurement at 13.5 mm. (b) The linearized Avrami equation fit to data for thin film on modified substrate during aging at 23 °C. The filled symbols were fit and the open symbols were not, because they were measured during the induction period (Induction period = 2 min, Avrami parameters, $n = 2.0$, $k = 0.00388 \text{ min}^{-2}$).

Table 2.1. Parameters found by fitting the Avrami equation to each of the films aged at 4 °C and high relative humidity.

Sample	Maximum Average Intensity (A.U.)	Induction Time (min)	<i>n</i>	k (min⁻ⁿ)	Half Life (min)
Thin film on modified substrate	0.68± 0.073	7	2.07 ± 0.22	0.00044	39.7
			0.97 ± 0.05	0.028	24.7
Thin film on unmodified substrate	0.34± 0.066	3	3.08 ± 0.11	0.00017	14.8
Thick film on modified substrate	0.32± 0.038	2	3.33 ± 0.32	0.00038	9.5
Thick film on unmodified substrate	0.40± 0.030	3	3.63 ± 0.30	0.000075	12.3

Copyright © Suraj R. Nagpure 2016

Chapter 3. Incorporating Poly(3-hexyl thiophene) into Orthogonally Aligned Cylindrical Nanopores of Titania for Inorganic-Organic Hybrid Solar Cells

3.1. Summary

The incorporation of hole conducting polymer poly(3-hexyl thiophene) (P3HT) into the 8-9 nm cylindrical nanopores of titania is investigated using films with a unique orthogonally oriented hexagonal close packed mesostructure. The films are synthesized using evaporation induced self-assembly (EISA) with Pluronic triblock copolymer F127 as the structure directing agent. The orthogonally oriented cylindrical nanopore structure was chosen over a cubic structure because confinement in uniform cylindrical channels is hypothesized to enhance hole conductivity of P3HT by inducing local polymer chain ordering. Orthogonal orientation of the cylindrical nanopores is achieved by modifying the substrate (FTO-coated glass slides) with crosslinked F127. After thermal treatment to remove organic templates from the films, P3HT is infiltrated into the nanopores by spin coating a 1 wt% P3HT solution in chlorobenzene onto the titania films followed by thermal annealing under vacuum at 200 °C. The results show that infiltration is essentially complete after 30 minutes of annealing, with little or no further infiltration thereafter. A final infiltration depth of ~14 nm is measured for P3HT into the nanopores of titania using neutron reflectometry measurements. Photoluminescence measurements demonstrate that charge transfer at the P3HT-TiO₂ interface improves as the P3HT is infiltrated into the pores, suggesting that an active organic-inorganic heterojunction is formed in the materials.

3.2. Introduction

Inorganic-organic hybrid bulk heterojunction solar cells have attracted considerable attention in recent years due to advantages such as low cost, tunable design, and simple fabrication processes that can be scaled for large-area devices²³⁸⁻²⁴³. In such bulk heterojunction solar cells, the active layer consists of an interdigitated or interpenetrating network of a conjugated polymer such as poly(3-hexylthiophene) (P3HT) as the donor material and an inorganic semiconductor (such as TiO₂, ZnO, CdS) as the electron acceptor. Out of all the inorganic-organic hybrid systems, TiO₂ is among the most widely used inorganic semiconductor in hybrid donor-acceptor blends because of advantages such as high availability, low toxicity and low cost. One major problem in hybrid solar cells, especially those composed of soft materials, is that the propensity for phase segregation leads to poor blending and morphological instability. This represents a significant hurdle to making good devices since enforcing acceptor and donor domain sizes on the order of a few nm is critical for good charge separation efficiency. One creative strategy to get around the phase segregation problem is to use templated inorganic hosts with nanoscale dimensions and backfill these with conjugated polymers. This approach has been used by many researchers using TiO₂-P3HT bulk heterojunctions with different morphologies of titania including nanotubes²⁴⁴⁻²⁴⁹, nanoparticles²⁵⁰, nanorods²⁵⁰⁻²⁵⁶, pompons²⁴⁵, and spherical nanoparticles²⁵⁷. All of these morphologies have dimensions of the range of 50-200 nm which is significantly higher than the diffusion length for P3HT (~5-20 nm^{72, 258-259}). Therefore there is a significant likelihood of recombination of electrons and holes generated in the P3HT before reaching the respective electrodes, which would be expected to lead to the poor efficiency. Thus, it is hypothesized that electron donor P3HT must be

intermixed with titania that has features defined on the 10 nm length scale in order to obtain a high charge separation yield.

As a transparent and n-type semiconductor, TiO₂ is a promising metal oxide for photovoltaic and opto-electronic devices²⁶⁰⁻²⁶¹ and has been used previously by many researchers to play different roles in photovoltaic devices such as antireflection coating²⁶²⁻²⁶³, the interlayer in organic solar cells²⁶⁴, as electron transport material in dye-sensitized solar cells and hybrid solar cells^{21, 265}. However, little attention has been paid to the influence of the nanostructure of TiO₂ on the performance of heterojunction solar cells. McGehee and coworkers studied infiltration of P3HT into cubic nanopores of titania of approx. 10 nm diameter^{72, 99, 266} and obtained a power conversion efficiency of 0.5 % after infiltration of P3HT into the nanopores of titania to a depth of 40 nm. They attributed the low efficiency to the polymer chain being able to coil within cubic nanopores rather than forming aligned chains where π -stacking would enhance charge carrier mobility. McGehee and coworkers have suggested that the hole conductivity of P3HT in the nanopores could be significantly enhanced if the chains were aligned by confinement by the surface of straight pore walls²⁶⁶. With this in mind, an ideal architecture for an inorganic-organic hybrid photovoltaic material is hypothesized to consist of P3HT infiltrated into vertically oriented cylindrical nanopores of titania with a pore diameter of ~10 nm.

The present work is the first to begin to address the infiltration of P3HT into vertically oriented cylindrical nanopores of titania with the long-term goal of increasing the efficiency of inorganic-organic hybrid photovoltaics based on these materials. The nanostructure employed here consists of continuous titania films with vertically aligned 2D hexagonal close packed (HCP) cylindrical nanopores with pore diameter of 8-9 nm. These

films have a pore diameter less than the diffusion length of P3HT, but two well-defined phases for conduction of charge carriers to each electrode²⁶⁶. In addition, the uniform cylindrical channels in these films are hypothesized to conduct holes 5 orders of magnitude faster than in interconnected cubic channels by confining polymer chains as regioregular, isolated wires rather than free coiled chains likely to be found cubic pores^{99, 266}. Because of these features, films with orthogonally aligned HCP (o-HCP) channels are expected to be ideal components for improved solid state inorganic-organic hybrid photovoltaics.

The specific strategy employed to prepare the titania films uses evaporation induced self-assembly (EISA)¹⁶⁴ with Pluronic surfactant F127 as the structure-directing agent. F127 is a non-ionic triblock copolymer with molecular formula $\text{EO}_{106}\text{PO}_{70}\text{EO}_{106}$, where EO is ethylene oxide and PO is propylene oxide, and has average molecular weight of 12,500 Da. Titania films with o-HCP phase using Pluronic surfactant P123 (MW = 5800) have previously been synthesized^{2, 65, 80}. The hypothesis behind using F127 to synthesize titania films is that since F127 has higher molecular weight than P123, it should produce larger pores than P123. Titania films with different morphologies and phases have been synthesized previously using F127 including cubic^{51, 267-270}, hexagonal^{51, 271-274}, and nanowire microspheres²⁷⁵. The most important factor determining the final mesostructure is the molar ratio of F127 to titania precursor (M). According to Crepaldi et al.⁵¹, titania films with hexagonal phase are obtained for $M = 0.008$ to 0.01 using titanium tetrachloride as titania precursor, ethanol as the solvent and F127 as the structure directing agent. A very well ordered hexagonal phase was found to be obtained for $M = 0.01$ ⁵¹ but because conventional oxide substrates were employed, the hexagonal films were oriented parallel to the solid surface. The new synthetic development reported here

is the synthesis of o-HCP cylindrical nanopores using F127 and TiCl_4 by modifying the glass substrate with cross-linked F127 prior of dip coating. The o-HCP oriented mesophase has been shown to form by a direct disorder-to-order transition for P123-templated TiO_2 films on glass slides modified with crosslinked P123⁴¹, and a similar mechanism is expected with F127. Very well ordered contrasting SEM images will be obtained for films cast onto plain glass and F127-modified glass indicating that glass modification works to provide vertical orientation of the nanopores. After confirming the o-HCP mesostructure, the infiltration of P3HT into the nanopores will be studied using UV-visible spectroscopy and neutron reflectometry, and the interactions between the two materials will be studied using photoluminescence measurements.

3.3. Experimental Section

NoChromix powder (Godax Laboratories, Inc.), sulfuric acid (95-98%, Sigma Aldrich), F127 ($M_n \sim 12,500$ Da, Sigma-Aldrich), 1,6-diisocyanatohexane (98%, Sigma Aldrich), glycerol (99+%, Sigma Aldrich), TiCl_4 (99.9%, Acros Organics), ethanol (200 Proof, Decon Laboratories), acetone (histological grade, Fisher Scientific), chlorobenzene (anhydrous 99.8%, Sigma-Aldrich), and regioregular P3HT (MW $\sim 54,000$ -75,000 Da, Sigma-Aldrich) were all used as received.

Commercially available borosilicate glass slides were cleaned using NoChromix solution in concentrated sulfuric acid and modified based on the method of Koganti et al.⁸⁰ using F127 as the Pluronic surfactant. The solution was prepared by first adding 0.696 mmol/L of F127 and a drop of glycerol as a cross-linker to 100 ml acetone. An equal number of moles of 1,6-diisocyanatohexane was added dropwise to the mixture in a nitrogen-filled glove bag. The freshly prepared solution was then dip coated onto glass slides and the slides were aged at 120 °C overnight (approx. 12 hours) to drive the

isocyanate-hydroxyl cross-linking reaction to completion. Titania films with F127 as the structure directing agent have been synthesized according to the procedure of Crepaldi et al. with a modified thermal treatment⁵¹. The coating solution was prepared by adding 0.01 mole (1.93 g) of TiCl_4 to a solution of 1.26 g F127 ($M = 0.01$) in 30 g anhydrous ethanol in a nitrogen-filled glove bag. To this solution, 0.1 mole (1.8 g) of water was slowly added and the sol was allowed to react for 10 minutes before coating. Films were prepared by dip coating glass substrates with the sol at room temperature. Titania films were aged after coating at a temperature of 4 °C for 2 hours at a relative humidity of approx. 94%. Titania films were then calcined by transferring them directly from the refrigerator to a muffle furnace and increasing the temperature at 25 °C/min to 400 °C and holding for 10 min followed by rapid cooling. Films were not only coated onto plain glass, but also onto modified glass in order to provide orthogonal alignment of cylindrical nanopores.

Vertically oriented mesoporous titania films were then used to study the infiltration mechanism of P3HT into the nanopores. 1 wt% P3HT solution was prepared in chlorobenzene with continuous stirring at 100 °C in a water bath to ensure complete dissolution. The P3HT solution (0.5 ml) was spin coated onto titania films using spin coater (Laurell Technologies Corporation, Model WS-400BZ-6NPP/LITE) at 1500 rpm for 45 seconds. In order to increase the infiltration of P3HT into pores, these films were then annealed at 200 °C in a vacuum oven at a pressure of 20 mm Hg for variable time. Annealing was done under vacuum because P3HT is sensitive to ambient air and can degrade in the presence of air or moisture.

For plan-view imaging of pore structures, scanning electron microscopy (SEM) was performed using a Hitachi S-4300 at 3 kV. SEM samples were prepared by cutting the

glass slide to the desired shape using a glass cutter and then mounting them exactly at the center of SEM stubs coated with carbon tape. The edges of the sample were coated with colloidal graphite (isopropanol base, Ted Pella, Inc.) to increase conductivity by keeping the top surface in electrical contact with the lower surface. The samples were aged at 120 °C overnight (approx. 12 hours) to evaporate all the solvent from the colloidal graphite solution. The GISAXS pattern of a representative titania film was collected at the Advanced Photon Source at Argonne National Labs on beamline 8-ID-E in order to confirm vertical orientation of the pores.

Infiltration of P3HT into the pores of titania was characterized using UV-visible spectroscopy with an Ocean Optics Jaz Spectrometer in transmission mode. Glass slides coated with thin films were positioned exactly vertically so that the spectrophotometer beam passed through glass slide and film in sequence. In order to quantify infiltration depth, neutron reflectometry experiments were performed at the Liquids Reflectometer (beamline 4B) at the Spallation Neutron Source (SNS) at Oak Ridge National Lab (ORNL). The reflectivity $R(Q)$, was measured as a function of perpendicular wave vector transfer, $Q = (4\pi/\lambda)\sin \theta$, where λ is the neutron wavelength and θ the angle between neutron beam and sample surface²⁷⁶. With the neutron spectrum covering wavelengths from 2.5 to 17.5 Å and three incident angles of $\theta = 0.30^\circ$, 0.8° , and 1.8° , neutron reflectivity (NR) data were collected in time-of-flight mode. The films were prepared on 5 mm thick circular silicon wafers with a diameter of 50 mm by the same modification and dip coating procedures described above. All reflectivity measurements were performed at room temperature and atmospheric pressure. Photoluminescence (PL) spectra were measured using a Renishaw inVia Raman microscope (Model: RE02) operating at room temperature. The PL of P3HT

infiltrated into nanoporous TiO₂ was measured at steady state by excitation using 442.1 nm light generated using a blue (HeCd) laser.

3.4. Results and Discussion

Figure 3.1 shows representative SEM images of F127-templated films on plain glass and crosslinked F127-modified glass prepared with $M = 0.01$ and 30 g of ethanol. The thickness of the titania films was estimated using ellipsometry of films cast onto silicon wafers to be 120 nm. For films on plain glass (Fig. 3.1a), most of the time (approx. 8 out of 10 times that a region was sampled), parallel stripes were observed in SEM images, which is consistent with cylindrical pores primarily aligned parallel to the substrate. For films on modified glass, the contrast between titania wall and the empty pore is much better, and as Fig. 3.1b illustrates, very well ordered, accessible pores are observed, suggesting that orthogonal alignment of mesopores has been increased for films cast onto modified glass. However, these pores are not 100% orthogonally oriented and thus we also see parallel stripes in some SEM images for the film on modified glass with $M = 0.01$. However, the frequency of parallel stripes was less than for unmodified glass, having been observed 3 out of 10 times. These SEM images suggest that a 2D HCP microstructure is formed with a pore diameter of about 8-9 nm for orthogonal pores. The unit cell parameter, which here corresponds to the distance between the center of consecutive pores, is 14.5 nm.

Figure 3.2a shows the GISAXS pattern of a TiO₂ film on modified glass after calcination at 400° C and Figure 3.2b the corresponding 1D linecut derived by integrating along the q_z direction from 0.08-0.1 Å⁻¹. The GISAXS pattern clearly shows two intense vertical rods located on both sides of the beam stop, $q_y = \pm 0.042$ Å⁻¹ indexed to the (100) plane of the HCP structure. The d-spacing calculated from the GISAXS pattern is 15 nm.

Also from the linecut (Fig. 3.2b), we can see a diffraction peak of low intensity approximately at $q_y = 0.083 \text{ \AA}^{-1}$, with a d-spacing of 7.55 nm, indexed to the (200) plane of the HCP structure. No distinct out of plane diffraction spots are visible. The presence of the vertical rods and absence of out of the plane diffraction spots clearly indicate that orthogonally oriented HCP pores are indeed present for the titania film prepared on modified glass.

Our initial hypothesis was that F127 should produce pores of larger diameter than those obtained using P123, as it has higher molecular weight than P123. However, when measured, the pore diameter for these mesoporous films was the same as obtained using P123 (8-9 nm)². The difference between F127 and P123 is that F127 (EO₁₀₆PO₇₀EO₁₀₆) has longer hydrophilic PEO (polyethylene oxide) blocks than P123 (EO₂₀PO₇₀EO₂₀). The likely reason that longer PEO blocks of F127 do not expand the pore size is that PPO (polypropylene oxide) blocks dictate the pore size while PEO mixes with titania matrix. The (100) diffraction peak for P123 templated titania films is observed at $q_y = 0.048 \text{ \AA}^{-1}$ ² corresponding to a d-spacing of 13 nm. The d-spacing using F127 (15 nm) is slightly larger, indicating that mixing of PEO blocks with TiO₂ precursor leads to thicker walls when F127 is used as the template. Similar results were reported by Feng et al. who reported a 2.4 nm increase in wall thickness for F127-templated silica films compared to P123-templated films, while the pore size remained the same²⁷⁷. Although F127 did not produce larger diameter pores than films made using P123, the characterization results demonstrate that the synthetic strategy reported by Koganti et al.⁸⁰ can be generalized to generate o-HCP titania films using other Pluronic surfactants. The thicker walls may impart stability to the films for further processing, although this advantage is not within

the scope of the current study.

After titania films with o-HCP nanopores were successfully synthesized using F127, the pores were infiltrated with the hole conducting polymer P3HT in order to begin the process of creating a bulk heterojunction for hybrid solar cells. To do this, the o-HCP films were spin coated using a 1 wt.% P3HT solution in chlorobenzene followed by annealing at 20 mm Hg and 200 °C for variable time periods. To rule out the possibility of P3HT undergoing degradation during annealing because of oxidation of alkyl side chains or the thiophene ring (which disrupts the π -conjugation and reduces the intensity of the absorption band accompanied with a blue shift²⁷⁸), a control experiment was performed with regioregular P3HT cast onto cleaned plain glass followed by annealing under the same conditions as the P3HT on o-HCP titania films. Figure 3.3a shows UV-vis absorption spectra of regioregular P3HT during annealing at 200 °C for times from 15 min to 5 hour. No changes in the absorption spectra of regioregular P3HT are observed with increasing annealing time, indicating that the polymer remains stable at this temperature and pressure. The absorption spectrum of P3HT features a maximum at ~520 nm which is attributed to the electron transition from the valence band (HOMO) to the conduction band (LUMO) of P3HT. The absorption spectrum also features two shoulder peaks at 550 nm and 600 nm, which are attributed to inter-chain absorption coming from locally ordered domains, i.e., interstrand π -conjugation²⁷⁹. The presence of absorption peaks of the same intensity with no blue shift throughout the annealing time demonstrates no change in chain structure or interactions simply due to annealing and cooling back to room temperature.

Figure 3.3b shows UV-vis absorption spectra of P3HT infiltrated into o-HCP titania films at 200 °C. The spectra of infiltrated P3HT are compared with the absorption spectrum

of regioregular P3HT on glass in Fig. 3.3b. According to Brown et al.²⁷⁹, when P3HT is infiltrated into the nanopores of titania, a blue shift relative to regioregular P3HT is observed, due to reduced π - π stacking of polymers confined within the pore. This blue shift with respect to regioregular P3HT is consistent with infiltration of P3HT into the pores of titania and is taken as preliminary evidence that infiltration is occurring. The as-spun P3HT on a mesoporous titania film displays little or no blue shift with respect to regioregular P3HT, as expected prior to incorporation. As the annealing time increases, the P3HT absorbance band displays a monotonic blue shift consistent with gradual infiltration into the titania pores. The magnitude of this blue shift increases with annealing time up to a plateau of about 7-8 nm after 60 min of annealing, consistent with previous reports of P3HT infiltration^{72, 280}.

A plot of blue shift of the maximum absorbance as a function of annealing time (Figure 3.4a) indicates a rapid increase during the first 30 min, followed by a plateau from 60 min on. Along with the blue shift, the intensity of the shoulder peak at 600 nm due to interstrand π -conjugation decreases during infiltration. The most likely reason for change is that the infiltration reduces the degree of inter-chain order in the microcrystalline domains of P3HT, as P3HT is confined into the nanopores of titania. According to Kim et al.²⁸⁰, this reduction in intensity of the shoulder peak at 600 nm is consistent with the infiltration of the polymer. However, the shoulder peak does not vanish completely, which suggests that all the P3HT might not have been infiltrated into the porous titania film. P3HT which has not been infiltrated might have formed an overlayer at the top surface that gives rise to the shoulder peak after infiltration.

The rate of P3HT infiltration was also studied by measuring optical density of the infiltrated polymer after removing unincorporated polymer from the top of the film by ultrasonically treating the films in toluene for 20 minutes (Figure 3.4b). The optical density increases with time from a small background value with no annealing, up to a plateau of ~0.2 from 60 min of annealing onwards. However, it is unreliable to estimate infiltration depending upon the optical density of the embedded polymer since it is possible that the P3HT overlayer might not have been rinsed off completely. Thus, we need a different technique to directly determine the infiltration depth of the polymer.

In order to quantify the infiltration depth, neutron reflectometry was performed. Reflectivity (R) data were obtained as a function of the wave vector transfer, Q for films with varying times of annealing and the data were analyzed using Motofit²⁸¹ software as implemented in Igor Pro. After analyzing the data, the model was fitted to the R vs. Q resulting in a multilayer neutron scattering length density (NSLD) profile as a function of normalized film depth. A material's SLD relates its chemical composition and density according to the relationship as follows:

$$\text{NSLD} = \frac{N_a \rho_m}{M} \sum_{i=1}^n b_i \quad (3.1)$$

where M is molecular weight of the compound, N_a is Avogadro's number, ρ_m mass density and b_i the bound coherent scattering length of i^{th} atom comprising the material²⁷⁶. These are calculated using the SLD calculator in Motofit. The theoretically calculated NSLD for nonporous titania is $2.34 \times 10^{-6} \text{ \AA}^{-2}$ based on the mass density of 3.78 g/cm^3 for anatase titania. From the top view SEM image, the porosity calculated for titania films with vertically oriented cylindrical nanopores is 45-47% (based on pore diameter of 8-9 nm and unit cell parameter of 14.5 nm), which would give a NSLD of $1.24 \times 10^{-6} \text{ \AA}^{-2}$. The

theoretically calculated NSLD for P3HT is $0.68 \times 10^{-6} \text{ \AA}^{-2}$ based on the mass density of 1.1 g/cm^3 for bulk P3HT. Previously, Rawolle et al. studied the infiltration of polymer hole-conductor into mesoporous titania and reported the NSLD of $0.705 \times 10^{-6} \text{ \AA}^{-2}$ for a compact P3HT layer and NSLD of $1.67 \times 10^{-6} \text{ \AA}^{-2}$ for P3HT infiltrated into the nanopores of titania with 41% porosity²⁸². Considering the porosity of the mesoporous films and NSLD of each material, the NSLD of P3HT infiltrated into the nanopores of titania is expected to be a volume-weight average value of $1.6\text{-}1.7 \times 10^{-6} \text{ \AA}^{-2}$.

Figure 3.5 shows the neutron reflectivity profile of P3HT infiltrated into the nanopores of titania after annealing at 200° C for 30 minutes, with a NSLD profile in the inset. The model matches very well with the experimental data. The NSLD profile that fits the data has four distinct layers: a bottom silica substrate, a nanoporous titania layer near the substrate, an interfacial P3HT layer infiltrated into the nanopores, and a top uniform P3HT layer. Attempting to fit the data with only three layers led to a significantly worse fit. The NSLD values of different layers obtained after fitting match very well with the theoretically calculated NSLD values. The best-fit parameters including the thickness, NSLD and surface roughness of each layer are summarized in Table 3.1 for 30 min of annealing. The profile clearly indicates the infiltration of P3HT about 14 nm into the nanopores of titania. Thus, the blue shift obtained in UV-Vis spectroscopy studies was indeed because of the infiltration of the polymer and neutron reflectivity confirms the infiltration.

Figure 3.6 shows the neutron reflectivity profile of P3HT infiltrated into the nanopores of titania after annealing at 200° C for 60 min. The fitting results are similar to those for Figure 3.6, and there is not much change in the infiltration depth of the polymer

after increasing annealing time. Even after 2 hours of annealing, an infiltration depth of 14 nm is still observed (data not shown but similar to Fig. 3.6). Thus, the plateau in blue shift and shoulder intensity decrease in Fig. 3.4 were, as expected, a result of having reached a maximum level of infiltration of the polymer into the pores. The infiltration depth is lower than that obtained in previous studies^{72, 99}, which reported a maximum infiltration depth of 40 nm or more for cubic mesoporous titania. However, a monotonic decrease in the external quantum efficiency was reported in those studies as the infiltration depth increased, which indicates that charge generation mostly occurs near the top of the TiO₂ film^{99, 266}. Thus, the holes generated below 10-20 nm below the top of TiO₂ film might undergo recombination with the electron from TiO₂ before escaping the P3HT-TiO₂ region since polymer chains located in the bottom of TiO₂ might act as the filter layer which prevents light from reaching the top of the interface²⁸³. Therefore, an infiltration depth of 14 nm may be sufficient for efficient solar cell performance. The reason for higher infiltration of P3HT within the first 30 minutes might be that the solvent chlorobenzene that we used to make the P3HT solution evaporated with increasing annealing time. The rate of evaporation of chlorobenzene is likely to be higher than the rate of infiltration of the polymer. After the one hour of annealing time, all the chlorobenzene should have evaporated. After this time, the infiltrated, solidified P3HT blocked the pores as a result of which, there is no further infiltration of P3HT with increasing annealing time. Another related reason for the reduced infiltration of P3HT into cylindrical channels is entropic; in order to enter into the pores, the chains are forced to adopt an elongated configuration less entropically favorable than the coiled configuration found in solution and in free melts. Polymers confined within anodized alumina membrane pores have been shown to form a

layer of reduced mobility near the pore wall, and alteration in crystallinity has been observed under extreme confinement²⁸⁴. These effects would be expected to inhibit the transport of neat P3HT into the pores.

The efficiency of electron transfer at the interface between P3HT and nanoporous TiO₂ can be investigated indirectly by means of photoluminescence (PL) quenching (Figure 3.7)^{244, 285}. The PL spectrum of regioregular P3HT shows a characteristic emission pattern with two peaks in the 550-740 nm wavelength range²⁸⁶. While the spectra exhibit significant noise because the films are so thin, the intensity of the PL spectrum decreases considerably as the P3HT-TiO₂ interface develops. The decrease in intensity is thought to be a result of quenching due to energy or charge transfer. As observed for the other measurements above, the PL intensity decreases most rapidly during the first 30 min of annealing, followed by a plateau in quenching (Fig. 3.7b). This is also consistent with the UV-Vis spectroscopy data indicating that infiltration occurs over the first 30 minutes of annealing and plateaus thereafter. Thus, infiltration correlates with the charge transfer at the interface, which suggests that an active p/n heterojunction is present in these systems which can be developed in future studies to understand photovoltaic performance and the effect of polymer confinement on organic-inorganic hybrid solar cells. Even though the infiltration depth is smaller than the previous reports^{72, 99, 266}, the infiltration depth is consistent with the active layer reported previously and the nanowire architecture of the incorporated polymer is expected to provide higher hole mobility of P3HT chains in the nanopores, which would improve the performance of P3HT-TiO₂ hybrid solar cells.

3.5. Conclusions

We have synthesized titania thin films with vertically oriented 2D-HCP cylindrical nanopores using Pluronic triblock copolymer surfactant F127. The pore size of F127

templated titania films is the same as that of P123-templated titania films because both surfactants have the same content of hydrophobic block (PPO) and but F127 provides a higher wall thickness because of its larger hydrophilic block (PEO). Regioregular P3HT has been incorporated into the vertically oriented cylindrical nanopores of the resulting films. An infiltration depth of ~14 nm is obtained after 30 minutes of annealing at 200 °C under vacuum and for higher annealing times, there is no further improvement in the infiltration depth. This infiltration is measured directly by neutron reflectivity, and causes a corresponding blue shift in the absorbance of the P3HT. The infiltration depth is lower than that reported in previous studies, most likely because of the higher cost of confinement of P3HT chains into straight cylindrical nanopores. The charge transfer across the P3HT-TiO₂ interface is significant and correlates with the degree of infiltration of P3HT. In the future, these results can be used to fabricate efficient solar cells by using the knowledge gained about the optimal conditions for incorporation of P3HT into the pores of orthogonal HCP titania films and comparing the performance with cubic nanopore arrangement of titania and planar titania.

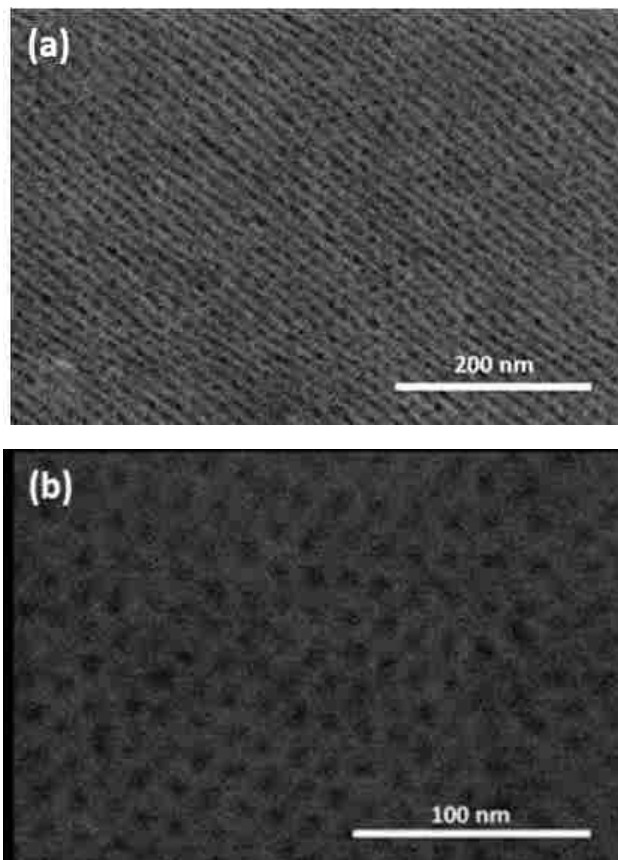


Figure 3.1. Representative plan view SEM images of mesoporous titania films prepared on (a) plain glass and (b) F127-modified glass prepared from sols containing 1.26 g F127 and 30 g of ethanol, aged at 4 °C and calcined at 400 °C at the rate of 25 °C/min.

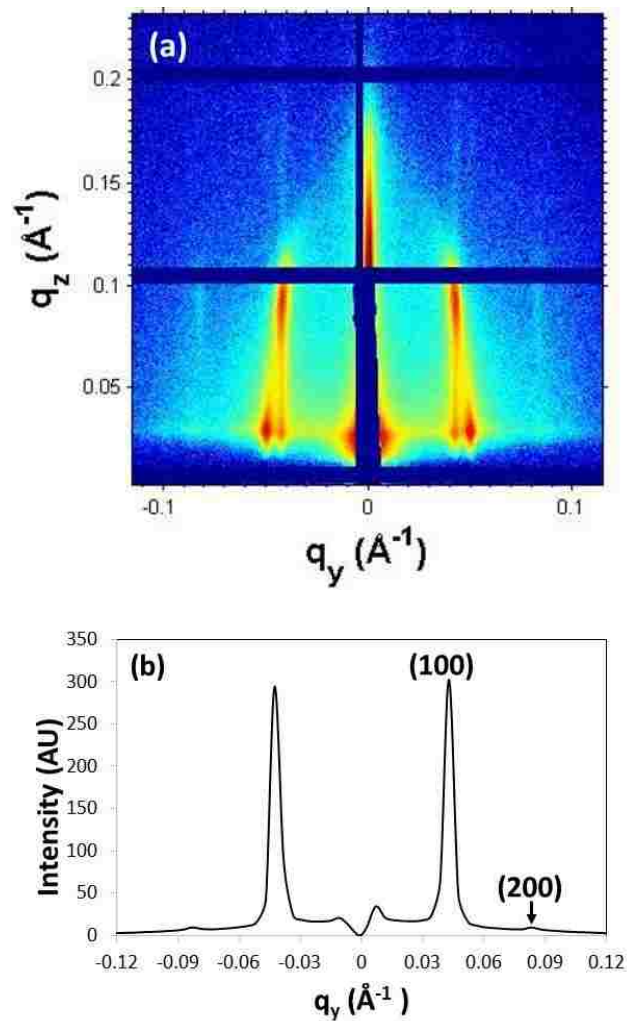


Figure 3.2. (a) GISAXS pattern of nanoporous titania film prepared on modified glass after calcination at 400° C at a rate of 25 °C/min and (b) the corresponding 1D linecut derived by integrating along the q_z direction from 0.08-0.1 \AA^{-1} .

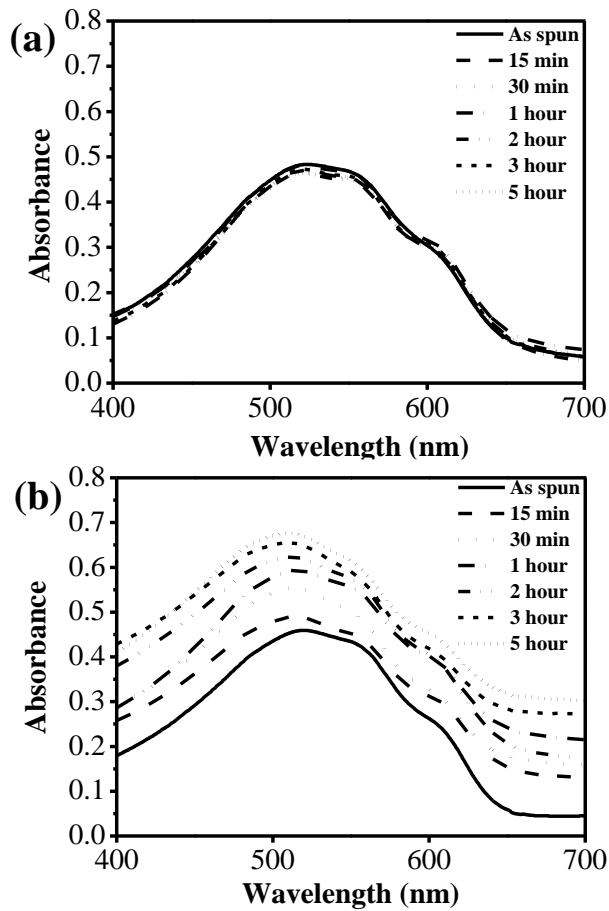


Figure 3.3. UV-vis absorption spectra of (a) regioregular P3HT and (b) regioregular P3HT infiltrated into titania films with thickness of 120 nm after annealing under vacuum for the indicated times at 200° C (The data has been shifted in part (b) for absorbance values).

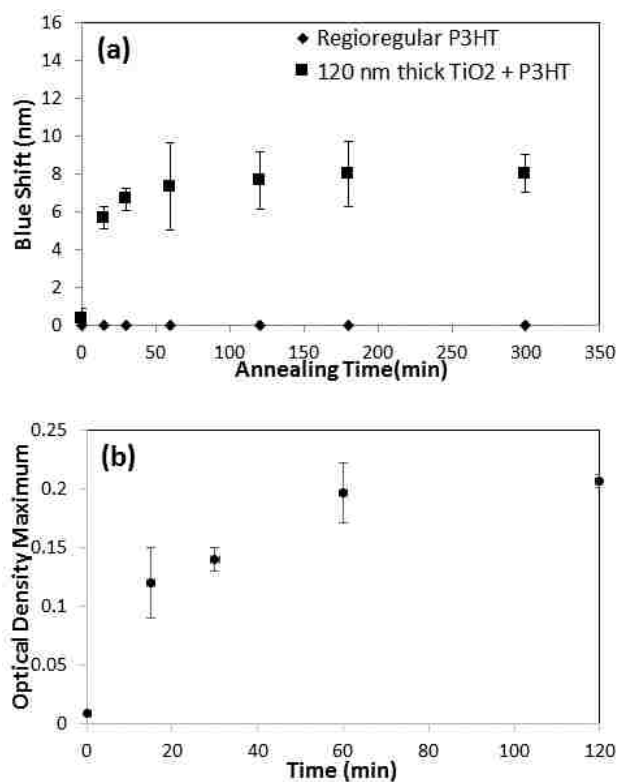


Figure 3.4. (a) Blue shift of P3HT UV-vis absorbance maximum as a function of annealing time and (b) optical density of embedded P3HT after infiltration for varying periods of time at 200 °C under vacuum.

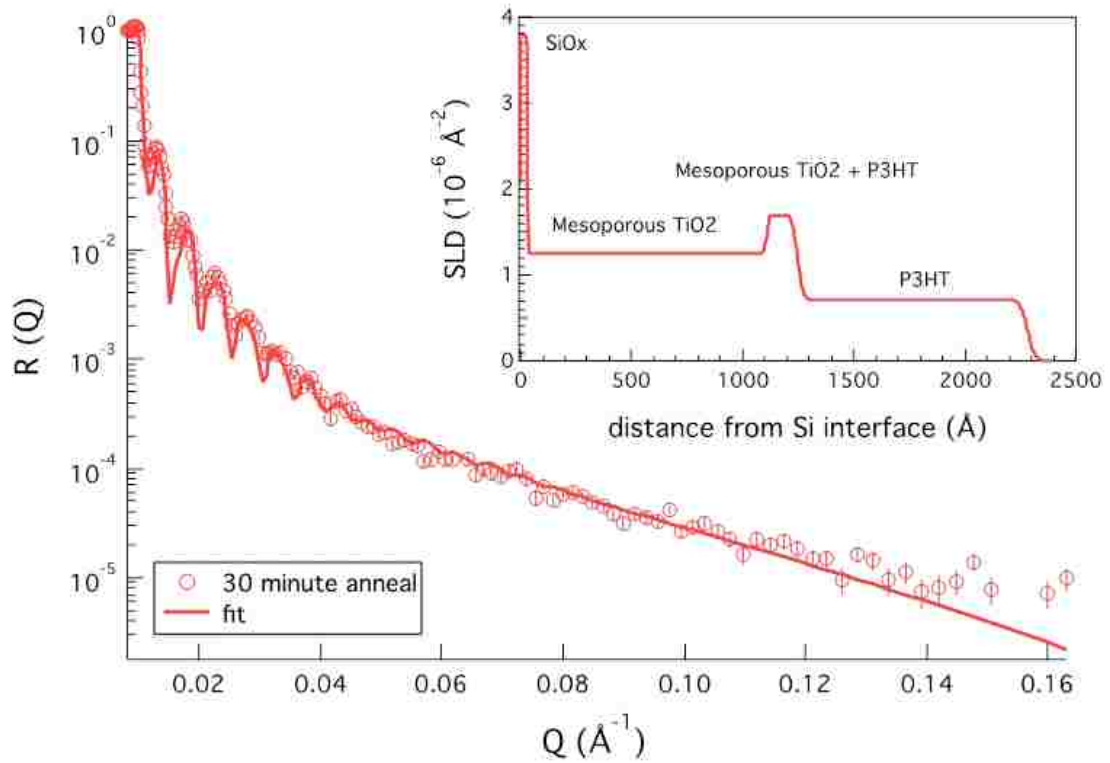


Figure 3.5. Neutron reflectivity profile of P3HT infiltrated into the nanopores of titania after annealing at 200° C for 30 minutes. The inset shows that scattering length density (SLD) profile of the fitted model.

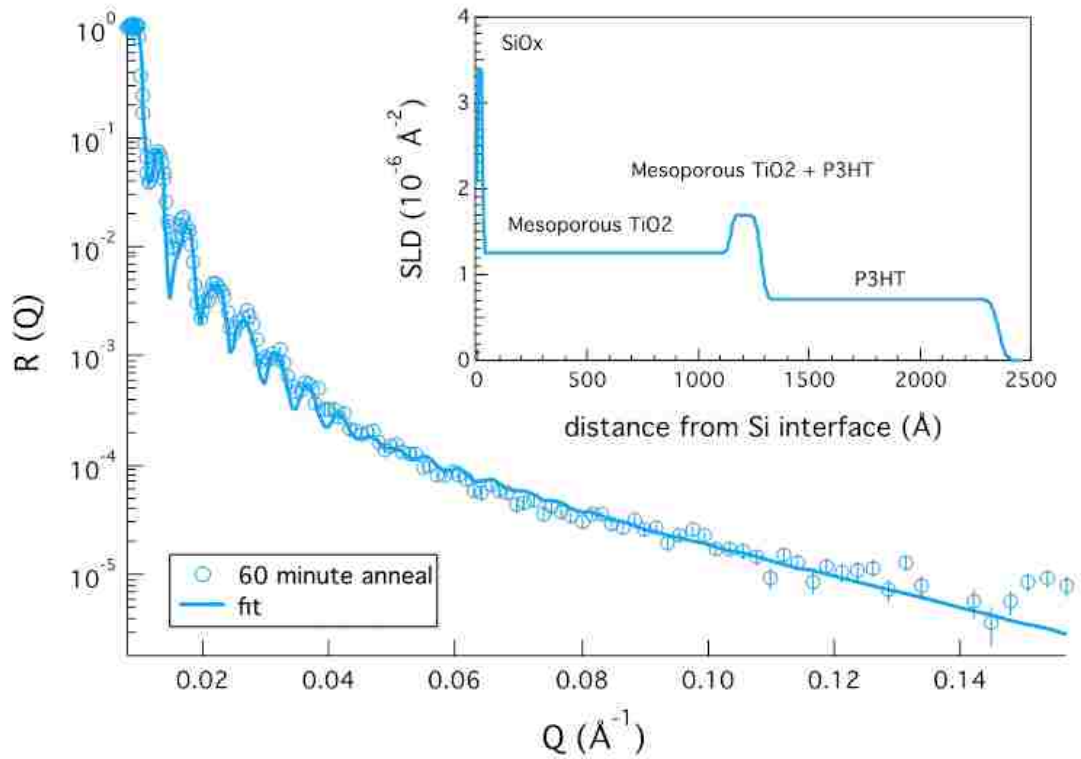


Figure 3.6. Neutron reflectivity profile of P3HT infiltrated into the nanopores of titania after annealing at 200° C for 60 minutes. The inset shows that scattering length density (SLD) profile of the fitted model.

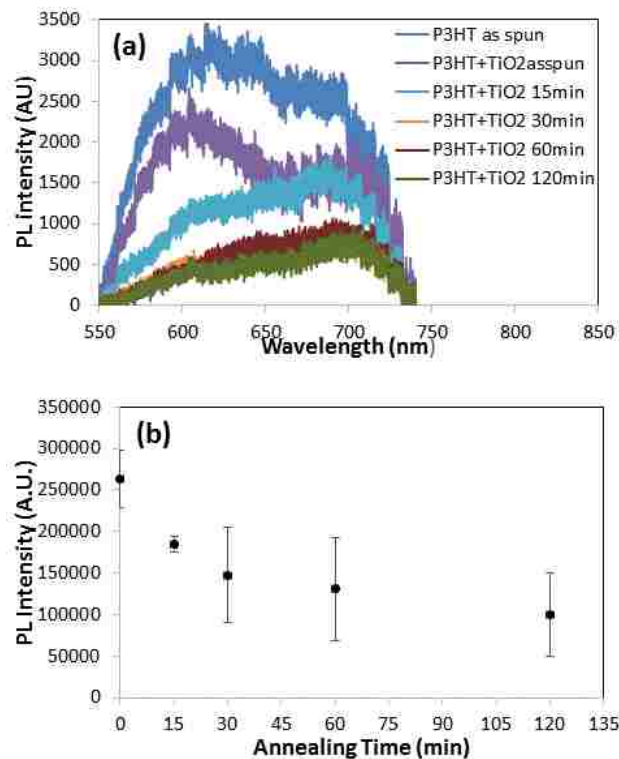


Figure 3.7. (a).PL spectra for P3HT infiltrated into nanoporous TiO₂ by spin coating 1 wt% P3HT solution followed by annealing at 200 °C for the indicated time and comparison with as spun P3HT, and (b) integrated PL intensity for P3HT infiltrated into nanoporous TiO₂ as a function of annealing time. The error bars represent the standard deviation of the PL intensity of three different samples.

Table 3.1. Characteristics of layers obtained by fitting a multilayer model to the neutron reflectivity profile of P3HT infiltrated into the nanopores of titania after annealing at 200° C for 30 minutes.

Layer	Thickness (Å)	SLD (*10 ⁻⁶ Å ⁻²)	Roughness (Å)
P3HT	1035	0.72	27
Interface	139	1.7	19
Mesoporous TiO ₂	1078	1.25	11
██████████	30	3.78	2

Table 3.2. Characteristics of layers obtained by fitting a multilayer model to the neutron reflectivity profile of P3HT infiltrated into the nanopores of titania after annealing at 200° C for 60 minutes.

Layer	Thickness (Å)	SLD (*10 ⁻⁶ Å ⁻²)	Roughness (Å)
P3HT	1072	0.7	26
Interface	137	1.7	19
Mesoporous TiO ₂	1118	1.25	14
██████████	27	3.4	3

Copyright © Suraj R. Nagpure 2016

Chapter 4. Nanoporous n-TiO₂/p-CdTe Heterojunction Solar Cells with Enhanced Response in the Near-UV Region of the Solar Spectrum

4.1. Summary

Solar cells utilizing TiO₂ with highly ordered cylindrical, 8 nm diameter nanopores for the window layer and p-CdTe for the absorber layer were fabricated, characterized and analyzed. Power conversion efficiency values as high as 5.53% were achieved, with an open circuit voltage of 700 mV, short circuit current of 19.2 mA/cm² and a fill factor value of 0.41. The solar cell performance is approximately 3 times higher for cells using nanoporous titania film as compared to the cells using planar titania film; this is attributed to the large surface area of nanoporous titania. CdTe deposited inside the nanopores of TiO₂ exhibits improved interface (reduced interface state density and higher open-circuit voltage) characteristics than the interface obtained when CdTe is deposited on a planar TiO₂ film. This is confirmed by the C-V measurements, which yield low doping concentration and higher depletion width in CdTe near the interface in case of nanoporous titania. These cells have a strong response to sunlight photons in the wavelength range of 380-850 nm, which represents an expansion in the photoactive window compared to the traditional CdS / CdTe photovoltaic cells. To our knowledge, a PCE value of 5.53% is the highest reported using this combination of semiconductors.

4.2 Introduction

Solar cells based on heterojunctions generally consist of a wide-band semiconductor “window” and a solar radiation “absorber”. One well known example is the highly studied and commercialized inorganic solar cell based on the CdS/CdTe structure^{130, 287-289}, where CdTe is the absorber and CdS acts as the window layer. CdTe is a nearly perfect material for PV application due to its direct band gap of 1.5 eV, which is closely matched to the terrestrial solar spectrum. However, when trying to maximize device performance, improvements have been hindered by the loss of photocurrent caused by light absorption in the n-type cadmium sulfide (CdS) window layer. A significant amount of radiation in the solar spectrum, with wavelength less than 512 nm, gets absorbed by CdS and does not contribute to the collected photocurrent. The resulting loss in photocurrent is estimated to be 7 mA/cm²¹²⁷. Also, forming a thinner layer of CdS to reduce its absorption has significant challenges of its own, such as formation of pinholes in the CdS which can cause the p-type semiconductor to come into direct contact with the transparent electrode forming micro-junctions and micro-shunts and degrading cell performance¹²⁸.

The above problem of CdS absorption can be effectively solved by replacing CdS with titanium dioxide (TiO₂) as a window layer. Since TiO₂ has higher energy band gap than CdS (3.2 eV), it is expected to improve the spectral response in lower wavelength region, especially in the 400-500 nm range, thereby improving quantum efficiency¹²⁹⁻¹³¹. Both TiO₂ and CdTe, due to their electrical, optical and operational properties, are well suited to be the “window” and “absorber” materials, respectively²⁹⁰⁻²⁹². The feasibility of TiO₂/CdTe heterojunctions for photoelectrical conversion has been shown in a number of works^{129, 293-297}. The CdTe conduction band lies approximately 0.7 eV above the TiO₂ conduction band²⁹⁸; as a result, electron transfer from CdTe to TiO₂ is energetically

avored, while hole transfer across this interface is prevented by an efficient barrier of more than 2 eV²⁹⁷. Photosensitive heterojunctions of n-TiO₂/p-CdTe were fabricated by Brus et al.¹²⁹ by dc reactive magnetron deposition of TiO₂ planar thin films which exhibited an open circuit potential of $V_{oc} = 0.69$ V, a short-circuit current of $J_{sc} = 6$ mA/cm² and a fill factor (FF) of 0.42. Ernst et al.²⁹⁷ prepared a CdTe-TiO₂ solar cell using a highly structured porous TiO₂ on a micrometer scale and found that the porous device outperforms the planar device. The reason for this was hypothesized to be that in the microporous configuration, the light has the possibility to travel not only perpendicularly, but also laterally with respect to the TiO₂/CdTe interface, so that even the longer wavelengths are absorbed near to the junction, resulting in higher collection efficiency²⁹⁹. In contrast, long wavelength light is expected to be absorbed far from the junction in planar TiO₂, resulting in low collection efficiency. The interface between planar anatase TiO₂ and CdTe is also characterized by a strong dipole of about 0.9 eV (in contradiction to the electron affinity rule) which suggests that planar titania-CdTe interface might not be ideal for high conversion yields²⁹⁸. Consistent with this, Ernst et al.²⁹⁷ observed a higher photocurrent of about 8.9 mA/cm² using porous TiO₂ substrate, which further improved to 15 mA/cm² after alloying CdTe with Hg. However, the fill factor was very poor (~20%) which was attributed to large band offset between CdTe and TiO₂. Yang et al.²⁹⁵ obtained an open circuit voltage of 1.03 V for TiO₂/CdTe solar cell using titania nanotubes and CdTe quantum dots, however the efficiency was limited because of poor fill factor and low current density. Yue et al.³⁰⁰ studied quantum dot sensitized solar cells employing Pt/C₆₀ as the counter electrode and obtained an efficiency of 2.06 % for Pt/C₆₀-TiO₂-CdTe-ZnS configuration.

TiO₂-CdTe solar cell systems have been studied extensively, mostly in the form of quantum dot sensitized solar cells (QDSSCs)³⁰⁰⁻³⁰². Even though QDSSCs have a wide range of advantages, such as tunability of effective band gap³⁰³, high absorption coefficient³⁰⁴ and the potential for multiexciton generation³⁰⁵⁻³⁰⁶, the efficiencies of most reported QDSSCs are less than 2.0%, mainly because of electron loss occurring through charge recombination at TiO₂-electrolyte and QD-electrolyte interfaces, a narrow range of absorption wavelengths in the solar spectrum, and non-radiative decay³⁰⁷⁻³¹¹. These limitations can be overcome by using CdTe in the form of thin film rather than QDs. CdTe thin films have an absorption coefficient as high as 10⁵ cm⁻¹, and 99% of photons with energy greater than the band gap can be absorbed within several micrometers of a CdTe film³¹². Another advantage of CdTe as a thin film is the flexibility in manufacturing technologies to fabricate high quality polycrystalline thin films^{131, 313-314}. The closed space sublimation (CSS) has been used to deposit CdTe thin films because of its high throughput and efficient material utilization³¹³.

The nanostructure employed here consists of continuous titania films with vertically aligned 2D hexagonal close packed (HCP) cylindrical nanopores with pore diameter of 8-9 nm. The pores of these films can be filled with p-type semiconductors to provide two well-defined phases for conduction of charge carriers to each electrode²⁶⁶. These nanoporous titania films are less ordered in terms of crystallinity and might have unknown impact on interfacial properties and dipole moment could be less as compared to planar anatase titania as observed by Tiefenbacher et al.²⁹⁸. In this study, we investigated the effect of nanoporous titania with vertically oriented 2D-HCP cylindrical nanopores on the photovoltaic performance of TiO₂/CdTe solar cell.

4.3 Experimental Section

To fabricate solar cells and to study the photovoltaic performance, fluorine-doped tin oxide (FTO) coated glass slides were used as substrates which also served as the bottom electrode. Before coating, all of the substrates were cleaned with deionized water, acetone and isopropanol. These FTO substrates were then treated in a UV-ozone cleaner for 20 minutes to remove any organic contaminants. The substrates were then modified based on the method of Koganti et al with F127 as the Pluronic surfactant (Sigma-Aldrich)⁸⁰. The solution for surface modification was prepared by first adding 0.696 mmol/L of F127 and a drop of glycerol as a cross-linker (99+%, Sigma-aldrich) to 100 ml acetone (histological grade, Fisher Scientific). An equal number of moles of 1,6-diisocyanatohexane (99+%, Acros Organics) was added dropwise to the mixture in a nitrogen-filled glove bag. The freshly prepared solution was then dip coated onto glass slides and the slides were aged at 120 °C overnight (approx. 12 hours) to drive the isocyanate-hydroxyl cross-linking reaction to completion.

Before preparing mesostructured films, planar titania films were prepared on FTO substrate to prevent short-circuit during solar cell characterization by adding 1.8 g of water to the solution of 0.01 mole (1.93 g) of TiCl_4 in 18 g anhydrous ethanol. After dip coating glass substrates with the sol at room temperature, films were then calcined by transferring them directly from the refrigerator to a muffle furnace and increasing the temperature at 25 °C/min to 400 °C and holding for 10 min followed by rapid cooling. The thickness of planar titania measured using profilometry is 60 nm. Nanoporous titania films with vertically oriented 2D HCP nanopores were synthesized according to the procedure of Crepaldi et al. with a modified thermal treatment using F127 as the structure directing agent⁵¹. The sol-gel required for nanoporous titania was prepared by adding 0.01 mole (1.93 g) of TiCl_4

(99.9%, Acros Organics) to a solution of 1.26 g F127 ($M = 0.01$) in 30 g anhydrous ethanol (200 proof, Dacron Laboratories, Inc.) in a nitrogen-filled glove bag. To this solution, 0.1 mole (1.8 g) of water was slowly added. Films were prepared by dip coating glass substrates with the sol at room temperature. Titania films were then aged at a temperature of 4 °C for 2 hours at a relative humidity of approx. 94%. Titania films were then calcined by transferring them directly from the refrigerator to a muffle furnace and increasing the temperature at 25 °C/min to 400 °C and holding for 10 min followed by rapid cooling.

In order to fabricate solar cells, p-type CdTe was deposited using a closed-space sublimation system based on procedures in the literature^{288, 315}. First, the source and substrate were ramped together to 550 °C. Then the source temperature was increased to 630 °C and substrate temperature to 575 °C and held there for 2 min at 16-18 torr of He (with 5% O₂, as background gas) pressure. For these conditions, the thickness of CdTe deposited is around 15 μm (see below). After CdTe deposition, the cells were treated with 1.5 wt % CdCl₂ solution in methanol for 15 min and were annealed at 385 °C for 30 min under 100 sccm flowing Argon. This annealing of CdTe in the presence of cadmium chloride was essential for achieving good performance in terms of open circuit voltage and fill factor of the photovoltaic device. Several mechanisms for these improvements have been proposed. These include the elimination of fast-recombination centers in the CdTe³¹⁶, reduction of recombination centers in the junction³¹⁵ and the elimination of small grains³¹⁷. Because of the high electron affinity of CdTe, a metal with a work function > 5.7 eV is needed to form an Ohmic contact on p-type CdTe. Since such metals are not available, the general strategy to overcome the naturally existing Schottky barrier is to create a heavily p-type doped CdTe surface by chemical etching and apply a buffer layer of high carrier

concentration between CdTe and the metal³¹⁸⁻³¹⁹. To do this, cells were etched in a mixture of nitric acid and phosphoric acid (1% HNO₃, 88% H₃PO₄, 35% DI water) for 35 s to form a thin tellurium rich (Te) layer³²⁰. Then a thin layer of copper, 5 nm in thickness, was sputtered using RF sputtering onto the surface of CdTe at the back contact area sites. Cu-based back contacts have become popular because Cu forms reasonably good Ohmic contacts with p-CdTe³²¹. This allows a beneficial band alignment which decreases the barrier width at the back contact interface. The tunneling barrier formed in this way is quasi-ohmic which should not exhibit a roll-over in the IV-characteristics at high forward bias³²². This was followed by the application of graphite paste–silver paste electrodes. Figure 4.1a shows the schematics of the fabricated solar cells of both types along with charge transfer mechanism in Figure 4.1b.

For plan-view imaging of pore structure, scanning electron microscopy (SEM) was performed using a Hitachi S-4300 at 3 kV. SEM samples were prepared by cutting the glass slide to the desired shape using a glass cutter and then keeping exactly at the center of SEM stub coated with carbon tape. The edges of the sample were coated with colloidal graphite (Isopropanol base, Ted Pella, Inc.) to increase conductivity by keeping the top surface in contact with the lower surface. The samples were aged at 120° C overnight (approx. 12 hours) to evaporate all the solvent from the colloidal graphite solution. The GISAXS pattern of the titania film was collected at the Advanced Photon Source at Argonne National Labs on beamline 8-ID-E in order to confirm vertical orientation of the pores. To directly examine the pore morphology, films were scraped from selected glass slides and dispersed into ethanol by using an ultrasonic cleaner (Cole-Parmer 8848). A drop of this solution was then placed onto a copper TEM grid and dried before analysis.

Transmission electron microscopy was performed at 200 kV with a JEOL 2010F high-resolution transmission electron microscope with field emission. I–V characteristics were measured using a solar simulator in the dark and under illumination intensity of 100 mW/cm². The solar simulator was calibrated with a standard light meter and with a standard crystalline silicon solar cell. C–V characteristics were measured with an Agilent 4284A capacitance meter (Agilent Technologies; 20 Hz to 1 MHz) at a frequency of 1 MHz.

4.4 Results and Discussion

Figure 4.2a shows SEM image of a titania film cast onto a glass slide modified with crosslinked P123, after calcination at 400 °C using a ramp of 25 °C/min. The thickness of the film as measured using ellipsometry is 120 ± 5 nm. The SEM image clearly shows a well ordered, accessible porous structure consistent with either orthogonal alignment of HCP mesopores or a globular (e.g. cubic) mesostructure. Direct analysis of the SEM image indicates that the diameter of the pores at the top of the film is 8-9 nm, and the distance between the centers of the closest neighbors is ~ 13-14 nm. To differentiate between possible pore structures, the GISAXS pattern of the TiO₂ film cast onto modified glass after calcination at 400 °C was measured (Fig. 4.2b). The pattern clearly shows two intense vertical Bragg rods located on both sides of the beam stop, at $q_y = 0.042 \text{ \AA}^{-1}$. These Bragg rods are observed because of an orthogonally tilted HCP phase, and the absence of out-of-plane diffraction spots rules out the possibility that the structure is Im3m cubic or another globular mesostructured⁸¹. The Bragg rods were indexed to the (100) plane of the HCP structure. The d-spacing calculated from the GISAXS pattern using the formula $d = 2\pi/q$ is 15 nm giving pore to pore distance of 17.3 nm. GISAXS pattern also features a diffraction peak of low intensity approximately at $q_y = 0.083 \text{ \AA}^{-1}$, with the d-spacing of 7.55

nm. Since (200) plane has almost the half of the d-spacing as that of (100) diffraction peak, this peak can be assigned as (200) plane of the HCP structure. The SAED pattern of titania films (Fig. 4.2c) shows two concentric rings with d-spacings of 0.19 nm and 0.146 nm which are indexed to the (200) and (204) crystallographic planes of the anatase structure⁸¹. The anatase phase is also confirmed by HRTEM image (Fig. 4.2d), which shows lattice fringes with a d-spacing of 0.19 nm corresponding to the (200) crystallographic plane of anatase TiO₂. However, it should be noted that these films are X-ray amorphous since it did not show any higher order diffraction peaks for titania. The films are thus a combination of amorphous titania and anatase polycrystalline titania. The porosity of the films as measured using software ImageJ comes out to be 43 ± 3 %.

When we see cross-sectional SEM image of these nanoporous titania films (Fig. 4.3a), we can clearly see vertically oriented cylindrical channels indicating that pores are indeed oriented vertically after surface modification. In order to determine whether CdTe has been incorporated into the nanopores, cross-sectional SEM imaging was performed after CdTe deposition. Figure 4.3b,c shows cross-sectional SEM images for CdTe deposited into the nanopores of titania using CSS system at the mentioned above. From the low-magnification image (Fig. 4.3b), we can clearly see the bulk CdTe layer of thickness 14.6 μm onto nanoporous titania layer. Also we can see that the texture of this bulk CdTe is different from the CdTe deposited near the interface. At higher magnification (Fig. 4.3c), we clearly see a 430 nm thick uniform film with a different texture near the substrate interface. We could not see any cylindrical channels of titania near the interface as in Fig. 4.3a. Considering 120 nm thickness of porous titania film, it might indicate that the pores are completely infiltrated with CdTe. After the infiltration into the nanopores, CdTe just

formed an overlayer at the top surface. These images also indicate that quality of CdTe grown near the interface and into the nanopores of titania might be different from the bulk CdTe.

In order to confirm that o-HCP Structure of nanoporous titania is stable after CdTe deposition into the nanopores, we have resublimated CdTe from CdTe-titania samples keeping the samples as source with the source temperature as 620 °C. Figure 4.4 shows GISAXS Pattern of titania thin films with o-HCO microstructure after CdTe Sublimated from CdTe-titania samples. The pattern clearly shows two vertical Bragg rods located on both sides of the beam stop, at $q_y = 0.042 \text{ \AA}^{-1}$. These Bragg rods are observed because of an orthogonally tilted HCP phase confirming o-HCP structure is stable after CdTe deposition into the nanopores. However the intensity of these rods reduced a little which might be because of residual CdTe into the pores or slight loss of mesoporous order because of high temperature.

Figure 4.5a shows current-voltage (J-V) characteristic of CdTe-nanoporous titania solar cell indicating a short-circuit photocurrent density (J_{SC}), open-circuit voltage (V_{OC}), and fill factor (FF) of 19.2 mA/cm², 700 mV, and 0.41, respectively, leading to a power conversion efficiency (PCE) of 5.53%. In order to observe the effects of the nanoporous structure of titania, the performance of the solar cell was compared with one without surfactant templates, i.e. CdTe-planar titania (Figure 4.5b), which shows J_{SC} , V_{OC} , and FF of 8.47 mA/cm², 576 mV, and 0.37, respectively, leading to a PCE of 1.8%. Thus, power conversion efficiency for nanoporous titania is 3 times higher than that for planar titania. This is the highest ever reported efficiency for CdTe- TiO₂ solar cell. The previous reported efficiencies are in the range between 0.07-1.87 %^{129, 293, 296, 300-302, 323-324}. Similar effects of

nanostructure on photovoltaic efficiency have been obtained by Yella et al.³²⁵, who reported 13.7% PCE for nanocrystalline TiO₂/CH₃NH₃PbI₃ based solar cells as compared to 3.7% PCE for planar TiO₂/CH₃NH₃PbI₃.

One reason for better performance with nanotubes is the formation of an intimate junction of large interfacial area between the nanoporous TiO₂ and CdTe layer, resulting in better extraction of photo-generated electrons than in the planar TiO₂ film. Based on the average thickness of 120 ± 5 nm and average porosity of 43 ± 3 % and considering that CdTe infiltrates into the nanopores of titania completely, the heterojunction area of nanoporous titania solar cell calculated comes out to be 22 ± 2 times the planar heterojunction solar cell. In general, a large junction area is indispensable for a high-performance photoelectrode³²⁶⁻³²⁷ because more optically generated electron-hole pairs would separate in the space charge region present at the interface. The biggest improvement after using mesostructured device is in the photocurrent which is attributed to the improved carrier collection of the device²⁹⁶. The photocurrent increased to 2.3 times after using porous structure which supports the hypothesis of improved charge collection for solar cell fabricated using nanoporous titania. Another reason is the reduced recombination at the interface. Recombinations might take place at the defect sites at the interface between TiO₂ and CdTe. The large concentration of the surface states at the interface induces higher concentration of such defect sites in the case of planar titania¹²⁹ and leads to relatively high series resistance. In addition, in case of planar titania, recombination may be enhanced by the non-ideal band offset at the p-n interface junction, giving rise to an alteration of the charge carrier transport²⁹⁸. Consistent with this, the quantum efficiency of the solar cells based on the porous structure of titania had been found

higher than planar titania²⁹⁷. As we can see from SEM images (Fig. 4.3), there is incorporation of CdTe into the nanopores of titania. Previous studied also showed that the quantum confinement effect of the uniform morphology leads to nanostructures with different optical properties than conventional bulk materials and leads to blue shift of the absorption edge of CdTe nanocrystals into titania matrix consistent with strong quantum confinement theory³²⁸.

These solar cells were further characterized by measuring capacitance (C) as a function of bias voltage (V) at a high frequency signal. This data enables using Mott-Schottky plots to determine important parameters including the dopant concentration of the device material and depletion length. Figure 4.6a shows Mott-Schottky plots of the nanoporous TiO₂/CdTe solar cell and planar TiO₂/CdTe solar cell. A linear region is obtained for both solar cells in the region with negative potential which can be used to calculate the density of defect states (p-doping in CdTe) derived from the slope by means of the Mott-Schottky relation (Eq. 4.1):

$$C^{-2} = \frac{2(V_{fb} - V)}{q\epsilon\epsilon_0 N} \quad (4.1)$$

Where q is the charge of one electron, ϵ_0 is the permittivity of the vacuum, ϵ is the dielectric constant of CdTe, V_{fb} is flat band potential, N is the dopant concentration in p-CdTe at the interface and equals to hole concentration in p-CdTe. Table 4.1 shows the parameters calculated for different solar cells using Mott-Schottky analysis under dark conditions. These calculations are based on the interfacial area. As discussed above, interfacial area in case of nanoporous titania is 22 ± 2 times than planar heterojunction solar cell. The total concentration of dark hole density for nanoporous TiO₂/CdTe is $1.7 \times 10^{13}/\text{cm}^3$, whereas it

is $4.5 \times 10^{15}/\text{cm}^3$ for planar TiO_2/CdTe solar cell. Thus, both active layers are not doped to the same extent. From the data shown in Table 4.1, we deduce that the defect density (and the hole concentration, space charge density) in CdTe in nanoporous TiO_2 case is almost 2 orders of magnitude lower than the CdTe deposited onto planar TiO_2 film. Lower defect density in case of nanoporous titania reduces loss of current caused by the tunneling of electrons from TiO_2 to the defect centers in CdTe. This results in a lower effective reverse saturation current and a higher V_{oc} . Also, the zero bias depletion length was calculated using the formula $W_{\text{dep}} = A \cdot \epsilon / C$ (where A is the junction area, and ϵ is the dielectric constant of CdTe) from C-V measurements. The zero bias depletion layer width is higher for nanoporous titania $15.7 \pm 1.4 \mu\text{m}$ where uncertainties are in the form of standard deviation. Thus, we can say that the entire $15 \mu\text{m}$ thickness of CdTe in case of nanoporous titania is depleted. Electric field exists in the entire CdTe layer and the solar cell acts like a p-i-n device. Because of this electric field, all light generated electrons in the CdTe absorber layer are efficiently collected. This leads to higher J_{sc} than the planar TiO_2 where depletion width is only $1.85 \mu\text{m}$ and electrons generated farther away than $1.85 \mu\text{m}$ from the interface are not efficiently collected. To summarize, CdTe growing vertically as it deposits into the nanopores of titania is of higher quality (lower defect/trap density) than the CdTe grown on top of the TiO_2 surface leading to higher J_{sc} and V_{oc} .

The spectral response of nanoporous TiO_2/CdTe solar cell is shown in Figure 4.6b in the form of incident photon to converted electron (IPCE) ratio as a function of wavelength. No response is obtained below 380 nm, which is the band gap edge of titania (3.2 eV). The results show that around 82-95 % photon efficiency is obtained for wavelengths between 380 and 500 nm, 70-80 % between 500 and 700 nm, 55 to 70 % in

the 700-820 nm wavelength range, and a sharp decrease above 820 nm. The location of long-wave edge of the spectral response is well correlated with the band gap energy of CdTe (1.5 eV). The short-wave edge spectrum is not measured effectively because of the ultraviolet limit (below 380 nm) of the Xenon-arc lamp used in the spectrophotometer. In spite of that, a very good photoresponse in 380-500 nm wavelength range was observed representing an expansion in the photoactive window compared to CdS/CdTe photovoltaics.

Even though the efficiency observed here is the highest ever reported for a CdTe-titania solar cell, it is still lower than the conventional CdS-CdTe solar cells. The biggest improvement that can still be done is in the design and execution for the top contact, which affects fill factor and thus power conversion efficiency. The fill factor reported here is only 0.4 which is very low in comparison with high efficiency solar cells and needs to be improved. In previous works, a lot of investigations of back contact and top contact materials like Cu/Au^{315, 319}, Cu doped ZnTe³²⁹⁻³³⁰ with Au or Ni metallization, Cu/Mo³³¹ or just Au³³² has already been done. Fill factors in excess of 0.7 can be achieved using these contacts. Even though all the studies have been done in case of CdS/CdTe solar cells, they can be effectively applied to TiO₂/CdTe solar cells. Also optimizing the thickness of CdTe will be crucial in order to reduce series resistance. Some of these approaches to improve power conversion efficiency in TiO₂/CdTe heterojunctions, will be the subjects of our investigation in the near future.

It is worth noticing that the main purpose of this study was to observe the effect of the porous TiO₂ layer, not the effect of the contacts and this study clearly indicated what

we intended for even though better fabrication techniques can be utilized to further improve the efficiency.

4.5 Conclusion

Nanoporous titania thin films with vertically oriented 2D HCP cylindrical nanopores with 8-9 nm pore diameter have been used as window layers for the fabrication of inorganic TiO₂-CdTe bulk heterojunction solar cell. The power conversion efficiency for nanoporous titania comes out to be 5.53 % which is almost three times higher than using planar titania as window layer (1.8%). The higher efficiency in case of nanoporous titania is attributed to the high surface area than planar titania leading to the formation of an intimate junction of large interfacial area between the nanoporous TiO₂ and CdTe layer which results in more effective extraction of photo-generated electrons than the planar TiO₂ film. Also, a better interface for nanoporous TiO₂/CdTe leads to lower defect density as compared to planar titania which in turn lead to higher V_{oc} . Further, all of the CdTe in case of nanoporous titania has been depleted leading to higher J_{sc} . The results are consistent with the previous work in the literature where the efficiency is higher in case of mesostructured materials as compared to planar structure. These solar cells have a good response in the wavelength range of 380-500 nm, unlike the case in traditional CdS-CdTe solar cells. Although the efficiency of these solar cells is much lower than traditional CdS-CdTe solar cells, this study suggests that nanoporous titania can be effectively used as window layer in inorganic solar cells. In future, we will try to improve the efficiency of the solar cell by using a better combination of back contact and top contact.

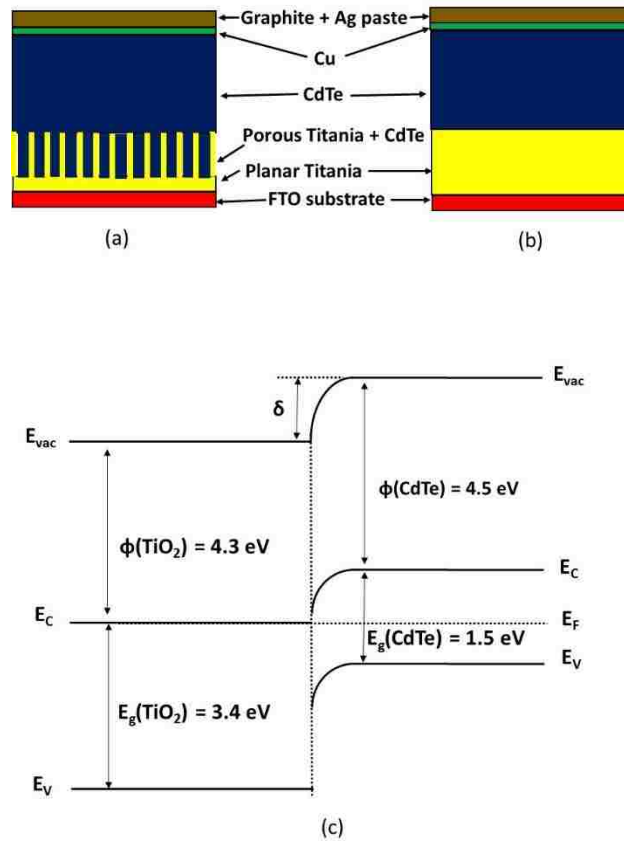


Figure 4.1. (a) Device structure for CdTe/nanoporous-TiO₂ solar cells, and (b) Device structure for CdTe/planar-TiO₂ solar cells c) Band alignment diagram for CdTe- TiO₂ system. E_g is energy band gap, ϕ is electron affinity, E_F is fermi level, E_{vac} is vacuum E_C and E_V are edges conduction and valence bands, δ is energy band offset.

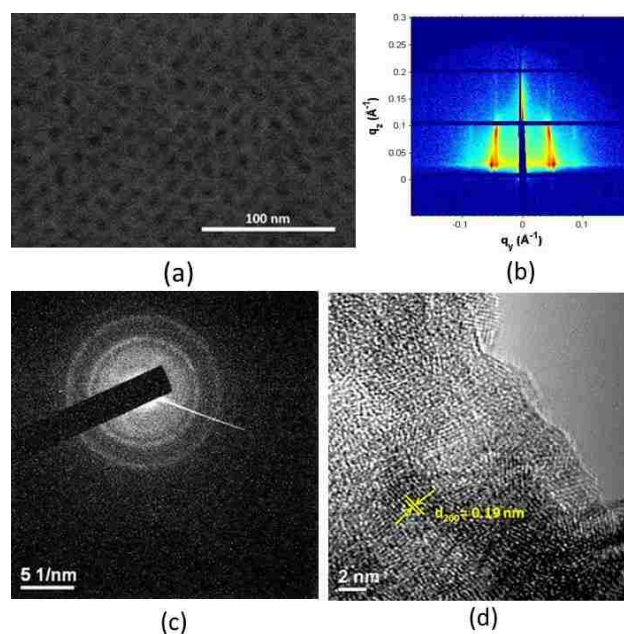
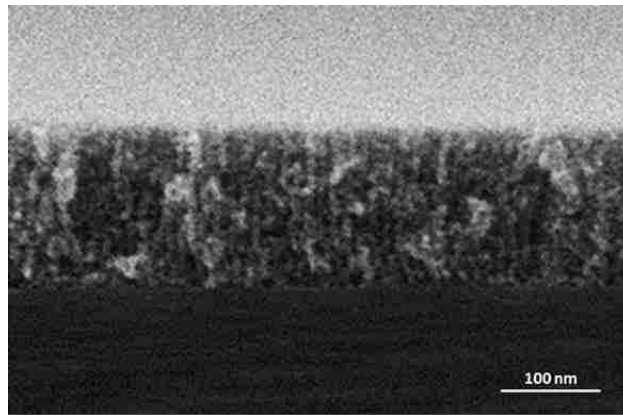
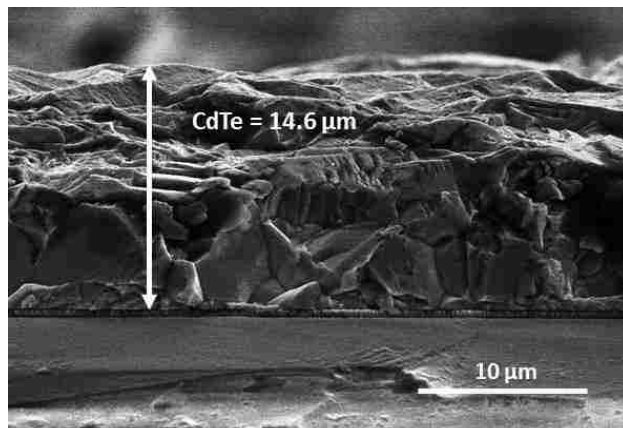


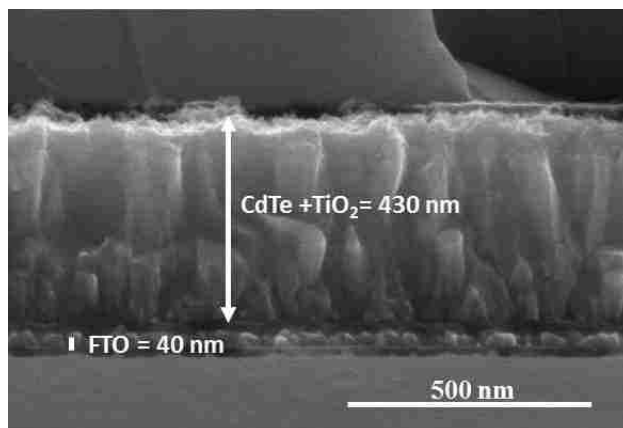
Figure 4.2. (a) SEM image (b) SAXS pattern (c) SAED pattern, and (d) HRTEM of titania film on modified glass from sols prepared using F127 with $M= 0.01$ and 30 g of ethanol, aged at 4°C and calcined at 400°C at the rate of $25^{\circ}/\text{min}$



(a)



(b)



(c)

Figure 4.3. Cross-sectional SEM image of (a) Titania film with vertically oriented cylindrical nanopores (b, c) CdTe infiltrated into the nanopores of titania at low magnification (b) and at high magnification (c)

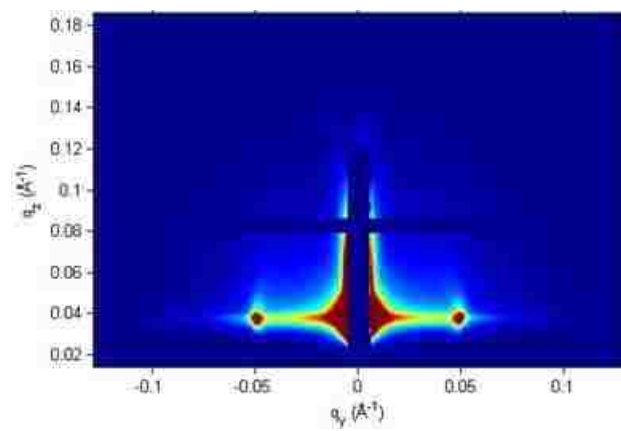
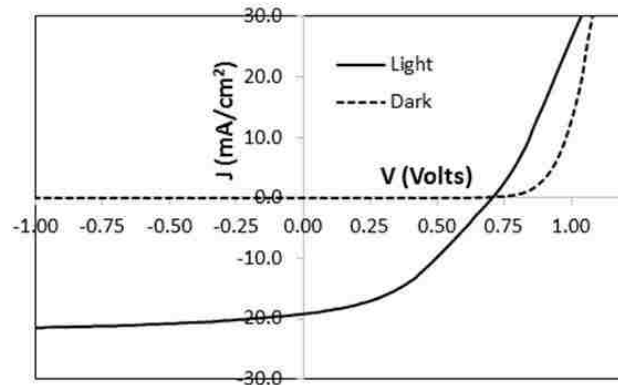
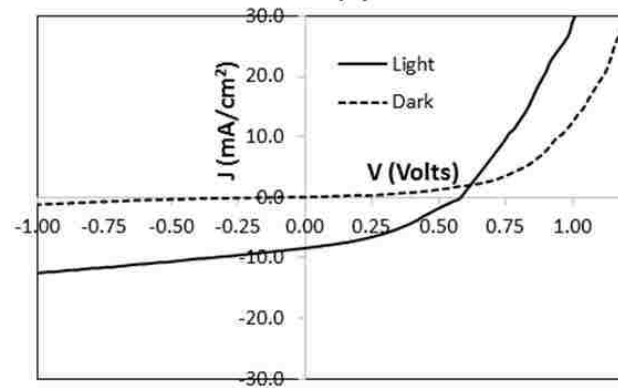


Figure 4.4. GISAXS Pattern of titania thin films with o-HCO microstructure after CdTe Sublimated from CdTe-titania samples



(a)



(b)

Figure 4.5. Solar cell performance of (a) CdTe-nanoporous TiO₂ solar cell, and (b) Cdte-planar TiO₂ solar cell

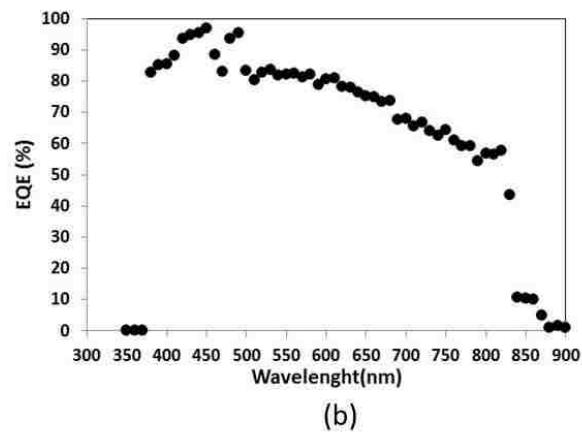
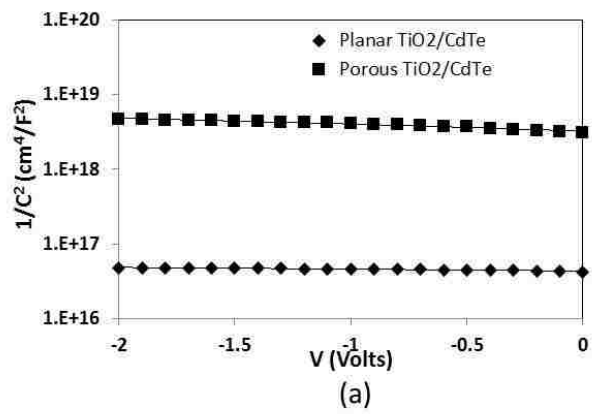


Figure 4.6. (a) Mott-schottky analysis of Planar TiO₂/CdTe and porous TiO₂/CdTe on a semi-log scale, and (b) External quantum efficiency of porous TiO₂/CdTe solar cell

Table 4.1. Photovoltaic parameters and results from Mott-Schottky analysis of nanoporous TiO₂/CdTe and planar TiO₂/CdTe Solar Cell

Solar Cell	V_{oc} (mV)	J_{sc} (mA/cm²)	FF	PCE (%)	Zero bias capacitance (F/cm²)	Charge carrier density (cm⁻³)	Zero bias depletion length (μm)
Nanoporous TiO₂/CdTe	700	19.2	0.41	5.53	5.25*10 ⁻¹⁰	1.7*10 ¹³	15.7± 1.4
Planar TiO₂/CdTe	576	8.47	0.37	1.8	4.86*10 ⁻⁹	4.5*10 ¹⁵	1.85

Copyright © Suraj R. Nagpure 2016

Chapter 5. Layer-by-layer Synthesis of Thick Mesoporous Titania Films with Vertically Oriented 2D-HCP Nanopores and Their Application as Negative Electrodes in Lithium Ion Batteries

5.1. Summary

Titania films of varying thickness with vertically oriented 2D Hexagonal Close Packed (HCP) 8-9 nm cylindrical nanopores have been synthesized using an evaporation-induced self-assembly layer-by-layer technique. The hypothesis behind the approach is that the vertically oriented mesostructured from one layer provides a surface patterned with the hydrophobic poly(propylene) blocks of the Pluronic surfactant template to epitaxially induce vertical orientation of micelles in the next deposited layer. Characterization using a combination of x-ray diffraction and electron microscopy indicates that the pores are oriented vertically even in relatively thick films (up to ~800 nm) after multiple layers of deposition. These films contain a combination of amorphous and nanocrystalline anatase titania in a nanostructured matrix of potential value for electrochemical energy storage. As proof of concept, these films have been successfully applied as negative electrode in lithium ion batteries. A battery capacity as high as 254 mAh/g has been obtained after 200 cycles for titania film with vertical pore orientation. The results showed higher capacity for vertical pore orientation as compared to parallel pore orientation and a nonporous titania film, which is attributed to high accessible surface area and reduced lithium ion diffusion length into the solid material. Films with vertically oriented pores but greater thickness have reduced battery capacity at a fixed rate of charging compared to thin films, which is attributed to reaching a thickness large enough that lithium diffusion within the pores limits the lithiation near the base of the film. These results confirm the hypothesis that epitaxial alignment occurs in multilayer sol-gel films with cylindrical HCP structure, and suggest

that further progress towards their use in battery applications is possible by lowering barriers to electrolyte diffusion within the oriented pore

5.2. Introduction

Lithium ion batteries (LIBs) are of great interest as energy storage systems due to their safety, stable cycle life, and relatively low cost³³³⁻³³⁴. LIBs function by a conceptually simple electrochemical process consisting of the extraction and insertion of Li ions between two electrodes with simultaneous removal and addition of electrons store or release electrical energy³³⁵. However, the performance of LIBs depends strongly on the composition, structure and chemistry of its primary components including the negative and positive electrodes and the electrolyte. Currently, the negative electrode (called the “anode” in the battery community) of commercially available LIBs is graphite. Although many alternative high capacity LIB anode materials are available including Si, Ge, and Sn, they cannot be used in bulk form for practical applications due to their low range of operating voltage, high stress generated by intercalation of lithium, and the formation of unstable solid-electrolyte interface (SEI) on the electrode surface by the decomposition of organic lithium salt based liquid electrolytes³³³.

TiO₂ is a suitable candidate for negative electrodes in LIBs with high discharging potentials in which the electrolyte solution is stable³³⁶. Although the theoretical capacity of TiO₂ (330 mAh/g³³⁷) is lower than that of Sn, Si, or graphite, TiO₂ anode offers better safety, which is one of the major criteria for practical use of batteries. TiO₂ also provides a high discharge voltage plateau of about 1.7 V, stable cycling performance, and small volume expansion (ca. 3%) during lithiation/delithiation³³³. The relatively high lithium insertion/extraction voltage of TiO₂ avoids the formation of solid-electrolyte interphase layers and electroplating of lithium during cycling³³⁸. TiO₂ possesses “zero-strain”

characteristics what makes it less susceptible to structural deformation during electrochemical processes. However, the major barrier to using bulk TiO₂ as an anode is its poor lithium ionic and electrical conductivities which limit the charge/discharge rate. Several studies have been carried out to improve the morphology of TiO₂, which determines the lithium intercalation activity and cycling stability of the batteries³³⁴. Among these studies, the use of porous TiO₂ has been proven to be effective for the improvement in kinetics of lithium ion insertion/de-insertion since the pore structure provides the materials with more ion transport paths and a large surface area for charge transfer reactions^{336, 339-340}. Also it has been found that an ordered mesoporous structure could decrease the polarization and enhance performance at high rates³⁴¹. Among several TiO₂ polymorphs, anatase-type TiO₂ nanostructures have been studied extensively and have been generally considered the most electroactive Li intercalation host^{340, 342-344}. These anatase TiO₂ nanostructures can facilitate the intercalation/deintercalation of Li ion charge/discharge because of their open crystal structure, which originates from the stacking of zigzag units that consist of highly distorted edge-sharing TiO₆ octahedra³⁴⁵⁻³⁴⁶.

To improve the performance of LIBs with TiO₂ anode by reducing the lithium diffusion length, nanostructured TiO₂ materials such as nanosized anatase titania, nanospheres, nanotubes, TiO₂-B nanowires and mesoporous rutile have been studied^{333, 347-353}. Wang et al. prepared anodes composed of titania nanotubes with mesoporous wall structures for LIBs³³⁶ and obtained an enhanced capacity of 162 mAh/g for current density of 1A/g after 100th discharge cycle and attributed it to the 3D network structure of the mesoporous nanotubes. These nanostructures provide both electron pathway and lithium ion pathway which are essential for high rate rechargeable lithium ion battery. Wu et al.

reported the preparation of LIBs with TiO₂ nanotube anode by anodizing pure Ti foil³³³ and showed stable capacities of 130-230 mAh/g and 520-880 mAh/cm³ up to 200 cycles. Generally, Li insertion into bulk rutile TiO₂ is negligible at room temperature. However, Kubiak et al.³⁵⁴ demonstrated that Li can be reversibly inserted into nanosized rutile TiO₂. Even though the capacity for nanosized rutile is somewhat lesser than anatase titania, the results obtained by Kubiak et al. are a further example of advantages of nanostructure materials in the field of lithium ion batteries. Wang et al.³⁵³ prepared anatase TiO₂ nanowires with minor TiO₂-B phase and found a high rate capacity of 280 mAh/g after 40 cycles and ascribed the improved performance to a shorter diffusion length for both electron and Li⁺, and a larger electrode/electrolyte contact area. However, one problem with the use of TiO₂ nanoscale materials such as nanospheres, nanowires and nanotubes is that the intrinsic aggregation of TiO₂ nanoparticles inevitably causes decreases of the electrochemical property with time³⁵⁵. To keep TiO₂ nanoparticles from aggregating, TiO₂-based mesoporous materials have been proposed. Mesoporous thin films are expected to have high accessible surface area for the introduction of lithium into the solid matrix, a short Li⁺ diffusion path length in the solid phase, and good electrical connectivity to the current collector.

Despite the advantages demonstrated in the literature of TiO₂ in LIBs, few have reported on the use of surfactant-templated ordered mesoporous TiO₂ thin films for anodes in LIBs. Kavan et al. studied the lithium ion electrochemistry in surfactant-templated mesoporous anatase TiO₂ films templated by P123 block copolymers²⁸. However, these titania films were thermally and mechanically unstable and the electrochemical study was only restricted to cyclic voltammetry. Fattakhova-Rohlfing et al. studied lithium insertion

into highly organized mesoporous TiO₂ films with 3D cubic pore arrangement using evaporation induced self-assembly (EISA) and pluronic P123 as templates³⁵⁶. However, the films prepared using Pluronic P123 collapsed at higher calcination temperature above 500 °C. In our group, we have successfully synthesized thermally and mechanically stable titania thin films with vertically oriented 2D Hexagonal Close Packed (HCP) cylindrical nanopores using evaporation induced self-assembly technique with a pore diameter of 8-9 nm. These films are highly resistant to thermal degradation and retain their mesostructural order even after calcination temperature of 600 °C⁴³. The vertical orientation of the pores has been achieved using surface modification technique as shown in our previous work^{2, 41, 43}. The vertically oriented cylindrical mesoporous channel would be a facilitated path for Li⁺ ion transfer; and small TiO₂ grains in the matrix would effectively reduce the diffusion length for Li⁺ ion insertion/extraction. The small pores will provide higher surface area than in TiO₂ nanotube arrays prepared by anodization for lithium ion insertion, and the small wall thickness will reduce the Li⁺ diffusion length. The surfactant-templated synthesis approach is also more readily scalable and adaptable to a variety of substrates, so this would represent a more commercially viable technology than batch anodization of titanium. In this work, we have applied ordered mesoporous TiO₂ thin film as an anode material in LIBs and studied the effect of pore orientation on the electrochemical performance. Another unique accomplishment of this work is successful development of thicker titania films using layer-by-layer technique accompanied with evaporation induced self-assembly (EISA) while retaining vertical pore orientation. This is a novel strategy to prepare continuous cylindrical channels across multiple layers. After the successful

synthesis of multilayer films, we have investigated the effects of film thickness on electrochemical transport and battery performance.

5.3. Experimental Section

Titania films were prepared by deposition onto titanium foil for Li-ion batteries. After cleaning with ethanol and water, titanium foil was modified (if modification was used) based on the method of Koganti et al.⁸⁰ using F127 as the Pluronic surfactant. The solution was prepared by first adding 0.696 mmol/L of F127 and a drop of glycerol as a cross-linker to 100 ml acetone. An equal number of moles of 1,6-diisocyanatohexane was added dropwise to the mixture in a nitrogen-filled glove bag. The freshly prepared solution was then dip coated onto titanium foil and the slides were aged at 120 °C overnight (approx. 12 hours) to drive the isocyanate-hydroxyl cross-linking reaction to completion.

Titania films with F127 as the structure directing agent were synthesized according to the procedure of Crepaldi et al. with a modified thermal treatment⁵¹. The coating solution was prepared by adding 0.01 mole (1.93 g) of TiCl_4 to a solution of 1.26 g F127 ($M = 0.01$) in 18.43 g anhydrous ethanol in a nitrogen-filled glove bag. The HCl produced by esterification acted as a catalyst to drive the hydrolysis reaction while also controlling condensation to prevent uncontrolled precipitation. To this solution, 0.1 mole (1.8 g) of water was slowly added and the sol was allowed to react for 10 minutes before coating. Films were prepared by dip coating glass substrates with the sol at room temperature. Titania films were aged after coating at a temperature of 4 °C for 2 hours at a relative humidity of approx. 94%. The high relative humidity environment was provided by placing the samples in a sealed chamber with two beakers containing deionized water. To prepare multilayer films, freshly coated and aged layers underwent heat treatment for

1 h at 120 °C for 1 hour to stabilize the titania network, after which the coating and aging process was repeated. After all layers were deposited, titania films were calcined by transferring them directly from the refrigerator to a muffle furnace and increasing the temperature at 25 °C/min to 400 °C and holding for 10 min followed by rapid cooling. Films were coated not only onto modified titanium foil but also onto plain titanium foil to see the effect of pore orientation on battery performance. In order to compare the effect of porosity over the battery performance, electrochemical characterization was also performed for nonporous titania. These nonporous films were prepared by adding 1.8 g of water to the solution of 0.01 mole (1.93 g) of TiCl_4 in 18 g anhydrous ethanol. After dip coating titanium foil with this sol at room temperature, films were then calcined by transferring them directly from the refrigerator to a muffle furnace and increasing the temperature at 25 °C/min to 400 °C and holding for 10 min followed by rapid cooling. The thickness of nonporous titania was measured using profilometry to be 60 nm.

The thickness of the films was also measured using profilometry. X-ray diffraction (XRD) analysis using $\text{Cu K}\alpha$ ($\lambda = 1.5406 \text{ \AA}$) radiation was employed to determine the titania film pore orientation. Measurements were conducted directly on the thin films in Bragg–Brentano geometry using a Bruker D8 Advance diffractometer. For plan-view imaging of pore structures, scanning electron microscopy (SEM) was performed using a Hitachi S-4300 at 3 kV. SEM samples were prepared by cutting the glass slide to the desired shape using a glass cutter and then mounting them exactly at the center of SEM stubs coated with carbon tape. The edges of the sample were coated with colloidal silver (isopropanol base, Ted Pella, Inc.) to increase conductivity by keeping the top surface in electrical contact with the lower surface. The samples were aged at 120 °C overnight

(approx. 12 hours) to evaporate all the solvent from the colloidal graphite solution. To observe the cross-section of the films, samples were prepared on silicon wafer and mechanically fractured by bending before mounting onto the stage.

The electrochemical performance of titania films was tested in CR2025 coin cells using titania foils as the working electrodes (WE) and pure Li metal foils as the counter electrodes (CE). Cells were fabricated in an Ar-filled glovebox (MBraun), where the oxygen and moisture levels were below 0.1 ppm. The electrolyte was 1 M LiPF₆ salt dissolved in an equal-volume mixture of ethylene carbonate and dimethyl carbonate (Novolyte). Coin cells were galvanostatically cycled between 1.0 and 2.7 V at a rate of C/3, which was controlled by a multichannel potentiostat (VMP3, Bio-Logic). This corresponds to 3 h charge/discharge cycles at a current of roughly 10 μ A. X-ray photoelectron spectroscopic (XPS) analysis was conducted using a ThermoScientific K-Alpha photoelectron spectrometer using monochromatic Al K- α radiation with photon energy of 1486.6 eV. Prior to XPS characterization, samples were cleaned with ethanol to remove dust from their surface.

5.4. Results and Discussion

Before looking at multilayer films, the effects of pore accessibility on LIB performance was assessed using single-layer films. Figure 5.1a shows top view SEM image of a single-layer nanoporous titania film prepared on F127-modified titanium foil prepared from sols containing 1.26 g F127 and 18.43 g of ethanol, aged at 4 °C and calcined at 400 °C at the rate of 25 °C/min. The thickness of these mesoporous films as measured using profilometry to be 186 ± 32 nm, where uncertainties are shown in the form of standard deviation of measurements at multiple points. A very well ordered, accessible porous

structure is observed, suggesting that orthogonal alignment of mesopores for films cast onto modified glass.

Figure 5.1b shows cycling performance for the same after coin cell fabrication using titanium foils as the working electrodes (WE) and pure Li metal foils as the counterelectrodes (CE). The battery cycle testing was performed up to 200 cycles at C/3 rate. The mass of active materials was estimated by estimating the volume fraction of pores on each sample and taking the density of the solid phase to be 3.8 g/cm^3 in the calculation. To study the effect of porosity and the effect of pore orientation, the performance of these films is compared with nonporous titania and titania with parallel HCP pores (cast onto cleaned titanium foil without modification with crosslinked F127). For vertically oriented nanoporous structures, a capacity as high as 254 mAh/g was observed after 200 cycles. However, for nonporous titania, the capacity was only 191 mA/g after 200 cycles. The higher capacity of the former is attributed to reduced lithium ion diffusion length into the solid phase and the high surface area of vertically oriented nanoporous titania. HCP pores cast onto hydrophilic oxide surface without modification by crosslinked F127 simply lead to parallel orientation of pores as shown previously^{2, 41, 43}. The battery capacity for films with parallel HCP pores fades rapidly to about 202 mAh/g, which close to that of the nonporous film. This suggests that the high capacity and stability towards capacity loss in the films with vertical HCP pores is due to their mesostructural stability. We have shown in the past that vertically oriented nanopores are more stable than parallel pores towards anisotropic stress associated with thermal treatment and crystallization^{2, 43}. After 200 cycles, the parallel pores most likely collapse to a significant extent, causing those films to

behave like the nonporous films, while the films with vertical HCP pores retain a high capacity due to their mechanical resilience.

The long-term stable capacity of the films with vertically oriented HCP pores is 77% of the theoretical capacity of titania. This is comparable to, but somewhat greater than the capacity reported for titania nanotube arrays prepared by anodization (up to 230 mAh/g after 200 cycles at C/3 rate³³³), most likely due to the thin walls of the present self-assembled structures. This is a significant finding because it demonstrates the promise of vertically aligned HCP films prepared by surfactant templating as a stable platform for high-capacity LIBs. However, the thickness of a single sol-gel film (186 nm) does not provide a high absolute capacity. Considering the average thickness of 186 nm, 45% porosity and mass density of 3.8 g/cm³ for anatase titania, the mass loading is 0.042 mg/cm².

In order to improve the mass loading and to exploit the properties of vertically oriented cylindrical nanopores, a strategy was developed to prepare thicker films with controlled pore orientation. Directly preparing thicker films with a single coating is not a viable strategy because the vertical orientation of micelles propagates a limited distance into the film⁸⁰. Instead, thickness was increased using a layer-by-layer technique. After aging at 4 °C for 2 hours, rather than calcining, these films were provided with intermediate heating at 120 °C for 1 hour. This temperature is high enough to dry the films without damaging the surfactant micelles. The hypothesis tested here is that the surfactant micelles in new layer will align epitaxially with micelles from the layer underneath, thereby proving continuous orthogonal cylindrical nanopores in a multilayered film. This is a novel strategy in preparing continuous cylindrical channels across multiple layers. The only

comparable example of this approach in the literature was from Richman et al., who reported vertical orientation of 2D HCP mesostructures cast onto films with a cubic mesophase³⁵⁷. Figure 5.2 shows thickness of films as a function of number of layers measured using profilometry. The error bars represent standard deviation in thickness values for multiple samples. The thickness values are also summarized in table SI1 of the supporting information (SI). As we expected, thickness varies linearly with the number of layers. Films as thick as 1050 nm were developed after 8 layers of deposition.

In order to characterize pore orientation, XRD and plan-view SEM were performed. Figure 5.3 shows low angle XRD patterns of calcined titania films on unmodified glass and modified glass for three different thicknesses. According to Hillhouse et al.¹, for ordered HCP mesoporous films, reflections corresponding to (100) and (200) lattice planes can be observed in Bragg-Brentano XRD when the mesostructure is oriented with the (100) plane parallel to the substrate. We see a single peak in the XRD pattern for film on unmodified glass. According to Kirsch et al.⁵⁶, the unit cell parameter of surfactant-templated films are typically above 10 nm. The (100) reflection corresponding to this unit cell parameter should have a d-spacing of 8.6 nm and would appear near $2\theta = 1^\circ$, which below the detection limit of the instrument. At best, this reflection would be obscured by background scattering of the direct x-ray beam. Thus, the reflection observed in the XRD pattern of all samples is indexed as the high-order (200) peak of the 2D hexagonal phase. The presence of this XRD reflection indicates that after aging at a temperature of 4 °C, a well-organized F127/titania composite mesostructure forms which is preserved during subsequent heating and removal of the template. We did not observe any XRD peaks in the range of 2θ values associated with anatase crystallites. This is because a calcination temperature of only 400

°C was used to avoid mesopore deformation, which also expected to gives crystallites only a few nanometers in diameter. Broadening of the diffraction from such small crystallites is so great that they cannot be observed by XRD in our thin films.

As seen in Figure 5.3, the (200) reflection is absent in case of films formed on modified surfaces for multilayer films. In the Bragg-Bentano geometry used for XRD, diffraction in the plane of substrate is not detected¹. Thus, completely orthogonally tilted mesophase should not yield any XRD diffraction intensity, and the intensity should decrease for more orthogonal structure. Therefore, the loss of intensities in the XRD patterns for films on modified glass is consistent with reorientation of the pores orthogonally with respect to the modified substrate. However, the reduction in XRD intensity might also be due to the loss of mesostructural order for thicker films. When we see top-view SEM images (Figure 5.4), we can clearly see that thicker films prepared by layer-by-layer technique have well-ordered accessible porous structures, which indicates that the reduction in XRD intensity is not because of the loss of mesoporous order. This shows that the orthogonal alignment of the pores is retained for thicker films after modification of the glass substrate and casting one layer onto another. However, the porosity of these films reduced after multiple layers. The porosity of these films were calculated by analyzing top-view SEM images using software ImageJ. The porosity reduced from 51% for a single layer to 44% after four layers which might be because of shrinking of the mesostructure as a result of intermediate heating.

Figure 5.5 shows cross-sectional SEM images for films with different thicknesses. We can clearly see vertically oriented cylindrical channels in figure 5.5a for films with thickness 186 ± 32 nm confirming orthogonal alignment of the pores and is consistent with

the XRD data. However, for thicker films, the magnification was not quite enough to directly visualize the nanopores. Nonetheless, thicknesses calculated from cross-sectional SEM images match very well with the profilometry data. The anisotropic fractured texture of the multilayer films is also consistent with a continuous vertically oriented porous structure, and there are no indications of boundaries between layers in the cross sectional images. These results clearly indicate that thicker titania films with vertically oriented 2D HCP cylindrical nanopores can be successfully synthesized using a layer-by-layer technique.

The cyclic voltammetry of a titania film electrode of thickness 186 ± 32 nm in 1 mol/l LiPF_6 solution of DEC/EC for the first 5 cycles is shown in figure 6a. The Li^+ ion insertion/extraction reaction in TiO_2 can be expressed as:



Where x is the insertion coefficient. From Figure 5.6a, We can clearly see one pair of redox peaks when scanning between 1 and 3 V vs. Li^+/Li at various cycles, around 1.7 and 1.95 V. These correspond to the insertion and extraction process of lithium ions into and from mesoporous an anatase titania anode according to equation (5.1), which has been reported in both single crystal³⁵⁸⁻³⁵⁹ and polycrystalline anatase titania³⁶⁰⁻³⁶³. Only very small intensity and voltage position changes can be observed with increasing cycles, suggesting good reversibility. In addition, the ratio of anodic to cathodic peak current is about 1, which can further demonstrate the redox electrode process of titania is relatively stable and reversible. One more interesting observation is the broadening of peaks at the lower potentials. According to previous studies, this broadening indicates the presence of amorphous titania¹³³. These results further indicate that these sol-gel titania films contain

a combination of anatase and amorphous titania. We did not see any other pairs of redox peaks in cyclic voltammetry as seen by other researchers for porous anatase titania^{28, 340}. Kavan et al.²⁸ found two peculiar cathodic/anodic peaks at around 1.5 V and 1.6 V respectively, which are absent in the ordinary anatase phase. They termed these S-peaks, and attributed their presence to a surface confined process and an indication of the structural perfection of the nanotextured framework. The absence of these peaks in our case indicate that the Li-electrochemistry is controlled only by a bulk insertion into the anatase lattice, as the system exhibits the “normal” behavior of anatase. The absence of S-peaks in larger anatase nanocrystals persists even if these nanocrystals are mesoscopically ordered via self-organization³⁶⁴. We see the similar results for multilayer films (Figure 5.6b) indicating stable mesoporous anatase structure for multilayer films.

The cycling performance of titania films with vertically oriented cylindrical nanopores of varying thickness is shown in Figure 5.7. After 200 cycles, the discharge capacity remains as high as 254 mAh/g for single layer titania film and decreases to 243 and 201 mAh/g after two and three layers respectively. The capacity differences among multilayer titania films is primarily due to the variation of thickness and porosity of the film. As the length of the pores increases in thicker films, it is reasonable that diffusion of lithium through the pores becomes a limiting factor, and material at the end of the pores remains less lithiated during cycling. This suggests that even though the film thickness increases after multiple layers, only a part of that film is available for the lithium diffusion and thus electrochemical reaction. Similar results were obtained by Wu et al.³³³ for titania nanotubes. However, the cycle capacity obtained here is higher than other morphologies of titania such as nanotubes^{333, 336}, nanoparticles³⁵⁴, nanowires³⁴⁹ and other polymorphs of

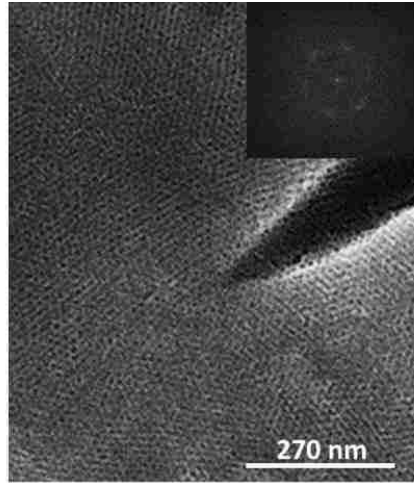
titania such as rutile³⁵⁴ and TiO₂-B. These titania films show excellent retention of capacity on cycling essential for a promising anode material for high-power lithium ion batteries.

Figure 5.8 shows XPS spectra of TiO₂ thin films before electrochemical characterization and after the completion of 200th discharging cycle. Two peaks are observed associated with the Ti 2p state³⁶⁵ and only a small shift by about 1.0 eV towards higher binding energies is observed after 200th cycle. A peak associated with the formation of Ti³⁺ upon Li intercalation has been observed by Södergren et al.³⁶⁶ at 456 eV. However, no peaks are seen at this energy in figure 8 which indicates that after the discharging cycle, almost all of titania structure is still intact and the process is reversible in terms of lithium intercalation/de-intercalation even after 200 cycles. The stable reversible capacity and stable cyclability of titania nanotube may be attributed to the intrinsic low volume expansion of titania during lithium-ion insertion and extraction³⁶⁷ and the hollow structure of titania nanopores which accommodates volume expansion and diffusion-induced stresses (DISs)³³³. We can also clearly see that the intensity of the Ti 2p peaks reduce after 200 cycles. Since XPS only measures TiO₂ on the surface, this might indicate that after cycling a surface layer of residual electrolyte salt deposited on top of titania pores which also made it difficult to study the effect pore morphology after cycling using SEM.

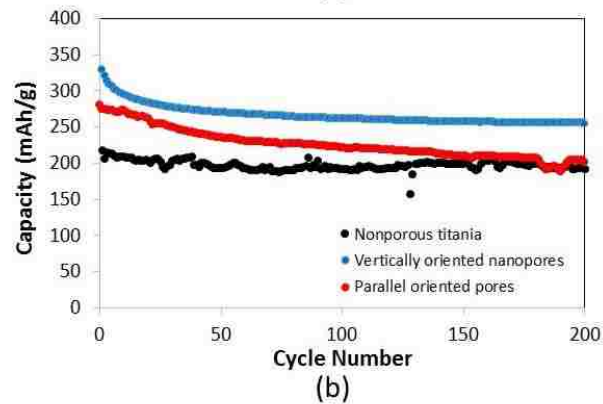
5.5. Conclusion

Surfactant-templated titania films with vertically oriented 8-9 nm 2D Hexagonal Close Packed (HCP) cylindrical nanopores and variable thickness were synthesized using evaporation induced self-assembly and layer-by-layer deposition. The surfactant micelles in newly deposited layer align epitaxially with micelles from the layer underneath, thereby providing continuous orthogonal cylindrical nanopores in multilayered films. These films have been successfully applied as negative electrode in lithium ion batteries. The results

showed higher capacity for vertical pore orientation as compared to parallel pore orientation and nonporous structure which is attributed to the high surface area and reduced lithium ion diffusion length in the vertical structures. The redox electrode process of titania is relatively stable and reversible and battery capacity remains stable even after 200 cycles. A battery capacity as high as 254 mAh/g has been obtained after 200 cycles for titania film for single layer with vertical pore orientation and reduced somewhat for thicker films, most likely due to limited lithiation near the base of the films. These titania films show excellent retention of capacity on cycling, which makes them promising anode materials for high-power lithium ion batteries. Thus, titania films with surfactant-templated nanopore arrays having thin walls and small pore diameters are promising application in LIBs with high capacity and long cycle life. Overcoming the axial diffusion limitation in the cylindrical pores would be the next challenge to address to move towards these materials, for example by expanding the pores using a hydrophobic swelling agent or hydrothermal treatment.



(a)



(b)

Figure 5.1. (a) Top view SEM image of a single-layer nanoporous titania film prepared on F127-modified titanium foil prepared from sols containing 1.26 g F127 and 18.43 g of ethanol, aged at 4 °C and calcined at 400 °C at the rate of 25 °C/min and (b) Cycling performance for titania thin films with different pore orientation and its comparison with a nonporous titania film up to 200 cycles at C/3 rate.

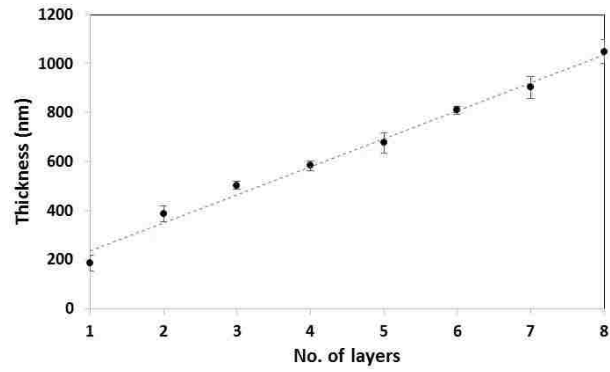


Figure 5.2. Thickness of films as a function of number of layers measured using profilometry. The error bars represent standard deviation in thickness values for three samples.

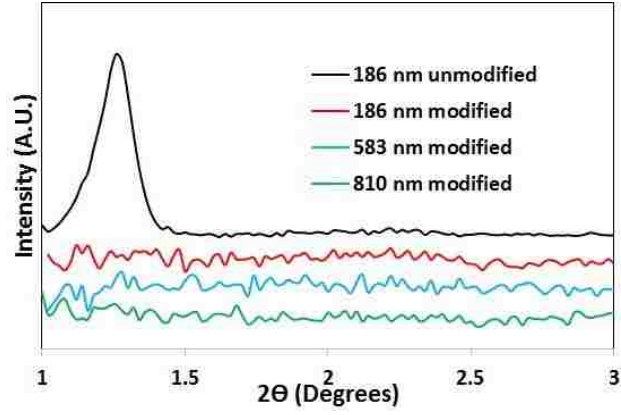
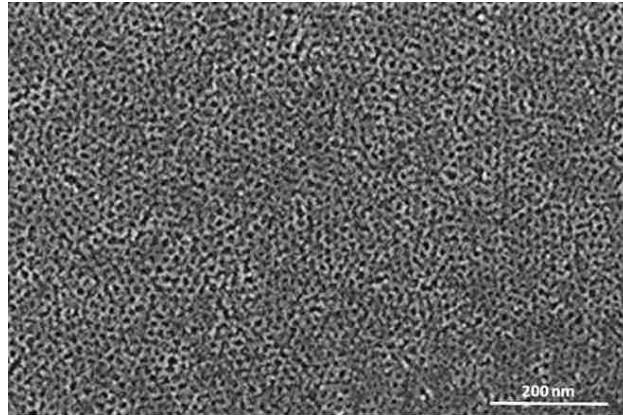
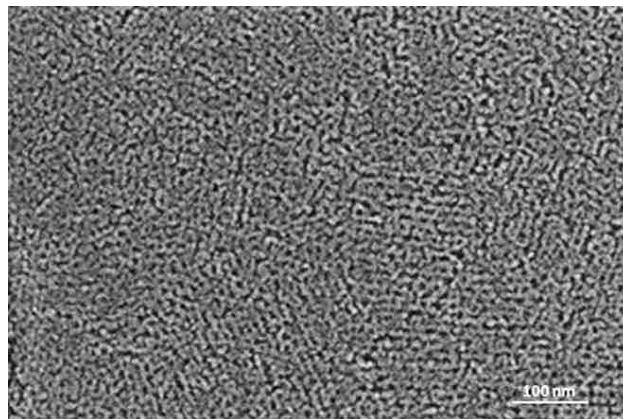


Figure 5.3. XRD patterns of calcined titania films on unmodified glass and modified glass for three different thicknesses from sols prepared using 1.26 g F127 and 18.43 g of ethanol, aged at 4 °C and calcined at 400 °C at the rate of 25 °/min



(a)



(b)

Figure 5.4. Top-view SEM images of titania thin films after (a) one layer and (b) three layers from sols prepared using 1.26 g F127 and 18.43 g of ethanol, aged at 4° C and calcined at 400° C at the rate of 25°/min. The thicknesses of titania film measured using profilometry were around 186 nm and 434 nm respectively.

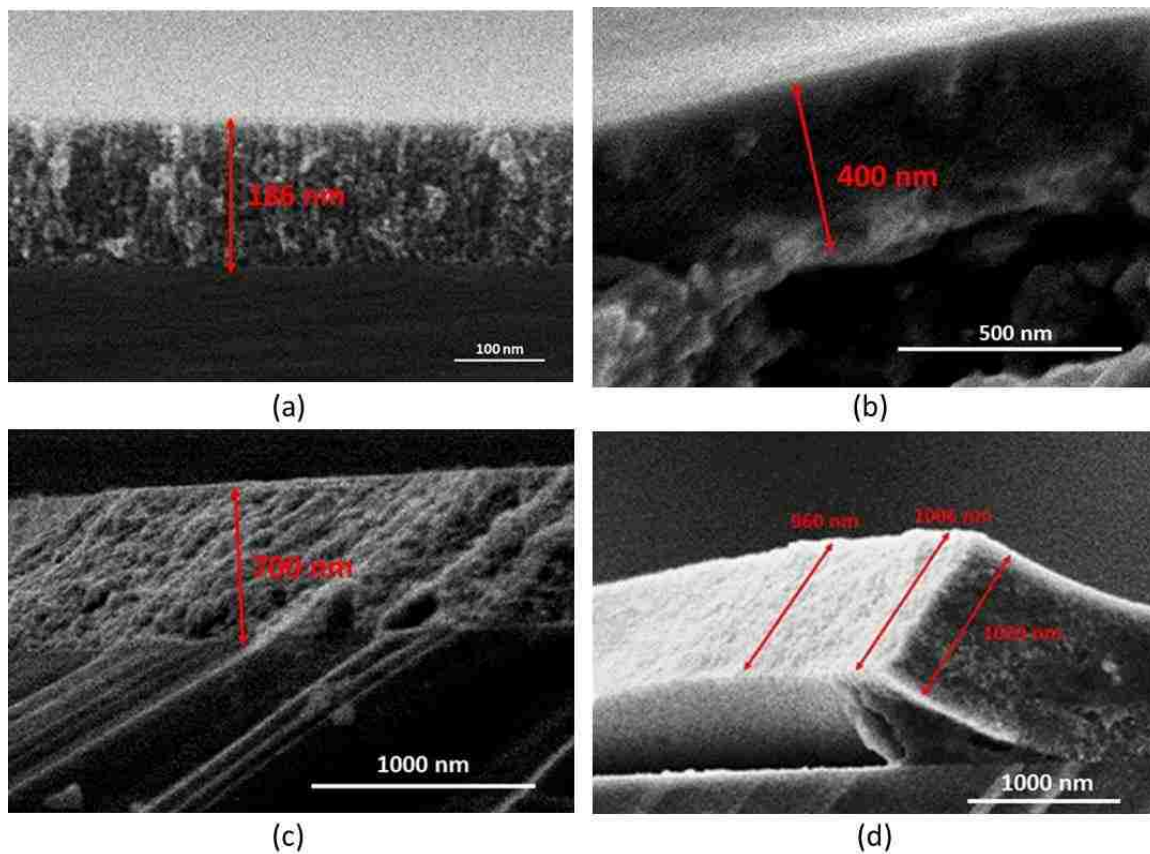


Figure 5.5. Cross-sectional SEM images of titania thin films after (a) one, (b) three, (c) five, or (d) eight layers were deposited from sols prepared using 1.26 g F127 and 18.43 g of ethanol, aged at 4° C and calcined at 400° C at the rate of 25°/min

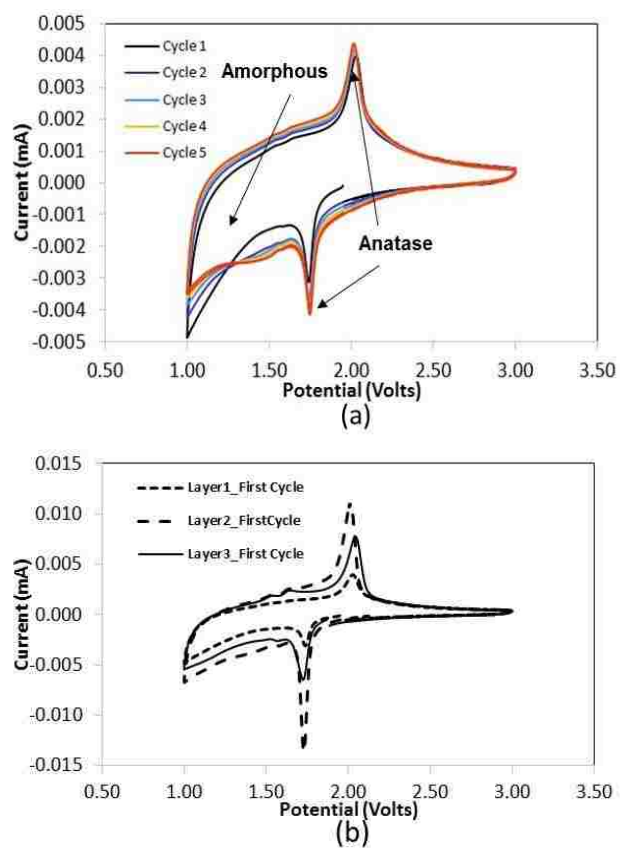


Figure 5.6. Cyclic voltammetry of (a) one layer for five cycles and (b) multilayer titania films for indicated layers for the first cycle, measured in 1 M LiPF₆ salt in an equal volume mixture of ethylene carbonate and dimethyl carbonate

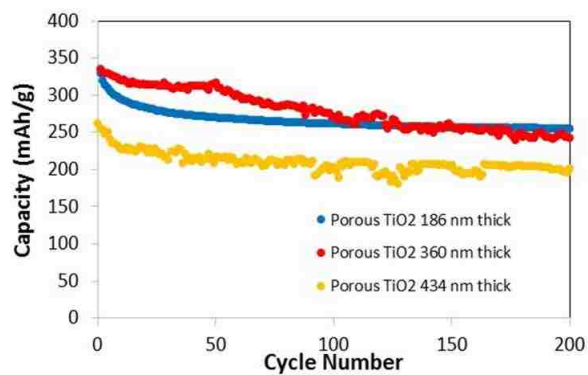


Figure 5.7. Cycling performance of titania films with vertical pore orientation for indicated thicknesses up to 200 cycles at C/3 rate.

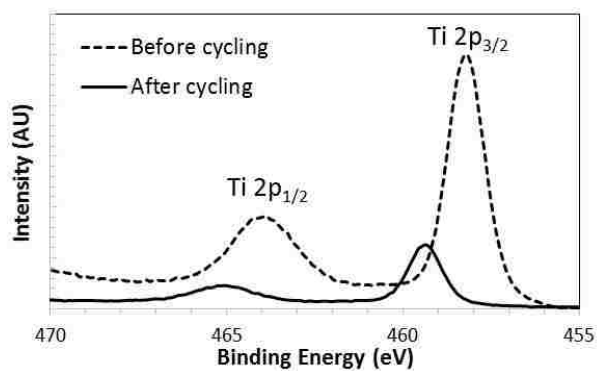


Figure 5.8. XPS spectra of TiO₂ thin films before electrochemical characterization and after the completion of the 200th discharging cycle.

Copyright © Suraj R. Nagpure 2016

Chapter 6. Conclusions and Future Work

6.1. Conclusions

This dissertation addressed the synthesis mechanism of mesoporous titania thin films with 2D Hexagonal Close Packed (HCP) cylindrical nanopores by an evaporation-induced self-assembly (EISA) method with Pluronic surfactants P123 and F127 as structure directing agents, and the application of these films in photovoltaics and lithium ion batteries.

In chapter 2, we investigated the development of mesostructure and orientation during low temperature aging at 4 °C under high humidity in surfactant-templated titania films using *in situ* GISAXS. Modification of glass slides with crosslinked template (Pluronic surfactant P123) was used to control surface chemistry to enhance orthogonal orientation of the hexagonal close packed (HCP) mesophase. For a thin (~60 nm) titania film on modified substrate, orthogonally oriented HCP cylindrical micelles started developing after a 7 minute induction period and the intensity evolution followed Avrami kinetics with an index of 2, most likely indicating a mechanism of two dimensional growth of the o-HCP mesophase with nucleation at the start of the process. At the end of the aging period, intense vertical rods due to scattering in the film were observed on both sides of the beam stop, indicating that only the o-HCP phase forms. Unlike prior GISAXS studies based on small molecule surfactant templates^{71, 90-91}, no intermediate phase was observed during the development of the o-HCP cylindrical micelles; it formed directly by a disorder-order transition. This observation is consistent with the expected effect of modifying the surface to give an interface equally attractive towards the PEO and PPO blocks of the template, and therefore to reorient the HCP phase orthogonal to the solid substrate. The

half-life for o-HCP development in this film after the induction period was about 39.7 min, and led to a well-ordered mesostructure within an hour. Although radiation damage interfered with the GISAXS intensity observed during repeated sampling of a single spot, the intensity recovered when the sampling frequency decreased and was found to be increased in regions of low sampling frequency.

Similar *in situ* GISAXS experiments at 4 °C were performed for three additional samples: thin films on unmodified slides and thicker films (~250 nm) on both modified and unmodified slides. Using plain glass and thicker films were both anticipated to reduce the degree of orthogonal orientation of the HCP phase. Surprisingly, only the o-HCP phase was observed in the GISAXS patterns of all of these samples. No evidence for HCP domains oriented parallel to the substrate or randomly could be found, although the ultimate intensity of these three samples was less than for the thin film on modified substrate (for example, the intensity was about half for the thin film on unmodified substrate than for the modified substrate). The finding of only an o-HCP GISAXS pattern contradicted prior studies which showed randomly oriented HCP patterns for thin films on unmodified substrates⁸⁰ or thick films without sandwiching with a second modified slide²²³. This was attributed to the low temperature and high relative humidity used from the start of the coating process (in prior studies, films were cast at room temperature and moderate RH prior to being transferred to a refrigerated high RH box for aging). The low temperature (4 °C) is below the temperature where PPO blocks have been shown in previous studies to exhibit a thermotropic shift from hydrophobic (high temperature) behavior to hydrophilic. Also, by analogy with solvent annealing mechanisms of orthogonally orienting HCP block copolymer phases²²⁵, the high RH may contribute to an

orthogonal orientation at the film/vapor interface. For all three samples at 4 °C, a similar Avrami coefficient was found ($n \sim 3$) indicating two-dimensional growth with continuous nucleation. Thus there is a clear difference in mesostructure growth mechanism for thin film on modified substrate and other films. Also the induction period was reduced to ~3 min with increased rate of the mesostructure evolution. Also the half life for thin film on modified substrate is higher than other three films indicating better orthogonal structure develops slowly. To confirm the temperature effect, aging a thin film sample on a modified substrate at 23 °C was found to lead to randomly oriented HCP channels.

Thus, the results obtained here suggest that the most well-defined orthogonally aligned HCP mesophase is obtained by a direct disorder-to-order transition during the transient steady state period after the coating has been deposited. However, the results indicate that aging at low temperature (4 °C) at high RH also contributes substantially to orthogonal orientation of the HCP phase, and that while the order and orientation may not be as complete, these conditions alone can induce partial o-HCP formation for thin films on unmodified slides or thick films. Thus, a temperature below the thermotropic transition temperature of the block copolymer template and a high relative humidity are suggested to be essential to forming orthogonally oriented block copolymer template films, while modifying the substrate for chemical neutrality towards the templating surfactant gives more complete orthogonal orientation across the entirety of the film.

We also synthesized titania thin films with o-HCP structure using Pluronic surfactant F127 (non-ionic triblock copolymer with molecular formula $\text{EO}_{106}\text{PO}_{70}\text{EO}_{106}$, where EO is ethylene oxide and PO is propylene oxide, and has average molecular weight of 12,500 Da). The hypothesis behind using F127 to synthesize titania films is that since

F127 has higher molecular weight than P123, it should produce larger pores than P123. . However, when measured, the pore diameter for these mesoporous films was the same as obtained using P123 (8-9 nm)². The difference between F127 and P123 is that F127 (EO₁₀₆PO₇₀EO₁₀₆) has longer hydrophilic PEO (polyethylene oxide) blocks than P123 (EO₂₀PO₇₀EO₂₀). The likely reason that longer PEO blocks of F127 do not expand the pore size is that PPO (polypropylene oxide) blocks dictate the pore size while PEO mixes with titania matrix. The (100) diffraction peak for P123 templated titania films is observed at $q_y = 0.048 \text{ \AA}^{-1}$ corresponding to a d-spacing of 13 nm. The d-spacing using F127 (15 nm) is slightly larger, indicating that mixing of PEO blocks with TiO₂ precursor leads to thicker walls when F127 is used as the template. Although F127 did not produce larger diameter pores than films made using P123, the characterization results demonstrate that the synthetic strategy reported by Koganti et al.⁸⁰ can be generalized to generate o-HCP titania films using other Pluronic surfactants. The thicker walls may impart stability to the films for further processing, although this advantage is not within the scope of the current study.

Regioregular P3HT was incorporated into the vertically oriented cylindrical nanopores of the resulting films in order to develop a bulk heterojunction for inorganic-organic hybrid solar cells. An infiltration depth of ~14 nm is obtained after 30 minutes of annealing at 200 °C under vacuum and for higher annealing times, there is no further improvement in the infiltration depth. This infiltration was measured directly by neutron reflectivity, and causes a corresponding blue shift in the absorbance of the P3HT. The infiltration depth is lower than that reported in previous studies, most likely because of the higher entropic cost of confinement of P3HT chains into straight cylindrical nanopores.

The charge transfer across the P3HT-TiO₂ interface was significant and correlated with the degree of infiltration of P3HT. In the future, these results can be used to fabricate efficient solar cells by using the knowledge gained about the optimal conditions for incorporation of P3HT into the pores of orthogonal HCP titania films and comparing the performance with cubic nanopore arrangement of titania and planar titania.

These thin films with vertically oriented 2D HCP cylindrical nanopores with 8-9 nm pore diameter have also been used as window layers for the fabrication of inorganic TiO₂-CdTe bulk heterojunction solar cell in chapter 4. The power conversion efficiency for nanoporous titania comes out to be 5.53 % which is almost three times higher than using planar titania as window layer (1.8%). The higher efficiency in the case of nanoporous titania was attributed to the high surface area than planar titania leading to the formation of an intimate junction of large interfacial area between the nanoporous TiO₂ and CdTe layer, which results in more effective extraction of photo-generated electrons than in the planar TiO₂ film. Also, a better interface for nanoporous TiO₂/CdTe leads to lower defect density as compared to planar titania which in turn lead to higher *V_{oc}*. Further, all of the CdTe in the case of nanoporous titania is within the depletion layer, leading to higher *J_{sc}*. The results are consistent with the previous work in the literature where the efficiency is higher in case of mesostructured materials as compared to planar structure. These solar cells have a good response in the wavelength range of 380-500 nm, unlike the case in traditional CdS-CdTe solar cells. Although the efficiency of these solar cells is much lower than traditional CdS-CdTe solar cells, this study suggests that nanoporous titania can be effectively used as a window layer in inorganic solar cells.

Finally, in chapter 6, we synthesized thick titania films with o-HCP nanostructure using an evaporation induced self-assembly layer-by-layer technique. The surfactant micelles in a new layer align epitaxially with micelles from the layer underneath, thereby proving continuous orthogonal cylindrical nanopores in a multilayered film. These films have been successfully applied as negative electrodes in lithium ion batteries. The results showed higher capacity for vertical pore orientation after extended cycling as compared to parallel pore orientation and planar structure which is attributed to high surface area and reduced lithium ion diffusion length. The redox electrode process of titania is relatively stable and reversible and battery capacity remains stable even after 200 cycles. A battery capacity as high as 254 mAh/g has been obtained after 200 cycles for titania film for single layer with vertical pore orientation and reduced a little for thicker films which is attributed to limitation to lithiation near the base of the film. These titania films show excellent retention of capacity on cycling, which makes them a promising anode material for high-power lithium ion batteries. This study of surfactant-templated electrode arrays with thin wall and small pore diameter to find high capacity and long cycling life is of significant importance for the design of lithium-ion batteries with superior electrochemical performance and provide further examples of the advantages of nanostructured materials in the field of lithium ion batteries.

6.2. Future Work

In chapter 2, we have shown the effect of aging temperature, surface modification and film thickness over the development of o-HCP nanostructure development. However, the effect of humidity was not yet investigated. After deposition of the sol on glass substrates, the relative humidity (RH) of the environment in which these films are aged have been shown to play a vital role in mesostructure development. A highly humid

environment is important during the aging of these films to slow down the evaporation of the water from the films (to provide sufficient time for reorientation and ordering of the mesostructure) and also to control the mesoscopic ordering of the surfactant^{56, 58, 67-69}. Crepaldi et al.⁵¹ explained that humidity during aging determines the water content in the coatings. This water content determines the fluidity of deposited coating and the possibility of occurrence of the disorder-to-order transition. The continuous exchange of water between the film and the atmosphere during the first hour of aging after deposition allows the condensation of the organic framework around micellar aggregates and controls the final mesophase. Jang et al.⁶⁶ studied the humidity of the curing environment on the mesostructure of titania films and suggested humidity of ~ 80% RH values to synthesize highly organized mesoporous titania films. In our study, we have used a slightly higher humidity (~ 94%) as humidity is thought to prevent rapid condensation of the inorganic precursor. However, the limits and effects of RH are not completely known for the development of the o-HCP structure. In future, it will be of interest to carry out in-situ GISAXS with varying RH (45% and 90% RH) for F127-templated TiO₂ films cast onto modified glass (the goal being to promote o-HCP orientation) and onto plain glass (to promote parallel HCP structure) to observe the importance and role of this parameter in the formation of the vertically aligned pore structure.

In chapter 6, we have developed thicker films with o-HCP nanostructure using a layer-by-layer approach for applications requiring more TiO₂, and scaled the film thickness up to 1000 nm. To fully utilize the materials, the pores need to be accessible across the film. The pore accessibility and vertical pore orientation has been confirmed by SEM and XRD. However, electrochemistry indicates that there may be mass transport limitations in

cylindrical channels of such large aspect ratio and small diameter (9 nm diameter \times 1000 nm long). In-situ GISAXS studies can shine more light onto the development of nanostructure using the layer-by-layer technique. Furthermore, in-situ GISAXS with varying incident angle should be performed to determine if the pores are orthogonally oriented throughout the thickness of multilayer films. GISAXS studies as a function of layer number are recommended to better understand the nature of the epitaxial alignment process. Expanding pore size as a way to enhance transport of electrolytes is also recommended in future studies.

In chapter 3, the hole conducting polymer poly(3-hexyl thiophene) was incorporated into orthogonally aligned cylindrical nanopores of titania in order to fabricate inorganic-organic hybrid solar cells. However, when measured, the power conversion efficiency was very poor as compared to previous reports. The main reason for low power conversion efficiency might be poor absorption of photons in the visible region and recombination of charge carriers before reaching the respective electrodes. Thus, there is need for some interfacial modification for these titania-P3HT system. One possible modification titania films is with dye N719 before coating of P3HT, which improves chemical incompatibility, accelerates charge separation and reduces charge recombination³⁶⁸. Previous work reported that N719 dye improves photovoltaic performance of P3HT:TiO₂ solar cells synthesized using titania nanorods³⁶⁸, nanotubes³⁶⁹⁻³⁷⁰ and nanofibers³⁷¹⁻³⁷². Modification of surfaces with this dye has been reported to enhance performance of the devices by improving carrier life time³⁷³ and reducing defects³⁷² at the interface of TiO₂/P3HT. It has been shown that interface modification by N719 dye can promote exciton dissociation between the two components, reduce

interfacial charger combination, and form a dipole layer at the interface that modulated the interface energy level to enhance the open circuit voltage and short circuit current³⁷⁴. The surface modification of titania by N719 and the resultant effect on device performance has also been reported using other window layers like ZnO³⁷⁵ and CdS³⁷⁴. N719 dye can also act as a bridge enhancing the charge transport between the two components as shown in the energy band diagram in Figure 6.1. It can possibly mediate charge transfer unidirectional charge transport from P3HT to TiO₂ resulting in more efficient charge separation due to cascading energy levels³⁷⁴.

In chapter 4, we fabricated highly efficient nanoporous n-TiO₂/p-CdTe heterojunction solar cells. Even though the efficiency observed here is the highest ever reported for a CdTe-titania solar cell, it is still lower than the conventional CdS-CdTe solar cells. The biggest improvement that can still be done is in the design and execution of the top contact, which affects fill factor and thus power conversion efficiency. The fill factor reported here is only 0.4 which is very low in comparison with what is possible in solar cells. In previous works, many investigations of back contact and top contact materials including Cu/Au^{315, 319}, Cu doped ZnTe³²⁹⁻³³⁰ with Au or Ni metallization, Cu/Mo³³¹ or just Au³³² has already been done. Fill factors in excess of 0.7 can be achieved using these contacts. Even though all the studies have been done in case of CdS/CdTe solar cells, they can be effectively applied to TiO₂/CdTe solar cells. If the fill factor can be improved, an efficiency of as much as 9.7% is anticipated with no further engineering of the titania material. Also optimizing the thickness of CdTe will be crucial in order to reduce series resistance. Some of these approaches to improve power conversion efficiency in

TiO₂/CdTe heterojunctions, will be recommended as subjects of investigation in the near future.

As shown in chapter 5, titania thin films with o-HCP nanopores have great potential in lithium ion batteries. Though TiO₂ has several advantages shown in that chapter, one of the major drawbacks of TiO₂ as a negative electrode in LIBs is its low capacity which is 330 mAh/g theoretically³⁷⁶. The capacity of TiO₂ can be increased by making a hybrid of TiO₂ and high capacity anode materials. Silicon and tin are known to be high-capacity materials but on their own, they are prone to damage and loss of capacity upon cycling. Silicon has a theoretical capacity of 4200 mAh/g. The major drawback of Si for anodic use in LIBs is the capacity loss due to the volume expansion during lithiation/delithiation process³⁷⁷. Making a composite of TiO₂ and Si can be a viable strategy to overcome the limitations of Si of short life cycle and TiO₂ of low capacity. Several studies have been performed to make a composite of Si and TiO₂ to control the expansion of Si³⁷⁸⁻³⁸⁰. Recently, Lotfabad et al. reported the preparation of Si nanotubes surrounded by a thin layer of TiO₂³⁸⁰. The capacity of 1.5 nm thick TiO₂ coated Si nanotubes was 1700 mAh/g after 200 cycles whereas Si nanotubes alone showed 1287 mAh/g. Though, the TiO₂/Si nanotubes composite showed relatively lower structural damage compared to pure Si nanotubes, about 7% degradation took place in this composite in between 100 – 200 cycles. The hypothesis suggested to be explored is that the expansion of the Si can be controlled even better by depositing the Si into the pores of TiO₂ thin films. Our ordered mesoporous TiO₂ thin films can accommodate Si in the pores of 8 nm diameter. The pore wall of 5-6 nm is expected to withstand the stress generated by Si during lithiation/delithiation. The

extended portion of the Si may come out of the pores but it will be prevented from fracture and the loss of initial capacity.

Tin (Sn) is another high capacity LIBs material³⁸¹⁻³⁸⁵. The theoretical capacity of Sn is 990 mAh/g³⁸³. Sn like Si has the low cycling performance due to the colossal volume changes during the lithiation/delithiation process, leading to severe mechanical stress and eventually failure. As already mentioned, TiO₂ has very small volume expansion during lithiation/delithiation. Sn/ TiO₂ composite can be made to address the issues of capacity loss of Sn after short cycle life. Zhao et al. prepared LIBs capacity on cycling for lithiation/delithiation was found to be 312 mAh/g after 50 cycles which is higher than that for individual Sn and TiO₂ nanotubes³⁸⁶. Wei et al. reported the synthesis of Sn/ TiO₂ composites by electroless deposition of Sn nanoparticles in the interspace of rutile TiO₂ nanowires prepared by solvothermal procedure³⁸⁷. The Sn nanoparticles decorated TiO₂ nanowires showed improvement in the capacity and cycling performance and the capacity retention is 62.3 % after 300 cycles. However, instead of depositing Sn nanoparticles, the capacity and cyclic performance can be improved by continuous and homogeneous Sn deposition in the pores of mesoporous TiO₂ thin film. Mesoporous TiO₂ thin films with o-HCP microstructure can accommodate Sn in the pores of 8 nm diameter. The pore wall of 5-6 nm is expected to withstand the stress generated by Sn during lithiation/delithiation. The extended portion of the Sn may come out of the pores but it will prevent fracture and eventually avoid the loss of initial capacity. Sn can be deposited using various methods such as chemical bath deposition and electrodeposition^{382, 387-389}. Electrodeposition method might provide a better control on depositing Sn in the pores of mesoporous TiO₂ thin films. If tin is incorporated into the pores of the titania films (~50% porosity) and all materials

retain their pure-component capacities, a capacity as high as ~725 mAh/g is possible for a composite film. This would approximately double the specific capacity of the negative electrode, while allowing for safer operation due to the low operating voltage of TiO₂ (1.7 V). Figure 6.2 shows the schematics for incorporation of Sn/Si into the nanopores of titania for lithium ion battery applications.

One final new direction to take this work would be to investigate the interactions and applications of dopamine at the titania surface. Dopamine (DA) is an important neurotransmitter in mammalian central nervous systems. DA (Figure 6.3) is an enediol ligand and has a large affinity for under-coordinated surface sites, restoring the coordination of Ti atoms to the octahedral geometry and forming ligand-to-metal charge-transfer complexes³⁹⁰. Formation of these charge-transfer complexes on TiO₂ has been shown to enhance interfacial electron-transfer rates³⁹¹⁻³⁹². In addition, because of its large band gap ($E_g = 3.2$ eV), TiO₂ absorbs mainly UV photons. Also the derivatives of dopamine can sensitize TiO₂ nanoparticles to improve the absorption in the visible region making them useful for photocatalysis and solar energy conversion³⁹³. DA is one of the major sources of reactive oxygen species (ROS)³⁹⁴. When DA is exposed to the daylight, it is oxidized very easily due to its chemical instability. DA contains an unstable catechol moiety with respect to its molecular structure; it can oxidize spontaneously in vitro, free radicals and quinones³⁹⁵⁻³⁹⁷. In addition, in the human substantia nigra, the oxidation products of DA may polymerize to form neuromelanin which may also be a highly cytotoxic substance³⁹⁸. The encapsulation of the DA into the nanoporous non-toxic TiO₂ matrix has been found to retard its oxidation process in order to maintain the stability of the drug³⁹⁹. It is also a good molecule to introduce amine functional groups into titania. It has a

benzenediol group (which binds strongly to titanium through chelation) and an amine, so it may be perfect. In future, it is recommended to develop dopamine-nanoporous titania composites and characterize these films for structural and functional properties by spectroscopy and electrochemical measurements. There might be three future directions for DA-TiO₂ composite films: (1) Amine functionalization of titania films, (2) The effect of TiO₂ matrix to reduce DA oxidation in visible light and (3) To improve light absorptions of TiO₂ in the visible region.

DA will be encapsulated into the TiO₂ matrix using simple sol-gel method accompanied with evaporation-induced self-assembly (EISA) described in chapters 1-5. After the preparation of TiO₂ sol, the DA will be added in the final stage and the sol will be stirred for 15 min at room temperature under darkness³⁹⁹. All the other steps will be the same for EISA as described in chapters 1-5. The incorporation of DA into TiO₂ matrix, the introduction of amine functional groups into titania and effect of TiO₂ matrix over DA oxidation will be studied using FTIR spectroscopy. In Appendix A, we have successfully functionalized TiO₂ with amine functional groups using 3-aminopropyltriethoxysilane (APTS). The amine functionalization of TiO₂ will be compared for DA and APTS. The amine functionalized DA sensitized TiO₂ will be used to develop nafion-titania composite films for potential applications in solid state batteries as already explained in appendix A. The effect of DA over the visible light absorption of TiO₂ will be studied using UV-Vis spectroscopy and photoconductivity measurements. Once we confirm that DA improves visible light absorption of TiO₂, these composite films will be effectively used for photocatalysis and solar energy conversion applications.

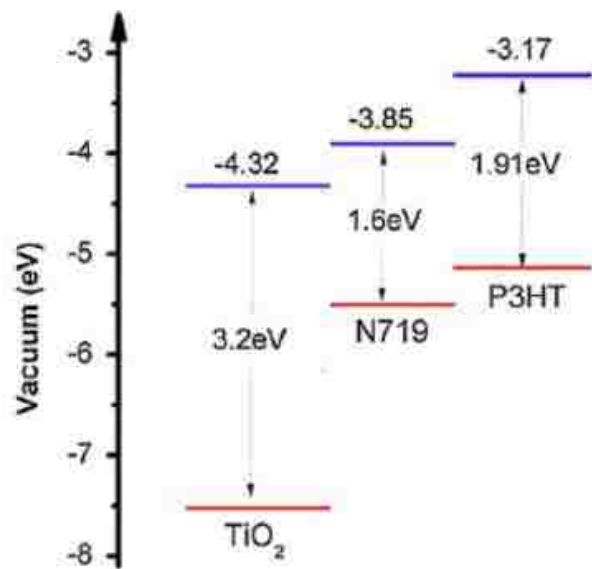


Figure 6.1. Energy level diagram for TiO₂+N719+P3HT system (adapted from Xia et al.³⁶⁸)

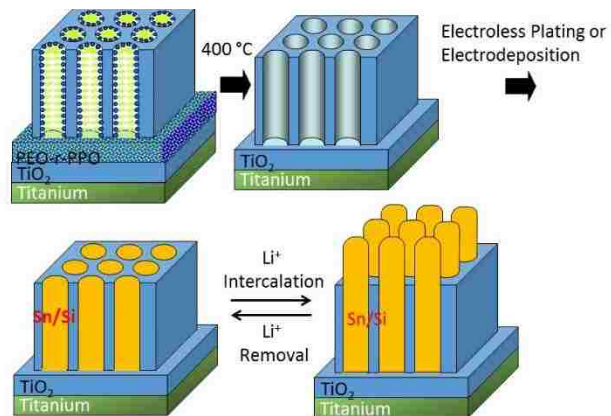


Figure 6.2. Schematics for incorporation of Sn/Si into the nanopores of titania for lithium ion battery applications.

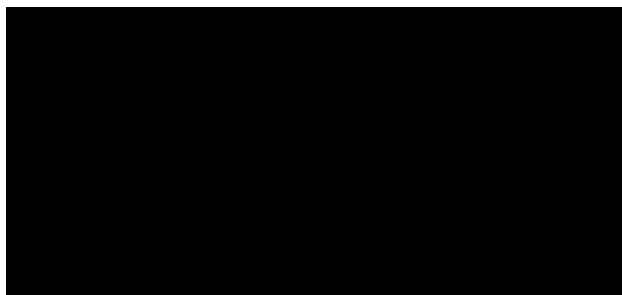


Figure 6.3. Chemical structure of dopamine

Copyright © Suraj R. Nagpure 2016

APPENDIX A Nafion-Titania Polymer Hybrids for Solid State Batteries

A.1. Introduction

In recent years, lithium-ion batteries have been intensively studied in order to meet the requirements of ever-growing global energy demand⁴⁰⁰⁻⁴⁰⁹. Most present commercial lithium-ion batteries use liquid electrolytes. Compared with the liquid electrolytes, polymer electrolytes are particularly attractive because they can provide flexible, compact, laminated solid-state structures free from leaks and available in different geometries⁴⁰⁰. However, because of their low ionic conductivities at room temperature and poor electrochemical stability, solid polymer electrolytes have not been widely used in commercial lithium-ion batteries⁴¹⁰. In principle, the ideal polymer electrolytes for lithium-ion batteries must satisfy several basic requirements: (i) ionic conductivity higher than 10^{-4} S cm⁻¹ at room temperature, (ii) good thermal, chemical and mechanical stability, (iii) a lithium transport number close to unity, and (iv) compatibility with the electrodes⁴⁰⁸. However, until now there is no “perfect” polymer electrolytes satisfying all of the demands of the ideal polymer electrolytes mentioned above.

The use of lithiated perfluorinated sulfonic ion-exchange membranes might be a promising approach to the development of future polymer electrolytes⁴¹¹. The perfluorinated backbone provides high chemical and thermal stability while the charged species are bound to the side chains of the polymer. Under applied electric field and an appropriate solvent, these free charges are forced to migrate in the direction of the electric field. Since the anions are bound to the polymer, the only mobile species are Li⁺ ions, resulting in a transference number of unity. More importantly, these polymers do not require the addition of lithium salts into the electrolyte, which is advantageous because the

salts used in lithium-ion batteries are relatively expensive and often both thermally and hydrolytically unstable (LiPF_6 , LiBF_4 , LiAsF_6 , etc.). Therefore, these perfluorinated sulfonic ion-exchange membranes can serve as both a separator and an electrolyte in lithium-ion batteries. However, there has been little work on the application of perfluoro-ionomers in lithium batteries due to low conductivities observed in nonaqueous media⁴¹². Thus, before lithiation of nafion membranes is approached, it is important to improve ionic conductivity and proton conductivity of Nafion membranes.

One interesting approach for modification of Nafion membrane is to impregnate nanostructured hygroscopic metal oxide or ceramic materials in the membrane. It has been shown in the past that ionic conductivity of polymer electrolytes can be significantly improved by adding ceramic fillers⁴¹⁰. Composite or nano-composite polymer electrolytes, in which inorganic (ceramic) particles are introduced into a polymer electrolyte have been studied previously to be useful as efficient polymer electrolyte system⁴¹³⁻⁴¹⁵. Among the nanostructured hygroscopic inorganic materials applied in polymer electrolyte membranes, nanostructured titania is of special interest because of its large surface area and unique physicochemical properties⁴¹⁶⁻⁴¹⁹. Already shown in Chapter 5, titania itself of great interest as an electrode material on its own, which perhaps can be incorporated into an all-solid-state battery architecture. The vertically oriented cylindrical mesoporous channel would be a facilitated path for Li^+ ion transfer; and small TiO_2 grains in the matrix would effectively reduce the diffusion length for Li^+ ion insertion/extraction. The small pores will provide higher surface area for lithium ion insertion, and the small wall thickness will reduce the Li^+ diffusion length. So, the idea developed here is to use nanostructured titania with o-HCP structure as an anode along with lithiated nafion in all-solid-state battery

architecture. However, the incompatibility between Nafion and titania could induce the defect and cracks of the formed composite membrane, which might limit charge carrier transfer at the interface and affect ion conductivity.

This has led our attention to surface modification of titania film for enhancing their compatibility with ionically conductive polymers⁴¹⁹. In this study, surface modification of titania with amine groups has been explored enhance the interfacial compatability between Nafion and titania, with the hypothesis that the positive charge of amines will improve the strength of the interfacial interaction and lower mass transfer resistance. In addition, amino groups grafted onto surfaces undergo a similar behavior toward proton to that of water, i.e. they can accept proton to form NH_3^+ and the formed NH_3^+ can further act as proton donor during the proton transport process. Thus, the existence of amino groups can enhance the proton conduction at relatively low water content.

A.2. Experimental Section

For this study, titania films were prepared onto conductive titanium foil substrates. Titania films with vertically oriented 2D-HCP cylindrical nanopores and nonporous titania films were prepared the same way as reported in chapter 4. Titania thin films on titanium foil were functionalized with 3-aminopropyltriethoxysilane, APTS (Sigma-Aldrich, 99%). A 1 vol% solution of APTS was prepared in isopropyl alcohol (Fisher Scientific, HPLC grade) and titania films were immersed into the solution for 1 hour with heating at 100 °C using a water bath. The excess APTS on the surface of titania was removed by rinsing with isopropyl alcohol. Nafion films were coated onto functionalized titania films and bare silicon wafers by spin coating 5 wt% Nafion[®] perfluorinated resin solution (Sigma-Aldrich, 5 wt. % in lower aliphatic alcohols and water, contains 15-20% water) at 1000

rpm for 20 secs. Gold was used as the top contact by depositing a 60 nm thick layer onto the Nafion layer using RF sputtering.

Fourier transform infrared (FTIR) spectroscopy was performed based on the principle of Reflection-Absorption Infrared Spectroscopy (RAIRS). An Agilent 680 with an MCT detector was employed, with a universal sampling accessory for grazing angle analysis of thin coatings on metal surfaces. Spectra were collected using 100 scans using clean titanium foil as a background.

In order to perform interfacial characterization and to calculate ionic conductivity, a conventional AC impedance method was used with two electrodes. The impedance was measured with a Solartron 1255B Frequency Response Analyzer interfaced with an Electrochemical Interface Solartron 1287 operating in the frequency range of 100 Hz–100 KHz. Two blocking stainless steel (SS) electrodes were employed. After collecting the data, an equivalent circuit model was fitted to the data using the software Zview to calculate parameters such as mass transfer resistance and mass transfer capacitance.

A.3. Results and Discussion

Figure A1 shows RAIRS spectra for a mesoporous titania thin film and APTS functionalized titania thin film. For bare mesoporous titania thin film, a peak is observed around 824 cm^{-1} which can be assigned to Ti-O vibrations⁴²⁰. However, this peak is absent after APTS functionalization, we might indicate that Ti-O bonds are actively reacting with amines. After amine functionalization, can clearly see peaks for different functional groups. The peak at 1123 cm^{-1} is attributed to Si-O twisting⁴²¹. In general, the N-H bending band appears in the region of $1500\text{-}1600\text{ cm}^{-1}$ (to be precise at 1560 cm^{-1})⁴²². The presence of the band around 1560 cm^{-1} indicate that amine groups are present on the surface of APTS

modified titania films. Also a peak is observed for N-H stretching at around 3434 cm^{-1} . Also, for APTS modified titania films, a peak is observed around 1620 cm^{-1} . According to the literature, a band around 1625 cm^{-1} appears due to the asymmetric deformation of NH_3^+ , that is hydrogen bonded to the unreacted surface hydroxyl groups, forming $\text{TiO}^- \text{-NH}_3^+$ zwitterions^{419, 423}. These spectra clearly indicate that amine functional groups are present on the surface. Scheme A1 shows a possible mechanism for amine functionalization of titania thin films using APTS.

After successfully functionalizing titania films with amines, we coated these films with Nafion to develop polymer/titania hybrid composite films. Nafion films were coated onto functionalized titania films and bare silicon wafers by spin a coating 5 wt% Nafion[®] perfluorinated resin solution (Sigma-Aldrich, 5 wt. % in lower aliphatic alcohols and water, contains 15-20% water) at 1000 rpm for 20 secs. Figure A2 shows RAIRS spectra after Nafion coating. We can clearly see from figure A2a that Nafion coated onto unfunctionalized titania does not change the chemical structure of titania as there is no change in peak positions as compared to a pure Nafion film. For pure Nafion and Nafion coated onto unfunctionalized titania, peaks are observed at 980 cm^{-1} (C-O-C sym stretch), 1060 cm^{-1} (SO_3^- Sym stretch), 1164 cm^{-1} (C-F Sym Stretch), 1272 cm^{-1} (SO_3^- Asymmetric stretch) and 1316 cm^{-1} (CF_3 Asymmetric stretch).

However, when Nafion is coated onto amine functionalized nanoporous titania, changes in peak positions and peak intensity can be seen, as seen in Figures A2b and A2c. Figure A2b shows that the intensity of the N-H bending and N-H stretching bands reduce significantly after depositing a Nafion layer, while the intensity of the C-H band remains the same. This indicates that amine groups on the surface of titania form strong hydrogen

or ionic bonds with the sulfonate functional groups of Nafion. For Nafion, the peak position for C-F symmetric stretching was observed to shift from 1164 to 1150 cm^{-1} , and for SO_3^- Sym stretching from 1060 to 1053 cm^{-1} after coating onto amine-functionalized titania. The intensity of these peaks significantly decreases, which is consistent with a strong interaction with amine functional groups.

In order to estimate the kinetic parameters of the electrode process, AC impedance tests were performed. Fig. A3 shows Nyquist plots for different Nafion-containing films. The Randles equivalent circuit model, as shown in the inset in Fig. A3, was used to fit the experimental data⁴²⁴. In this model, R_1 represents the bulk resistance of the electrolyte, separator and electrode; R_2 is related to the charge transfer resistance at the Nafion-titania interface; and CPE is a constant phase element representing the interfacial capacitance of the Nafion-titania interface. Table A1 gives values for these parameter obtained by fitting the Randles model using the software Zview. The value of mass transfer resistance, R_2 , is especially important because it provides insight into the interface between materials. A lower R_2 indicates a better interface in terms of mass transfer and conductivity. In order to see the effect of the porous titania layer, AC impedance spectroscopy was performed for Nafion coated onto amine-functionalized (nonporous) planar titania (Fig. A3a) and Nafion coated onto amine-functionalized nanoporous titania (Fig. 3b). As indicated in Table A1, R_2 is one order of magnitude less for nanoporous titania, indicating a better interface for charge transfer. In order to see the effect of amine functionalization and the enhancement in interfacial compatability that it provides, AC impedance spectroscopy was also performed for Nafion coated onto nonfunctionalized nanoporous titania (Fig. A3.3). R_2 is found to be one order of magnitude less for amine functionalized nanoporous titania than

nonfunctionalized nanoporous titania, which again indicates a better interface after amine functionalization. These results indicate that the interface between titania and nafion can be improved using a combination of nanoscale structuring using surfactant-templated pores, and amine functionalization to provide more intimate contact between the sulfonate groups of Nafion and the titania surface. The next step in this research will be to lithiate these Nafion-titania polymer hybrids to more completely understand the potential to apply them in solid state lithium ion batteries.

A.4. Conclusion

In this work, we aimed at improving interfacial compatibility between Nafion and nanoporous titania using amine functionalization. Amine functional groups were successfully grafted onto the surface of titania using 3-aminopropyltriethoxysilane (APTS) as indicated by FTIR spectroscopy. Strong interactions between Nafion and functionalized titania were indicated by reductions in peak intensity for both Nafion and amine groups. AC spectroscopy showed that nanoporous titania exhibits reduced mass transfer resistance at the interface with Nafion, which is consistent with greater area for interaction between the materials. The enhancement in interaction with Nafion induced by amine functionalization is also shown to translate to reduced mass transfer resistance by an order of magnitude, to $3.93 \times 10^{-6} \Omega$, at the nanoporous titania / Nafion interface.

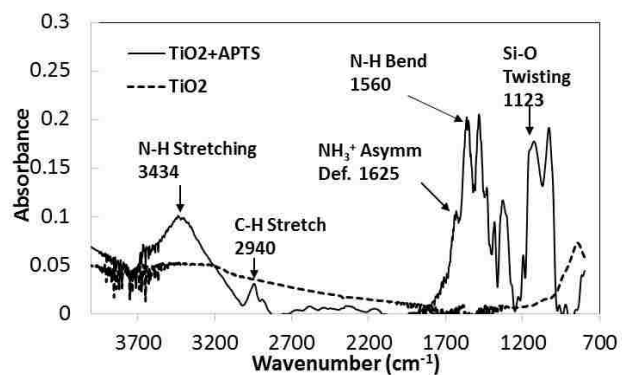


Figure A.1. Reflection Absorption Infrared (RAIRS) spectra for mesoporous titania thin film and APTS functionalized titania thin film

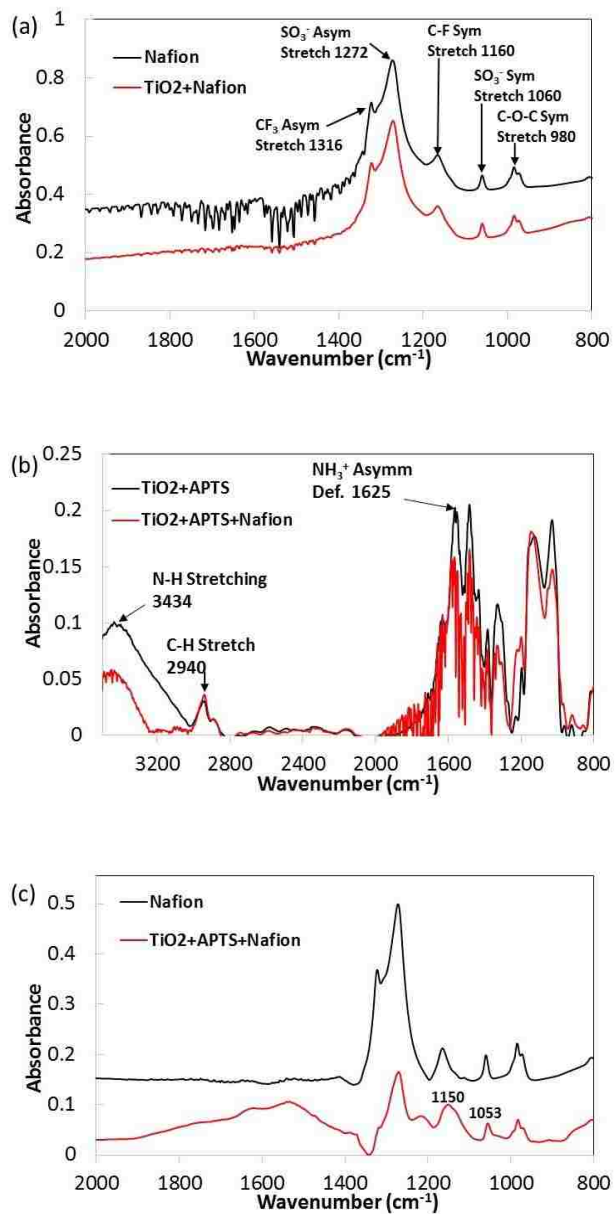


Figure A.2. Reflection Absorption Infra-red spectra for the indicated samples.

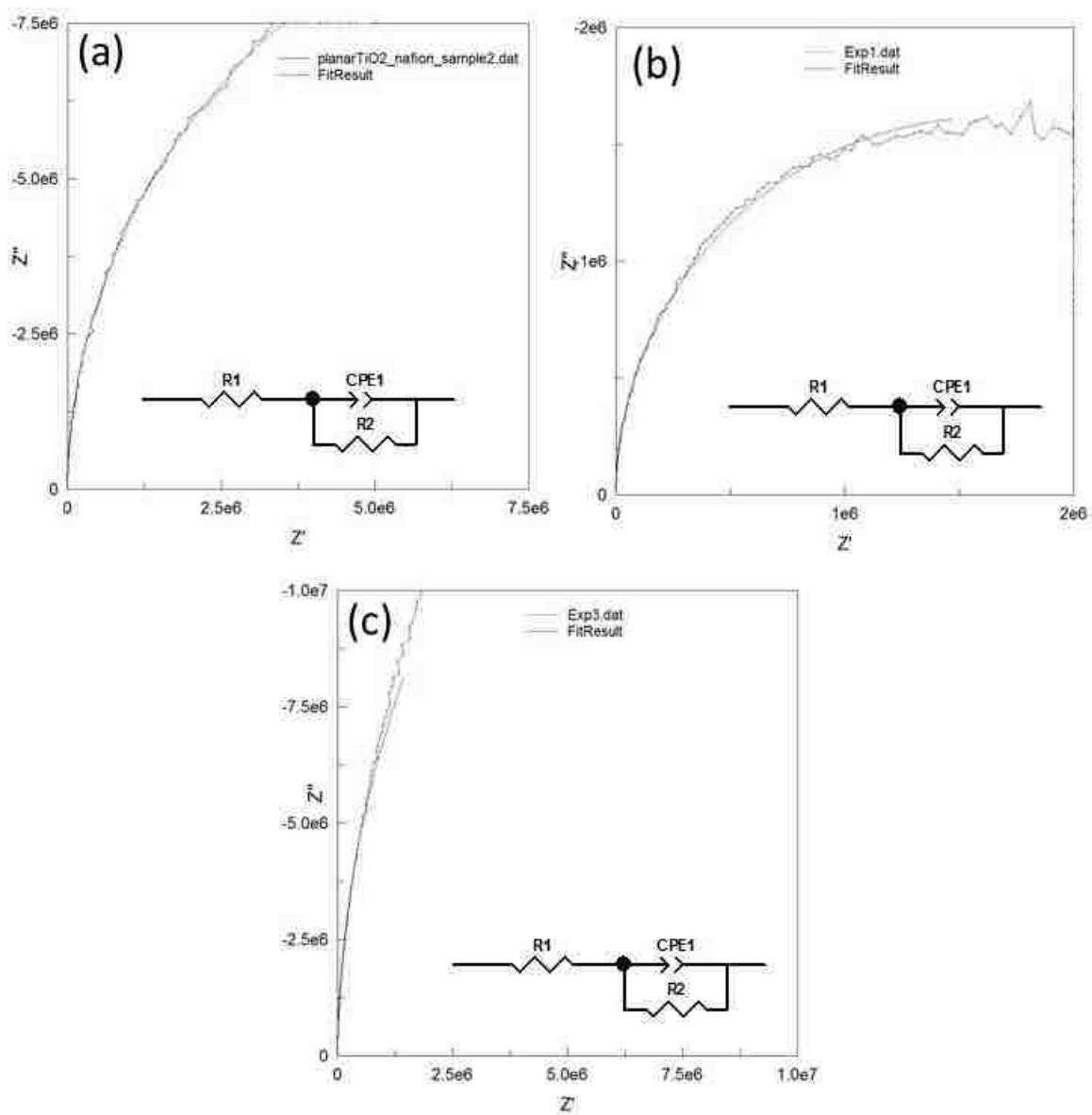
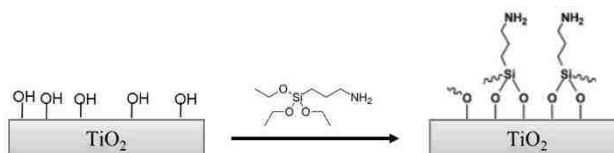


Figure A.3. AC impedance spectrum and equivalent circuit model for (a) Nafion and amine functionalized nonporous titania (b) Nafion and amine functionalized nanoporous titania (c) Nafion and nonfunctionalized nanoporous titania.

Table A1. Mass transfer capacitance (CPE1) and mass transfer resistance (R_2) for different films obtained by equivalent circuit model fitting to AC impedance spectroscopy data shown in Figure A3

Sample	CPE1(F)	$R_2(\Omega)$
Nanoporous Titania + APTS + Nafion	1.9E-10	3.93E6
Nanoporous Titania + Nafion	1.54E-10	3.9E7
Planar Titania + APTS + Nafion	1.81E-10	4.58E7



Scheme A1. Amine Functionalization of Titania Thin Films using APTS

Copyright © Suraj R. Nagpure 2016

APPENDIX B Electrochemical Impedance Spectroscopy (EIS) Characterization of Titania Films with Controlled Pore Orientation and Incorporation of Lipid Bilayers into the Nanopores of Titania

B.1. Introduction

As the barriers between cells and external environment, biological membranes exhibit highly selective permeability that is maintained by their main component, amphipathic lipid molecules. Supported lipid bilayers on mesoporous materials material offer biomimetic approaches to highly selective separations in dilute aqueous systems. The pore walls of mesoporous materials provide stability to the membrane and the pores are hypothesized to result in a desirable lipid environment⁴²⁵. The properties of mesoporous materials, such as pore size, pore geometry, and surface chemistry, can be tailored, which allows us to precisely design the support for a target application⁴²⁶. Our previous investigation of lipid bilayer interactions with mesoporous silica particles demonstrated both lipid bilayer enveloping and pore filling by the lipids as a function of pore size through vesicle fusion and evaporation deposition, respectively⁴²⁷. Similar to silica, titania (TiO₂) is also a highly biocompatible material⁸ which makes it a popular choice in medical implants⁴²⁸. Also the high refractive index of titania makes it ideal for optics based sensing applications⁴²⁸.

Recent work has developed strategies to form planar lipid bilayers on titanium oxide by using positively or negatively charged vesicles, suggesting the importance of electrostatic interactions⁴²⁹⁻⁴³⁰. TiO₂ can tightly adsorb PC liposomes because of the lipid phosphate interacting directly with the TiO₂ surface, forming a chemical bonds via bridging oxygens⁴³¹. This interaction is much stronger compared to that with silica, where hydrogen bonding or electrostatic interactions with quaternary ammonium components of

phosphocholine headgroups dictates the interaction. Supported lipid bilayers on TiO₂ represents an attractive platform for a number of applications including medical implants⁴³² and biosensors⁴³³. However, the fundamental characterization of the substrate's interaction with lipid vesicles has only recently received attention⁴³³.

Here, Electrochemical Impedance Spectroscopy (EIS) has been used to characterize porous titania films and incorporated lipid bilayers into the nanopores of titania. This methodology is based on complex impedance measurements at a wide range of frequencies. Important parameters to analyze using EIS are the capacitance and resistance of the membrane. Previously, this technique has been used to characterize self-assembled nanoporous silica thin films⁴³⁴ and to monitor the bilayer incorporation of a ligand gated ion channel protein and the modulation of its channel activity by the selective binding of an antibody⁴³⁵⁻⁴³⁶. For these tests, a periodic voltage signal of variable frequency is applied to the electrodes. The absolute value of the current response of the system is analyzed in terms of the complex impedance and the phase shift. The theoretical analysis of EIS data by fitting to a model representing an equivalent electrical circuit allows the understanding of processes associated with the interface between biomaterials and functionalized electrodes⁴³⁷. Previously Lundgren et al.⁴³⁸ studied the formation of bilayers made from lipid POPC on SiO₂ using EIS. In this preliminary study, we will mainly show the effect of porosity, pore orientation and film thickness of titania thin films with o-HCP cylindrical nanopores affect ion mass transport and lipid bilayer formation.

B.2. Experimental Section

For this study, titania films were deposited onto conductive FTO glass substrate which acts as the working electrode. Multilayered titania films with vertically oriented 2D-HCP cylindrical nanopores were prepared the same way as reported in chapter 5. A lipid bilayer solution was prepared by our collaborator Shanshan Zhou from Dr. Barbara Knutson's group at the University of Kentucky. 10 mg of dipalmitoylphosphatidylcholine (DPPC) was dissolved in 1 ml chloroform, then the lipid was blown with air for 1 hour and was further dried under vacuum at room temperature for at least 2 hours. The dried lipid was then rehydrated in 1 mL PBS to form multilamellar vesicles. The resulting mixture was then extruded at 45°C through a polycarbonate filter with 200 nm diameter pores 21 times, which produces small unilamellar vesicles with a mean diameter of 200 nm. Small unilamellar vesicles of DPPC in PBS prepared through extrusion were placed in contact with mesoporous titania films for 15 min, followed by rinsing with PBS to wash off excess lipid.

Electrochemical Impedance Spectroscopy (EIS) was performed according to the procedure described by Wei et al.⁴³⁴. A standard three-electrode cell connected to a potentiostat was used for all electrochemical experiments. Samples of calcined nanoporous titania films with vertically oriented pores (up to 4 layers) or parallel pores on FTO were used as the working electrode, with a platinum counter electrode and an Ag/AgCl reference electrode. All potentials reported are with respect to the Ag/AgCl reference electrode reaction. The electrolyte was composed of 1 mM 1,1'-ferrocenedimethanol (FDM) redox couple with 1 M KCl and 0.01 M HCl supporting electrolyte such that pH~2. The formal reduction potential for the FDM⁺/FDM redox couple ranged from 0.21 to 0.23 V. A dc bias equal to the measured formal potential was first applied. While maintaining this dc bias, a

small amplitude sinusoidal ac bias (10 mV rms) of a given frequency (f) was then applied about this equilibrium potential. The impedance of the cell was measured at each frequency over the range 0.1 Hz to 100 kHz. All experiments were carried out at room temperature. After collecting the data, an equivalent circuit model was fitted to the data using the software *Zview* to calculate parameters such as mass transfer resistance and mass transfer capacitance.

B.3. Results and Discussion

The equivalent circuit model, as shown in the inset in Fig. B1, namely the Randles model was adopted for EIS data analysis⁴²⁴. It depends on three parameters, R_1 represents the bulk resistance of the electrolyte, separator and electrode; R_2 representing the charge transfer resistance; and CPE, a constant phase element which represents the double-layer capacitance of the electrolyte-sample interface. In particular, the value of mass transfer resistance R_2 , as the name suggests, provides insight into behavior at the interface and mass transport. Lower values of R_2 indicate better interface with the electrolyte in terms of mass transfer and ion conductivity. For lipid bilayer formation, this mass transfer resistance is an indicator of bilayer quality. Higher values of R_2 suggest formation of a more defect-free lipid bilayer, which creates a barrier for mass transport across the membrane.

Figure B2 compares AC impedance spectra of a bare FTO electrode, dense titania on FTO electrode, and nanoporous titania with either parallel or vertical mesopore channels on FTO electrodes. The corresponding parameters obtained by equivalent circuit model fitting are shown in Table B1. R_2 is very low for bare FTO electrode, consistent with direct contact with the electrolyte. When a dense layer of titania is deposited onto FTO, R_2 increases by over an order of magnitude, indicating dense titania acts as an effective barrier for mass transfer of FDM. However, R_2 values are reduced for nanoporous titania thin films

as compared to dense titania because of the ability of FDM to be transported through accessible pores. In order to see the effect of pore orientation, EIS spectra were measured for titania thin films with parallel and vertical pore orientation of HCP nanopores. The vertical pore orientation was achieved by using surface modification technique as indicated in chapters 3-5. As indicated in Table B1, mass transfer resistance is lower for vertical pore orientation as compared to parallel pore orientation indicating that vertical pore orientation provides an accessible porous structure for FDM consistent with the expected effect. The mass transfer of films with parallel pores is not as high as a dense TiO₂ layer because of either the presence of defects near the surface that make a fraction of pores accessible, or to FDM transport directly through micropores within the Pluronic-templated structure. Despite this small complication, the EIS measurements provide further confirmation of the hypothesis that pores are oriented vertically after surface modification.

In order to see the effects of the thickness of TiO₂ film with orthogonal 2D hexagonal close packed (o-HCP) cylindrical nanopores on mass transport, EIS was also performed for multilayered titania films. Figure B3 shows AC impedance spectra for multilayered nanoporous titania films on FTO electrodes with up to 4 o-HCP layers. The corresponding parameters obtained by equivalent circuit model fitting are shown in table B2. It was reported in chapter 5 that thick titania films with o-HCP nanopores can be successfully synthesized using evaporation induced self-assembly combined with a layer-by-layer technique. The vertical pore orientation and increased thickness were confirmed using SEM and XRD. With EIS, mass transfer resistance was found to increase somewhat with increasing film thickness, indicating either that porosity is reduced slightly for multilayered films, or that the length of the pore channels decreases the ease with which

FDM can reach the electrode surface. However, a reduction in porosity was indicated in plan-view SEM images reported in chapter 5. The porosity reduced from 51% for one layer to 44% after four layers, which might be because of micelle shrinkage during heating on intermediate layers. However, for all of the multilayered films, R_2 has lower value as compared to films with parallel mesopores, indicating that even though porosity reduced after multilayer film synthesis, most of the pores are oriented vertically providing ordered, an accessible porous structure for mass transport.

Figure B4 shows AC impedance spectra for lipid bilayers deposited onto various titania films on FTO electrodes, and the corresponding parameters obtained by equivalent circuit model fitting are shown in Table B3. The equivalent circuit model used is formally the same as that used for the bare FTO and titania films. It should be noted that now the mass transfer resistance R_2 of the supported system covered with lipid combines contributions to resistance from both the lipid bilayer and the titania coated FTO electrode (calculated previously and shown in Table B1). The lipid film increased the mass transfer resistance quite markedly, showing the formation of a lipid bilayer membrane. However, as compared to previous studies, the resistance is low and capacitance is very high which points towards a fairly leaky membrane^{437, 439-441}. Defects may be present in the bilayers either because DPPC is slow to anneal out imperfections at room temperature due to its high gel/fluid transition temperature, or because the porous support may pin parts of the bilayer in place, which act as sites for defect nucleation. Nonetheless, the increase in mass transfer resistance indicates that nanoporous titania films can be used as substrates for lipid bilayer formation. These are just preliminary experiments towards lipid bilayer formation, and there is room to improve the deposition conditions. In future, many more experiments

need to be performed in order to develop more densely packed lipid bilayers on nanoporous titania thin films. Experiments should be designed to observe the effects of porosity and pore orientation of titania films on lipid bilayer formation. Also, lipid bilayers of varying composition and deposited by different methods can be studied to see which method gives the most densely packed lipid bilayer.

B.4. Conclusion

In this work, preliminary electrochemical impedance spectroscopy (EIS) studies were conducted of ionic mass transport across titania films with controlled pore orientation, and with incorporation of lipid bilayers onto the nanopores of titania. Mass transfer resistance was observed to be reduced for nanoporous titania thin films as compared to dense titania, consistent with their porous nature. Mass transfer resistance was lower for vertically oriented pore channels as compared to parallel pores, which is consistent with previous observations of vertical alignment to give an aligned, ordered accessible porous structure for the electrolyte. Mass transfer resistance increased somewhat for multilayered titania films with o-HCP cylindrical nanopores which is more consistent with a small reduction in porosity due to processing, while retaining continuous pore paths from the electrolyte to the electrode interface. After lipid bilayer incorporation, mass transfer resistance increased indicating the formation of lipid bilayers. However, as compared to previous studies of lipid bilayers on nonporous electrode surfaces, the resistance is low and capacitance is high, which points towards leaky membranes and the presence of defects in the lipid bilayers. There is room to improve the quality of the lipid bilayers by tuning their composition, deposition conditions, and postdeposition processing.

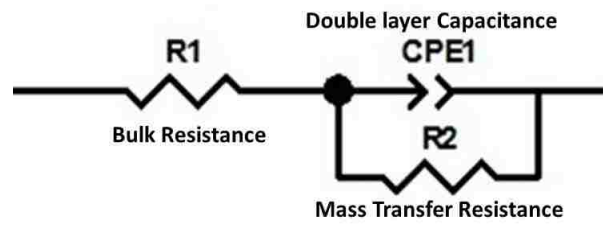


Figure B.1. Randles Equivalent Circuit Model used for fitting EIS data.

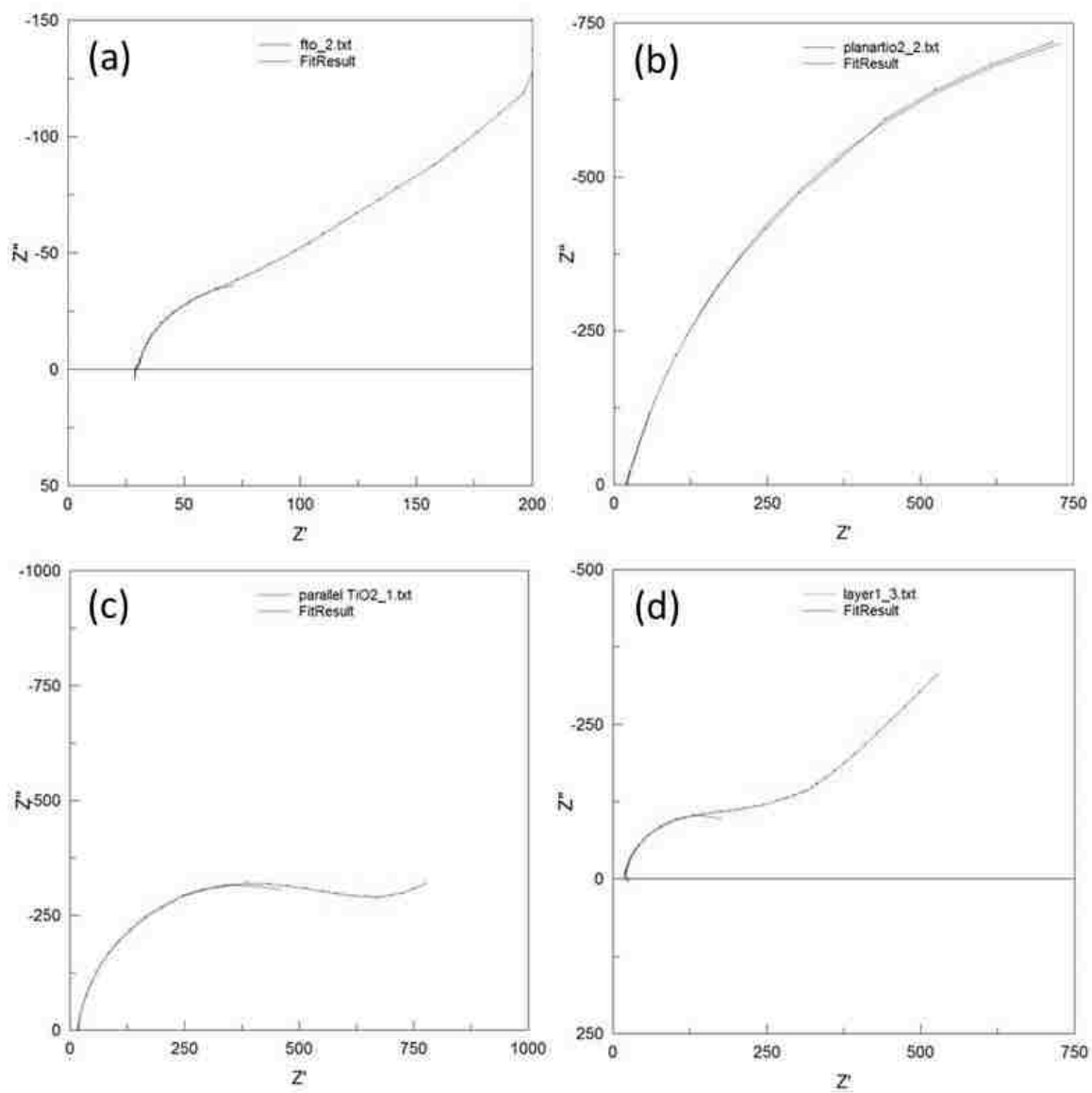


Figure B.2. EIS Spectra for (a) bare FTO electrode (b) dense titania on FTO electrode (c) nanoporous titania with parallel pore orientation on FTO electrode, and (d) vertically oriented 2D-HCP nanoporous titania thin film on FTO electrode.

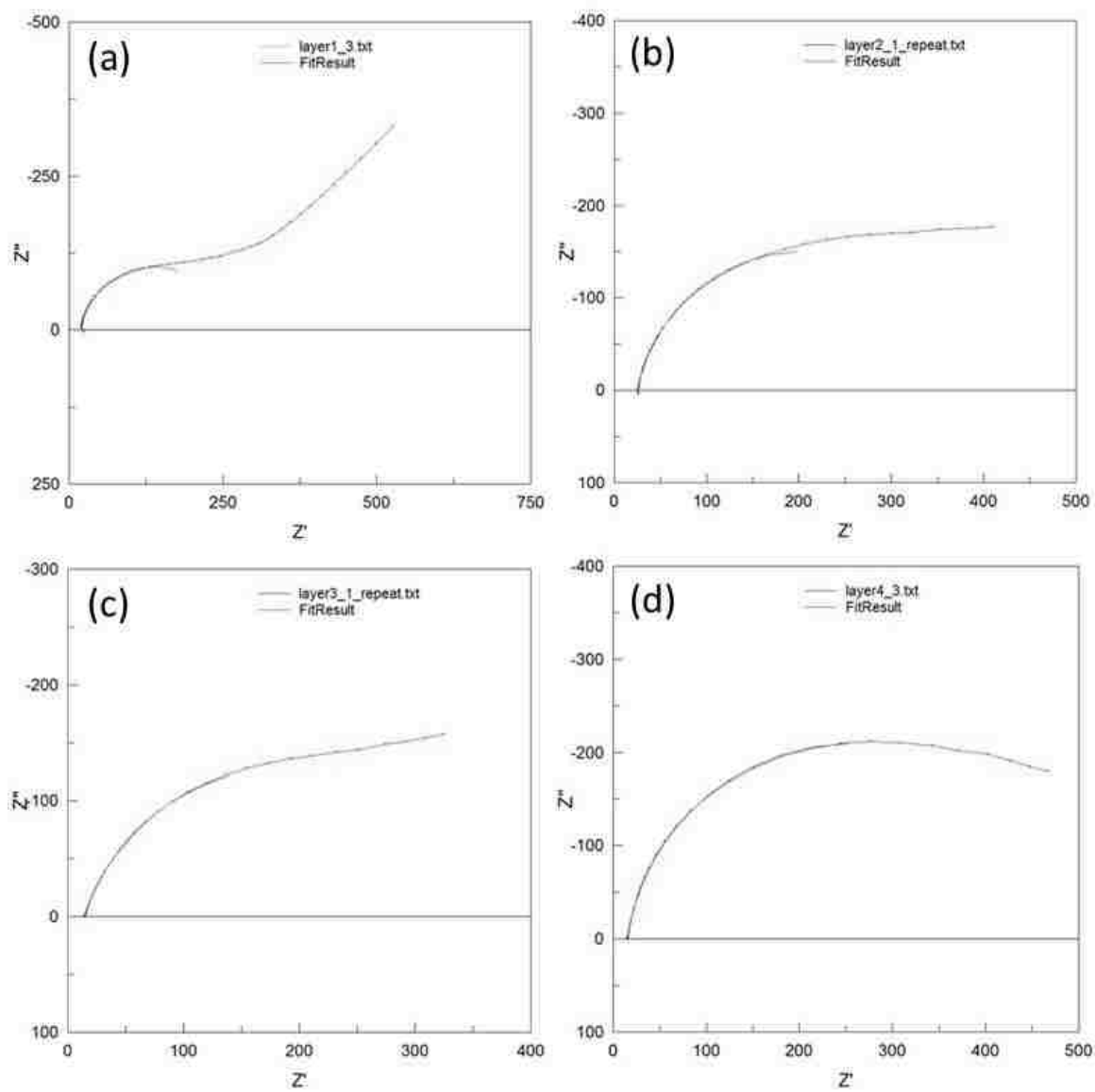


Figure B.3. EIS Spectra for multilayered nanoporous titania films on FTO electrode with o-HCP nanopores after (a) one layer (b) two layers (c) three layers or (d) four layers

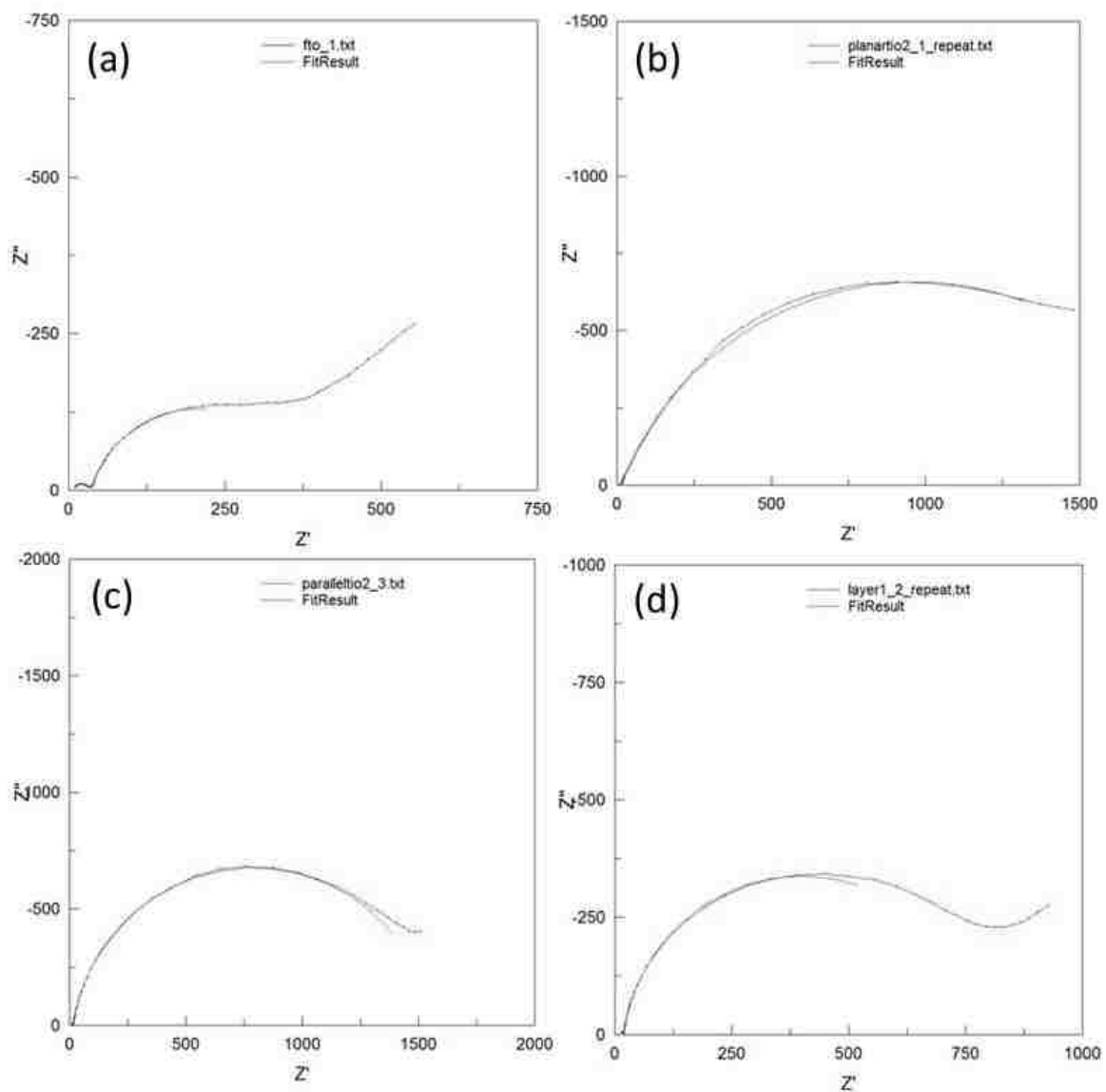


Figure B.4. EIS Spectra for lipid bilayers deposited onto (a) bare FTO electrode (b) dense titania on FTO electrode, (c) nanoporous titania with parallel pore orientation on FTO electrode, and (d) vertically oriented 2D-HCP nanoporous titania thin film on FTO electrode.

Table B.1. Parameters obtained by equivalent circuit model fitting to AC impedance spectroscopy data shown in Figure B2

Sample	R1(Ω)	CPE1(F)	R2(Ω)
Bare FTO	29.75	0.0003	87.71
Dense TiO ₂	17.9	0.000195	1574.5
Nanoporous TiO ₂ with parallel pore orientation	20.43	0.000175	697.3
Nanoporous TiO ₂ with vertical pore orientation	31.74	0.000095	268.1

Table B.2. Parameters obtained by equivalent circuit model fitting to AC impedance spectroscopy data for titania films on FTO electrode with o-HCP nanopores for indicated number of layers as shown in Figure B3

No. of layers	R1(Ω)	CPE1(F)	R2(Ω)
1	31.74	0.000095	268.1
2	21.48	0.000141	392.2
3	13.97	0.00025	344.45
4	15.42	0.000156	432.76

Table B.3. Parameters obtained by equivalent circuit model fitting to AC impedance spectroscopy data for lipid bilayers on different films as shown in Figure B4.

Sample	R1(Ω)	CPE1(F)	R2(Ω)
Lipid Bilayer + Bare FTO	51	0.000124	399.65
Lipid Bilayer + Dense TiO ₂	51.69	0.0002	1804.5
Lipid Bilayer + Nanoporous TiO ₂ with parallel pore orientation	28.48	0.0001	1691
Lipid Bilayer + Nanoporous TiO ₂ with vertical pore orientation	20	0.00008	628.7

APPENDIX C Supporting Information of Chapter 2

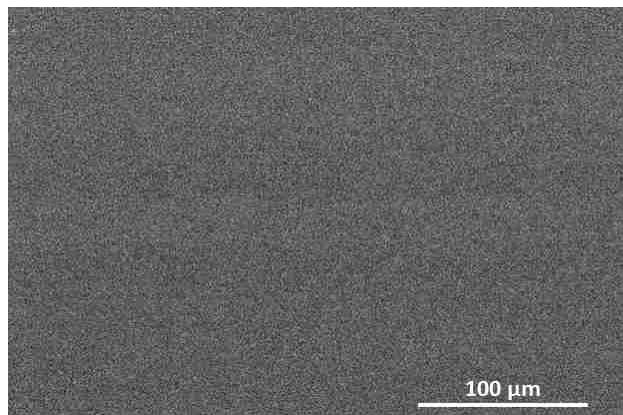


Figure C.1. Low magnification (*350 Magnification) SEM image of titania thin film on modified substrate aged at 4 °C after calcination at 400 °C for 10 minutes using a ramp rate of 25 °C/min. We do not see any cracks or defects indicating that the adhesion of the titania film is not affected by the removal of organic layer after calcination

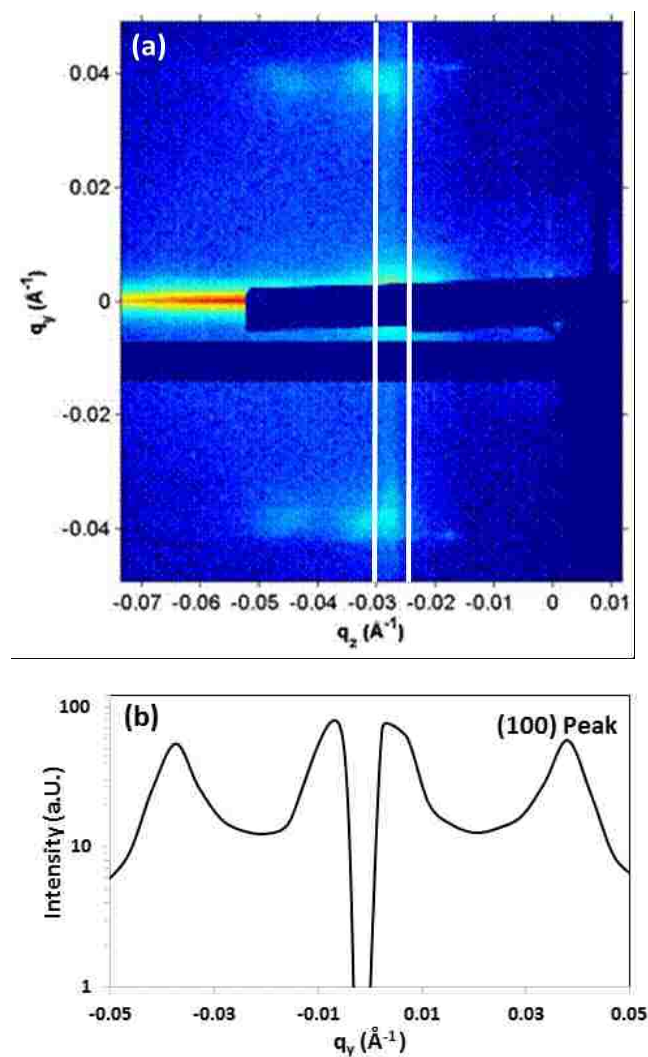


Figure C.2. (a) Representative 2D GISAXS pattern with the region used for linecuts shown by vertical white lines and (b) the corresponding 1D linecut derived by integrating along the q_z direction from 0.025-0.03 \AA^{-1} .

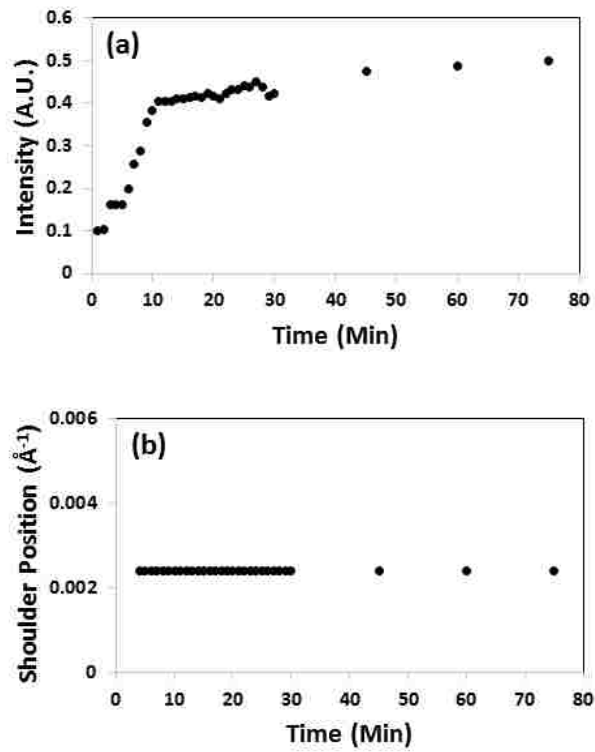


Figure C.3. (a) Evolution of the integrated intensities of the shoulder region, $q_{y,\min} < q_y < q_{y,\max}$, for thin titania film on modified substrate during aging at 4 °C at 13.5 mm above the bottom of the slide (b) Shoulder position as a function of aging time

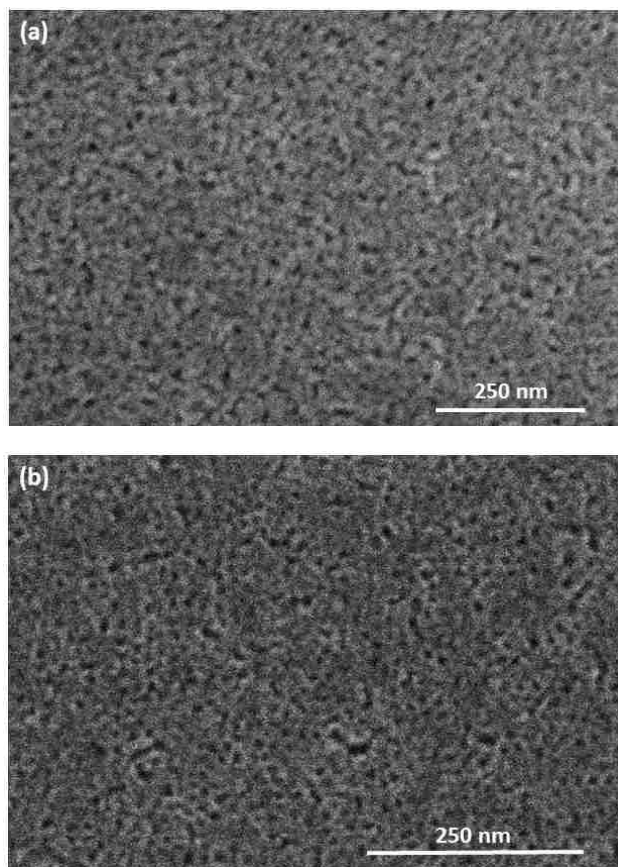


Figure C.4. Top view SEM images of thin titania films near the modified substrate aged at (a) 23 °C and (b) 4 °C after calcination at 400 °C for 10 minutes using a ramp rate of 25 °C/min

Copyright © Suraj R. Nagpure 2016

References

1. Hillhouse, H. W.; van Egmond, J. W.; Tsapatsis, M.; Hanson, J. C.; Larese, J. Z., The Interpretation of X-Ray Diffraction Data for the Determination of Channel Orientation in Mesoporous Films. *Microporous Mesoporous Mater.* **2001**, *44–45*, 639-643.
2. Das, S.; Wu, Q.; Garlapalli, R. K.; Nagpure, S.; Strzalka, J.; Jiang, Z.; Rankin, S. E., In-Situ Gixsax Investigation of Pore Orientation Effects on the Thermal Transformation Mechanism in Mesoporous Titania Thin Films. *J. Phys. Chem. C* **2013**, *118*, 968-976.
3. Popat, K. C.; Eltgroth, M.; LaTempa, T. J.; Grimes, C. A.; Desai, T. A., Titania Nanotubes: A Novel Platform for Drug-Eluting Coatings for Medical Implants? *Small* **2007**, *3*, 1878-81.
4. Rajeshwar, K.; Chenthamarakshan, R.; Goeringer, S.; Djukic, M., Titania-Based Heterogeneous Photocatalysis. Materials, Mechanistic Issues, and Implications for Environmental Remediation. *Pure Appl. Chem.* **2001**, *73*, 1849-1860.
5. Primo, A.; Corma, A.; Garcia, H., Titania Supported Gold Nanoparticles as Photocatalyst. *Phys. Chem. Chem. Phys.* **2011**, *13*, 886-910.
6. Wang, D. W.; Fang, H. T.; Li, F.; Chen, Z. G.; Zhong, Q. S.; Lu, G. Q.; Cheng, H. M., Aligned Titania Nanotubes as an Intercalation Anode Material for Hybrid Electrochemical Energy Storage. *Adv. Funct. Mater.* **2008**, *18*, 3787-3793.
7. Guo, W.; Miao, Q. Q.; Xin, G.; Wu, L. Q.; Ma, T. L., Dye-Sensitized Solar Cells Based on Nitrogen-Doped Titania Electrodes. *Key Eng. Mater.* **2010**, *451*, 321-327.
8. Kokubo, T.; Kim, H. M.; Kawashita, M., Novel Bioactive Materials with Different Mechanical Properties. *Biomaterials* **2003**, *24*, 2161-2175.
9. Lopez, T.; Ortiz-Islas, E.; Manjarrez, J.; Reinoso, F. R.; Sepulveda, A.; Gonzalez, R. D., Biocompatible Titania Microtubes Formed by Nanoparticles and Its Application in the Drug Delivery of Valproic Acid. *Opt. Mater.* **2006**, *29*, 70-74.
10. Ou, H. H.; Lo, S. L., Review of Titania Nanotubes Synthesized Via the Hydrothermal Treatment: Fabrication, Modification, and Application. *Sep. Purif. Technol.* **2007**, *58*, 179-191.
11. Linsebigler, A. L.; Lu, G.; Yates, J. T., Photocatalysis on TiO_2 Surfaces: Principles, Mechanisms, and Selected Results. *Chem. Rev.* **1995**, *95*, 735-758.
12. Liga, M. V.; Bryant, E. L.; Colvin, V. L.; Li, Q., Virus Inactivation by Silver Doped Titanium Dioxide Nanoparticles for Drinking Water Treatment. *Water Res.* **2011**, *45*, 535-544.
13. Blake, D. M.; Maness, P. C.; Huang, Z.; Wolfrum, E. J.; Huang, J.; Jacoby, W. A., Application of the Photocatalytic Chemistry of Titanium Dioxide to Disinfection and the Killing of Cancer Cells. *Sep. Purif. Rev.* **1999**, *28*, 1-50.
14. Khan, M. A.; Jung, H. T.; Yang, O. B., Synthesis and Characterization of Ultrahigh Crystalline TiO_2 Nanotubes. *J. Phys. Chem. B* **2006**, *110*, 6626-6630.
15. Yu, J.; Yu, H.; Cheng, B.; Zhao, X.; Zhang, Q., Preparation and Photocatalytic Activity of Mesoporous Anatase TiO_2 Nanofibers by a Hydrothermal Method. *J. Photochem. Photobiol. A* **2006**, *182*, 121-127.
16. O'Regan, B.; Grätzel, M., A Low-Cost, High-Efficiency Solar Cell Based on Dye-Sensitized Colloidal TiO_2 Films. *Nature* **1991**, *353*, 737-740.
17. Nazeeruddin, M. K.; Kay, A.; Rodicio, I.; Humphry-Baker, R.; Mueller, E.; Liska, P.; Vlachopoulos, N.; Graetzel, M., Conversion of Light to Electricity by Cis-X₂bis(2,2'-Bipyridyl-4,4'-Dicarboxylate)Ruthenium(II) Charge-Transfer Sensitizers (X = Cl-, Br-, I-, Cn-, and Scn-) on Nanocrystalline Titanium Dioxide Electrodes. *J. Am. Chem. Soc.* **1993**, *115*, 6382-6390.
18. Oishi, T.; Matsubara, T.; Katagiri, A., Formation of Porous TiO_2 by Anodic Oxidation and Chemical Etching of Titanium. *Electrochemistry* **2000**, *68*, 106-111.

19. Azad, A. M.; McKelvey, S. L.; Zainab, A. F., Fabrication of Antibacterial Titania Nanofibers by Electrospinning. *Ammtiac Quaterly* **2008**, *3*, 3-7.
20. Li, Y.; Jia, L.; Wu, C.; Han, S.; Gong, Y.; Chi, B.; Pu, J.; Jian, L., Mesoporous (N, S)-Codoped TiO₂ Nanoparticles as Effective Photoanode for Dye-Sensitized Solar Cells. *J. Alloys Compd.* **2012**, *512*, 23-26.
21. O'Regan, B.; Gratzel, M., A Low-Cost, High-Efficiency Solar Cell Based on Dye-Sensitized Colloidal TiO₂ Films. *Nature* **1991**, *353*, 737-740.
22. Balis, N.; Dracopoulos, V.; Antoniadou, M.; Lianos, P., Solid-State Dye-Sensitized Solar Cells Made of Multilayer Nanocrystalline Titania and Poly(3-Hexylthiophene). *J. Photochem. Photobiol. A* **2010**, *214*, 69-73.
23. Varghese, O. K.; Paulose, M.; Grimes, C. A., Long Vertically Aligned Titania Nanotubes on Transparent Conducting Oxide for Highly Efficient Solar Cells. *Nature Nanotechnol.* **2009**, *4*, 592-597.
24. Wagemaker, M.; Kearley, G. J.; van Well, A. A.; Mutka, H.; Mulder, F. M., Multiple Li Positions inside Oxygen Octahedra in Lithiated TiO₂ Anatase. *J. Am. Chem. Soc.* **2002**, *125*, 840-848.
25. Wang, D.; Choi, D.; Yang, Z.; Viswanathan, V. V.; Nie, Z.; Wang, C.; Song, Y.; Zhang, J. G.; Liu, J., Synthesis and Li-Ion Insertion Properties of Highly Crystalline Mesoporous Rutile TiO₂. *Chem. Mater.* **2008**, *20*, 3435-3442.
26. Ortiz, G. F.; Hanzu, I.; Djenizian, T.; Lavela, P.; Tirado, J. L.; Knauth, P., Alternative Li-Ion Battery Electrode Based on Self-Organized Titania Nanotubes. *Chem. Mater.* **2008**, *21*, 63-67.
27. Guo, Y. G.; Hu, Y. S.; Sigle, W.; Maier, J., Superior Electrode Performance of Nanostructured Mesoporous TiO₂ (Anatase) through Efficient Hierarchical Mixed Conducting Networks. *Adv. Mater.* **2007**, *19*, 2087-2091.
28. Kavan, L.; Rathouský, J.; Grätzel, M.; Shklover, V.; Zukal, A., Surfactant-Templated TiO₂ (Anatase): Characteristic Features of Lithium Insertion Electrochemistry in Organized Nanostructures. *J. Phys. Chem. B* **2000**, *104*, 12012-12020.
29. Yamada, H.; Yamato, T.; Moriguchi, I., Porous TiO₂ (Anatase) Electrodes for High-Power Batteries. *Chem. Lett.* **2004**, *33*, 1548-1549.
30. Antonelli, D. M.; Ying, J. Y., Synthesis of Hexagonally Packed Mesoporous TiO₂ by a Modified Sol-Gel Method. *Angew. Chem. Int. Ed.* **1995**, *34*, 2014-2017.
31. Yu, J.; Zhang, L.; Cheng, B.; Su, Y., Hydrothermal Preparation and Photocatalytic Activity of Hierarchically Sponge-Like Macro-/Mesoporous Titania. *J. Phys. Chem. C* **2007**, *111*, 10582-10589.
32. Wang, H.; Miao, J. J.; Zhu, J. M.; Ma, H. M.; Zhu, J. J.; Chen, H. Y., Mesoporous Spherical Aggregates of Anatase Nanocrystals with Wormhole-Like Framework Structures: Their Chemical Fabrication, Characterization, and Photocatalytic Performance. *Langmuir* **2004**, *20*, 11738-11747.
33. Liu, X.; Gao, Y.; Cao, C.; Luo, H.; Wang, W., Highly Crystalline Spindle-Shaped Mesoporous Anatase Titania Particles: Solution-Phase Synthesis, Characterization, and Photocatalytic Properties. *Langmuir* **2010**, *26*, 7671-7674.
34. Joo, J. B.; Zhang, Q.; Lee, I.; Dahl, M.; Zaera, F.; Yin, Y., Mesoporous Anatase Titania Hollow Nanostructures Through Silica-Protected Calcination. *Adv. Funct. Mater.* **2012**, *22*, 166-174.
35. Da Silva, R. O.; Goncalves, R. H.; Stroppa, D. G.; Ramirez, A. J.; Leite, E. R., Synthesis of Recrystallized Anatase TiO₂ Mesocrystals with Wulff Shape Assisted by Oriented Attachment. *Nanoscale* **2011**, *3*, 1910-1916.

36. Bleta, R.; Alphonse, P.; Lorenzato, L., Nanoparticle Route for the Preparation in Aqueous Medium of Mesoporous TiO₂ with Controlled Porosity and Crystalline Framework. *J. Phys. Chem. C* **2010**, *114*, 2039-2048.
37. Moonosawmy, K. R.; Katzke, H.; Es-Souni, M.; Dietze, M.; Es-Souni, M., Mesoporous and Macroporous Brookite Thin Films Having a Large Thermal Stability Range. *Langmuir* **2012**, *28*, 6706-6713.
38. Wang, J.; Li, H.; Li, H.; Zuo, C.; Wang, H., Thermal Stability and Optimal Photoinduced Hydrophilicity of Mesoporous TiO₂ Thin Films. *J. Phys. Chem. C* **2012**, *116*, 9517-9525.
39. Yin, J. B.; Zhao, X. P., Enhanced Electrorheological Activity of Mesoporous Cr-Doped TiO₂ from Activated Pore Wall and High Surface Area. *J. Phys. Chem. B* **2006**, *110*, 12916-12925.
40. Guo, C.; Xu, J.; Zhang, Y.; He, Y., Hierarchical Mesoporous TiO₂ Microspheres for the Enhanced Photocatalytic Oxidation of Sulfonamides and Their Mechanism. *RSC Adv.* **2012**, *2*, 4720-4727.
41. Nagpure, S.; Das, S.; Garlapalli, R. K.; Strzalka, J.; Rankin, S. E., In Situ Gixs Investigation of Low-Temperature Aging in Oriented Surfactant-Mesostructured Titania Thin Films. *J. Phys. Chem. C* **2015**, *119*, 22970-22984.
42. Das, S.; Wu, Q.; Garlapalli, R. K.; Nagpure, S.; Strzalka, J.; Jiang, Z.; Rankin, S. E., In-Situ Gixs Investigation of Pore Orientation Effects on the Thermal Transformation Mechanism in Mesoporous Titania Thin Films. *J. Phys. Chem. C* **2014**, *118*, 968-976.
43. Das, S.; Nagpure, S.; Garlapalli, R. K.; Wu, Q.; Islam, S. Z.; Strzalka, J.; Rankin, S. E., Pore Orientation Effects on the Kinetics of Mesostructure Loss in Surfactant Templated Titania Thin Films. *Phys. Chem. Chem. Phys.* **2016**, *18*, 2896-2905.
44. Islam, S. Z.; Reed, A.; Kim, D. Y.; Rankin, S. E., N₂/Ar Plasma Induced Doping of Ordered Mesoporous TiO₂ Thin Films for Visible Light Active Photocatalysis. *Microporous Mesoporous Mater.* **2016**, *220*, 120-128.
45. Han, O. H.; Paik, Y.; Moon, Y. S.; Lee, S. K.; Kim, T. Y.; Lee, Y. H.; Lee, W. I., Selective Synthesis of Lamellar Titania with Carboxylate Precursor and Characterization by Solid-State Nmr. *Chem. Mater.* **2007**, *19*, 3615-3623.
46. Zhang, R.; Elzatahry, A. A.; Al-Deyab, S. S.; Zhao, D., Mesoporous Titania: From Synthesis to Application. *Nano Today* **2012**, *7*, 344-366.
47. Beck, J. S., et al., A New Family of Mesoporous Molecular Sieves Prepared with Liquid Crystal Templates. *J. Am. Chem. Soc.* **1992**, *114*, 10834-10843.
48. Kresge, C. T.; Leonowicz, M. E.; Roth, W. J.; Vartuli, J. C.; Beck, J. S., Ordered Mesoporous Molecular Sieves Synthesized by a Liquid-Crystal Template Mechanism. *Nature* **1992**, *359*, 710-712.
49. Antonelli, D. M., Synthesis of Phosphorus-Free Mesoporous Titania Via Templating with Amine Surfactants. *Microporous Mesoporous Mater.* **1999**, *30*, 315-319.
50. Brinker, C. J.; Lu, Y.; Sellinger, A.; Fan, H., Evaporation-Induced Self-Assembly: Nanostructures Made Easy. *Adv. Mater.* **1999**, *11*, 579-585.
51. Crepaldi, E. L.; Soler-Illia, G. J. D. A. A.; Grosso, D.; Cagnol, F.; Ribot, F.; Sanchez, C., Controlled Formation of Highly Organized Mesoporous Titania Thin Films: From Mesostructured Hybrids to Mesoporous Nanoanatase TiO₂. *J. Am. Chem. Soc.* **2003**, *125*, 9770-9786.
52. Grosso, D.; Babonneau, F.; Sanchez, C.; Soler-Illia, G. J. D. A. A.; Crepaldi, E. L.; Albouy, P. A.; Amenitsch, H.; Balkenende, A. R.; Brunet-Bruneau, A., A First Insight in the Mechanisms Involved in the Self-Assembly of 2d-Hexagonal Templated SiO₂ and TiO₂ Mesostructured Films During Dip-Coating. *J Sol-Gel Sci Technol* **2003**, *26*, 561-565.

53. Soler-Illia, G. J. D. A. A.; Sanchez, C., Interactions between Poly(Ethylene Oxide)-Based Surfactants and Transition Metal Alkoxides: Their Role in the Templated Construction of Mesoporous Hybrid Organic-Inorganic Composites. *New J. Chem.* **2000**, *24*, 493-499.
54. Kallala, M.; Sanchez, C.; Cabane, B., Structures of Inorganic Polymers in Sol-Gel Processes Based on Titanium Oxide. *Phys. Rev. E* **1993**, *48*, 3692-3704.
55. Alberius, P. C. A.; Frindell, K. L.; Hayward, R. C.; Kramer, E. J.; Stucky, G. D.; Chmelka, B. F., General Predictive Syntheses of Cubic, Hexagonal, and Lamellar Silica and Titania Mesoporous Thin Films. *Chem. Mater.* **2002**, *14*, 3284-3294.
56. Kirsch, B. L.; Richman, E. K.; Riley, A. E.; Tolbert, S. H., In-Situ X-Ray Diffraction Study of the Crystallization Kinetics of Mesoporous Titania Films. *J. Phys. Chem. B* **2004**, *108*, 12698-12706.
57. Choi, S. Y.; Mamak, M.; Coombs, N.; Chopra, N.; Ozin, G. A., Thermally Stable Two-Dimensional Hexagonal Mesoporous Nanocrystalline Anatase, Meso-Nc-TiO₂: Bulk and Crack-Free Thin Film Morphologies. *Adv. Funct. Mater.* **2004**, *14*, 335-344.
58. Haseloh, S.; Choi, S. Y.; Mamak, M.; Coombs, N.; Petrov, S.; Chopra, N.; Ozin, G. A., Towards Flexible Inorganic "Mesomaterials": One-Pot Low Temperature Synthesis of Mesoporous Nanocrystalline Titania. *Chem. Comm.* **2004**, *13*, 1460-1461.
59. Sanchez, C.; Boissière, C.; Grosso, D.; Laberty, C.; Nicole, L., Design, Synthesis, and Properties of Inorganic and Hybrid Thin Films Having Periodically Organized Nanoporosity. *Chem. Mater.* **2008**, *20*, 682-737.
60. Livage, J.; Henry, M.; Sanchez, C., Sol-Gel Chemistry of Transition Metal Oxides. *Prog. Solid State Chem.* **1988**, *18*, 259-341.
61. Park, J. K.; Myoung, J. J.; Kyong, J. B.; Kim, H. K., Reaction Mechanism for the Hydrolysis of Titanium Alkoxides. *Bull. Korean Chem. Soc.* **2003**, *24*, 671-673.
62. Weymann-Schildknecht, S.; Henry, M., Mechanistic Aspects of the Hydrolysis and Condensation of Titanium Alkoxides Complexed by Tripodal Ligands. *J. Chem. Soc., Dalton Trans.* **2001**, *0*, 2425-2428.
63. Huo, Q.; Margolese, D. I.; Stucky, G. D., Surfactant Control of Phases in the Synthesis of Mesoporous Silica-Based Materials. *Chem. Mater.* **1996**, *8*, 1147-1160.
64. Bosc, F.; Ayrat, A.; Albouy, P. A.; Datas, L.; Guizard, C., Mesoporous Anatase Thin Films Prepared by Mesoporous Templating. *Chem. Mater.* **2004**, *16*, 2208-2214.
65. Wu, Q.; Rankin, S. E., Tuning the Wall Thickness and Pore Orientation in Mesoporous Titania Films Prepared with Low-Temperature Aging. *J Sol-Gel Sci Technol* **2011**, *60*, 81-90.
66. Jang, K. S.; Song, M. G.; Cho, S. H.; Kim, J. D., Using the Effects of Ph and Moisture to Synthesize Highly Organized Mesoporous Titania Thin Films. *Chem. Comm.* **2004**, *13*, 1514-1515.
67. Lee, U. H.; Lee, H.; Wen, S.; Mho, S.; Kwon, Y. U., Mesoporous Titania Thin Films with Pseudo-Cubic Structure: Synthetic Studies and Applications to Nanomembranes and Nanotemplates. *Microporous Mesoporous Mater.* **2006**, *88*, 48-55.
68. Liu, K.; Fu, H.; Shi, K.; Xiao, F.; Jing, L.; Xin, B., Preparation of Large-Pore Mesoporous Nanocrystalline TiO₂ Thin Films with Tailored Pore Diameters. *J. Phys. Chem. B* **2005**, *109*, 18719-18722.
69. Li, X. S.; Fryxell, G. E.; Birnbaum, J. C.; Wang, C., Effects of Template and Precursor Chemistry on Structure and Properties of Mesoporous TiO₂ Thin Films. *Langmuir* **2004**, *20*, 9095-9102.
70. Yu, J. C.; Wang, X.; Fu, X., Pore-Wall Chemistry and Photocatalytic Activity of Mesoporous Titania Molecular Sieve Films. *Chem. Mater.* **2004**, *16*, 1523-1530.

71. Grosso, D.; Soler-Illia, G. J. D. A. A.; Crepaldi, E. L.; Cagnol, F.; Sinturel, C.; Bourgeois, A.; Brunet-Bruneau, A.; Amenitsch, H.; Albouy, P. A.; Sanchez, C., Highly Porous TiO₂ Anatase Optical Thin Films with Cubic Mesostructure Stabilized at 700 °C. *Chem. Mater.* **2003**, *15*, 4562-4570.
72. Coakley, K. M.; Liu, Y.; McGehee, M. D.; Frindell, K. L.; Stucky, G. D., Infiltrating Semiconducting Polymers into Self-Assembled Mesoporous Titania Films for Photovoltaic Applications. *Adv. Funct. Mater.* **2003**, *13*, 301-306.
73. Cadby, A. J.; Tolbert, S. H., Controlling Optical Properties and Interchain Interactions in Semiconducting Polymers by Encapsulation in Periodic Nanoporous Silicas with Different Pore Sizes. *J. Phys. Chem. B* **2005**, *109*, 17879-17886.
74. Kellogg, G. J.; Walton, D. G.; Mayes, A. M.; Lambooy, P.; Russell, T. P.; Gallagher, P. D.; Satija, S. K., Observed Surface Energy Effects in Confined Diblock Copolymers. *Phys. Rev. Lett.* **1996**, *76*, 2503-2506.
75. Huang, E.; Pruzinsky, S.; Russell, T. P.; Mays, J.; Hawker, C. J., Neutrality Conditions for Block Copolymer Systems on Random Copolymer Brush Surfaces. *Macromol.* **1999**, *32*, 5299-5303.
76. Huang, E.; Russell, T. P.; Harrison, C.; Chaikin, P. M.; Register, R. A.; Hawker, C. J.; Mays, J., Using Surface Active Random Copolymers to Control the Domain Orientation in Diblock Copolymer Thin Films. *Macromol.* **1998**, *31*, 7641-7650.
77. Thurn-Albrecht, T.; Steiner, R.; DeRouchey, J.; Stafford, C. M.; Huang, E.; Bal, M.; Tuominen, M.; Hawker, C. J.; Russell, T., Nanoscopic Templates from Oriented Block Copolymer Films. *Adv. Mater.* **2000**, *12*, 787-791.
78. Huinink, H. P.; Brokken-Zijp, J. C. M.; van Dijk, M. A.; Sevink, G. J. A., Asymmetric Block Copolymers Confined in a Thin Film. *J. Chem. Phys.* **2000**, *112*, 2452-2462.
79. Pickett, G. T.; Balazs, A. C., Equilibrium Orientation of Confined Diblock Copolymer Films. *Macromol.* **1997**, *30*, 3097-3103.
80. Koganti, V. R.; Dunphy, D.; Gowrishankar, V.; McGehee, M. D.; Li, X.; Wang, J.; Rankin, S. E., Generalized Coating Route to Silica and Titania Films with Orthogonally Tilted Cylindrical Nanopore Arrays. *Nano Lett.* **2006**, *6*, 2567-2570.
81. Das, S.; Wu, Q.; Garlapalli, R. K.; Nagpure, S.; Strzalka, J.; Zhang, J.; Rankin, S. E., In-Situ Gixs Investigation of Pore Orientation Effects on the Thermal Transformation Mechanism in Mesoporous Titania Thin Films. *J. Phys. Chem. C* **2013**, *118*, 968-976.
82. Koganti, V. R.; Rankin, S. E., Synthesis of Surfactant-Templated Silica Films with Orthogonally Aligned Hexagonal Mesophase. *J. Phys. Chem. B.* **2005**, *109*, 3279-3283.
83. Rankin, S. E.; Malanoski, A. P.; Swol, F., Monte Carlo Simulation of Amphiphile Self-Assembly During Dip Coating. *MRS Proceedings* **2000**, *MRS Proceedings*, 121.
84. Tasinkevych, M.; Ciach, A., Structural Transformations in Confined Lamellar Phases in Oil-Water-Surfactant Mixtures. *J. Chem. Phys.* **2001**, *115*, 8705-8713.
85. Rankin, S. E.; Malanoski, A. P.; Van Swol, F. In *Monte Carlo Simulation of Amphiphile Self-Assembly During Dip Coating*, Nonlithographic and Lithographic Methods of Nanofabrication - From Ultralarge-Scale Integration to Photonics to Molecular Electronics, November 26, 2000 - December 1, 2000, Boston, MA, United states, Materials Research Society: Boston, MA, United states, 2001; pp D121-D126.
86. Richman, E. K.; Brezesinski, T.; Tolbert, S. H., Vertically Oriented Hexagonal Mesoporous Films Formed through Nanometre-Scale Epitaxy. *Nature Mater.* **2008**, *7*, 712-717.
87. Grosso, D.; Babonneau, F.; Albouy, P. A.; Amenitsch, H.; Balkenende, A. R.; Brunet-Bruneau, A.; Rivory, J., An in Situ Study of Mesostructured Ctab-Silica Film Formation During Dip Coating Using Time-Resolved Sx and Interferometry Measurements. *Chem. Mater.* **2002**, *14*, 931-939.

88. Grosso, D.; Balkenende, A. R.; Albouy, P. A.; Ayrat, A.; Amenitsch, H.; Babonneau, F., Two-Dimensional Hexagonal Mesoporous Silica Thin Films Prepared from Block Copolymers: Detailed Characterization and Formation Mechanism. *Chem. Mater.* **2001**, *13*, 1848-1856.
89. Grosso, D.; Babonneau, F.; Soler-Illia, G. J. D. A. A.; Albouy, P. A.; Amenitsch, H., Phase Transformation During Cubic Mesostructured Silica Film Formation. *Chem. Comm.* **2002**, 748-749.
90. Ko, Y. S.; Koh, C. W.; Lee, U. H.; Kwon, Y. U., Synthesis of Mesoporous Titania Thin Films with Vertical Pore Channels and Thick and Crystalline Walls. *Micropor. Mesopor. Mater.* **2011**, *145*, 141-145.
91. Koh, C. W.; Lee, U. H.; Song, J. K.; Lee, H. R.; Kim, M. H.; Suh, M.; Kwon, Y. U., Mesoporous Titania Thin Film with Highly Ordered and Fully Accessible Vertical Pores and Crystalline Walls. *Chem.-Asian J.* **2008**, *3*, 862-867.
92. M.D., C. K. M. L. Y. G. C. M., Ordered Organic-Inorganic Bulk Heterojunction Photovoltaic Cells. *MRS Bulletin* **2005**, *30*, 37-40.
93. Grätzel, M., Photoelectrochemical Cells. *Nature* **2001**, *414*, 338-344.
94. Ngamsinlapasathian, S.; Sreethawong, T.; Suzuki, Y.; Yoshikawa, S., Single- and Double-Layered Mesoporous TiO₂/P25 TiO₂ Electrode for Dye-Sensitized Solar Cell. *Sol. Ener. Mat. Sol. Cells* **2005**, *86*, 269-282.
95. Grätzel, M., Mesoporous Oxide Junctions and Nanostructured Solar Cells. *Curr. Opin. Colloid Interface Sci.* **1999**, *4*, 314-321.
96. Wang, D., et al., Electrodeposition of Metallic Nanowire Thin Films Using Mesoporous Silica Templates. *Adv. Mater.* **2003**, *15*, 130-133.
97. Ziegler, K. J.; Polyakov, B.; Kulkarni, J. S.; Crowley, T. A.; Ryan, K. M.; Morris, M. A.; Erts, D.; Holmes, J. D., Conductive Films of Ordered Nanowire Arrays. *J. Mater. Chem.* **2004**, *14*, 585-589.
98. Fox, M. A.; Dulay, M. T., Heterogeneous Photocatalysis. *Chem. Rev.* **1993**, *93*, 341-357.
99. Coakley, K. M.; McGehee, M. D., Photovoltaic Cells Made from Conjugated Polymers Infiltrated into Mesoporous Titania. *Appl. Phys. Lett.* **2003**, *83*, 3380-3382.
100. Boettcher, S. W.; Bartl, M. H.; Hu, J. G.; Stucky, G. D., Structural Analysis of Hybrid Titania-Based Mesostructured Composites. *Journal of the American Chemical Society* **2005**, *127*, 9721-9730.
101. Crepaldi, E. L.; Soler-Illia, G. J. d. A. A.; Grosso, D.; Cagnol, F.; Ribot, F.; Sanchez, C., Controlled Formation of Highly Organized Mesoporous Titania Thin Films: From Mesostructured Hybrids to Mesoporous Nanoanatase TiO₂. *Journal of the American Chemical Society* **2003**, *125*, 9770-9786.
102. Doshi, D. A., et al., In-Situ X-Ray Scattering Study of Continuous Silica-Surfactant Self-Assembly During Steady-State Dip Coating. *J. Phys. Chem. B* **2003**, *107*, 7683-7688.
103. Pícol, L.; Grosso, D.; Soler-Illia, G. J. D. A. A.; Crepaldi, E. L.; Sanchez, C.; Albouy, P. A.; Amenitsch, H.; Euzen, P., Hexagonally Organised Mesoporous Aluminium-Oxo-Hydroxide Thin Films Prepared by the Template Approach. In Situ Study of the Structural Formation. *J. Mater. Chem.* **2002**, *12*, 557-564.
104. Doshi, D. A.; Gibaud, A.; Goletto, V.; Lu, M.; Gerung, H.; Ocko, B.; Han, S. M.; Brinker, C. J., Peering into the Self-Assembly of Surfactant Templated Thin-Film Silica Mesophases. *J. Am. Chem. Soc.* **2003**, *125*, 11646-11655.
105. Gibaud, A.; Grosso, D.; Smarsly, B.; Baptiste, A.; Bardeau, J. F.; Babonneau, F.; Doshi, D. A.; Chen, Z.; Brinker, C. J.; Sanchez, C., Evaporation-Controlled Self-Assembly of Silica Surfactant Mesophases. *J. Phys. Chem. B* **2003**, *107*, 6114-6118.

106. Grosso, D.; Cagnol, F.; Soler-Illia, G. J. D. A. A.; Crepaldi, E. L.; Amenitsch, H.; Brunet-Bruneau, A.; Bourgeois, A.; Sanchez, C., Fundamentals of Mesostructuring through Evaporation-Induced Self-Assembly. *Adv. Funct. Mater.* **2004**, *14*, 309-322.
107. Faustini, M.; Boissiere, C.; Nicole, L.; Grosso, D., From Chemical Solutions to Inorganic Nanostructured Materials: A Journey into Evaporation-Driven Processes. *Chem. Mat.* **2014**, *26*, 709-723.
108. Gibaud, A.; Dourdain, S.; Gang, O.; Ocko, B. M., In Situ Grazing Incidence Small-Angle X-Ray Scattering Real-Time Monitoring of the Role of Humidity During the Structural Formation of Templated Silica Thin Films. *Phys. Rev. B* **2004**, *70*, 4.
109. Cagnol, F. G., D.; Soler-Illia, G. J.; Crepaldi, E. L.; Babonneau, F.; Amenitsch, H.; Sanchez, C., Humidity-Controlled Mesostructuration in Ctab-Templated Silica Thin Film Processing. The Existence of a Modulable Steady State. *J. Mater. Chem.* **2003**, *13*, 61-66.
110. Urade, V. N.; Bollmann, L.; Kowalski, J. D.; Tate, M. P.; Hillhouse, H. W., Controlling Interfacial Curvature in Nanoporous Silica Films Formed by Evaporation-Induced Self-Assembly from Nonionic Surfactants. II. Effect of Processing Parameters on Film Structure. *Langmuir* **2007**, *23*, 4268-4278.
111. Besson, S.; Gacoin, T.; Ricolleau, C.; Jacquiod, C.; Boilot, J. P., Phase Diagram for Mesoporous Ctab-Silica Films Prepared under Dynamic Conditions. *J. Mater. Chem.* **2003**, *13*, 404-409.
112. Boudot, M.; Gaud, V.; Louarn, M.; Selmane, M.; Grosso, D., Sol-Gel Based Hydrophobic Antireflective Coatings on Organic Substrates: A Detailed Investigation of Ammonia Vapor Treatment (Avt). *Chem. Mater.* **2014**, *26*, 1822-1833.
113. Grosso, D. B., A. R.; Albouy, P. A.; Ayril, A.; Amentisch, H.; Babonneau, F, Two-Dimensional Hexagonal Mesoporous Silica Thin Films Prepared from Block Copolymers: Detailed Characterization and Formation Mechanism. *Chem. Mater.* **2001**, *13*, 1848-1856.
114. Collard, X.; Van der Schueren, B.; Rooke, J. C.; Aprile, C.; Su, B. L., A Comprehensive Study of the Reaction Parameters Involved in the Synthesis of Silica Thin Films with Well-Ordered Uni-Directional Mesopores. *J. Colloid Interface Sci.* **2013**, *401*, 23-33.
115. Lee, Y.-F.; Chang, K.-H.; Chu, C.-Y.; Chen, H.-L.; Hu, C.-C., Microstructure Tuning of Mesoporous Silica Prepared by Evaporation-Induced Self-Assembly Processes: Interactions among Solvent Evaporation, Micelle Formation/Packing and Sol Condensation. *RSC Adv.* **2011**, *1*, 401-407.
116. Keller, A.; Segal-Peretz, T.; Kauffmann, Y.; Frey, G. L., Control over in-Channel Mesostructure Orientation through Aam Surface Modification. *Phys. Chem. Chem. Phys.* **2013**, *15*, 13637-13645.
117. Platschek, B.; Keilbach, A.; Bein, T., Mesoporous Structures Confined in Anodic Alumina Membranes. *Adv. Mater.* **2011**, *23*, 2395-2412.
118. Koganti, V. R.; Dunphy, D.; Gowrishankar, V.; McGehee, M. D.; Li, X.; Wang, J.; Rankin, S. E., Generalized Coating Route to Silica and Titania Films with Orthogonally Tilted Cylindrical Nanopore Arrays. *Nano Letters* **2006**, *6*, 2567-2570.
119. Koganti, V. R.; Rankin, S. E., Synthesis of Surfactant-Templated Silica Films with Orthogonally Aligned Hexagonal Mesophase. *J. Phys. Chem. B* **2005**, *109*, 3279-3283.
120. Stein, A.; Rudisill, S. G.; Petkovich, N. D., Perspective on the Influence of Interactions between Hard and Soft Templates and Precursors on Morphology of Hierarchically Structured Porous Materials. *Chem. Mat.* **2014**, *26*, 259-276.
121. Cagnol, F.; Grosso, D.; Soler-Illia, G. J. D. A. A.; Crepaldi, E. L.; Babonneau, F.; Amenitsch, H.; Sanchez, C., Humidity-Controlled Mesostructuration in Ctab-Templated Silica Thin Film Processing. The Existence of a Modulable Steady State. *J. Mater. Chem.* **2003**, *13*, 61-66.

122. Jiang, Z., Gisxgui: A Matlab Toolbox for Grazing-Incidence X-Ray Scattering Data Visualization and Reduction, and Indexing of Buried Three-Dimensional Periodic Nanostructured Films. *J. Appl. Crystallogr.* **2015**, *48*, 917-926.
123. Williams, D. B.; Carter, C. B., *Transmission Electron Microscopy: A Textbook for Materials Science*; Springer US: Boston, MA, 2009.
124. Honsberg, C.; Bowden, S. Solar Cell Structure
<http://www.pveducation.org/pvcdrom/Solar-Cell-Operation/Solar-Cell-Structure>.
<http://www.pveducation.org/pvcdrom/solar-cell-operation/solar-cell-structure>.
125. Honsberg, C.; Bowden, S., Formation of a Pn-Junction
<http://www.pveducation.org/pvcdrom/Pn-Junction/Formation-Pn-Junction>.
126. Honsberg, C.; Bowden, S., The Photovoltaic Effect
<http://www.pveducation.org/pvcdrom/Solar-Cell-Operation/Photovoltaic-Effect>.
127. Ferekides, C. S.; Balasubramanian, U.; Mamazza, R.; Viswanathan, V.; Zhao, H.; Morel, D. L., Cdte Thin Film Solar Cells: Device and Technology Issues. *Sol. Energy* **2004**, *77*, 823-830.
128. Dang, H.; Singh, V.; Rajaputra, S.; Guduru, S.; Chen, J.; Nadimpally, B., Cadmium Sulfide Nanowire Arrays for Window Layer Applications in Solar Cells. *Sol. Energ. Mat. Sol. Cells* **2014**, *126*, 184-191.
129. Brus, V. V.; Ilashchuk, M. I.; Kovalyuk, Z. D.; Maryanchuk, P. D.; Ulyanytsky, K. S., Electrical and Photoelectrical Properties of Photosensitive Heterojunctions N-TiO₂/P-Cdte. *Semicond. Sci. Technol.* **2011**, *26*, 125006.
130. Britt, J.; Ferekides, C., Thin-Film Cds/Cdte Solar Cell with 15.8% Efficiency. *Appl. Phys. Lett.* **1993**, *62*, 2851-2852.
131. Cunningham, D.; Rubcich, M.; Skinner, D., Cadmium Telluride Pv Module Manufacturing at Bp Solar. *Prog. Photovolt. Res. Appl.* **2002**, *10*, 159-168.
132. Bilal, S., Cyclic Voltammetry. In *Encyclopedia of Applied Electrochemistry*, Kreysa, G.; Ota, K. I.; Savinell, R. F., Eds. Springer New York: New York, NY, 2014; pp 285-289.
133. Hibino, M.; Abe, K.; Mochizuki, M.; Miyayama, M., Amorphous Titanium Oxide Electrode for High-Rate Discharge and Charge. *J. Power Sources* **2004**, *126*, 139-143.
134. Brinker, C. J.; Lu, Y.; Sellinger, A.; Fan, H., Evaporation-Induced Self-Assembly. Nanostructures Made Easy. *Adv. Mater.* **1999**, *11*, 579-585.
135. Ogawa, M., Formation of Novel Oriented Transparent Films of Layered Silica-Surfactant Nanocomposites. *J. Am. Chem. Soc.* **1994**, *116*, 7941-7942.
136. Ogawa, M., A Simple Set-Gel Route for the Preparation of Silica-Surfactant Mesostructured Materials. *Chem. Comm.* **1996**, 1149-1150.
137. Ogawa, M., Preparation of Transparent Thin Films of Silica-Surfactant Mesostructured Materials. *Supramol. Sci.* **1998**, *5*, 247-251.
138. Lu, Y. G., R.; Drewien, C. A.; Anderson, M. T.; Brinker, C. J.; Gong, W.; Guo, Y.; Soyez, H.; Dunn, B.; Huang, M. H.; Zink, J. I., Continuous Formation of Supported Cubic and Hexagonal Mesoporous Films by Sol-Gel Dip-Coating. *Nature* **1997**, *389*, 364-368.
139. Guliants, V. V.; Carreon, M. A.; Lin, Y. S., Ordered Mesoporous and Macroporous Inorganic Films and Membranes. *J. Membrane Sci.* **2004**, *235*, 53-72.
140. Brinker, C. J.; Dunphy, D. R., Morphological Control of Surfactant-Templated Metal Oxide Films. *Current Opin. Colloid Interface Sci.* **2006**, *11*, 126-132.
141. Yamauchi, Y.; Suzuki, N.; Radhakrishnan, L.; Wang, L., Breakthrough and Future: Nanoscale Controls of Compositions, Morphologies, and Mesochannel Orientations toward Advanced Mesoporous Materials. *Chem. Record* **2009**, *9*, 321-339.
142. Innocenzi, P.; Malfatti, L., Mesoporous Thin Films: Properties and Applications. *Chem. Soc. Rev.* **2013**, *42*, 4198-4216.

143. Li, X.; Song, L.; Vogt, B. D., Tuning Mechanical Properties of Mesoporous Silicas Using Associating Homopolymers/Block Copolymer Blends as Templates. *J. Phys. Chem. C* **2007**, *112*, 53-60.
144. Wang, J.; Cheng, Q.; Tang, Z., Layered Nanocomposites Inspired by the Structure and Mechanical Properties of Nacre. *Chem. Soc. Rev.* **2012**, *41*, 1111-1129.
145. Soler-Illia, G. J. A. A.; Innocenzi, P., Mesoporous Hybrid Thin Films: The Physics and Chemistry Beneath. *Chemistry – A European Journal* **2006**, *12*, 4478-4494.
146. Plawsky, J. L.; Kim, J. K.; Schubert, E. F., Engineered Nanoporous and Nanostructured Films. *Mater. Today* **2009**, *12*, 36-45.
147. Volksen, W.; Miller, R. D.; Dubois, G., Low Dielectric Constant Materials. *Chem. Rev.* **2009**, *110*, 56-110.
148. Bearzotti, A.; Bertolo, J. M.; Innocenzi, P.; Falcaro, P.; Traversa, E., Humidity Sensors Based on Mesoporous Silica Thin Films Synthesised by Block Copolymers. *J. Eur. Ceram. Soc.* **2004**, *24*, 1969-1972.
149. Bearzotti, A.; Bertolo, J. M.; Innocenzi, P.; Falcaro, P.; Traversa, E., Relative Humidity and Alcohol Sensors Based on Mesoporous Silica Thin Films Synthesised from Block Copolymers. *Sens. Actuators, B* **2003**, *95*, 107-110.
150. Melde, B.; Johnson, B., Mesoporous Materials in Sensing: Morphology and Functionality at the Meso-Interface. *Anal Bioanal Chem* **2010**, *398*, 1565-1573.
151. Coll, C.; Bernardos, A.; Martínez-Mañez, R.; Sancenón, F., Gated Silica Mesoporous Supports for Controlled Release and Signaling Applications. *Acc. Chem. Res.* **2012**, *46*, 339-349.
152. Wagner, T.; Haffer, S.; Weinberger, C.; Klaus, D.; Tiemann, M., Mesoporous Materials as Gas Sensors. *Chem. Soc. Rev.* **2013**, *42*, 4036-4053.
153. Walcarius, A., Mesoporous Materials and Electrochemistry. *Chem. Soc. Rev.* **2013**, *42*, 4098-4140.
154. Urbanova, V.; Walcarius, A., Vertically-Aligned Mesoporous Silica Films. *Zeitschrift für anorganische und allgemeine Chemie* **2014**, *640*, 537-546.
155. Holmes, J. D.; Spalding, T. R.; Ryan, K. M.; Lyons, D.; Crowley, T.; Morris, M. A., The Use of Templated Mesoporous Materials as Templates for the Development of Ordered Arrangements of Nanowire and Nanorods of Electronically Important Materi. In *Studies in Surface Science and Catalysis*, Sayari, A.; Jaroniec, M., Eds. Elsevier: 2002; Vol. Volume 141, pp 337-344.
156. Ryan, K. M.; Erts, D.; Olin, H.; Morris, M. A.; Holmes, J. D., Three Dimensional Architectures of Ultra-High Density Semiconducting Nanowires Deposited on Chip. *J. Am. Chem. Soc.* **2003**, *125*, 6284-6288.
157. Guo, D. J.; Ding, Y., Porous Nanostructured Metals for Electrocatalysis. *Electroanalysis* **2012**, *24*, 2035-2043.
158. Lee, K. R.; Kwon, Y. K., Hard Templates for Fabrication of Nanostuctured Films. *Nano* **2010**, *05*, 75-87.
159. Tian, B., et al., Facile Synthesis and Characterization of Novel Mesoporous and Mesorelief Oxides with Gyroidal Structures. *J. Am. Chem. Soc.* **2003**, *126*, 865-875.
160. Yang, H.; Zhao, D., Synthesis of Replica Mesostructures by the Nanocasting Strategy. *J. Mater. Chem.* **2005**, *15*, 1217-1231.
161. Nishiyama, N.; Park, D. H.; Koide, A.; Egashira, Y.; Ueyama, K., A Mesoporous Silica (Mcm-48) Membrane: Preparation and Characterization. *J. Membr. Sci.* **2001**, *182*, 235-244.
162. Park, D. H.; Nishiyama, N.; Egashira, Y.; Ueyama, K., Enhancement of Hydrothermal Stability and Hydrophobicity of a Silica Mcm-48 Membrane by Silylation. *Ind. Eng. Chem. Res.* **2001**, *40*, 6105-6110.

163. Liu, N.; Dunphy, D. R.; Atanassov, P.; Bunge, S. D.; Chen, Z.; López, G. P.; Boyle, T. J.; Brinker, C. J., Photoregulation of Mass Transport through a Photoresponsive Azobenzene-Modified Nanoporous Membrane. *Nano Lett.* **2004**, *4*, 551-554.
164. Brinker, C. J., Evaporation-Induced Self-Assembly: Functional Nanostructures Made Easy. *MRS Bull.* **2004**, *29*, 631-640.
165. Kumar, P.; Guliyants, V. V., Periodic Mesoporous Organic-Inorganic Hybrid Materials: Applications in Membrane Separations and Adsorption. *Microporous Mesoporous Mater.* **2010**, *132*, 1-14.
166. Alonso, B.; Fayon, F.; Massiot, D.; Amenitsch, H.; Malfatti, L.; Kidchob, T.; Costacurta, S.; Innocenzi, P., Hybrid Organic-Inorganic Mesostructured Membranes: Interfaces and Organization at Different Length Scales. *J. Phys. Chem. C* **2010**, *114*, 11730-11740.
167. Chen, Z., et al., DNA Translocation through an Array of Kinked Nanopores. *Nat. Mater.* **2010**, *9*, 667-75.
168. Fujita, S.; Koiwai, A.; Kawasumi, M.; Inagaki, S., Enhancement of Proton Transport by High Densification of Sulfonic Acid Groups in Highly Ordered Mesoporous Silica. *Chem. Mater.* **2013**, *25*, 1584-1591.
169. Elbert, J.; Krohm, F.; Rüttiger, C.; Kienle, S.; Didzoleit, H.; Balzer, B. N.; Hugel, T.; Stühn, B.; Gallej, M.; Brunsen, A., Polymer-Modified Mesoporous Silica Thin Films for Redox-Mediated Selective Membrane Gating. *Adv. Funct. Mater.* **2014**, *24*, 1591-1601.
170. Islam, S. Z.; Reed, A.; Kim, D. Y.; Rankin, S. E., N₂/Ar Plasma Induced Doping of Ordered Mesoporous TiO₂ Thin Films for Visible Light Active Photocatalysis *Micropor. Mesopor. Mater.* **2015**, *in press*.
171. Liu, Y.-C.; Lu, Y.-F.; Zeng, Y.-Z.; Liao, C.-H.; Chung, J.-C.; Wei, T.-Y., Nanostructured Mesoporous Titanium Dioxide Thin Film Prepared by Sol-Gel Method for Dye-Sensitized Solar Cell. *International Journal of Photoenergy* **2011**, *2011*.
172. Vivero-Escoto, J. L.; Chiang, Y. D.; C-Wwu, K.; Yamauchi, Y., Recent Progress in Mesoporous Titania Materials: Adjusting Morphology for Innovative Applications. *Sci. Technol. Adv. Mater.* **2012**, *13*.
173. Soni, S. S.; Henderson, M. J.; Bardeau, J.-F.; Gibaud, A., Visible-Light Photocatalysis in Titania-Based Mesoporous Thin Films. *Advanced Materials* **2008**, *20*, 1493-1498.
174. Ismail, A. A.; Bahnemann, D. W., Mesoporous Titania Photocatalysts: Preparation, Characterization and Reaction Mechanisms. *J. Mater. Chem.* **2011**, *21*, 11686-11707.
175. Nakata, K.; Fujishima, A., TiO₂ Photocatalysis: Design and Applications. *J. Photochem. Photobiol. C* **2012**, *13*, 169-189.
176. Pan, J. H.; Zhao, X. S.; Lee, W. I., Block Copolymer-Templated Synthesis of Highly Organized Mesoporous TiO₂-Based Films and Their Photoelectrochemical Applications. *Chem. Eng. J.* **2011**, *170*, 363-380.
177. Zhou, W.; Fu, H. G., Mesoporous TiO₂: Preparation, Doping, and as a Composite for Photocatalysis. *Chemcatchem* **2013**, *5*, 885-894.
178. Hazra, S.; Basu, S., High Sensitivity and Fast Response Hydrogen Sensors Based on Electrochemically Etched Porous Titania Thin Films. *Sensors and Actuators B: Chemical* **2006**, *115*, 403-411.
179. Hagfeldt, A.; Gratzel, M., Light-Induced Redox Reactions in Nanocrystalline Systems. *Chemical Reviews* **1995**, *95*, 49-68.
180. Villanueva-Cab, J.; Jang, S. R.; Halverson, A. F.; Zhu, K.; Frank, A. J., Trap-Free Transport in Ordered and Disordered TiO₂ Nanostructures. *Nano Lett.* **2014**, *14*, 2305-2309.
181. Jiang, C. H.; Zhang, J. S., Nanoengineering Titania for High Rate Lithium Storage: A Review. *J. Mater. Sci. Technol.* **2013**, *29*, 97-122.

182. Wu, Q. L.; Li, J. C.; Deshpande, R. D.; Subramanian, N.; Rankin, S. E.; Yang, F. Q.; Cheng, Y. T., Aligned TiO₂ Nanotube Arrays as Durable Lithium-Ion Battery Negative Electrodes. *J. Phys. Chem. C* **2012**, *116*, 18669-18677.
183. Lindsay, M. J.; Blackford, M. G.; Attard, D. J.; Luca, V.; Skyllas-Kazacos, M.; Griffith, C. S., Anodic Titania Films as Anode Materials for Lithium Ion Batteries. *Electrochim. Acta* **2007**, *52*, 6401-6411.
184. Lindsay, M. J.; Skyllas-Kazacos, M.; Luca, V., Anodically Synthesized Titania Films for Lithium Batteries: Effect of Titanium Substrate and Surface Treatment. *Electrochim. Acta* **2009**, *54*, 3501-3509.
185. Ortiz, G. F.; Hanzu, I.; Djenizian, T.; Lavela, P.; Tirado, J. L.; Knauth, P., Alternative Li-Ion Battery Electrode Based on Self-Organized Titania Nanotubes. *Chem. Mat.* **2009**, *21*, 63-67.
186. Cauda, V.; Torre, B.; Falqui, A.; Canavese, G.; Stassi, S.; Bein, T.; Pizzi, M., Confinement in Oriented Mesopores Induces Piezoelectric Behavior of Polymeric Nanowires. *Chem. Mat.* **2012**, *24*, 4215-4221.
187. Coakley, K. M.; Srinivasan, B. S.; Ziebarth, J. M.; Goh, C.; Liu, Y. X.; McGehee, M. D., Enhanced Hole Mobility in Regioregular Polythiophene Infiltrated in Straight Nanopores. *Adv. Funct. Mater.* **2005**, *15*, 1927-1932.
188. Cadby, A. J.; Tolbert, S. H., Controlling Optical Properties and Interchain Interactions in Semiconducting Polymers by Encapsulation in Periodic Nanoporous Silicas with Different Pore Sizes. *J. Phys. Chem. B* **2005**, *109*, 17879-17886.
189. Nguyen, T. Q.; Wu, J. J.; Doan, V.; Schwartz, B. J.; Tolbert, S. H., Control of Energy Transfer in Oriented Conjugated Polymer-Mesoporous Silica Composites. *Science* **2000**, *288*, 652-656.
190. Sarker, S.; Mukherjee, B.; Crone, E.; Subramanian, V., Development of a Highly Efficient 1d/0d TiO₂ Nanotube/N-CdTe Photoanode: Single-Step Attachment, Coverage, and Size Control by a Solvothermal Approach. *J. Mater. Chem. A* **2014**, *2*, 4890-4893.
191. Jagannathan, H.; Deal, M.; Nishi, Y.; Kim, H. C.; Freer, E. M.; Sundstrom, L.; Topuria, T.; Rice, P. M., Templated Germanium Nanowire Synthesis Using Oriented Mesoporous Organosilicate Thin Films. *J. Vac. Sci. Technol. B* **2006**, *24*, 2220-2224.
192. Farrell, R. A.; Petkov, N.; Morris, M. A.; Holmes, J. D., Self-Assembled Templates for the Generation of Arrays of 1-Dimensional Nanostructures: From Molecules to Devices. *J. Colloid Interface Sci.* **2010**, *349*, 449-472.
193. Barth, S.; Hernandez-Ramirez, F.; Holmes, J. D.; Romano-Rodriguez, A., Synthesis and Applications of One-Dimensional Semiconductors. *Prog. Mater. Sci.* **2010**, *55*, 563-627.
194. Park, O. H.; Cheng, J. Y.; Hart, M.; Topuria, T.; Rice, P. M.; Krupp, L. E.; Miller, R. D.; Ito, H.; Kim, H. C., High Aspect-Ratio Cylindrical Nanopore Arrays and Their Use for Templating Titania Nanoposts. *Adv. Mater.* **2008**, *20*, 738-742.
195. Yagi, I.; Hayashi, A.; Kimijima, K.; Notsu, H.; Ohta, N.; Yamaguchi, A., Mesoporous Materials toward Nanofabricator and Nanoreactor. *Electrochemistry* **2010**, *78*, 105-113.
196. Gong, D.; Grimes, C. A.; Varghese, O. K.; Hu, W. C.; Singh, R. S.; Chen, Z.; Dickey, E. C., Titanium Oxide Nanotube Arrays Prepared by Anodic Oxidation. *J. Mater. Res.* **2001**, *16*, 3331-3334.
197. Macak, J. M.; Tsuchiya, H.; Ghicov, A.; Yasuda, K.; Hahn, R.; Bauer, S.; Schmuki, P., TiO₂ Nanotubes: Self-Organized Electrochemical Formation, Properties and Applications. *Current Opin. Solid State Mater. Sci.* **2007**, *11*, 3-18.
198. Mor, G. K.; Varghese, O. K.; Paulose, M.; Shankar, K.; Grimes, C. A., A Review on Highly Ordered, Vertically Oriented TiO₂ Nanotube Arrays: Fabrication, Material Properties, and Solar Energy Applications. *Solar Energy Mater. Solar Cells* **2006**, *90*, 2011-2075.

199. Chen, X.; Mao, S. S., Titanium Dioxide Nanomaterials: Synthesis, Properties, Modifications, and Applications. *Chem. Rev.* **2007**, *107*, 2891-2959.
200. Shankar, K.; Basham, J. I.; Allam, N. K.; Varghese, O. K.; Mor, G. K.; Feng, X. J.; Paulose, M.; Seabold, J. A.; Choi, K. S.; Grimes, C. A., Recent Advances in the Use of Tio₂ Nanotube and Nanowire Arrays for Oxidative Photoelectrochemistry. *J. Phys. Chem. C* **2009**, *113*, 6327-6359.
201. Regonini, D.; Bowen, C. R.; Jaroenworuluck, A.; Stevens, R., A Review of Growth Mechanism, Structure and Crystallinity of Anodized Tio₂ Nanotubes. *Mater. Sci. Eng. R - Reports* **2013**, *74*, 377-406.
202. Huang, J. Y.; Zhang, K. Q.; Lai, Y. K., Fabrication, Modification, and Emerging Applications of Tio₂ Nanotube Arrays by Electrochemical Synthesis: A Review. *Int. J. Photoenergy* **2013**.
203. Grosso, D.; Soler-Illia, G. J. d. A. A.; Crepaldi, E. L.; Cagnol, F.; Sinturel, C.; Bourgeois, A.; Brunet-Bruneau, A.; Amenitsch, H.; Albouy, P. A.; Sanchez, C., Highly Porous Tio₂ Anatase Optical Thin Films with Cubic Mesostructure Stabilized at 700 °C. *Chemistry of Materials* **2003**, *15*, 4562-4570.
204. Urade, V. N.; Wei, T. C.; Tate, M. P.; Kowalski, J. D.; Hillhouse, H. W., Nanofabrication of Double-Gyroid Thin Films. *Chem. Mat.* **2007**, *19*, 768-777.
205. Alberius, P. C. A.; Frindell, K. L.; Hayward, R. C.; Kramer, E. J.; Stucky, G. D.; Chmelka, B. F., General Predictive Syntheses of Cubic, Hexagonal, and Lamellar Silica and Titania Mesostructured Thin Films. *Chemistry of Materials* **2002**, *14*, 3284-3294.
206. Klotz, M.; Albouy, P. A.; Ayrat, A.; Ménager, C.; Grosso, D.; Van der Lee, A.; Cabuil, V.; Babonneau, F.; Guizard, C., The True Structure of Hexagonal Mesophase-Templated Silica Films as Revealed by X-Ray Scattering: Effects of Thermal Treatments and of Nanoparticle Seeding. *Chem. Mater.* **2000**, *12*, 1721-1728.
207. Grosso, D.; Babonneau, F.; Sanchez, C.; de A.A. Soler-Illia, G. J.; Crepaldi, E. L.; Albouy, P. A.; Amenitsch, H.; Balkenende, A. R.; Brunet-Bruneau, A., A First Insight in the Mechanisms Involved in the Self-Assembly of 2d-Hexagonal Templated Sio₂ and Tio₂ Mesostructured Films During Dip-Coating. *Journal of Sol-Gel Science and Technology* **2003**, *26*, 561-565.
208. Innocenzi, P.; Malfatti, L.; Kidchob, T.; Costacurta, S.; Falcaro, P.; Piccinini, M.; Marcelli, A.; Morini, P.; Sali, D.; Amenitsch, H., Time-Resolved Simultaneous Detection of Structural and Chemical Changes During Self-Assembly of Mesostructured Films. *J. Phys. Chem. C* **2007**, *111*, 5345-5350.
209. Grosso, D.; Ribot, F.; Boissiere, C.; Sanchez, C., Molecular and Supramolecular Dynamics of Hybrid Organic-Inorganic Interfaces for the Rational Construction of Advanced Hybrid Nanomaterials. *Chem. Soc. Rev.* **2011**, *40*, 829-48.
210. Innocenzi, P.; Malfatti, L.; Kidchob, T.; Falcaro, P.; Costacurta, S.; Guglielmi, M.; Mattei, G.; Bello, V.; Amenitsch, H., Thermal-Induced Phase Transitions in Self-Assembled Mesostructured Films Studied by Small-Angle X-Ray Scattering. *Journal of synchrotron radiation* **2005**, *12*, 734-8.
211. Innocenzi, P.; Kidchob, T.; Bertolo, J. M.; Piccinini, M.; Guidi, M. C.; Marcelli, C., Time-Resolved Infrared Spectroscopy as an in Situ Tool to Study the Kinetics During Self-Assembly of Mesostructured Films. *J. Phys. Chem. B* **2006**, *110*, 10837-10841.
212. Innocenzi, P.; Malfatti, L.; Kidchob, T.; Grosso, D., Controlling the Processing of Mesoporous Titania Films by in Situ Ftir Spectroscopy: Getting Crystalline Micelles into the Mesopores. *J. Phys. Chem. C* **2010**, *114*, 10806-10811.
213. Flodström, K.; Teixeira, C. V.; Amenitsch, H.; Alfredsson, V.; Lindén, M., In Situ Synchrotron Small-Angle X-Ray Scattering/X-Ray Diffraction Study of the Formation of Sba-15 Mesoporous Silica. *Langmuir* **2004**, *20*, 4885-4891.

214. Koganti, V. R.; Dunphy, D.; Gowrishankar, V.; McGehee, M. D.; Li, X. F.; Wang, J.; Rankin, S. E., Generalized Coating Route to Silica and Titania Films with Orthogonally Tilted Cylindrical Nanopore Arrays. *Nano Lett.* **2006**, *6*, 2567-2570.
215. Jiang, Z.; Li, X.; Strzalka, J.; Sprung, M.; Sun, T.; Sandy, A. R.; Narayanan, S.; Lee, D. R.; Wang, J., The Dedicated High-Resolution Grazing-Incidence X-Ray Scattering Beamline 8-Id-E at the Advanced Photon Source. *Journal of synchrotron radiation* **2012**, *19*, 627-636.
216. Z, J. Gixgui, a Matlab-Based Software for Visualization and Reduction of Grazing Incidence X-Ray Scattering Data.
<http://www.aps.anl.gov/Sectors/Sector8/Operations/GIXSGUI.html>.
217. Smilgies, D. M., Scherrer Grain-Size Analysis Adapted to Grazing-Incidence Scattering with Area Detectors. *J. Appl. Crystallogr.* **2009**, *42*, 1030-1034.
218. Koganti, V. R.; Das, S.; Rankin, S. E., In Situ Ftir Investigation of the Kinetics of Silica Polycondensation in Surfactant Templated, Mesostuctured Thin Films. *J. Phys. Chem. C* **2014**, *in press*.
219. Kim, S. H.; Misner, M. J.; Xu, T.; Kimura, M.; Russell, T. P., Highly Oriented and Ordered Arrays from Block Copolymers Via Solvent Evaporation. *Adv. Mater.* **2004**, *16*, 226-+.
220. Maret, M., et al., Probing Self-Assembly of Cylindrical Morphology Block Copolymer Using in Situ and Ex Situ Grazing Incidence Small-Angle X-Ray Scattering: The Attractive Case of Graphoepitaxy. *Macromol.* **2014**, *47*, 7221-7229.
221. Wanka, G.; Hoffmann, H.; Ulbricht, W., Phase Diagrams and Aggregation Behavior of Poly(Oxyethylene)-Poly(Oxypropylene)-Poly(Oxyethylene) Triblock Copolymers in Aqueous Solutions. *Macromolecules* **1994**, *27*, 4145-4159.
222. Malfatti, L.; Kidchob, T.; Costacurta, S.; Falcaro, P.; Schiavuta, P.; Amenitsch, H.; Innocenzi, P., Highly Ordered Self-Assembled Mesostuctured Hafnia Thin Films: An Example of Rewritable Mesostucture. *Chem. Mater.* **2006**, *18*, 4553-4560.
223. Das, S.; Wu, Q.; Garlapalli, R. K.; Nagpure, S.; Strzalka, J.; Jiang, Z.; Rankin, S. E., In-Situ Gisaxs Investigation of Pore Orientation Effects on the Thermal Transformation Mechanism in Mesoporous Titania Thin Films. *The Journal of Physical Chemistry C* **2013**, *118*, 968-976.
224. Kothari, R.; Winter, H. H.; Watkins, J. J., Rheological Study of Order-to-Disorder Transitions and Phase Behavior of Block Copolymer–Surfactant Complexes Containing Hydrogen-Bonded Small Molecule Additives. *Macromolecules* **2014**, *47*, 8048-8055.
225. Paradiso, S. P.; Delaney, K. T.; Garcia-Cervera, C. J.; Ceniceros, H. D.; Fredrickson, G. H., Block Copolymer Self Assembly During Rapid Solvent Evaporation: Insights into Cylinder Growth and Stability. *ACS Macro Lett.* **2014**, *3*, 16-20.
226. Phillip, W. A.; Hillmyer, M. A.; Cussler, E. L., Cylinder Orientation Mechanism in Block Copolymer Thin Films Upon Solvent Evaporation. *Macromol.* **2010**, *43*, 7763-7770.
227. Kolmogorov, A., A Statistical Theory for the Recrystallization of Metals. *Akad. nauk SSSR, Izv., Ser. Matem* **1937**, *1*.
228. Avrami, M., Kinetics of Phase Change. I General Theory. *J. Chem. Phys.* **1939**, *7*, 1103-1112.
229. Avrami, M., Kinetics of Phase Change. Ii Transformation-Time Relations for Random Distribution of Nuclei. *J. Chem. Phys.* **1940**, *8*, 212-224.
230. Avrami, M., Granulation, Phase Change, and Microstructure Kinetics of Phase Change. Iii. *J. Chem. Phys.* **1941**, *9*, 177-184.
231. Jena, A. K.; Chaturvedi, M. C., *Phase Transformations in Materials*. Prentice Hall, 1992.
232. Zhao, Y.; Chen, X.; Yang, C.; Zhang, G., Mesoscopic Simulation on Phase Behavior of Pluronic P123 Aqueous Solution. *J. Phys. Chem. B* **2007**, *111*, 13937-13942.

233. Lund, R.; Willner, L.; Richter, D., Kinetics of Block Copolymer Micelles Studied by Small-Angle Scattering Methods. *Adv. Polym Sci.* **2013**, *259*, 51-158.
234. Ding, Z.; Spruiell, J. E., Interpretation of the Nonisothermal Crystallization Kinetics of Polypropylene Using a Power Law Nucleation Rate Function. *J. Polym. Sci., Part B: Polym. Phys.* **1997**, *35*, 1077-1093.
235. Toro-Vazquez, J. F.; Dibildox-Alvarado, E.; Charó-Alonso, M.; Herrera-Coronado, V.; Gómez-Aldapa, C. A., The Avrami Index and the Fractal Dimension in Vegetable Oil Crystallization. *J Amer Oil Chem Soc* **2002**, *79*, 855-866.
236. Lyakhova, K. S.; Sevink, G. J. A.; Zvelindovsky, A. V.; Horvat, A.; Magerle, R., Role of Dissimilar Interfaces in Thin Films of Cylinder-Forming Block Copolymers. *J. Chem. Phys.* **2004**, *120*, 1127-1137.
237. Su, Y. L.; Wang, J.; Liu, H. Z., Ftir Spectroscopic Investigation of Effects of Temperature and Concentration on Peo-Ppo-Peo Block Copolymer Properties in Aqueous Solutions. *Macromolecules* **2002**, *35*, 6426-6431.
238. Lu, N.; Chen, S.; Wang, H.; Quan, X.; Zhao, H., Synthesis of Molecular Imprinted Polymer Modified TiO₂ Nanotube Array Electrode and Their Photoelectrocatalytic Activity. *J. Solid State Chem.* **2008**, *181*, 2852-2858.
239. Tepavcevic, S.; Darling, S. B.; Dimitrijevic, N. M.; Rajh, T.; Sibener, S. J., Improved Hybrid Solar Cells Via in Situ Uv Polymerization. *Small* **2009**, *5*, 1776-1783.
240. Jiang, K. J.; Manseki, K.; Yu, Y. H.; Masaki, N.; Suzuki, K.; Song, Y. L.; Yanagida, S., Photovoltaics Based on Hybridization of Effective Dye-Sensitized Titanium Oxide and Hole-Conductive Polymer P3ht. *Adv. Funct. Mater.* **2009**, *19*, 2481-2485.
241. Muktha, B.; Mahanta, D.; Patil, S.; Madras, G., Synthesis and Photocatalytic Activity of Poly(3-Hexylthiophene)/TiO₂ Composites. *J. Solid State Chem.* **2007**, *180*, 2986-2989.
242. Mall, M.; Kumar, P.; Chand, S.; Kumar, L., Influence of Zns Quantum Dots on Optical and Photovoltaic Properties of Poly(3-Hexylthiophene). *Chem. Phys. Lett.* **2010**, *495*, 236-240.
243. Po, R.; Maggini, M.; Camaioni, N., Polymer Solar Cells: Recent Approaches and Achievements. *J. Phys. Chem. C* **2009**, *114*, 695-706.
244. Li, Y.; Wang, C. W.; Zhao, Y.; Wang, J.; Zhou, F., Performance Improvement of P3ht/TiO₂ Coaxial Heterojunction Polymer Solar Cells by Introducing a Cds Interface Modifier. *J. Solid State Chem.* **2012**, *196*, 349-355.
245. Zhang, T. H.; Piao, L. Y.; Zhao, S. L.; Xu, Z.; Wu, Q.; Kong, C., Application of TiO₂ with Different Structures in Solar Cells. *Chin. Phys. B* **2012**, *21*, 118401.
246. Hao, Y.; Cao, Y.; Sun, B.; Li, Y.; Zhang, Y.; Xu, D., A Novel Semiconductor-Sensitized Solar Cell Based on P3ht@Cds@TiO₂ Core-Shell Nanotube Array. *Sol. Ener. Mat. Sol. Cells* **2012**, *101*, 107-113.
247. Lee, J.; Jho, J. Y., Fabrication of Highly Ordered and Vertically Oriented TiO₂ Nanotube Arrays for Ordered Heterojunction Polymer/Inorganic Hybrid Solar Cell. *Sol. Ener. Mat. Sol. Cells* **2011**, *95*, 3152-3156.
248. Yodyingyong, S.; Zhou, X.; Zhang, Q.; Triampo, D.; Xi, J.; Park, K.; Limketkai, B.; Cao, G., Enhanced Photovoltaic Performance of Nanostructured Hybrid Solar Cell Using Highly Oriented TiO₂ Nanotubes. *J. Phys. Chem. C* **2010**, *114*, 21851-21855.
249. Sanghoon, K.; Mor, G. K.; Paulose, M.; Varghese, O. K.; Shankar, K.; Grimes, C. A., Broad Spectrum Light Harvesting in TiO₂ Nanotube Array - Hemicyanine Dye - P3ht Hybrid Solid-State Solar Cells. *IEEE J. Sel. Top. Quantum Electr.* **2010**, *16*, 1573-1580.
250. Lin, C. C., et al., Dependence of Nanocrystal Dimensionality on the Polymer Nanomorphology, Anisotropic Optical Absorption, and Carrier Transport in P3ht:TiO₂ Bulk Heterojunctions. *J. Phys. Chem. C* **2012**, *116*, 25081-25088.

251. Lin, Y.; Wei, Q.; Qian, G.; Yao, L.; Watkins, J., Morphology Control in TiO₂ Nanorod/Polythiophene Composites for Bulk Heterojunction Solar Cells Using Hydrogen Bonding. *Macromolecules* **2012**, *45*, 8665-8673.
252. Wang, J.; Zhang, T.; Wang, D.; Pan, R.; Wang, Q.; Xia, H., Influence of Cdse Quantum Dot Interlayer on the Performance of Polymer/TiO₂ Nanorod Arrays Hybrid Solar Cell. *Chem. Phys. Lett.* **2012**, *541*, 105-109.
253. Xu, T.; Yan, M.; Hoefelmeyer, J. D.; Qiao, Q., Exciton Migration and Charge Transfer in Chemically Linked P3ht-TiO₂ Nanorod Composite. *RSC Adv.* **2012**, *2*, 854-862.
254. Zeng, T. W.; Ho, C. C.; Tu, Y. C.; Tu, G. Y.; Wang, L. Y.; Su, W. F., Correlating Interface Heterostructure, Charge Recombination, and Device Efficiency of Poly(3-Hexyl Thiophene)/TiO₂ Nanorod Solar Cell. *Langmuir* **2011**, *27*, 15255-15260.
255. Huang, Y. C.; Hsu, J. H.; Liao, Y. C.; Yen, W. C.; Li, S. S.; Lin, S. T.; Chen, C. W.; Su, W. F., Employing an Amphiphilic Interfacial Modifier to Enhance the Performance of a Poly(3-Hexyl Thiophene)/TiO₂ Hybrid Solar Cell. *J. Mater. Chem.* **2011**, *21*, 4450-4456.
256. Bouclé, J.; Chyla, S.; Shaffer, M. S. P.; Durrant, J. R.; Bradley, D. D. C.; Nelson, J., Hybrid Solar Cells from a Blend of Poly(3-Hexylthiophene) and Ligand-Capped TiO₂ Nanorods. *Adv. Funct. Mater.* **2008**, *18*, 622-633.
257. Guo, W.; Shen, Y.; Wu, M.; Ma, T., Highly Efficient Inorganic-Organic Heterojunction Solar Cells Based on Sensitized Spherical TiO₂ Electrodes. *Chem. Commun.* **2012**, *48*, 6133-6135.
258. Nunzi, J. M., Organic Photovoltaic Materials and Devices. *C. R. Phys.* **2002**, *3*, 523-542.
259. Kroeze, J. E.; Savenije, T. J.; Vermeulen, M. J. W.; Warman, J. M., Contactless Determination of the Photoconductivity Action Spectrum, Exciton Diffusion Length, and Charge Separation Efficiency in Polythiophene-Sensitized TiO₂ Bilayers. *J. Phys. Chem. B* **2003**, *107*, 7696-7705.
260. Forro, L.; Chauvet, O.; Emin, D.; Zuppiroli, L.; Berger, H.; Lévy, F., High Mobility N-Type Charge Carriers in Large Single Crystals of Anatase (TiO₂). *J. Appl. Phys.* **1994**, *75*, 633-635.
261. Campus, F.; Bonhôte, P.; Grätzel, M.; Heinen, S.; Walder, L., Electrochromic Devices Based on Surface-Modified Nanocrystalline TiO₂ Thin-Film Electrodes. *Sol. Ener. Mat. Sol. Cells* **1999**, *56*, 281-297.
262. Nakayama, K.; Kubo, T.; Nishikitani, Y., Electrophoretically Deposited TiO₂ Nanotube Light-Scattering Layers of Dye-Sensitized Solar Cells. *Jpn. J. Appl. Phys.* **2008**, *47*, 6610-6614.
263. Fujibayashi, T.; Matsui, T.; Kondo, M., Improvement in Quantum Efficiency of Thin Film Si Solar Cells Due to the Suppression of Optical Reflectance at Transparent Conducting Oxide/Si Interface by TiO₂/Zno Antireflection Coating. *Appl. Phys. Lett.* **2006**, *88*, 183508.
264. Steim, R.; Kogler, F. R.; Brabec, C. J., Interface Materials for Organic Solar Cells. *J. Mater. Chem.* **2010**, *20*, 2499-2512.
265. Tricoli, A.; Wallerand, A. S.; Righettoni, M., Highly Porous TiO₂ Films for Dye Sensitized Solar Cells. *J. Mater. Chem.* **2012**, *22*, 14254-14261.
266. Coakley, K. M.; Liu, Y.; Goh, C.; McGehee, M. D., Ordered Organic-Inorganic Bulk Heterojunction Photovoltaic Cells. *MRS Bull.* **2005**, *30*, 37-40.
267. Pan, J. H.; Lei, Z.; Lee, W. I.; Xiong, Z.; Wang, Q.; Zhao, X. S., Mesoporous TiO₂ Photocatalytic Films on Stainless Steel for Water Decontamination. *Cat. Sci. Technol.* **2012**, *2*, 147-155.
268. Kimura, T.; Miyamoto, N.; Meng, X.; Ohji, T.; Kato, K., Rapid Fabrication of Mesoporous Titania Films with Controlled Macroporosity to Improve Photocatalytic Property. *Chemistry – An Asian Journal* **2009**, *4*, 1486-1493.

269. Meng, X.; Kimura, T.; Ohji, T.; Kato, K., Triblock Copolymer Templated Semi-Crystalline Mesoporous Titania Films Containing Emulsion-Induced Macropores. *J. Mater. Chem.* **2009**, *19*, 1894-1900.
270. Pan, J. H.; Lee, W. I., Preparation of Highly Ordered Cubic Mesoporous WO_3/TiO_2 Films and Their Photocatalytic Properties. *Chem. Mater.* **2006**, *18*, 847-853.
271. Kandiel, T. A.; Ismail, A. A.; Bahnemann, D. W., Mesoporous TiO_2 Nanostructures: A Route to Minimize Pt Loading on Titania Photocatalysts for Hydrogen Production. *Phys. Chem. Chem. Phys.* **2011**, *13*, 20155-20161.
272. Ismail, A. A.; Kandiel, T. A.; Bahnemann, D. W., Novel (and Better?) Titania-Based Photocatalysts: Brookite Nanorods and Mesoporous Structures. *J. Photochem. Photobiol., B* **2010**, *216*, 183-193.
273. Ismail, A. A.; Bahnemann, D. W.; Robben, L.; Yarovy, V.; Wark, M., Palladium Doped Porous Titania Photocatalysts: Impact of Mesoporous Order and Crystallinity. *Chem. Mater.* **2009**, *22*, 108-116.
274. Yuan, Q.; Liu, Y.; Li, L. L.; Li, Z. X.; Fang, C. J.; Duan, W. T.; Li, X. G.; Yan, C. H., Highly Ordered Mesoporous Titania-Zirconia Photocatalyst for Applications in Degradation of Rhodamine-B and Hydrogen Evolution. *Microporous Mesoporous Mater.* **2009**, *124*, 169-178.
275. Zhang, X.; Pan, J. H.; Du, A. J.; Ng, J.; Sun, D. D.; Leckie, J. O., Fabrication and Photocatalytic Activity of Porous TiO_2 Nanowire Microspheres by Surfactant-Mediated Spray Drying Process. *MRS Bull.* **2009**, *44*, 1070-1076.
276. Veith, G. M.; Baggetto, L.; Sacci, R. L.; Unocic, R. R.; Tenhaeff, W. E.; Browning, J. F., Direct Measurement of the Chemical Reactivity of Silicon Electrodes with LiPF_6 -Based Battery Electrolytes. *Chem. Comm.* **2014**, *50*, 3081-3084.
277. Feng, P.; Bu, X.; Pine, D. J., Control of Pore Sizes in Mesoporous Silica Templated by Liquid Crystals in Block Copolymer-Cosurfactant-Water Systems. *Langmuir* **2000**, *16*, 5304-5310.
278. Manceau, M.; Rivaton, A.; Gardette, J. L.; Guillerez, S.; Lemaître, N., The Mechanism of Photo- and Thermo-oxidation of Poly(3-Hexylthiophene) (P3ht) Reconsidered. *Polym. Degrad. Stab.* **2009**, *94*, 898-907.
279. Brown, P. J.; Thomas, D. S.; Köhler, A.; Wilson, J. S.; Kim, J. S.; Ramsdale, C. M.; Siringhaus, H.; Friend, R. H., Effect of Interchain Interactions on the Absorption and Emission of Poly(3-Hexylthiophene). *Phys. Rev. B* **2003**, *67*, 064203.
280. Kim, M. H.; Suh, M.; Gowrishankar, V.; McGehee, M. D.; Kwon, Y. U., Confinement Effects of P3ht in Nanochannels and Their Implications for Bulk Heterojunction Solar Cells. *J. Nanosci. Nanotechnol.* **2010**, *10*, 279-284.
281. Nelson, A., Co-Refinement of Multiple-Contrast Neutron/X-Ray Reflectivity Data Using Motofit. *J. Appl. Crystallogr.* **2006**, *39*, 273-276.
282. Rawolle, M., et al., Infiltration of Polymer Hole-Conductor into Mesoporous Titania Structures for Solid-State Dye-Sensitized Solar Cells. *ACS Appl. Mater. Interfaces* **2012**, *5*, 719-729.
283. Harrison, M. G.; Grüner, J.; Spencer, G. C. W., Analysis of the Photocurrent Action Spectra of MeH-Ppv Polymer Photodiodes. *Phys. Rev. B* **1997**, *55*, 7831-7849.
284. Martín, J.; Maiz, J.; Sacristan, J.; Mijangos, C., Tailored Polymer-Based Nanorods and Nanotubes by "Template Synthesis": From preparation to Applications. *Polymer* **2012**, *53*, 1149-1166.
285. Xu, J.; Wang, J.; Mitchell, M.; Mukherjee, P.; Jeffries-El, M.; Petrich, J. W.; Lin, Z., Organic-Inorganic Nanocomposites Via Directly Grafting Conjugated Polymers onto Quantum Dots. *J. Am. Chem. Soc.* **2007**, *129*, 12828-12833.

286. Kwong, C. Y.; Choy, W. C. H.; Djurišić, A. B.; Chui, P. C.; Cheng, K. W.; Chan, W. K., Poly(3-Hexylthiophene):TiO₂ Nanocomposites for Solar Cell Applications. *Nanotechnology* **2004**, *15*, 1156.
287. Paudel, N.; Xiao, C.; Yan, Y., Close-Space Sublimation Grown Cds Window Layers for Cds/Cdte Thin-Film Solar Cells. *J. Mater. Sci. -Mater. Electron.* **2014**, *25*, 1991-1998.
288. Rose, D. H.; Hasoon, F. S.; Dhere, R. G.; Albin, D. S.; Ribelin, R. M.; Li, X. S.; Mahathongdy, Y.; Gessert, T. A.; Sheldon, P., Fabrication Procedures and Process Sensitivities for Cds/Cdte Solar Cells. *Prog. Photovolt. Res. Appl.* **1999**, *7*, 331-340.
289. Wu, X., High-Efficiency Polycrystalline Cdte Thin-Film Solar Cells. *Sol. Energy* **2004**, *77*, 803-814.
290. Diebold, U., The Surface Science of Titanium Dioxide. *Surf. Sci. Reports* **2003**, *48*, 53-229.
291. Barrera, M.; Plá, J.; Bocchi, C.; Migliori, A., Antireflecting–Passivating Dielectric Films on Crystalline Silicon Solar Cells for Space Applications. *Sol. Energ. Mat. Sol. Cells* **2008**, *92*, 1115-1122.
292. Singh, R. S.; Rangari, V. K.; Sanagapalli, S.; Jayaraman, V.; Mahendra, S.; Singh, V. P., Nano-Structured Cdte, Cds and TiO₂ for Thin Film Solar Cell Applications. *Sol. Energ. Mat. Sol. Cells* **2004**, *82*, 315-330.
293. Karaagac, H.; Parlak, M.; Aygun, L. E.; Ghaffari, M.; Biyikli, N.; Okyay, A. K., A Baseball-Bat-Like Cdte/TiO₂ Nanorods-Based Heterojunction Core–Shell Solar Cell. *Scripta Mater.* **2013**, *69*, 323-326.
294. Luo, B.; Deng, Y.; Wang, Y.; Zhang, Z.; Tan, M., Heterogeneous Flammulina Velutipes-Like Cdte/TiO₂ Nanorod Array: A Promising Composite Nanostructure for Solar Cell Application. *J. Alloys Compd.* **2012**, *517*, 192-197.
295. Yang, H.; Fan, W.; Vaneski, A.; Susha, A. S.; Teoh, W. Y.; Rogach, A. L., Heterojunction Engineering of Cdte and Cdse Quantum Dots on TiO₂ Nanotube Arrays: Intricate Effects of Size-Dependency and Interfacial Contact on Photoconversion Efficiencies. *Adv. Funct. Mater.* **2012**, *22*, 2821-2829.
296. Zhang, M.; Wang, Y. N.; Moulin, E.; Grutzmacher, D.; Chien, C. J.; Chang, P. C.; Gao, X.; Carius, R.; Lu, J. G., Core-Shell Cdte-TiO₂ Nanostructured Solar Cell. *J. Mater. Chem.* **2012**, *22*, 10441-10443.
297. Ernst, K.; Belaidi, A.; Könenkamp, R., Solar Cell with Extremely Thin Absorber on Highly Structured Substrate. *Semicond. Sci. Technol.* **2003**, *18*, 475.
298. Tiefenbacher, S.; Pettenkofer, C.; Jaegermann, W., Ultrahigh Vacuum Preparation and Characterization of TiO₂/Cdte Interfaces: Electrical Properties and Implications for Solar Cells. *J. Appl. Phys.* **2002**, *91*, 1984-1987.
299. Grasso, C.; Ernst, K.; Könenkamp, R.; Lux-Steiner, M.; Burgelman, M., Photoelectrical Characterisation and Modelling of the Eta-Solar Cell. *Proceedings of the 17th European Photovoltaic Solar Energy Conference* **2001**, *1*, 211-214.
300. Yue, G. T.; Wu, J.; Xiao, Y. M.; Lin, J. M.; Huang, M. L.; Fan, L.; Lan, Z., Quantum Dot-Sensitized Solar Cells Employing Pt/C60 Counter Electrode Provide an Efficiency Exceeding 2%. *Science China Chemistry* **2013**, *56*, 93-100.
301. Lin, X.; Wang, C.; Xu, S.; Cui, Y., Manipulation of Inter-Particle Interactions between TiO₂ and Cdte: An Effective Method to Enhance the Performance of Quantum Dot Sensitized Solar Cells. *J. Phys. D: Appl. Phys.* **2014**, *47*, 015103.
302. Lekha, P.; Balakrishnan, A.; Subramanian, K. R. V.; Nair, S. V., Size Dependent Electron Transfer from Cdte Quantum Dots Linked to TiO₂ Thin Films in Quantum Dot Sensitized Solar Cells. *Mater. Chem Phys.* **2013**, *141*, 216-222.

303. Murray, C. B.; Norris, D. J.; Bawendi, M. G., Synthesis and Characterization of Nearly Monodisperse Cde (E = Sulfur, Selenium, Tellurium) Semiconductor Nanocrystallites. *J. Am. Chem. Soc.* **1993**, *115*, 8706-8715.
304. Yu, W.; Qu, L.; Guo, W.; Peng, X., Experimental Determination of the Extinction Coefficient of Cdte, Cdse and Cds Nanocrystals. *Chem. Mater.* **2004**, *16*, 560-560.
305. Sambur, J. B.; Novet, T.; Parkinson, B. A., Multiple Exciton Collection in a Sensitized Photovoltaic System. *Science* **2010**, *330*, 63-66.
306. Semonin, O. E.; Luther, J. M.; Choi, S.; Chen, H. Y.; Gao, J.; Nozik, A. J.; Beard, M. C., Peak External Photocurrent Quantum Efficiency Exceeding 100% Via Meg in a Quantum Dot Solar Cell. *Science* **2011**, *334*, 1530-1533.
307. Liu, D.; Kamat, P. V., Photoelectrochemical Behavior of Thin Cadmium Selenide and Coupled Titania/Cadmium Selenide Semiconductor Films. *J. Phys. Chem.* **1993**, *97*, 10769-10773.
308. Vogel, R.; Hoyer, P.; Weller, H., Quantum-Sized Pbs, Cds, Ag₂s, Sb₂s₃, and Bi₂s₃ Particles as Sensitizers for Various Nanoporous Wide-Bandgap Semiconductors. *J. Phys. Chem.* **1994**, *98*, 3183-3188.
309. Gerischer, H.; Lübke, M., A Particle Size Effect in the Sensitization of Tio₂ Electrodes by a Cds Deposit. *J. Electroanal. Chem. Interfacial Electrochem.* **1986**, *204*, 225-227.
310. Hyun, B. R.; Zhong, Y. W.; Bartnik, A. C.; Sun, L.; Abruña, H. D.; Wise, F. W.; Goodreau, J. D.; Matthews, J. R.; Leslie, T. M.; Borrelli, N. F., Electron Injection from Colloidal Pbs Quantum Dots into Titanium Dioxide Nanoparticles. *ACS Nano* **2008**, *2*, 2206-2212.
311. Günes, S.; Neugebauer, H.; Sariciftci, N. S.; Roither, J.; Kovalenko, M.; Pillwein, G.; Heiss, W., Hybrid Solar Cells Using Hgte Nanocrystals and Nanoporous Tio₂ Electrodes. *Adv. Funct. Mater.* **2006**, *16*, 1095-1099.
312. Bai, Z.; Yang, J.; Wang, D., Thin Film Cdte Solar Cells with an Absorber Layer Thickness in Micro- and Sub-Micrometer Scale. *Appl. Phys. Lett.* **2011**, *99*, 143502.
313. Ferekides, C. S.; Marinskiy, D.; Viswanathan, V.; Tetali, B.; Palekis, V.; Selvaraj, P.; Morel, D. L., High Efficiency Cds Cdte Solar Cells. *Thin Solid Films* **2000**, *361-362*, 520-526.
314. Compaan, A. D.; Gupta, A.; Drayton, J.; Lee, S. H.; Wang, S., 14% Sputtered Thin-Film Solar Cells Based on Cdte. *Phys. Status Solidi B* **2004**, *241*, 779-782.
315. Bonnet, D.; Henrichs, B.; Richter, H., Some Phenomena in Cdte/Cds Thin Film Solar Cells Made by Close-Spaced Sublimation. *Int. J. Sol. Energ.* **1992**, *12*, 133-136.
316. Moutinho, H. R.; Al-Jassim, M. M.; Levi, D. H.; Dippo, P. C.; Kazmerski, L. L., Effects of Cdcl₂ Treatment on the Recrystallization and Electro-Optical Properties of Cdte Thin Films. *J. Vac. Sci. Technol., A* **1998**, *16*, 1251-1257.
317. Abou-Elfotouh, F. A.; Moutinho, H. R.; Hasoon, F. S.; Ahrenkiel, R. K.; Levi, D.; Kazmerski, L. L. In *Effects of Processing on the Properties of Polycrystalline Cdte Grown by Various Deposition Techniques*, Twenty-Third IEEE Photovoltaic Specialists Conference, Louisville, KY, 10-14 May 1993; Louisville, KY, May 10-14, 1993; pp 491-494.
318. Sarlund, J.; Ritala, M.; Leskelä, M.; Siponmaa, E.; Zilliacus, R., Characterization of Etching Procedure in Preparation of Cdte Solar Cells. *Sol. Energ. Mat. Sol. Cells* **1996**, *44*, 177-190.
319. Ferekides, C. S.; Viswanathan, V.; Morel, D. L. In *Rf Sputtered Back Contacts for Cdte/Cds Thin Film Solar Cells*, Twenty-Sixth IEEE Photovoltaic Specialists Conference, Anaheim, CA, 29 Sep-3 Oct 1997; Anaheim, CA, September 29-October 3, 1997; pp 423-426.
320. Niles, D. W.; Li, X.; Sheldon, P.; Höchst, H., A Photoemission Determination of the Band Diagram of the Te/Cdte Interface. *J. Appl. Phys.* **1995**, *77*, 4489-4493.
321. Corwine, C. R.; Pudov, A. O.; Gloeckler, M.; Demtsu, S. H.; Sites, J. R., Copper Inclusion and Migration from the Back Contact in Cdte Solar Cells. *Sol. Energ. Mat. Sol. Cells* **2004**, *82*, 481-489.

322. Bätzner, D. L.; Romeo, A.; Zogg, H.; Wendt, R.; Tiwari, A. N., Development of Efficient and Stable Back Contacts on Cdte/Cds Solar Cells. *Thin Solid Films* **2001**, *387*, 151-154.
323. Zou, Y.; Li, D.; Sheng, X.; Wang, L.; Yang, D., Fabrication of TiO₂ Nanorod Array/Semiconductor Nanocrystal Hybrid Structure for Photovoltaic Applications. *Sol. Energy* **2012**, *86*, 1359-1365.
324. Badawi, A.; Al-Hosiny, N.; Abdallah, S.; Negm, S.; Talaat, H., Tuning Photocurrent Response through Size Control of Cdte Quantum Dots Sensitized Solar Cells. *Sol. Energy* **2013**, *88*, 137-143.
325. Yella, A.; Heiniger, L. P.; Gao, P.; Nazeeruddin, M. K.; Grätzel, M., Nanocrystalline Rutile Electron Extraction Layer Enables Low-Temperature Solution Processed Perovskite Photovoltaics with 13.7% Efficiency. *Nano Lett.* **2014**, *14*, 2591-2596.
326. Qiu, Y.; Chen, W.; Yang, S., Double-Layered Photoanodes from Variable-Size Anatase TiO₂ Nanospindles: A Candidate for High-Efficiency Dye-Sensitized Solar Cells. *Angew. Chem. Int. Ed.* **2010**, *49*, 3675-3679.
327. Sommeling, P. M.; O'Regan, B. C.; Haswell, R. R.; Smit, H. J. P.; Bakker, N. J.; Smits, J. J. T.; Kroon, J. M.; van Roosmalen, J. A. M., Influence of a TiCl₄ Post-Treatment on Nanocrystalline TiO₂ Films in Dye-Sensitized Solar Cells. *J. Phys. Chem. B* **2006**, *110*, 19191-19197.
328. Sharma, S. N.; Kohli, S.; Rastogi, A. C., Quantum Confinement Effects of Cdte Nanocrystals Sequestered in TiO₂ Matrix: Effect of Oxygen Incorporation. *Physica E* **2005**, *25*, 554-561.
329. Tang, J.; Mao, D.; Ohno, T. R.; Kaydanov, V.; Trefny, J. U. In *Properties of ZnTe:Cu Thin Films and Cds/Cdte/ZnTe Solar Cells*, Twenty-Sixth IEEE Photovoltaic Specialists Conference, Anaheim, CA, 29 Sep-3 Oct 1997; Anaheim, CA, September 29-October 3, 1997; pp 439-442.
330. Gessert, T. A.; Sheldon, P.; Li, X.; Dunlavy, D.; Niles, D.; Sasala, R.; Albright, S.; Zadler, B. In *Studies of ZnTe Back Contacts to Cds/Cdte Solar Cells*, Twenty-Sixth IEEE Photovoltaic Specialists Conference, Anaheim, CA, 29 Sep-3 Oct 1997; Anaheim, CA, September 29-October 3, 1997; pp 419-422.
331. Romeo, N.; Bosio, A.; Canevari, V., Large Crystalline Grain Cdte Thin Films for Photovoltaic Application. *Int. J. Sol. Energ.* **1992**, *12*, 183-186.
332. Niemegeers, A.; Burgelman, M., Effects of the Au/Cdte Back Contact on Iv and Cv Characteristics of Au/Cdte/Cds/Tco Solar Cells. *J. Appl. Phys.* **1997**, *81*, 2881-2886.
333. Wu, Q. L.; Li, J.; Deshpande, R. D.; Subramanian, N.; Rankin, S. E.; Yang, F.; Cheng, Y. T., Aligned TiO₂ Nanotube Arrays as Durable Lithium-Ion Battery Negative Electrodes. *J. Phys. Chem. C* **2012**, *116*, 18669-18677.
334. Shen, L.; Uchaker, E.; Yuan, C.; Nie, P.; Zhang, M.; Zhang, X.; Cao, G., Three-Dimensional Coherent Titania-Mesoporous Carbon Nanocomposite and Its Lithium-Ion Storage Properties. *ACS Appl. Mater. Interfaces* **2012**, *4*, 2985-2992.
335. Scrosati, B.; Garche, J., Lithium Batteries: Status, Prospects and Future. *J. Power Sources* **2010**, *195*, 2419-2430.
336. Wang, K.; Wei, M.; Morris, M. A.; Zhou, H.; Holmes, J. D., Mesoporous Titania Nanotubes: Their Preparation and Application as Electrode Materials for Rechargeable Lithium Batteries. *Adv. Mater.* **2007**, *19*, 3016-3020.
337. Chen, Z.; Belharouak, I.; Sun, Y. K.; Amine, K., Titanium-Based Anode Materials for Safe Lithium-Ion Batteries. *Adv. Funct. Mater.* **2013**, *23*, 959-969.
338. Li, W.; Wu, Z.; Wang, J.; Elzatahry, A. A.; Zhao, D., A Perspective on Mesoporous TiO₂ Materials. *Chem. Mater.* **2014**, *26*, 287-298.

339. Fu, L. J.; Zhang, T.; Cao, Q.; Zhang, H. P.; Wu, Y. P., Preparation and Characterization of Three-Dimensionally Ordered Mesoporous Titania Microparticles as Anode Material for Lithium Ion Battery. *Electrochemistry Communications* **2007**, *9*, 2140-2144.
340. Shim, H. W.; Lee, D. K.; Cho, I. S.; Hong, K. S.; Kim, D. W., Facile Hydrothermal Synthesis of Porous TiO₂ Nanowire Electrodes with High-Rate Capability for Li Ion Batteries. *Nanotechnology* **2010**, *21*, 255706.
341. Yu, J. C.; Li, G.; Wang, X.; Hu, X.; Leung, C. W.; Zhang, Z., An Ordered Cubic Im3m Mesoporous Cr-TiO₂ Visible Light Photocatalyst. *Chem. Comm.* **2006**, 2717-2719.
342. Zachau-Christiansen, B.; West, K.; Jacobsen, T.; Atlung, S., Lithium Insertion in Different TiO₂ Modifications. *Solid State Ionics* **1988**, *28*, 1176-1182.
343. Huang, S. Y.; Kavan, L.; Exnar, I.; Grätzel, M., Rocking Chair Lithium Battery Based on Nanocrystalline TiO₂ (Anatase). *J. Electrochem. Soc.* **1995**, *142*, L142-L144.
344. Kavan, L.; Grätzel, M.; Rathouský, J.; Zukalb, A., Nanocrystalline TiO₂ (Anatase) Electrodes: Surface Morphology, Adsorption, and Electrochemical Properties. *J. Electrochem. Soc.* **1996**, *143*, 394-400.
345. Nuspl, G.; Yoshizawa, K.; Yamabe, T., Lithium Intercalation in TiO₂ Modifications. *J. Mater. Chem.* **1997**, *7*, 2529-2536.
346. Deng, D.; Kim, M. G.; Lee, J. Y.; Cho, J., Green Energy Storage Materials: Nanostructured TiO₂ and Sn-Based Anodes for Lithium-Ion Batteries. *Energy Environ. Sci.* **2009**, *2*, 818-837.
347. Hu, Y. S.; Kienle, L.; Guo, Y. G.; Maier, J., High Lithium Electroactivity of Nanometer-Sized Rutile TiO₂. *Adv. Mater.* **2006**, *18*, 1421-1426.
348. Kavan, L.; Kalbáč, M.; Zúkalová, M.; Exnar, I.; Lorenzen, V.; Nesper, R.; Grätzel, M., Lithium Storage in Nanostructured TiO₂ Made by Hydrothermal Growth. *Chem. Mater.* **2004**, *16*, 477-485.
349. Armstrong, A. R.; Armstrong, G.; Canales, J.; García, R.; Bruce, P. G., Lithium-Ion Intercalation into TiO₂-B Nanowires. *Adv. Mater.* **2005**, *17*, 862-865.
350. Attia, A.; Zúkalová, M.; Rathouský, J.; Zukal, A.; Kavan, L., Mesoporous Electrode Material from Alumina-Stabilized Anatase TiO₂ for Lithium Ion Batteries. *J Solid State Electrochem* **2005**, *9*, 138-145.
351. Li, J.; Tang, Z.; Zhang, Z., Preparation and Novel Lithium Intercalation Properties of Titanium Oxide Nanotubes. *Electrochem. Solid-State Lett.* **2005**, *8*, A316-A319.
352. Wang, J.; Zhou, Y.; Hu, Y.; O'Hayre, R.; Shao, Z., Facile Synthesis of Nanocrystalline TiO₂ Mesoporous Microspheres for Lithium-Ion Batteries. *J. Phys. Chem. C* **2011**, *115*, 2529-2536.
353. Wang, Y.; Wu, M.; Zhang, W. F., Preparation and Electrochemical Characterization of TiO₂ Nanowires as an Electrode Material for Lithium-Ion Batteries. *Electrochim. Acta* **2008**, *53*, 7863-7868.
354. Kubiak, P.; Pfanzelt, M.; Geserick, J.; Hörmann, U.; Hüsing, N.; Kaiser, U.; Wohlfahrt-Mehrens, M., Electrochemical Evaluation of Rutile TiO₂ Nanoparticles as Negative Electrode for Li-Ion Batteries. *J. Power Sources* **2009**, *194*, 1099-1104.
355. Lee, S. G.; Deng, H.; Hu, J.; Zhou, L.; Liu, H., Anodic Performance of Mesoporous TiO₂-C Composites with Cu Nanoparticles Embedded for Lithium Ion Battery. *Int. J. Electrochem. Sci.* **2013**, *8*, 2204-2219.
356. Fattakhova-Rohlfing, D.; Wark, M.; Brezesinski, T.; Smarsly, B. M.; Rathouský, J., Highly Organized Mesoporous TiO₂ Films with Controlled Crystallinity: A Li-Insertion Study. *Adv. Funct. Mater.* **2007**, *17*, 123-132.
357. Richman, E. K.; Brezesinski, T.; Tolbert, S. H., Vertically Oriented Hexagonal Mesoporous Films Formed through Nanometre-Scale Epitaxy. *Nat. Mater.* **2008**, *7*, 712-717.

358. Hengerer, R.; Kavan, L.; Krtil, P.; Grätzel, M., Orientation Dependence of Charge-Transfer Processes on TiO₂ (Anatase) Single Crystals. *J. Electrochem. Soc.* **2000**, *147*, 1467-1472.
359. Kavan, L.; Grätzel, M.; Gilbert, S. E.; Klemenz, C.; Scheel, H. J., Electrochemical and Photoelectrochemical Investigation of Single-Crystal Anatase. *J. Am. Chem. Soc.* **1996**, *118*, 6716-6723.
360. Attia, A.; Zukalová, M.; Rathouský, J.; Zukal, A.; Kavan, L., Mesoporous Electrode Material from Alumina-Stabilized Anatase TiO₂ for Lithium Ion Batteries. *J. Solid State Electrochem.* **2004**, *9*, 138-145.
361. Lindström, H.; Södergren, S.; Solbrand, A.; Rensmo, H.; Hjelm, J.; Hagfeldt, A.; Lindquist, S. E., Li⁺ Ion Insertion in TiO₂ (Anatase). 2. Voltammetry on Nanoporous Films. *J. Phys. Chem. B* **1997**, *101*, 7717-7722.
362. van de Krol, R.; Goossens, A.; Schoonman, J., Spatial Extent of Lithium Intercalation in Anatase TiO₂. *J. Phys. Chem. B* **1999**, *103*, 7151-7159.
363. van de Krol, R.; Goossens, A.; Meulenkamp, E. A., In Situ X-Ray Diffraction of Lithium Intercalation in Nanostructured and Thin Film Anatase TiO₂. *J. Electrochem. Soc.* **1999**, *146*, 3150-3154.
364. Krtil, P.; Fattakhova, D.; Kavan, L.; Burnside, S.; Grätzel, M., Lithium Insertion into Self-Organized Mesoscopic TiO₂ (Anatase) Electrodes. *Solid State Ionics* **2000**, *135*, 101-106.
365. Yang, H. G.; Zeng, H. C., Preparation of Hollow Anatase TiO₂ Nanospheres Via Ostwald Ripening. *J. Phys. Chem. B* **2004**, *108*, 3492-3495.
366. Södergren, S.; Siegbahn, H.; Rensmo, H.; Lindström, H.; Hagfeldt, A.; Lindquist, S. E., Lithium Intercalation in Nanoporous Anatase TiO₂ Studied with Xps. *J. Phys. Chem. B* **1997**, *101*, 3087-3090.
367. Wagemaker, M.; Kearley, G. J.; van Well, A. A.; Mutka, H.; Mulder, F. M., Multiple Li Positions inside Oxygen Octahedra in Lithiated TiO₂ Anatase. *J. Am. Chem. Soc.* **2003**, *125*, 840-848.
368. Xia, H.; Zhang, T.; Wang, D.; Wang, J.; Liang, K., Composite Interfacial Modification in TiO₂ Nanorod Array/Poly(3-Hexylthiophene) Hybrid Photovoltaic Devices. *J. Alloys Compd.* **2013**, *575*, 218-222.
369. Rattanavoravipa, T.; Sagawa, T.; Yoshikawa, S., Photovoltaic Performance of Hybrid Solar Cell with TiO₂ Nanotubes Arrays Fabricated through Liquid Deposition Using ZnO Template. *Sol. Ener. Mat. Sol. Cells* **2008**, *92*, 1445-1449.
370. Wang, Z. J.; Qu, S. C.; Zeng, X. B.; Liu, J. P.; Zhang, C. S.; Tan, F. R.; Jin, L.; Wang, Z. G., Hybrid Bulk Heterojunction Solar Cells from a Blend of Poly(3-Hexylthiophene) and TiO₂ Nanotubes. *Appl. Surf. Sci.* **2008**, *255*, 1916-1920.
371. TANVEER, M.; HABIB, A.; KHAN, M. B., Dependence of Organic/Inorganic Photovoltaic Device Performance on Precursor's Concentration Used for Electrospun TiO₂ Nanofibers. *Nano* **2013**, *08*, 1350033.
372. Tai, Q.; Zhao, X.; Yan, F., Hybrid Solar Cells Based on Poly(3-Hexylthiophene) and Electrospun TiO₂ Nanofibers with Effective Interface Modification. *J. Mater. Chem.* **2010**, *20*, 7366-7371.
373. Lin, Y. Y.; Chu, T. H.; Li, S. S.; Chuang, C. H.; Chang, C. H.; Su, W. F.; Chang, C. P.; Chu, M. W.; Chen, C. W., Interfacial Nanostructuring on the Performance of Polymer/TiO₂ Nanorod Bulk Heterojunction Solar Cells. *J. Am. Chem. Soc.* **2009**, *131*, 3644-3649.
374. Zhong, M.; Yang, D.; Zhang, J.; Shi, J.; Wang, X.; Li, C., Improving the Performance of CdS/P3ht Hybrid Inverted Solar Cells by Interfacial Modification. *Sol. Ener. Mat. Sol. Cells* **2012**, *96*, 160-165.

375. Gadisa, A.; Liu, Y.; Samulski, E. T.; Lopez, R., Minimizing Interfacial Losses in Inverted Organic Solar Cells Comprising Al-Doped ZnO. *Appl. Phys. Lett.* **2012**, *100*, 253903.
376. Casino, S.; Di Lupo, F.; Francia, C.; Tuel, A.; Bodoardo, S.; Gerbaldi, C., Surfactant-Assisted Sol Gel Preparation of High-Surface Area Mesoporous TiO₂ Nanocrystalline Li-Ion Battery Anodes. *J. Alloys Compd.* **2014**, *594*, 114-121.
377. Zhao, G.; Meng, Y.; Zhang, N.; Sun, K., Electrodeposited Si Film with Excellent Stability and High Rate Performance for Lithium-Ion Battery Anodes. *Mater. Lett.* **2012**, *76*, 55-58.
378. Yan, D.; Bai, Y.; Yu, C.; Li, X.; Zhang, W., A Novel Pineapple-Structured Si/TiO₂ Composite as Anode Material for Lithium Ion Batteries. *J. Alloys Compd.* **2014**, *609*, 86-92.
379. Zeng, Z. Y.; Tu, J. P.; Huang, X. H.; Wang, X. L.; Zhao, X. B.; Li, K. F., Electrochemical Properties of a Mesoporous Si/TiO₂ Nanocomposite Film Anode for Lithium-Ion Batteries. *Electrochem. Solid-State Lett.* **2008**, *11*, A105-A107.
380. Lotfabad, E. M.; Kalisvaart, P.; Kohandehghan, A.; Cui, K.; Kupsta, M.; Farbod, B.; Mitlin, D., Si Nanotubes Ald Coated with TiO₂, Tin or Al₂O₃ as High Performance Lithium Ion Battery Anodes. *J. Mater. Chem. A* **2014**, *2*, 2504-2516.
381. Nam, D. H.; Kim, R. H.; Han, D. W.; Kwon, H. S., Electrochemical Performances of Sn Anode Electrodeposited on Porous Cu Foam for Li-Ion Batteries. *Electrochim. Acta* **2012**, *66*, 126-132.
382. Jiang, T.; Zhang, S.; Qiu, X.; Zhu, W.; Chen, L., Preparation and Characterization of Tin-Based Three-Dimensional Cellular Anode for Lithium Ion Battery. *J. Power Sources* **2007**, *166*, 503-508.
383. Im, H. S.; Cho, Y. J.; Lim, Y. R.; Jung, C. S.; Jang, D. M.; Park, J.; Shojaei, F.; Kang, H. S., Phase Evolution of Tin Nanocrystals in Lithium Ion Batteries. *ACS Nano* **2013**, *7*, 11103-11111.
384. Xu, L.; Kim, C.; Shukla, A. K.; Dong, A.; Mattox, T. M.; Milliron, D. J.; Cabana, J., Monodisperse Sn Nanocrystals as a Platform for the Study of Mechanical Damage During Electrochemical Reactions with Li. *Nano Lett.* **2013**, *13*, 1800-1805.
385. Kravchuk, K.; Protesescu, L.; Bodnarchuk, M. I.; Krumeich, F.; Yarema, M.; Walter, M.; Guntlin, C.; Kovalenko, M. V., Monodisperse and Inorganically Capped Sn and Sn/SnO₂ Nanocrystals for High-Performance Li-Ion Battery Anodes. *J. Am. Chem. Soc.* **2013**, *135*, 4199-4202.
386. Zhao, Z. W.; Guo, Z. P.; Wexler, D.; Ma, Z. F.; Wu, X.; Liu, H. K., Titania Nanotube Supported Tin Anodes for Lithium Intercalation. *Electrochem. Commun.* **2007**, *9*, 697-702.
387. Wei, Z.; Mao, H.; Huang, T.; Yu, A., Facile Synthesis of Sn/TiO₂ Nanowire Array Composites as Superior Lithium-Ion Battery Anodes. *J. Power Sources* **2013**, *223*, 50-55.
388. Han, C.; Liu, Q.; Ivey, D. G., Kinetics of Sn Electrodeposition from Sn(II)-Citrate Solutions. *Electrochim. Acta* **2008**, *53*, 8332-8340.
389. Hanzu, I.; Djenizian, T.; Ortiz, G. F.; Knauth, P., Mechanistic Study of Sn Electrodeposition on TiO₂ Nanotube Layers: Thermodynamics, Kinetics, Nucleation, and Growth Modes. *J. Phys. Chem. C* **2009**, *113*, 20568-20575.
390. Rajh, T.; Chen, L. X.; Lukas, K.; Liu, T.; Thurnauer, M. C.; Tiede, D. M., Surface Restructuring of Nanoparticles: An Efficient Route for Ligand-Metal Oxide Crosstalk. *J. Phys. Chem. B* **2002**, *106*, 10543-10552.
391. Redmond, G.; Fitzmaurice, D.; Graetzel, M., Effect of Surface Chelation on the Energy of an Intraband Surface State of a Nanocrystalline Titania Film. *J. Phys. Chem.* **1993**, *97*, 6951-6954.
392. Moser, J.; Punchedewa, S.; Infelta, P. P.; Graetzel, M., Surface Complexation of Colloidal Semiconductors Strongly Enhances Interfacial Electron-Transfer Rates. *Langmuir* **1991**, *7*, 3012-3018.

393. Rajh, T.; Nedeljkovic, J. M.; Chen, L. X.; Poluektov, O.; Thurnauer, M. C., Improving Optical and Charge Separation Properties of Nanocrystalline TiO₂ by Surface Modification with Vitamin C. *J. Phys. Chem. B* **1999**, *103*, 3515-3519.
394. Kang, C. D.; Jang, J. H.; Kim, K. W.; Lee, H. J.; Jeong, C. S.; Kim, C. M.; Kim, S. H.; Chung, B. S., Activation of C-Jun N-Terminal Kinase/Stress-Activated Protein Kinase and the Decreased Ratio of Bcl-2 to Bax Are Associated with the Auto-Oxidized Dopamine-Induced Apoptosis in Pc12 Cells. *Neurosci. Lett.* **1998**, *256*, 37-40.
395. Cohen, G.; Heikkila, R. E.; With the technical assistance of MacNamee, D., The Generation of Hydrogen Peroxide, Superoxide Radical, and Hydroxyl Radical by 6-Hydroxydopamine, Dialuric Acid, and Related Cytotoxic Agents. *J. Biol. Chem.* **1974**, *249*, 2447-2452.
396. Graham, D. G.; Tiffany, S. M.; Bell, W. R., Jr.; Gutknecht, W. F., Autoxidation Versus Covalent Binding of Quinones as the Mechanism of Toxicity of Dopamine, 6-Hydroxydopamine, and Related Compounds toward C1300 Neuroblastoma Cells in Vitro. *Mol. Pharmacol.* **1978**, *14*, 644-53.
397. Hastings, T. G., Enzymatic Oxidation of Dopamine: The Role of Prostaglandin H Synthase. *J. Neurochem.* **1995**, *64*, 919-24.
398. Jenner, P.; Olanow, C. W., Oxidative Stress and the Pathogenesis of Parkinson's Disease. *Neurology* **1996**, *47*, S161-70.
399. Valverde-Aguilar, G.; Prado-Prone, G.; Vergara-Aragón, P.; Garcia-Macedo, J.; Santiago, P.; Rendón, L., Photoconductivity Studies on Nanoporous TiO₂/Dopamine Films Prepared by Sol-Gel Method. *Appl. Phys. A* **2013**, *116*, 1075-1084.
400. Etacheri, V.; Marom, R.; Elazari, R.; Salitra, G.; Aurbach, D., Challenges in the Development of Advanced Li-Ion Batteries: A Review. *Energy Environ. Sci.* **2011**, *4*, 3243-3262.
401. Tarascon, J. M.; Armand, M., Issues and Challenges Facing Rechargeable Lithium Batteries. *Nature* **2001**, *414*, 359-367.
402. Bruce, P. G.; Scrosati, B.; Tarascon, J. M., Nanomaterials for Rechargeable Lithium Batteries. *Angew. Chem. Int. Ed. Engl.* **2008**, *47*, 2930-46.
403. Scrosati, B.; Hassoun, J.; Sun, Y. K., Lithium-Ion Batteries. A Look into the Future. *Energy Environ. Sci.* **2011**, *4*, 3287-3295.
404. Goodenough, J. B.; Kim, Y., Challenges for Rechargeable Batteries. *J. Power Sources* **2011**, *196*, 6688-6694.
405. Wu, H.; Cui, Y., Designing Nanostructured Si Anodes for High Energy Lithium Ion Batteries. *Nano Today* **2012**, *7*, 414-429.
406. Bouchet, R., et al., Single-Ion Bab Triblock Copolymers as Highly Efficient Electrolytes for Lithium-Metal Batteries. *Nat. Mater.* **2013**, *12*, 452-457.
407. Fergus, J. W., Ceramic and Polymeric Solid Electrolytes for Lithium-Ion Batteries. *J. Power Sources* **2010**, *195*, 4554-4569.
408. Quartarone, E.; Mustarelli, P., Electrolytes for Solid-State Lithium Rechargeable Batteries: Recent Advances and Perspectives. *Chem. Soc. Rev.* **2011**, *40*, 2525-2540.
409. Smith, D. M.; Dong, B.; Marron, R. W.; Birnkrant, M. J.; Elabd, Y. A.; Natarajan, L. V.; Tondiglia, V. P.; Bunning, T. J.; Li, C. Y., Tuning Ion Conducting Pathways Using Holographic Polymerization. *Nano Lett.* **2012**, *12*, 310-314.
410. Liu, W.; Liu, N.; Sun, J.; Hsu, P. C.; Li, Y.; Lee, H. W.; Cui, Y., Ionic Conductivity Enhancement of Polymer Electrolytes with Ceramic Nanowire Fillers. *Nano Lett.* **2015**, *15*, 2740-2745.

411. Cai, Z.; Liu, Y.; Liu, S.; Li, L.; Zhang, Y., High Performance of Lithium-Ion Polymer Battery Based on Non-Aqueous Lithiated Perfluorinated Sulfonic Ion-Exchange Membranes. *Energy Environ. Sci.* **2012**, *5*, 5690-5693.
412. Heitner-Wirguin, C., Recent Advances in Perfluorinated Ionomer Membranes: Structure, Properties and Applications. *J. Membr. Sci.* **1996**, *120*, 1-33.
413. Croce, F.; Appetecchi, G. B.; Persi, L.; Scrosati, B., Nanocomposite Polymer Electrolytes for Lithium Batteries. *Nature* **1998**, *394*, 456-458.
414. Croce, F.; Sacchetti, S.; Scrosati, B., Advanced, Lithium Batteries Based on High-Performance Composite Polymer Electrolytes. *J. Power Sources* **2006**, *162*, 685-689.
415. Riley, M.; Fedkiw, P. S.; Khan, S. A., Transport Properties of Lithium Hectrite-Based Composite Electrolytes. *J. Electrochem. Soc.* **2002**, *149*, A667-A674.
416. Bavykin, D. V.; Friedrich, J. M.; Walsh, F. C., Protonated Titanates and TiO₂ Nanostructured Materials: Synthesis, Properties, and Applications. *Adv. Mater.* **2006**, *18*, 2807-2824.
417. Ou, H.-H.; Lo, S.-L., Review of Titania Nanotubes Synthesized Via the Hydrothermal Treatment: Fabrication, Modification, and Application. *Separation and Purification Technology* **2007**, *58*, 179-191.
418. Bavykin, D. V.; Walsh, F. C., Elongated Titanate Nanostructures and Their Applications. *Eur. J. Inorg. Chem.* **2009**, *2009*, 977-997.
419. Li, Q.; Zhang, H.; Tu, Z.; Yu, J.; Xiong, C.; Pan, M., Impregnation of Amine-Tailored Titanate Nanotubes in Polymer Electrolyte Membranes. *J. Membr. Sci.* **2012**, *423-424*, 284-292.
420. Vasconcelos, D. C. L.; Costa, V. C.; Nunes, E. H. M.; Sabioni, A. n. C. S.; Gasparon, M.; Vasconcelos, W. L., Infrared Spectroscopy of Titania Sol-Gel Coatings on 316L Stainless Steel. *Materials Sciences and Applications* **2011**, *Vol.02No.10*, 8.
421. Vandenberg, E. T.; Bertilsson, L.; Liedberg, B.; Uvdal, K.; Erlandsson, R.; Elwing, H.; Lundström, I., Structure of 3-Aminopropyl Triethoxy Silane on Silicon Oxide. *J. Colloid Interface Sci.* **1991**, *147*, 103-118.
422. Tasviri, M.; Rafiee-Pour, H. A.; Ghourchian, H.; Gholami, M. R., Amine Functionalized TiO₂-Carbon Nanotube Composite: Synthesis, Characterization and Application to Glucose Biosensing. *Appl. Nanosci.* **2011**, *1*, 189-195.
423. Shimizu, I.; Okabayashi, H.; Taga, K.; Nishio, E.; O'Connor, C. J., Diffuse Reflectance Infrared Fourier Transform Spectral Study of the Thermal and Adsorbed-Water Effects of a 3-Aminopropyltriethoxysilane Layer Modified onto the Surface of Silica Gel. *Vib. Spectrosc.* **1997**, *14*, 113-123.
424. Yang, S.; Feng, X.; Müllen, K., Sandwich-Like, Graphene-Based Titania Nanosheets with High Surface Area for Fast Lithium Storage. *Adv. Mater.* **2011**, *23*, 3575-3579.
425. Claesson, M.; Cho, N. J.; Frank, C. W.; Andersson, M., Vesicle Adsorption on Mesoporous Silica and Titania. *Langmuir* **2010**, *26*, 16630-16633.
426. Palmqvist, A. E. C., Synthesis of Ordered Mesoporous Materials Using Surfactant Liquid Crystals or Micellar Solutions. *Curr. Opin. Colloid Interface Sci.* **2003**, *8*, 145-155.
427. Schlipf, D. M. Biomolecule Localization and Surface Engineering within Size Tunable Nanoporous Silica Particles. University of Kentucky, Lexington, KY, 2015.
428. Kasemo, B.; Lausmaa, J., Aspects of Surface Physics on Titanium Implants. *Swed. Dent. J. Suppl.* **1985**, *28*, 19-36.
429. Kunze, A.; Sjövall, P.; Kasemo, B.; Svedhem, S., In Situ Preparation and Modification of Supported Lipid Layers by Lipid Transfer from Vesicles Studied by Qcm-D and Tof-Sims. *J. Am. Chem. Soc.* **2009**, *131*, 2450-1.

430. Rossetti, F. F.; Textor, M.; Reviakine, I., Asymmetric Distribution of Phosphatidyl Serine in Supported Phospholipid Bilayers on Titanium Dioxide. *Langmuir* **2006**, *22*, 3467-3473.
431. Wang, F.; Liu, J., Liposome Supported Metal Oxide Nanoparticles: Interaction Mechanism, Light Controlled Content Release, and Intracellular Delivery. *Small* **2014**, *10*, 3927-3931.
432. Kasemo, B.; Lausmaa, J., Biomaterial and Implant Surfaces: On the Role of Cleanliness, Contamination, and Preparation Procedures. *J. Biomed. Mater. Res.* **1988**, *22*, 145-158.
433. Höök, F.; Kasemo, B.; Grunze, M.; Zauscher, S., Quantitative Biological Surface Science: Challenges and Recent Advances. *ACS Nano* **2008**, *2*, 2428-2436.
434. Wei, T. C.; Hillhouse, H. W., Mass Transport and Electrode Accessibility through Periodic Self-Assembled Nanoporous Silica Thin Films. *Langmuir* **2007**, *23*, 5689-5699.
435. Spencelayh, M. J.; Cheng, Y.; Bushby, R. J.; Bugg, T. D.; Li, J. J.; Henderson, P. J.; O'Reilly, J.; Evans, S. D., Antibiotic Action and Peptidoglycan Formation on Tethered Lipid Bilayer Membranes. *Angew. Chem. Int. Ed. Engl.* **2006**, *45*, 2111-6.
436. Chernomordik, L. V.; Sukharev, S. I.; Popov, S. V.; Pastushenko, V. F.; Sokirko, A. V.; Abidor, I. G.; Chizmadzhev, Y. A., The Electrical Breakdown of Cell and Lipid Membranes: The Similarity of Phenomenologies. *Biochim. Biophys. Acta* **1987**, *902*, 360-373.
437. Legin, M.; Laputkova, G.; Sabo, J.; Vojcikova, L., Impedance Spectroscopy of Bilayer Lipid Membranes Self-Assembled on Agar Support - Interaction with Hdl. *Physiol. Res.* **2007**, *56 Suppl 1*, S85-91.
438. Lundgren, A.; Hedlund, J.; Andersson, O.; Brändén, M.; Kunze, A.; Elwing, H.; Höök, F., Resonance-Mode Electrochemical Impedance Measurements of Silicon Dioxide Supported Lipid Bilayer Formation and Ion Channel Mediated Charge Transport. *Anal. Chem.* **2011**, *83*, 7800-7806.
439. Naumann, R.; Baumgart, T.; Gräber, P.; Jonczyk, A.; Offenhäusser, A.; Knoll, W., Proton Transport through a Peptide-Tethered Bilayer Lipid Membrane by the H⁺-Atp Synthase from Chloroplasts Measured by Impedance Spectroscopy. *Biosensors and Bioelectronics* **2002**, *17*, 25-34.
440. Purrucker, O.; Hillebrandt, H.; Adlkofer, K.; Tanaka, M., Deposition of Highly Resistive Lipid Bilayer on Silicon-Silicon Dioxide Electrode and Incorporation of Gramicidin Studied by Ac Impedance Spectroscopy. *Electrochimica Acta* **2001**, *47*, 791-798.
441. Atanasov, V.; Knorr, N.; Duran, R. S.; Ingebrandt, S.; Offenhäusser, A.; Knoll, W.; Köper, I., Membrane on a Chip: A Functional Tethered Lipid Bilayer Membrane on Silicon Oxide Surfaces. *Biophysical Journal* **2005**, *89*, 1780-1788.

Vita

PLACE OF BIRTH:

Nagpur, India

EDUCATION:

Bachelor of Chemical Engineering, Institute of Chemical Technology, Mumbai, India, 2011

PUBLICATIONS:

Nagpure, S., Zhang, Q., Islam, S., Xu, J., Cheng, Y. T., Rankin, S. E., “Layer-by-layer Synthesis of Thick Mesoporous Titania Films with Vertically Oriented 2D-HCP Nanopores and Their Application as Negative Electrodes in Lithium Ion Batteries” **In Preparation**

Nagpure, S., Guduru, S., Govindrajan, R., Singh, V., Rankin, S. E., “Highly Efficient Nanoporous n-TiO₂/p-CdTe Thin Film Solar Cells with Enhanced Response in the Near-UV Region of the Solar Spectrum” **In Preparation**

Nagpure, S., Browning, J., Rankin, S. E., “Incorporating Poly(3-hexylthiophene) into Orthogonally Aligned Cylindrical Nanopores of Titania for Inorganic-Organic Hybrid Solar Cells” **Under Review Microporous and Mesoporous Materials**

Nagpure, S., Das, S., Garlapalli, R., Strzalka, J., Rankin, S. E., “*In-Situ* GISAXS Investigation of Low-Temperature Aging in Oriented Surfactant-Mesostructured Titania Thin Films” **Journal of Physical Chemistry C**, 2015, 119, 22970-22984

Das, S., **Nagpure, S.**, Garlapalli, R., Wu, Q., Islam, S., Strzalka, J., Rankin, S. E., “Pore Orientation Effects on the Kinetics of Mesostructure Loss in Surfactant Templated Titania Thin Films” **Physical Chemistry Chemical Physics**, 2016, 18, 2896-2905

Das, S., Wu, Q., Garlapalli, R., **Nagpure, S.**, Strzalka, J., Jiang, Z., Rankin, S. E., “*In-Situ* GISAXS Investigation of Pore Orientation Effects on the Thermal Transformation Mechanism in Mesoporous Titania Thin Film”, **Journal of Physical Chemistry C**, 2013, 118, 968-976

PRESENTATIONS:

“Energy Conversion and Storage Applications of Mesoporous Titania Thin Films with Controlled Pore Orientation” **TMS Annual Meeting, Nashville, 2016**

“Synthesis of Layer-by-layer Thick Mesoporous Titania Films with Vertically Oriented 2D-HCP Nanopores and Their Use in Lithium Ion Batteries as Negative Electrodes”, **AICHE Annual meeting, Salt Lake City (2015)**

“In-Situ GISAXS Investigation of Mesostructure Formation during Aging in Mesoporous Titania Thin Films”, **AICHE Annual meeting, Atlanta, GA, (2014)**

“Use of Mesoporous Titania Thin Films with Controlled Pore Orientation in Photovoltaic Applications”, **AICHE Annual meeting, Atlanta, GA, (2014)**

“Strategies for Incorporating P3HT into Orthogonally Aligned Cylindrical Nanopores of Titania for Inorganic-Organic Hybrid Solar Cells” **MRS Photovoltaic Materials and Manufacturing Issues III, Golden, CO, (2013)**

“Incorporating P3HT into Orthogonally Aligned Cylindrical Nanopores of Titania for Inorganic-Organic Hybrid Solar Cells”, **AICHE Annual meeting, San Francisco, CA, (2013)**

“Titania Films with Orthogonally Aligned Cylindrical Nanopores for Bulk Heterojunction Solar Cells”, **MRS Spring Meeting, San Francisco, CA, (2013)**

“Tuning the structure of titania films with orthogonally aligned cylindrical nanopores for bulk heterojunction inorganic-organic solar cells”, **AICHE Annual meeting, Pittsburgh, PA, (2012)**

Suraj R. Nagpure

08/11/2016